p-ISSN 1811-1165
e-ISSN 2413-2179
VOLUME 17, No. 2(34), 2020

EURASIAN PHYSICAL TECHNICAL JOURNAL

E.A. BUKETOV KARAGANDA UNIVERSITY

KARAGANDA, THE REPUBLIC OF KAZAKHSTAN

EURASIAN PHYSICAL TECHNICAL JOURNAL

p - ISSN 1811-1165
e - ISSN 2413-2179

Volume 17, No. 2(34), 2020

1st issue – March, 2004

Journal Founder:

E.A. BUKETOV KARAGANDA UNIVERSITY

Е.А.БӨКЕТОВ АТЫНДАҒЫ ҚАРАҒАНДЫ УНИВЕРСИТЕТІ

КАРАГАНДИНСКИЙ УНИВЕРСИТЕТ ИМ. Е.А.БУКЕТОВА

Contact information:

Editorial board of EPhTJ (Build. 2, room 216)
E.A. Buketov Karaganda University
Universitetskaya Str.28, Karaganda,
Kazakhstan, 100028
Subscription index: 75240

Tel: +7(7212)77-04-03
Fax: +7(7212)77-03-84
E-mail: ephtj@mail.ru

Signed to print on 24.12.2020.
Format 60x84 1/8. Offset paper.
Volume 21.0 p.sh. Circulation 300 copies.
Agreed price. Order No. 97.

Басуға 24.12.2020 ж. қол қойылды.
Пішімі 60×84 1/8. Офсеттік қағазы.
Көлемі 21.0 ес.-б.т. Таралымы 300 дана.
Бағасы келісім бойынша. Тапсырыс № 97.

Подписано к печати 24.12.2020.
Формат 60 × 84 1/8. Офсетная бумага.
Объем 21.0 печ.л. Тираж 300 экз.
Цена договорная. Заказ № 97.

Printed in the Publishing House
of the E.A. Buketov KarU

Е.А. Бөкетов атындағы ҚарУ баспасының
баспаханасында басылып шықты

Отпечатано в типографии Издательства
КарУ имени Е.А. Букетова
г. Караганда, ул. Университетская, 28

Registration Certificate No.4382-Zh, November 7, 2003.
Re-registration Certificate No.KZ50VPY00027647, October 6, 2020 issued by Information Committee of the Ministry of Information and Public Development of the Republic of Kazakhstan

Eurasian Physical Technical Journal, Vol. 17, No. 2(34) 2020

CONTENTS

Dear authors and readers!
Dear Colleagues!

The prevalence of our scientific Journal in international citation bases continues to expand. On December 15, 2020, an Official Confirmation and a Certificate were received that «Eurasian Physical Technical Journal» was included in the indexing database of the Russian Science Citation Index (RSCI) on the Web of Science platform!

In October 2020, the «Eurasian phys. tech. j.» was registered on the website eLibrary.ru, assigned eLIBRARY ID: 73915 (www.elibrary.ru/title_about_new.asp?id=73915).

Since May 2019 «Eurasian phys. tech. j.» has been indexed in the Scopus database. As December 7, 2020 Journal's CiteScoreTracker is 0.4 with a maximum percentile of 16% in Energy, https://www2.scopus.com/sourceid /21100920795#tabs=0

These remarkable confirmations of international recognition were achieved thanks to our article authors, who presented the results of scientific research on the most pressing problems of modern physics and technology and due to the high-quality work of the editorial board members and experts who prepared materials for publication. It should be noted that the implementation and formation of the «Eurasian phys. tech.j.» as an international scientific journal with a non-zero impact factor in the Scopus database became possible thanks to the support of our University, which fully provides funding for the publication.

By tradition, we congratulate happy birthday to our editors and experts.

Congratulations to Ernst Rafailovich Schrager, Doctor of Physics and Mathematics, Professor of Tomsk National University, on his 80th birthday! Professor Shrager E.R. is a representative of the scientific direction of combustion and gas dynamics. Author of over 250 works, among which there is a stamp "for special use". Admiration is caused by such names as "... development of new high-energy materials and technical solutions for promising hybrid engines for space purposes", methods for determining the parameters of model engines ... solid-propellant rocket engines»… Professor Shrager E.R. are known as an erudite professional, an experienced teacher, a scientific leader who has brought up more than one generation of physicists and teachers, scientific personnel and engineers of many research centers in Russia, Kazakhstan and other countries. Achievements Professor E.R. Schrager awarded with high state awards of the Russian Federation. Professor E.R. Schrager is a member of the editorial board of the «Eurasian phys. tech. j.» since 2004, works on joint scientific projects. Thanks to his assistance, many employees of our Faculty became holders of RFBR grants and had the opportunity to train and conduct research in TSU laboratories.

On the eve of Energy Day, December 21, we congratulated with 70th birthday Doctor of Physical and Mathematical Sciences, Professor Yershina Ainakul Kapasovna. Professor Yershina A.K. is a laureate of the first K.I. Satpayev prize. She is member of the National Committee on Theoretical and Applied Mechanics, member of the Use of Renewable Energy Sources Committee of the Russian Union of Scientific and Engineering Organizations, holder of the International Scholarship "Bolashak" and grant "The Best Teacher of the University of the Republic of Kazakhstan". A.K. Yershina's scientific interests are related to the problems of wind power, she is one of the developers of the vertical-axial wind turbine, Bidarrieus-2. She is author of over 120 scientific papers. Professor Yershina A.K. awarded with international and state awards, including the Wilhelm Leibniz medal, the Silver medal "Ulagat" for a special contribution to the development of the of Kazakh National Women's Teacher Training University (Almaty), etc. Professor Yershina A.K. for many years is an expert of the «Eurasian phys. tech. j.».

In accordance with the requirements for international scientific publications, the editorial board is updated. In 2020, two leading scientists who previously published their papers in «Eurasian phys. tech.j.».

One of them is Doctor of Physical and Mathematical Sciences, Professor, Academician of the International Engineering Academy, member of the Presidium of the National Engineering Academy of Sciences of the Republic of Kazakhstan, Academician of the Russian Academy of Natural Sciences, Academician and member of the Presidium of the Kazakhstan National Academy of Natural Sciences, Kadyrzhanov Kairat Kamalovich, who celebrated his 75th anniversary on December 5. Professor Kadyrzhanov K.K. is widely known as a specialist in the field of radiation physics of solids, elemental and

phase-structural analysis of surface layers of materials, thermodynamics of layered solid-state structures, ion implantation and ion-plasma deposition, radiation ecology and high-tech nuclear technologies. He passed the way of formation from a teacher to the director of the Institute of Nuclear Physics of the National Nuclear Center of the Republic of Kazakhstan. Since 1997 Kadyrzhanov K.K. is the head of radioecological research of the former nuclear test sites territories and man-made objects in the west of Kazakhstan. Professor Kadyrzhanov K.K. is winner of the Academician Chokin Sh. Prize (2004), awarded the gold badge "Honored Worker of the Nuclear Industry of the Kazakhstan", the Orden "Kurmet" (2008), "E.P.Slavsky" medal (Russia), honored the State Prize of the Republic of Kazakhstan for Science and Technology (2009), ect. He is member of the International Council for the Application of the Mössbauer Effect, etc.

The second new editor is Narimanova Gufana Nurlanbekovna, Candidate of Physical and Mathematical Sciences, Professor, Dean of the Faculty of Innovative Technologies, Head of the Department of Innovation Management, Tomsk University of Control Systems and Radioelectronics. She is author of the 80 scientific publications. Professor Narimanova G.N. is an accredited expert in the field of state accreditation of the Russian Federation educational institutions and scientific organizations in the following areas: physics, mechatronics and robotics, management in technical systems. She is member of the Federal Educational and Methodological Association in the system of higher education according to UGSN 27.00.00 "Management in technical systems". Professor Narimanova G.N. for many years is an expert of «Eurasian phys. tech.j.». She was a member of organizing committee of the international conference "Chaos and structures in nonlinear systems" and organizer of the undergraduates educational program with the issuance of double diplomas of E.A. Buketov Karaganda University and Tomsk University of Control Systems and Radioelectronics.

We wish health, prosperity and creative success! We hope that in the future, joint work in the editorial board will contribute to strengthening international cooperation and improving the quality of our journal.

This issue has been present original scientific articles devoted to solving urgent problems of modern technical physics. For example, the study of changes in the structural properties of nanoporous semiconductors or ferrites under various conditions of heat treatment, the effect of the phase composition on the properties of various films and coatings, etc. There are interesting results of modeling complex physical and technical processes of convective heat transfer in a turbulent medium, heat and mass transfer at high humidity, etc. The structure of cohomological models of electrodynamics and general theory of relativity, as well as the problems of alternative energy and methods for solving modern engineering problems are considered.

In addition, we inform You that on October 6, 2020 «Eurasian phys. tech. j.» is received a Certificate of re-registration No.KZ50VPY00027647 issued by Information Committee of the Ministry of Information and Public Development of the Republic of Kazakhstan. According this since 2021 «Eurasian phys. tech. j.» will be published quarterly.

We hope to see you more often among the authors in the next issues.

Respectfully,
Chief Editor, Saule E. Sakipova
Kazakhstan, December, 2020

DOI 10.31489/2020No2/6-10

UDC 538.9

FORMATION OF MAGNETIC PROPERTIES OF FERRITES DURING RADIATION-THERMAL SINTERING

Stary O[1]., Malyshev A.V.[2], Lysenko E.N.[2], Petrova A.[2]

[1]Czech Technical University in Prague, Prague, Czech Republic
[2]Tomsk Polytechnic University, 30 Lenin Avenue, 634050 Tomsk, Russia, *malyshev@tpu.ru

The results of a comparative analysis of the laws governing the formation of ferrite hysteresis loop parameters sintered in thermal and radiation-thermal conditions were shown. The influence of radiation exposure on the interconversion of microstructure defects and their content in ferrites, depending on the duration and temperature of treatment, was established. Also, it was shown that recrystallization grain growth under irradiation conditions is ahead of grain growth during thermal heating. The observed radiation effects were associated with the effect of radiation on the microstructure. The magnetic parameters are uniquely determined by the compaction of the sample.

Keywords: effects of radiation, ferrites, magnetic properties, microstructure, sintering, hysteresis loop, coercive force, pore volume.

Introduction

The most universal requirement for the microstructure of ferrites is the condition for the maximum density of the material and the equigranular structure [1, 2]. For comply with these requirements, at economically reasonable firing times, several methods have been developed to increase the activity of sintering processes. This is the two-stage introduction of the components, the addition of ferrite with a ferrite powder of the same composition, the presence of a liquid phase, forced sintering, the application of ultrasound to the sintering process [1, 3, 4–12].

In recent years, the effects of ionizing radiation fluxes in the preparation and modification of materials were developed. In this case, the fundamental phenomenon of multiple increases in the synthesis of multicomponent powder materials [13–15] and sintering [16–20] under radiation-thermal conditions was discovered. The sintering processes of lithium titanium ferrites were most fully studied under such specific conditions of the combined action of high temperatures and intense electron flows [21, 22]. The patterns of compaction of ferrite compacts were established and a multiple increase in the compaction rate of lithium-titanium ferrite compacts under such sintering conditions was shown [23, 24]. Moreover, almost all studies concerned the study of the structural, phase, and mechanical properties of the materials thus obtained, i.e. concerned such areas of science as sintering physics and powder metallurgy.

However, the main functional characteristics of ferrimagnets are their magnetic properties, and the ultimate goal of any ferrite production technology is to achieve a given level of operational properties. Therefore, control over the formation of the basic electromagnetic parameters is a prerequisite in the development of new technological processes. On the other side, the processes of magnetization reversal and electric transport in ferrites are closely related to the features of their microstructure. Therefore, the regularities of change in electromagnetic characteristics can be used as a source of important information about the nature of the processes occurring during sintering and, therefore, can help in a more in-depth interpretation of the mechanisms of radiation-thermal sintering.

1. Object of study and experimental technique

In the present work powders of lithium-titanium ferrite synthesized from a mechanical mixture of oxides and carbonates containing (wt.%) were used: Li_2CO_3 - 11.2; TiO_2 - 18.65; ZnO - 7.6; $MnCO_3$ - 2.74; the rest is Fe_2O_3. For prepare a press powder, a 10% solution of polyvinyl alcohol in an amount of 12 wt. % of charge. Press samples in the form of tablets and ring cores with a thickness of 2 mm are made by cold unilateral pressing. The optimum pressing pressure is selected experimentally. It was found that at pressing pressures below 40 MPa, the press samples are characterized by a low density, and at pressing pressures of

more than 250 MPa, the samples have cracks and delaminations (the phenomenon of repressing). Thus, the most optimal pressing pressure, which provides an acceptable density of both raw and sintered samples, is in the range (110–200) MPa.

The following pressing mode was used in the work: P = 130 MPa, the exposure time of the material under pressure 1 min; and two modes of sintering of press samples: radiation-thermal (RT) and thermal (T). RT-sintering was carried out by irradiating the samples with a pulsed electron beam with an energy of the (1.5-2.0) MeV using the ILU-6 accelerator. The beam current in the pulse was (0.5-0.9) A, the irradiation pulse duration was 500 μs, the pulse repetition rate was (5–50) Hz, and the work piece heating rate was 1000 °C/min. The samples were irradiated in a box of lightweight fireclay with a bottom thickness of 15 mm. On the irradiation side, the box was covered with a radiation-transparent tread of mass thickness 0.1 g cm^{-1}. The temperature was measured by a control sample placed close to the sintered blanks.

Sintering in thermal furnaces (T-sintering) was carried out in a preheated chamber electric furnace, which ensured a heating rate comparable with the rate of radiation heating. The cell design and temperature control technique are similar to those used in RT-sintering. Both sintering modes were carried out in air. The magnetic characteristics of ferrites were measured by a standard method with an F 5063 ferrometer. The magnitude of the magnetizing field was 5 Oersted (Oe) at a field frequency of 50 Hz. The degree of porosity and grain size were studied on polished, polished and etched sections of sintered samples using an MBI-15Us optical microscope. The kinetic dependencies of the hysteresis loop parameters B_m, B_r/B_m and H_c of ferrite samples calcined in the temperature range (1173–1373) K were studied.

2. Results and discussion

Figure 1 shows the kinetic dependencies of the saturation magnetic induction B_m for samples with a sintering temperature of 1173, 1273, 1373 K. It can be seen that the B_m increases with increasing duration and sintering temperature. Under conditions of radiation-thermal sintering, the absolute values of B_m exceed the data obtained by thermal sintering. The maximum difference falls on the lower boundary of the sintering temperature range: with increasing temperature, the effect of activating the change in B_m decreases.

The saturation magnetic induction is determined by the crystal chemistry of the material and the relative magnitude of nonmagnetic phases, including pores [25]. The influence of non-magnetic phases is associated with the appearance of demagnetizing fields in their vicinity, and also, these phases do not contribute to the magnetization of ferrite. The initial state of the sample can be considered as a set of magnetic particles separated by air layers, i.e., as a magnetodielectric. This state is characterized by a large internal demagnetizing factor *N*. It is also significant that the saturation magnetization of a magnetodielectric is proportional not only to the saturation magnetization of particles but also to the volumetric filling coefficient $P/\bar{J}_S = P\hat{f}_S$ [6]. Therefore, the resulting saturation induction of the billet is characterized by small B_m. According to Figure 1, it can be seen that the rearrangement of particles (reduction of the air gap) occurs both at the stage of heating and in the isothermal sintering mode. Exposure to radiation also intensifies particle rapprochement. It is characteristic that at the nonisothermal stage of sintering, the radiation effect increases with temperature, and at the isothermal stage, it decreases. This can be seen from the transition from the asymmetric curves *1* and *1*' (at T = 1173 K) to the almost symbate curves *3* and *3*' (at T = 1373 K). The initial values of B_m (at $\tau = 0$), on the contrary, differ more from one another with increasing temperature. Obviously, the polar differences in the temperature dependence of the radiation effect during heating and at the isothermal sintering stage indicate a difference in the mechanisms of particle compaction at these stages.

Figure 2 shows the kinetic curves of the variation of the coefficient of squareness $\gamma = B_r/B_m$ in the temperature range (1173–1373) K. The existence of the time dependence of γ indicates that during sintering, partial elimination of defects that are the sources of magnetization reversal nuclei with a critical magnetic field strength Hni < 0. Indeed, if there are nuclei for which the critical strength of the magnetic field is caused not only by rotations of elementary magnetic moments in the direction of the axis of easy magnetization but also an induction created by reverse magnetic domains. Therefore, elimination of defects – sources of reverse magnetization domains during heat treatment – will increase Br and, accordingly, increase $\gamma.H_{ni} < 0$, then the difference between the saturation induction B_m and the residual induction B_r.

Of all the variety of sources of reverse magnetization domains fired under the conditions of our experiment, the most probable are inclusions of side phases — intermediate synthesis products or unreacted oxides. This is supported by a sign of the diffusion nature of firing, which consists in reducing the effect of radiation stimulation of the process with an increase in sintering temperature (see Fig. 2).

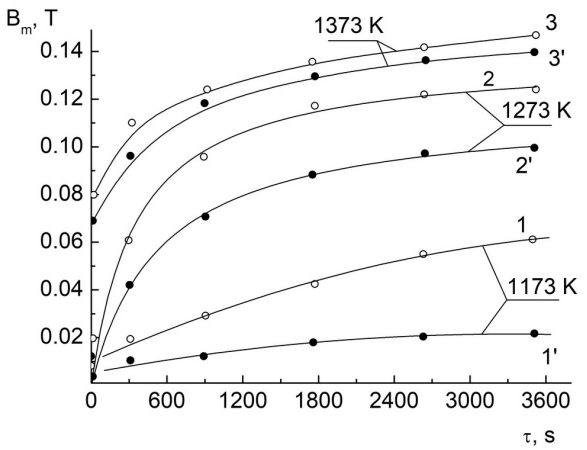

Fig.1. Dependence of saturation induction on time and sintering temperature of ferrite:
● – T-sintering; □ – RT-sintering.

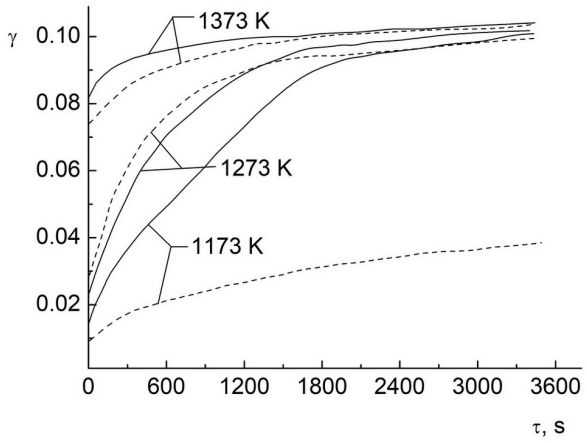

Fig.2. Dependence of coefficient of squareness of the hysteresis loop (γ) on time and sintering temperature of ferrite: solid line – RT-sintering; dash line – T-sintering.

The radiation effect of high-temperature self-diffusion in metals behaves in a similar way, which we established under irradiation conditions identical to our experiment. Figure 3 shows the dependencies of the change in the coercive force H_c on the duration of sintering in radiation-thermal and thermal regimes. At T = 1173 K, the H_c monotonically increases in the entire studied sintering time interval. At T = 1273 K, an increase in H_c at the initial stage of sintering becomes a decreasing dependence. The maximum time dependence of H_c in the conditions of our experiment falls on the sintering duration (12-17 min). At T = 1373 K, only a decreasing dependence of H_c on sintering time is observed. According to existing ideas, the coercive force H_c is determined by averaging the braking forces arising from material defects. The greatest resistance to displacements of domain walls is exerted by grain boundaries (Globus theory [26–28]), as well as intragranular linear, planar, and volume inclusions (Kersten theory [29, 30], Neel [31, 32]).

At T = 1173 K, an increase in H_c is obviously due to a decrease in the internal demagnetizing factor N due to compaction of the billet (with a corresponding increase in the effective magnetic field). As in the case of B_m, the effect of radiation effects of compaction is clearly manifested at this temperature. At 1273 K, an increase in H_c at the initial stage of sintering is also due to compaction of the billet. However, upon reaching a sufficient degree of compaction, changes in the intensity of the internal magnetic field no longer play a noticeable role. From this moment in time, the changes in B_m are also relatively small (Fig. 1). A subsequent decrease in H_c can be associated with a recrystallization increase in grain size and a decrease in the volume fraction of inclusions. At this stage, radiation effects are also clearly manifested. At T = 1373 K, the necessary degree of compaction is achieved in the process of heating the billet for sintering. Therefore, in the isothermal mode, only a decrease in H_c is observed due to the above reasons.

It is characteristic that the radiation effects, depending on H_c on the sintering duration at 1373 K, are not explicitly expressed. At the same time, recrystallization grain growth under irradiation conditions is ahead of grain growth during thermal heating. On this basis, the healing process of intragranular defect can be considered a more probable reason for the decrease in H_c. This process, obviously, has a diffusion character. But, as discussed above, with increasing temperature, the intensity of diffusion processes weakly depends on the effect of radiation. This fact is consistent with the assumptions made.

In discussing the above results, we ignored the possible direct effect of radiation on the formation of the magnetic structure (for example, due to the effect on the cation distribution). The observed radiation effects were associated with the effect of radiation on the microstructure. The validity of this approach is proved by the data presented in Fig. 4, Fig. 5 and Fig. 6, where the dependencies of the magnetic parameters on the pore volume are plotted. The parameters were taken from the data in Fig. 1, Fig. 2 and Fig. 3. The results are depicted in Fig. 4, Fig. 5 and Fig. 6 show that the all parameters are uniquely determined by the compaction of the ferrite samples. It also follows from the presented results that the role of stimulating factors (temperature and radiation) in accelerating of sintering process is reduced.

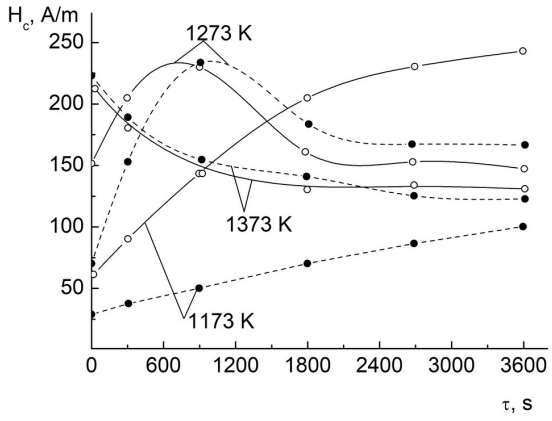

Fig.3. Dependence of coercive force on time and sintering temperature of ferrite: ● – T-sintering; ○ – RT-sintering.

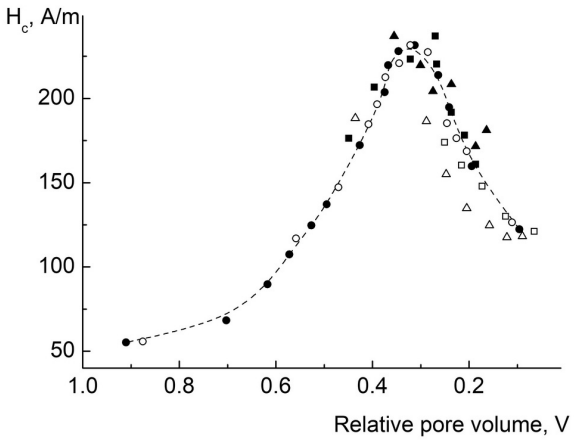

Fig.4. Dependence of coercive force on relative pore volume: ●, ○–1173K; ■, □ – 273K; ▲, Δ – 1373 K.

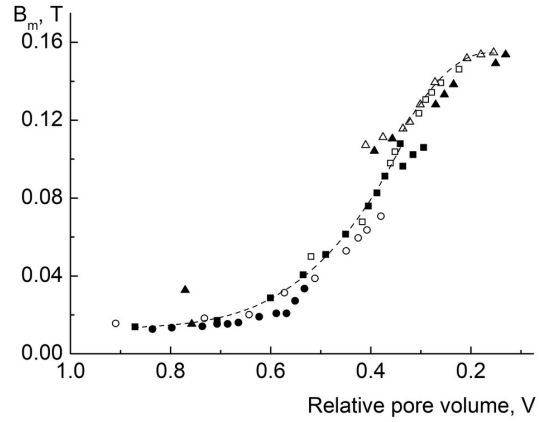

Fig.5. Dependence of saturation induction on relative pore volume of ferrites sintered at various temperatures: ●, ○ – 1173 K; ■, □ – 1273 K; ▲, Δ – 1373 K.

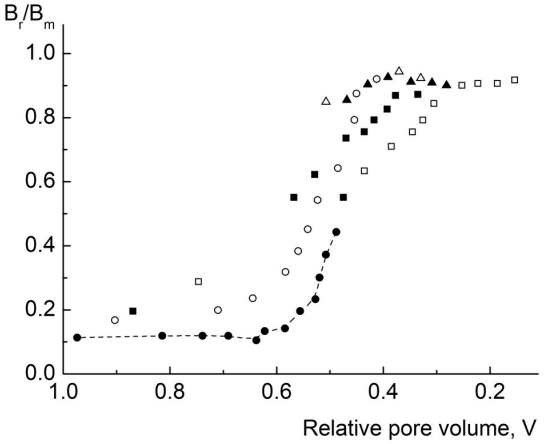

Fig.6. Dependence of coefficient of squareness of the hysteresis loop on relative pore volume of samples sintered at various temperatures:
●, ○ — 1173 K; ■, □ – 1273 K; ▲, Δ – 1373 K.

Conclusion

This investigation presents the results of a study of kinetic laws of formation of the parameters of the hysteresis loop for ferrites sintered under thermal and radiation-thermal conditions. The scientific novelty of the study is to determine the effect of radiation exposure on the mutual conversion of microstructure defects and their content in ferrites, depending on the duration and temperature of treatment. The authors showed for the first time that recrystallization grain growth under irradiation conditions is ahead of grain growth during thermal heating. The observed radiation effects were associated with the effect of radiation on the ferrite microstructure. In addition, it is reliably established that all magnetic parameters are uniquely determined by the compaction of ferrite samples.

Acknowledgments

The research is funded by The Ministry of Education and Science of the Russian Federation as part of the "Science" Program (project FSWW-2020-0014). The results of the coercive force of ferrite samples were obtained within the RFBR grant (project No. 20-07-00662). The experimental calculations are carried out at Tomsk Polytechnic University within the framework of Tomsk Polytechnic University Competitiveness Enhancement Program grant.

REFERENCES

1 Letyuk L.M., Nifontov V.A., Babich E.A., Gorelik S.S. Effect of low-melting additives on the formation of the microstructure and the properties of ferrites with a rectangular hysteresis loop. *Izv. Akad. Nauk Neorg. Mater.* 1976, Vol.12, pp. 2023 – 2026.

2 Zhuravlev G.I., Golubkov L.A., Strakhova T.A. Basic types of microstructure of ferrites and means of obtaining them. *Soviet Powder Metallurgy and Metal Ceramics*. 1990, Vol.29, pp. 478 – 480.

3 Dmitriev M.V., Letyuk L.M., Shipko M.N. Study of oxygen diffusion in the surface layers of Mn-Zn ferrites. *Technical physics*. 1982, Vol.27, pp. 338 – 339.

4 Letyuk L.M. Recrystallization of ferrites and its effect on the processes of microstructure formation in ferrospinels. *Soviet Powder Metallurgy and Metal Ceramics*. 1980, Vol.19, No.5, pp. 359 – 364.

5 Zinovik M.A., Zinovik E.V. Ferrites with rectangular and square hysteresis loops. *Powder Metallurgy and Metal Ceramics*. 2005, Vol.44, p. 66 – 74.

6 Letyuk L.M., et al. Special features of the formation of the microstructure of ferrites sintered in the presence of a liquid phase. Izv.Vysshikh Uchebnykh Zavedenij. Chernaya Metallurgiya. 1979, Vol.11, pp. 124 – 127.

7 Micheli A.L. Preparation of lithium ferrites by coprecipitation. *IEEE Transactions on Magnetics*. 1970, Vol.6, pp. 606 – 608.

8 Bronshteyn I.M., Dyubua B.Ch., Karasik B.S., Khinich I.I. Secondary electron emission of a platinum-barium alloy made by evaporation. *Radio Eng. Electron Phys.* 1974, Vol.19, pp. 108 – 111.

9 Minin V.M. Effect of sintering conditions on the microstructure and electromagnetic properties of Li-Mg-Mn ferrite memory elements. *Soviet Powder Metallurgy and Metal Ceramics*. 1982, Vol.21, pp. 698 – 701.

10 Zahir R., Chowdhury F.-U.-Z., Uddin M.M., et al. Structural, magnetic and electrical characterization of Cd-substituted Mg ferrites synthesized by double sintering technique. *J. Magn. Magn. Mater*. 2016, Vol. 410, pp. 55 – 62.

11 Manjura Hoque S., Abdul Hakim M., Mamun Al, et al. Study of the bulk magnetic and electrical properties of $MgFe_2O_4$ synthesized by chemical method. *Materials Sciences and Applications.* 2011, Vol.2, pp. 1564 – 1569.

12 Hu J., Yan M., Luo W., Wu J.M. Effects of microstructure on the temperature dependence of relative initial permeability of NiCuZn ferrites. *Physica B*. 2007, Vol.400, pp. 119 – 123.

13 Surzhikov A.P., Pritulov A.M., Lysenko E.N., et al. Calorimetric investigation of radiation-thermal synthesized lithium pentaferrite. *Journal of Thermal Analysis and Calorimetry*. 2010, Vol. 101, No. 1, pp. 11-13.

14 Yurov V.M., Baltabekov A.S., Laurinas V.C., Guchenko S.A. Dimensional effects and surface energy of ferroelectric crystals. *Eurasian Physical Technical Journal.* 2019, Vol.16, No.1, pp. 18 – 23.

15 Surzhikov A.P., Frangulyan T.S., Ghyngazov S.A., et al. Pysics of magnetic phenomena: Investigation of electroconductivity of lithium pentaferrite. *Russian Physics Journal*. 2006, Vol. 49, No. 5, pp. 506-510.

16 El-Shobaky G.A., Ibrahim A.A. Solid-solid interactions between ferric oxide and lithium carbonate and the thermal stability of the lithium ferrites produced. Thermochim. Acta. 1987, Vol.118, pp. 151 – 158.

17 Salimov R.A., Cherepkov V.G., Golubenko J.I., et al. D.C. high power electron accelerators of ELV-series: status, development, applications. *J. Radiation Phys.* Chem. 2000, Vol.57, pp. 661 – 665.

18 Cleland M.R., Parks L.A. Medium and high-energy electron beam radiation processing equipment for commercial applications. *Nucl. Instr. Meth. B*. 2003, Vol.208, pp. 74 – 89.

19 Mehnert R. Review of industrial applications of electron accelerators. *Nucl.Instr.Meth.* 1996, Vol.113, pp.81-87.

20 Neronov V.A., Voronin A.P., Tatarintseva M.I., Melekhova T.E., Auslender V.L. Sintering under a high-power electron beam. *J. Less-Common Metals.* 1986, Vol.117, pp. 391 – 394.

21 Surzhikov A.P., Peshev V.V., Pritulov A.M., Gyngazov S.A. Grain-boundary diffusion of oxygen in polycrystalline ferrites. *Russian Physics Journal.* 1999, Vol. 42, No. 5, pp. 490-495.

22 Boldyrev V.V., Voronin A.P., Gribkov O.S., Tkachenko E.V., Karagedov G.R., Yakobson B.I., Auslender V.L. Radiation-thermal synthesis. Current achievement and outlook. *J. Solid State Ion*. 1989, Vol.36, pp. 1 – 6.

23 Surzhikov A.P., Lysenko E.N., Malyshev A.V., et al. Study of the Radio-Wave Absorbing Properties of a Lithium-Zinc Ferrite Based Composite. *Russian Physics Journal.* 2014, Vol. 57, No. 5, pp. 621-626.

24 Surzhikov A.P., et al. Structural, electromagnetic, and dielectric properties of lithium-zinc ferrite ceramics sintered by pulsed electron beam heating. *Ceramics International.* 2017, Vol. 43, No. 13, pp. 9778-9782.

25 Smith J., Wijn H.P.J. Ferrites: Physical properties of ferromagnetic oxides in relation to their technical application. 1959, Eindhoven, Phillips Technical Library, 233p.

26 Globus A. Influence des dimensions des parois la permeability. *C. R. Acad. Sci.* 1962, Vol.255, pp. 1709 – 1711. [in French]

27 Globus A., Guyot M. Wall displacement and bulging in magnetization mechanisms of the hysteresis loop. *Phys. Status Solidi B.* 1972, Vol.52, pp. 427 – 431.

28 Globus A. Some physical consideration about the domain wall sine. Theory of magnetization mechanisms, *J.Phys.* (France). 1977, Vol.38, pp. 1 – 15.

29 Kersten M. Zur wirkung der versetzungen auf die anfangspermeabilität von nickel im rekristallisierten und im plastisch verformten. *Zustand Annalen der Physik.* 1957, Vol.20, No.1-6, pp. 337 – 344. [in German]

30 Kersten M. Reversible und irreversible magnetisierun-gsanderungerlangs der hystereschleife, *Z. Angew. Phys.* 1955, Vol.7, pp. 397 – 407. [in German]

31 Neel L. Energie magnetocrictalline d'ur macrocristal subdivise on crystallites guadretigues, Compt. Rend. Acad. Sci. 1963, Vol.257, pp. 2917 – 2921.

32 Neel L. Defaults ponetuels dansles solides ferromagnetiques et ordre directional. *J. Phys.* (France). 1963, Vol.24, pp. 513 – 516.

Article accepted for publication 19.10.2020

DOI 10.31489/2020No2/11-18

UDC 538.956

VARIATION OF STRUCTURAL PROPERTIES OF Al DOPED Ni-Cd FERRITES WITH SINTERING TIME

Halamani Koushallya M.[1], Mathad Shalini K.[1], Kulkarni Akshay B.[2], Mathad Shridhar N.[3], Jeergal Pundalik. R.[1], Hiremath Chidanandayya.S.[4], Pujar Appanna S.[5], Pujar Rangappa B.[1*]

[1]P.C. Jabin Science College, Karnataka, India

[2]South Konkan Education Society's (SKES's) Govindram Seksaria Science College, Belagavi, India

[3]Karnataka Lingayat Education (K.L.E) Institute of Technology, Gokul, Hubballi, Karnataka, India, physicssiddu@gmail.com,

[4]Shri Kadasiddheshwar Arts College & H.S.Kotambri Science Institute, Vidyanagar, Hubballi, India

[5] Raja Lakhamagouda Science Institute, Belgavi, India, p_rangappa@rediffmail.com

The aim of present work is to synthesis and study the structural properties of Al doped Ni-Cd ferrites, series by ceramic method. The samples are sintered at a temperature of 1100 C with sintering time of t=9, 11, 13, 15 hrs. The samples were characterized by X-ray diffraction, scanning electron microscope, energy dispersive X-ray analysis and Fourier transform-Infrared. The single phase simple cubic spinel structure is confirmed by X-ray diffraction patterns. The lattice parameter is found to be in the range of 8.478 Å - 8.481 Å. The uniform size distribution is observed in the scanning electron microscope micrographs. The elemental analysis is done by energy dispersive X-ray analysis confirming the presence of all the metal ions present in the ferrite formula. Fourier transform-Infrared spectra showed two bands υ_1 (581-582 cm^{-1}) and υ_2 (less than 400 cm^{-1}) which are attributed to metal oxygen bond vibrations at tetrahedral and octahedral sites respectively.

Keywords: X-ray diffraction, scanning electron microscope, energy dispersive X-ray analysis, Fourier transform-Infrared

Introduction

Ferrites are an attractive class of research materials because of their comprehensive physical properties and application in advanced technology. Modification of their structure has been shown to play an important role in the optimization of their structural, optical and electrical properties [1-2]. Cubic spinel ferrites are chemical compounds with the formula of AB_2O_4, where A and B represent various metal cat-ions, usually including iron. In the normal spinel structure, the 8 divalent metal ions go into the A sites, and the 16 trivalent iron ions have preference for B sites [1]. Among the magnetic materials that have found broad practical application in technology, ferrites deserve attention [2].

Cobalt ferrite ($CoFe_2O_4$) has attracted much attention owing to its excellent properties, such as its relatively high saturation magnetization (M_s), high coercivity (H_c), magnetic anisotropy, good chemical stability and good catalytic activity. Its physical properties are strongly dependent on the cation distribution among the tetrahedral (A) and the octahedral (B) sites in the crystal lattice. Depending upon the distribution of the various cat-ion substituents over tetrahedral and octahedral sites, its magnetic and electrical properties can be modified according to the research interest [3].

Spinel ferrite is known to be good candidate for magnetic recording and microwave applications [4]. Nano-sized grains of ferrite are being applied in permanent magnets [5], magnetic drug delivery [6], and high-density information storage [7]. Soft magnetic material have a widespread applications in recording heads, antenna rods, loading coils, microwave devices, core material for power transformers due to their high resistivity and low eddy current losses [8]. Ferrite materials can be prepared by numbers of methods such different routes like co-precipitation [9],solid state reaction [10-11], citrate precursor [12], sol–gel and auto-combustion [13], ball milling [14] hydrothermal [15].

This paper presents the influence of sintering time with the general chemical formula $Ni_{0.5}Cd_{0.5}Al_{0.1}Fe_{1.9}O_4$ series which are prepared by ceramic method. Using X-ray diffraction (XRD), scanning

electron microscope (SEM), energy dispersive X-ray analysis (EDAX) and Fourier transform-Infrared (FT-IR) analysis, detailed structural and mechanical properties of crystalline Ni-Cd-Al spinel ferrites reported in this paper.

1. Experiments

In photo acoustic effect, interaction of electromagnetic radiation with matter generates sound. This effect consists of the absorption of incident radiation by target molecule. Photo acoustic effect is popular due to a minimal sample preparation during execution, the ability to examine scattering and opaque sample [12] along with the capability to access depth profile [13]. The ferrites with general chemical formula $Ni_{0.5}Cd_{0.5}Al_{0.1}Fe_{1.9}O_4$ were synthesized by ceramic method using AR grade Nickel oxide, Cadmium oxide, and Ferric oxide in molar preparation and mixed mechanically in agate motor in acetone medium as shown in Fig.1. Then the ferrites were pre sintered with temperature constant 1100ºc for different time 9 hours, 11 hours, 13 hours, and 15 hours.

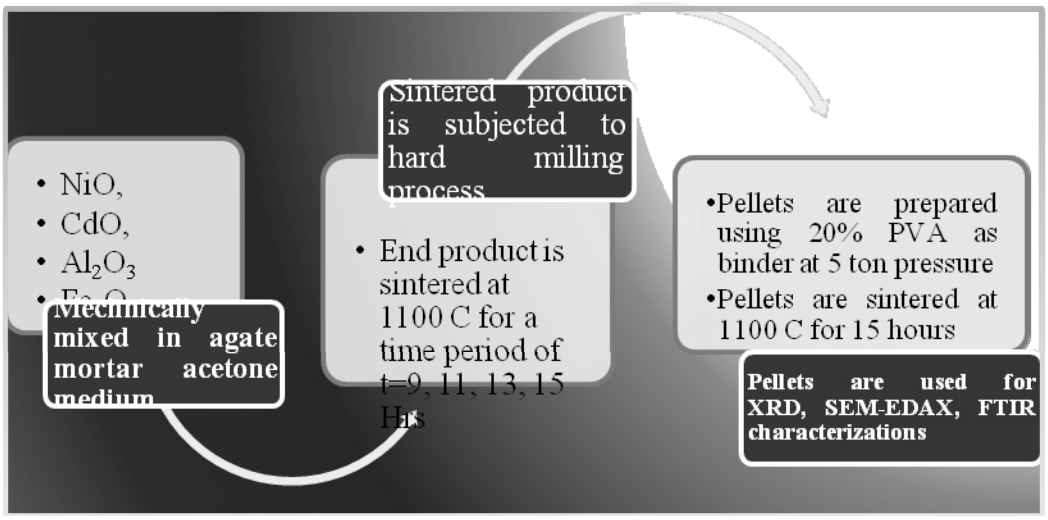

Fig.1. Flow chart of synthesis of ferrite samples using ceramic method.

The pre sintered powders were subjected to hard milling process in acetone medium. One or two drops of PVA solution of 20% concentration was added as binder. All the samples were pressed into two pellets of 1cm in diameter and 0.2 cm in height by applying a pressure of about 5tons/square inch for 5 minutes. The pellets were subjected to final sintering at 1100ºc for 15 hours.

The Structural characterization of the ferrite pellets is carried out the X-ray diffraction patterns of the samples have been obtained on Bruker AXS D8 Advance Diffractometer (XRD), (with Cu-K_α radiation, wavelength, λ= 1.5406 Å), the SEM-EDAX spectrographs of the samples have been obtained on JEOL Model JSM - 6390LV and the FTIR of the samples have been obtained on Thermo Nicolet, Avatar 370.

2. Results and Discussion

2.1. X-ray diffraction (XRD) analysis

XRD patterns of the $Ni_{0.5}Cd_{0.5}Al_{0.1}Fe_{1.9}O_4$ (t=9, 11, 13, 15 hrs) ferrite series is shown in Fig.2. The peaks matched well with those from the Joint Committee on Powder Diffraction Standards (JCPDS) card no.00-022-1086. The reflections observed from the planes (220), (311), (400), (422), (511), (440) and (533) for the samples confirm the formation of a cubic spinel structure.

The lattice parameter of all the samples was calculated and the values are given in Table 1. The lattice parameter was found to remain constant. The hopping length; the bond length, ionic radii and the value of X-ray density (Δx) and stacking fault coefficient were calculated elsewhere [10, 11] and the values are tabulated in Table 1. The actual density is calculated using standard method. The values are tabulated in Table 1.

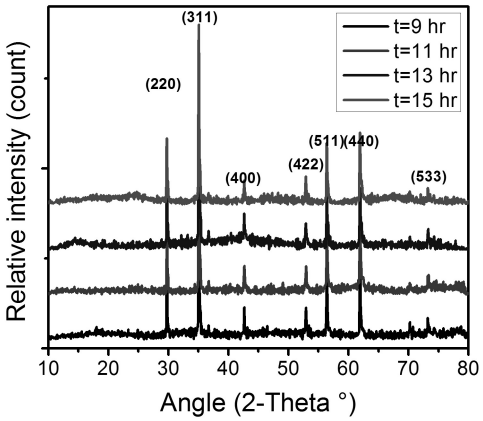

Fig.2. XRD graph of $Ni_{0.5}Cd_{0.5}Al_{0.1}Fe_{1.9}O_4$ferrite synthesized by ceramic method.

Table 1 - Calculated values of lattice parameter, volume of unit cell, hopping length, bond length, ionic radii, stacking fault coefficient, x-ray density, actual density and porosity.

Sintering time (t)	**9 hr**	**11 hr**	**13 hr**	**15 hr**
Lattice parameter a (Å)	8.48	8.47	8.48	8.48
Volume of unit cell V (10^{-30} m^{-3})	609	608	609	610
Hopping length L_A (Å)	3.67	3.67	3.67	3.67
Hopping length L_B (Å)	3.00	3.00	3.00	3.00
Bond Length A-O (Å)	1.94	1.94	1.94	1.94
Bond length B-O (Å)	2.06	2.06	2.06	2.06
Ionic Radii r_A (Å)	0.59	0.59	0.59	0.59
Ionic Radii r_B (Å)	0.71	0.71	0.71	0.71
Stacking fault coefficient α (10^{-3})	0.43	0.45	0.36	0.53
x-ray density Δx (gr/cm^3)	5.63	5.64	5.63	5.63
Actual density d_a (gr/cm^3)	4.38	3.51	3.82	3.76
Porosity (%)	22.24	37.67	32.17	33.25

The crystallite size of ferrite samples was calculated by using Debye-Scherrer [10, 11] equation $D = 0.9 \cdot \lambda / \beta_D \cos\theta$, where D is the crystallite size, β_D is pure diffraction broadening given by the full width half maximum (FWHM) of the peaks, λ is the wavelength of the radiation used, θ is the angle of diffraction. The Dislocation density calculated using two different formulas $\rho_D = 1/D^2$, $\rho_D = 15\varepsilon/aD$ and micro-strain calculated using $\varepsilon = \beta\cos\theta/4$ are also tabulated in Table 2.

Table 2 - Calculated values of crystallite size, micro strain and dislocation density using WH plots, SSP and standard formula.

	Crystallite size (in Å)			Micro strain (10^{-3})			Dislocation density (ρ) (10^{14})	
Sintering time t in hr	From WH graph	From SSP	From formula	Micro strain ε=slope/4 (WH)	Micro strain ε=2*sqrt (intercept) (SSP)	From formula ε=βcosθ/4	$\rho=1/D^2$	$\rho=15\varepsilon/aD$
9	835	651	522	0.61	4.43	0.67	3.84	2.28
11	766	700	439	0.84	7.40	0.81	5.55	3.26
13	462	415	457	0.11	1.81	0.80	5.61	3.09
15	510	501	503	0.05	1.76	0.70	4.22	2.47

2.2. Williamson Hall (WH) plot and Size-Strain (SS) Plot Method

The distinct θ dependencies of size and strain broadening of the diffraction lines laid the basis for Williamson and Hall method (WH). An additional component $\beta_s = 4\varepsilon \tan\theta$ to the Scherrer equation results in WH equation $\beta_{hkl}\cos\theta = \frac{K\cdot\lambda}{D} + 4\varepsilon\sin\theta$, [11, 16].

The WH plots for the $Ni_{0.5}Cd_{0.5}Al_{0.1}Fe_{1.9}O_4$ (t= 9, 11, 13, 15 hrs) are shown Fig. 3 (a-d).

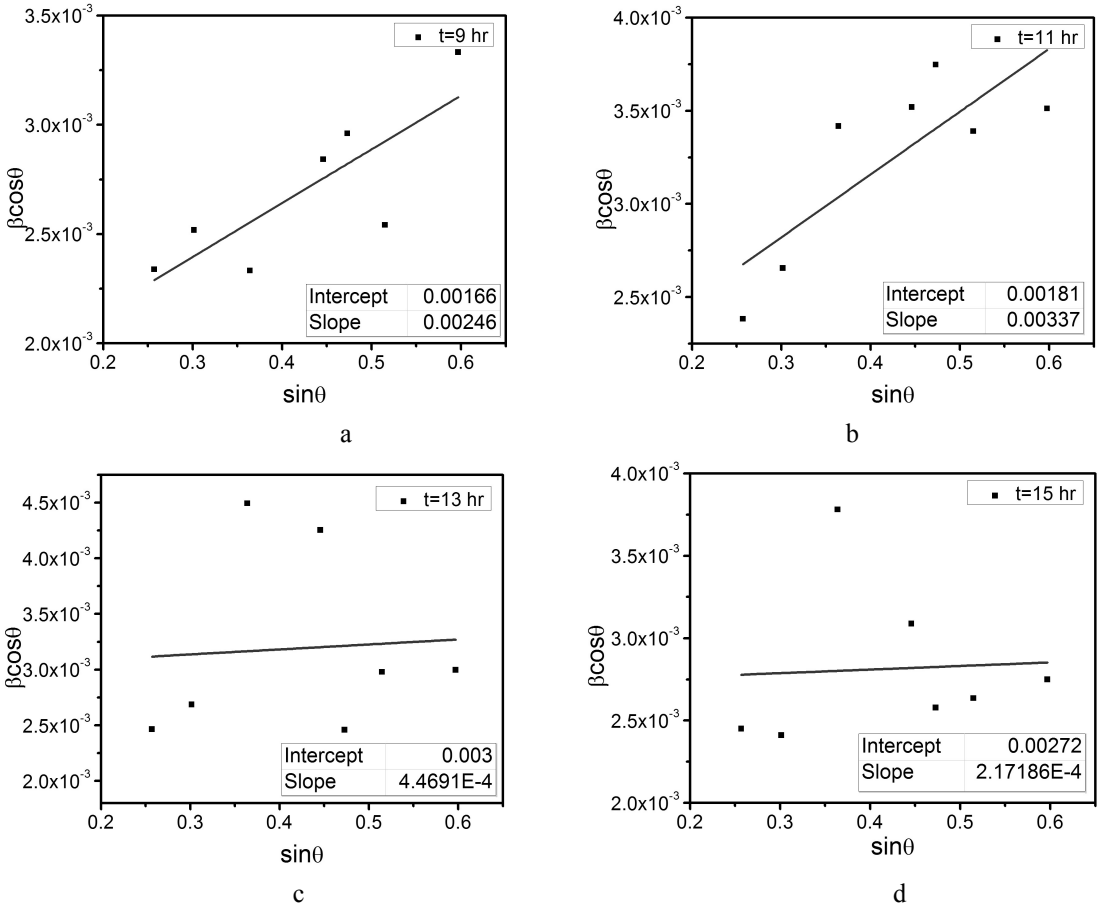

Fig.3. WH plots of $Ni_{0.5}Cd_{0.5}Al_{0.1}Fe_{1.9}O_4$ ferrite series synthesized by ceramic method.

Using the slope and intercept values of the graph of βcosθ with respect to sinθ; the value of crystallite size and microstrain are calculated and are tabulated in the Table 2.

The SS plot is a tool to understand the isotropic nature and micro-strain contribution. The SS plots of $Ni_{0.5}Cd_{0.5}Al_{0.1}Fe_{1.9}O_4$ (t= 9, 11, 13, 15 hrs) ferrite series is shown in Fig. 4 (a-d). In this approximation, crystallite size and strain are having a relation given by the equation $(d_{hkl}\beta_{hkl}\cos\theta)^2 = \frac{K.\lambda}{D}(d_{hkl}^2\beta_{hkl}\cos\theta) + \left(\frac{\varepsilon}{2}\right)^2$, where K is a constant [11, 17-18]. The calculated value of crystallite size and microstrain are tabulated in the Table 2. The microstrain is observed to be decreasing with increase in sintering time. The crystallite size is observed to be steady. All the samples showed the dislocation density in the range of 10^{14}.

2.3. Scanning electron microscope studies

The SEM micrographs of $Ni_{0.5}Cd_{0.5}Al_{0.1}Fe_{1.9}O_4$ (t= 9, 11, 13, 15 hrs) series are shown in the Fig. 5(a-d). The images show uniform distribution of the grains with uniform grain size of the order of 1 μm. The grains are having octahedral and tetrahedral structures showing very sharp boundary growth. The grain size increased with increase in the sintering time.

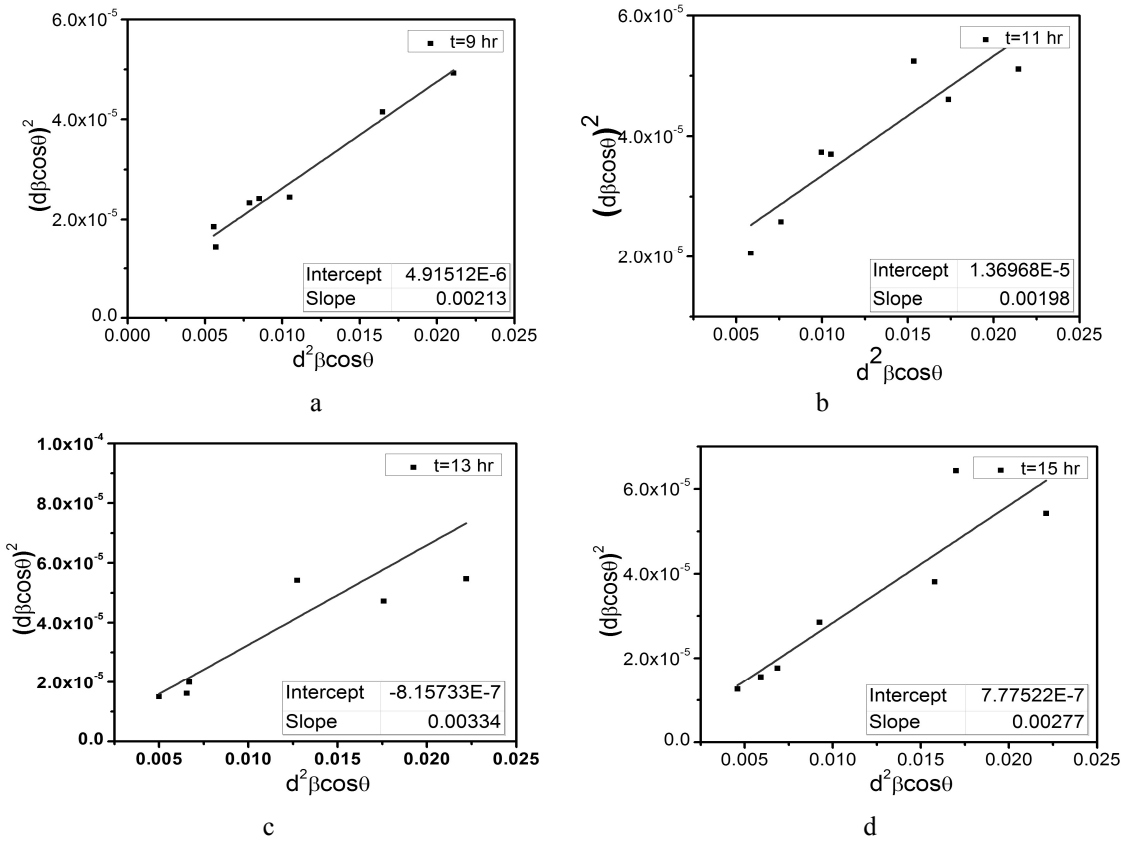

Fig.4. SS plots of $Ni_{0.5}Cd_{0.5}Al_{0.1}Fe_{1.9}O_4$ferrite series synthesized by ceramic method.

The elemental analysis is done by EDAX analysis and the diffraction spectra of $Ni_{0.5}Cd_{0.5}Al_{0.1}Fe_{1.9}O_4$ (t= 9, 11, 13, 15 hrs) series are shown in Fig. 6, a-d.

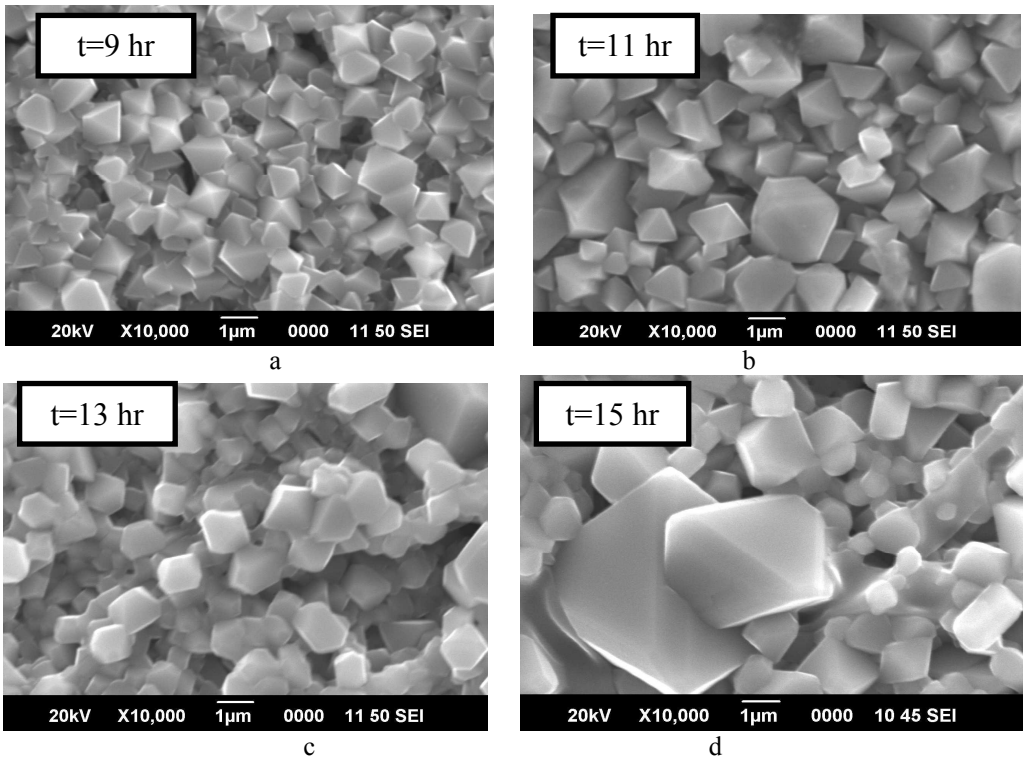

Fig. 5. SEM micrographs of $Ni_{0.5}Cd_{0.5}Al_{0.1}Fe_{1.9}O_4$ ferrite series synthesized by ceramic method.

2.4. Energy dispersive X-ray analysis studies

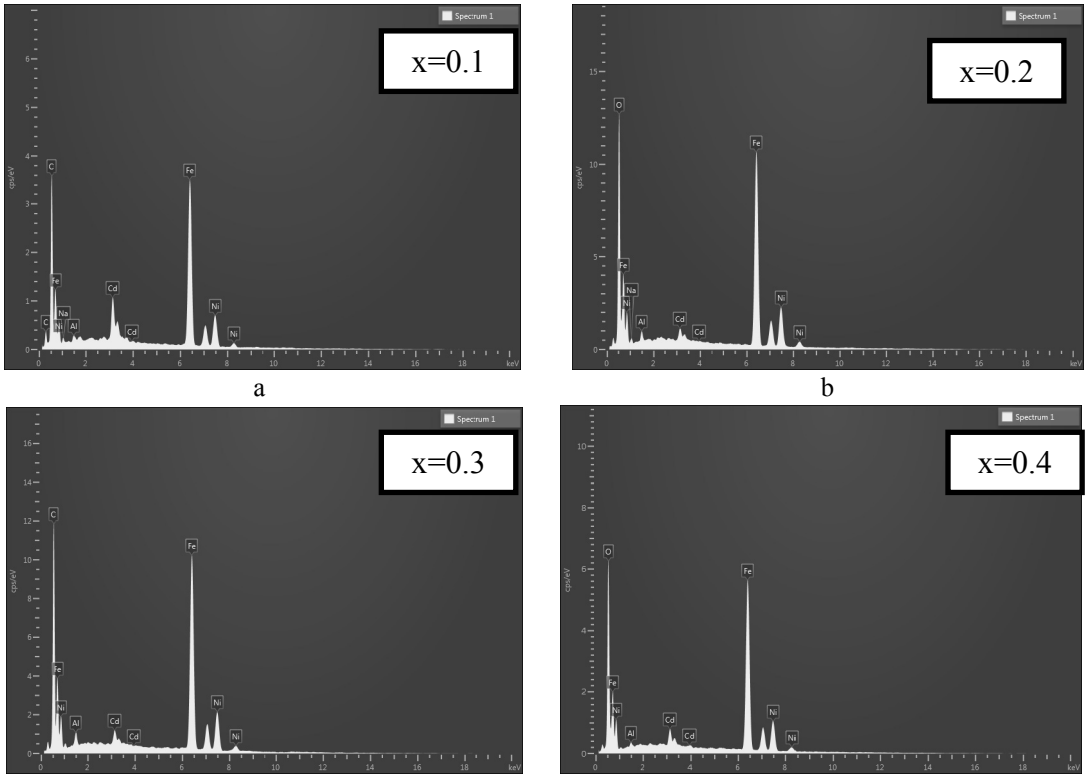

Fig. 6. EDAX of $Ni_{0.5}Cd_{0.5}Al_{0.1}Fe_{1.9}O_4$ ferrite series synthesized by ceramic method.

The spectra confirming the presence of all the metal ions present in the ferrite formula and the atomic proportion tabulated in Table 3.

Table 3 - Initial values of atomic proportions of metal ions taken by stoichio-metric proportion and observed values using EDAX analysis of in the samples of $Ni_{0.5}Cd_{0.5}Al_{0.1}Fe_{1.9}O_4$ ferrite series with sintering time t=9, 11, 13, 15 hrs.

	Weight (%)				Observed atomic proportion using EDAX				Stoichiometric composition taken for synthesis			
	t=9 hr	t=11 hr	t=13 hr	t=15 hr	t=9 hr	t=11 hr	t=13 hr	t=15 hr	t=9 hr	t=11 hr	t=13 hr	t=15 hr
O	25.21	25.33	25.53	25.71	4.056	3.850	3.836	3.890	4	4	4	4
Al	0.52	1.04	1.27	0.46	0.049	0.093	0.113	0.041	0.1	0.1	0.1	0.1
Fe	45.44	52.54	53.53	53.87	2.094	2.288	2.304	2.335	1.9	1.9	1.9	1.9
Ni	13.52	17.17	16.74	15.39	0.593	0.711	0.685	0.635	0.5	0.5	0.5	0.5
Cd	9.07	2.64	2.93	4.57	0.208	0.057	0.062	0.099	0.5	0.5	0.5	0.5
Tot	93.76	98.72	100	100	7.000	7	7	7	7	7	7	7

2.5. Fourier transform infrared (FT-IR) studies

The FT-IR spectra of $Ni_{0.5}Cd_{0.5}Al_{0.1}Fe_{1.9}O_4$ ferrite series with sintering time t=9, 11, 13, 15 hrs Fig. 7. The transmittance spectra showed two peaks for all the samples of the series. The first peak υ_1 (568-580 cm^{-1}) corresponds to the tetrahedral metal oxygen bond and second peak υ_2 (near 400 cm^{-1}) corresponds to octahedral metal oxygen bond in the ferrite structure [19].

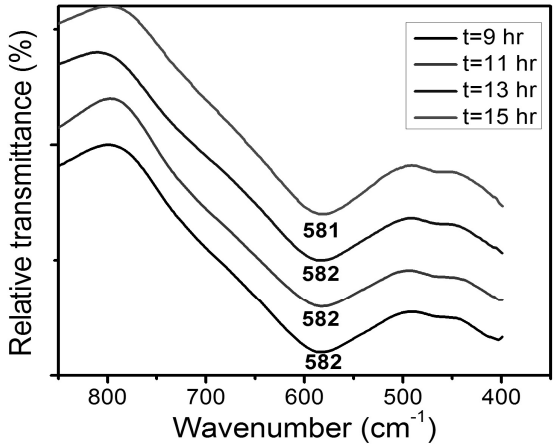

Fig.7. FTIR spectra of $Ni_{0.5}Cd_{0.5}Al_{0.1}Fe_{1.9}O_4$ ferrite series synthesized by ceramic method.

Conclusion

The $Ni_{0.5}Cd_{0.5}Al_{0.1}Fe_{1.9}O_4$ ferrite series with sintering time t=9, 11, 13, 15 hrs are successfully synthesized by ceramic method. The XRD studies confirm the single phase cubic spinel structure of the samples. The lattice parameter (8.47 Å - 8.48 Å) remains almost constant with increase in sintering temperature. Stacking fault coefficient observed to be very low, affirming the XRD peak position are at the expected value. The crystallite size is calculated using three different methods showed almost constancy (~50 nm) with increase in the sintering time. The SEM images show uniform size of the grains of size of the range of 1μm. The octahedral and tetrahedral structures are observed in morphology study. The grain size increased with increase in the sintering time. The EDAX studies confirm the presence of all the metal ions used in synthesis. The FTIR studies show two peaks υ_1(581-582 cm^{-1}) and υ_2(less than 400 cm^{-1}) confirming the presence of octahedral and tetrahedral positions inside the structure.

REFERENCES

1 Wrinkler, G., Crystallography, Chemistry and Technology of ferrites in Magnetic Properties of Materials, McGraw-Hill, London, UK, 1971.

2 Goldman, A. Modern Ferrite Technology, Springer, Boston Springer, Boston, 2006. doi: 0.1007/978-0-387-29413-1

3 Jauhar, S., Kaur, J., Goyal, A., Singhal, S., Tuning the properties of cobalt Ferrite: A road towards diverse applications. *RSC Adv*., 2016, Vol.6, no.100, pp. 97694-97719. doi 10.1039/C6RA21224G

4 Nedkov, I., Petkov, A., Cheparin, V., Microstructure and resonant properties of polycrystalline Sr-hexaferrite. J. Magn. Magn.Mater., 1990, Vol. 83, No.(1-3), pp. 430-432. doi10.1016/0304-8853(90)90573-9

5 Falk, R.B., Hooper,G.D., Elongated Iron-Cobalt: Ferrite, a New, Lightweight, Permanent Magnet Material. J. Appl. Phys. S, 1961, Vol. 32, No. 3, pp. 190-191. doi10.1063/1.2000396

6 Pon-On, W., Charoenphandhu, N., Tang, I.-M., Jongwattanapisan, P., Krishnamra, N., Hoonsawat, R., Encapsulation of magnetic $CoFe_2O_4$ in SiO_2 nanocomposites using hydroxyapatite as templates: A drug delivery system. Mater. Chem. Phys. 2011, Vol. 131, No. (1-2), pp. 485 – 494. doi 10.1016/j.matchemphys.2011.10.008

7 Bi, K., Zhu, W., Lei, M., Zhou, J., Magnetically tunable wideband microwave filter using ferrite-based metamaterials. *Appl. Phys. Lett*., 2015, Vol. 106, No. 17, pp. 173507(1-4). doi 10.1063/1.4918992

8 Hagfeldt, A., Graetzel, M., Light-Induced Redox Reactions in Nanocrystalline Systems. *Chemical Rev.*, 1995, Vol. 95, No. 1, pp. 49 – 68. doi 10.1021/cr00033a003

9 Farooq, H., Ahmad, M.R., Jamil, Y., Hafeez, A., Anwar, M. Structural, dielectric and magnetic properties of superparamagnetic zinc ferrite nanoparticles synthesized through coprecipitation technique, Kovove Mater., 2013, Vol. 51, pp. 305-310. doi 10.4149/km_2013_5_305

10 Kulkarni, A.B., Mathad, S.N., Synthesis and structural analysis of Co-Zn-Cd ferrite by Williamson-Hall and Size-Strain Plot Methods. Int. J. Self-Propag. High-Temp.Synth., 2018, Vol. 27, No. 1, pp. 37–43. doi10.3103/S106138621801003X

11 Kulkarni, A. B., Mathad, S. N., Variation in structural and mechanical properties of Cd-doped Co-Zn ferrites. Mater. Sci. Energy Techn., 2019, Vol. 2, No. 3, pp. 455 – 462. doi 10.1016/j.mset.2019.03.003

.

12 Lohar, K.S., Patange, S.M., Mane, M.L., Shirsath, S.E.,Cation distribution investigation and characterizations of $Ni_{1-x}Cd_xFe_2O_4$ nanoparticles synthesized by citrate gel process. J. Mol. Str., 2013, Vol. 1032, pp. 105-110. doi 10.1016/j.molstruc.2012.07.055

13 Raghavender, A.T., Jadhav, K.M., Dielectric properties of Al-substituted Co ferrite nanoparticles. *Bull. Mater. Sci.,* 2009, Vol. 32, No. 6, pp. 575 – 578. doi10.1007/s12034-009-0087-8

14 Pedrosa, F.J., Rial, J., Golasinski, K.M., Rodríguez-Osorio, M., Salas, G., Granados, D., Camarero, J., Bollero, A. Tunable nanocrystalline $CoFe_2O_4$ isotropic powders obtained by co-precipitation and ultrafast ball milling for permanent magnet applications. *RSC Adv.,* 2016, Vol. 6, No. 90, pp. 87282 – 87287. doi10.1039/C6RA15698C

15 Gomes, J.A., Sousa, M.H., Tourinho, F.A., Aquino, R., Silva, G.J., Depeyrot, J., Dubois, E., Perzynski, R. Synthesis of Core-Shell Ferrite Nanoparticles for Ferrofluids: Chemical and Magnetic Analysis. J. Phys. Chem. C, 2008, Vol. 112, No. 16, pp. 6220 – 6227. doi 10.1021/jp7097608

16 Zak, A.K., Abrishami, M.E., Majid, W.H.A., Yousefi ,R., Hosseini, S.M., X-ray analysis of ZnO nanoparticles by Williamson-Hall and size-strain plot methods. *Solid State Sci.*, 2011, Vol. 13, No. 1, pp.251 – 256. doi10.1016/j.solidstatesciences.2010.11.024

17 Tagliente, M.A., Massaro, M. Nucl. Instruments Methods. *Phys. Res. Sect. B Beam Interact. Mater. Atoms,* 2008, Vol. 266, No. 7, pp. 1055 – 1061. doi10.1016/j.nimb.2008.02.036

18 Prabhu, Y.T., Rao, K.V., Kumar V.S.S., Kumari B.S., X-Ray Analysis by Williamson-Hall and Size-Strain Plot Methods of ZnO Nanoparticles with Fuel Variation. World J. Nano Sci. Engg., 2014,V. 4, No.1, pp. 43743(1-8). doi 10.4236/wjnse.2014.41004

19 Pathan, A.T., Mathad, S.N., Shaikh, A.M., Infrared Spectral studies of Co^{2+} substituted Li-Ni-Zn Nano-structured Ferrites. Int. J. Self-Prop. High Temp. Synth., 2014, Vol. 23, No. 2, pp. 112-117. doi 10.3103/S1061386214020083

Article accepted for publication 27.07.2020

DOI 10.31489/2020No2/19-24

UDC 538.975

DETERMINATION OF THE INFLUENCE OF THE PHASE COMPOSITION OF Cu-Bi COATINGS ON THE EFFICIENCY OF SHIELDING FROM IONIZING RADIATION.

Kadyrzhanov K.K.[1], Shlimas D.I.[1], Kaniukov E.Yu.[2], Kaliyekperov M.E.[1]

[1]L.N. Gumilyov Eurasian National University, Nur-Sultan, Kazakhstan, kayrat.kadyrzhanov@mail.ru

[2]Scientific-Practical Materials Research Centre of National Academy of Sciences of Belarus, Minsk, Belarus

The work is devoted to the study of the efficiency of shielding the radiation exposure of heavy ions depending on the phase composition of Cu-Bi coatings. As a method of producing protective coatings, an electrochemical deposition method was used. The change in phase composition was carried out by varying the applied potentials difference during deposition. The study found that the change in phase composition leads to an increase in coating density, as a result of the dominance of the $CuBi_2O_4$ phase and an increase in the structural ordering degree. During shielding efficiency tests, it was found that the greatest decrease in the degree of crystallinity is observed for copper coatings, for which the amorphization of the structure at the maximum irradiation fluence didn't exceed 12 %, while for coatings based on $CuBi_2O_4$ the value of amorphization was no more than 1.2 % of initial value. Amorphization and fragmentation of grains at high radiation doses leads to a decrease in the shielding efficiency, as well as an increase in the value of the deviation ΔU.

Keywords: protective coatings, shielding, ionizing radiation, heavy ions, radiation resistance.

Introduction

The rapid development of technologies in the field of nuclear energy and reactor building is inextricably linked to the problem of radiation safety and protection against the negative impact of ionizing radiation [1-3]. In the transition to the widespread use of microelectronic devices, as well as the reduction in the size of semiconductor chips, their resistance to the destabilizing effects of ionizing radiation plays a large role. Reduction of mass-dimensional dimensions of microelectronic devices led to a sharp decrease in the level of natural protection against ionizing radiation [4, 5]. At the same time, a negative impact that leads to destabilization of performance and failure can lead to both long-term irradiation and a single cascade of secondary dislodged particles caused by the collision of a heavy ion [6-10]. Radiation-resistant materials based on nitrides [11-13], carbides [14, 15] or nanostructured films and coatings are used as the most common methods of protection against ionizing radiation.

The most promising solution to the problem of maintaining the stability of microelectronic devices operating in conditions of high radiation background is the use of composite protective coatings of complex composition [16-20]. The choice of protective coatings is based on the principles of preservation of physical, chemical and mechanical properties as a result of prolonged exposure to external factors and loads [21-24]. Moreover, it should be noted that in most cases it is impossible to create a protective coating capable of protecting against all types of exposure, but at the same time it is possible to significantly reduce one or another type of radiation that can cause the greatest negative impact on performance [25-27].

The purpose of this work is to study the possibility of using Cu-Bi films for protection against heavy ions, as well as the effect of the phase composition on the efficiency of shielding and weakening the negative impact on microelectronic circuits. Copper-bismuth (Cu-Bi) - based coatings were selected as research objects to determine the effect of the crystal structure, including the phase composition of the synthesized coatings, as well as surface morphology (grain size) on the shielding efficiency [28,29]. The choice of this type of coating is due to the possibility of obtaining coatings with different phase compositions, including both two-phase and single-phase coatings. The change in phase composition, and hence crystal structure, can have a significant impact on shielding efficiency by varying coating density as well as absorption capacity

and affecting energy losses. The change in grain size has a great effect on dislocation density, which can also lead to strengthening of coatings and reduction of radiation damage.

1. Experimental part

As a method of obtaining protective coatings, the method of electrochemical deposition from electrolyte solutions was chosen: $CuSO_4 \cdot 5H_2O$ (238 g/l), $Bi_2(SO_4)_3$ (10 g/l), H_2SO_4 (21 g/l) [28,29]. The applied potentials difference for deposition was varied from 1.5 V to 2.0 V. The change in the applied potentials difference is due to the possibility of varying the phase composition of the synthesized coatings.

Evaluation of structural changes and phase composition of the synthesized samples was carried out using the method of X-ray phase analysis performed on a D8 Advance ECO X-ray diffractometer.

Xe^{22+} ions with an energy of 230 MeV and fluences of $10^{13} – 10^{15}$ ions/cm^2 were selected for shielding efficiency tests. The irradiation was performed on a DC-60 heavy ion accelerator [12]. The choice of fluences is due to the possibility of modeling the effects of overlapping defect areas that occur during irradiation. With the selected energy of incident ions, the path length in the selected materials for testing exceeds 12-20 μm, depending on the type of ions, comparable to the thickness of the films.

The efficiency of shielding radiation damage caused by ionizing radiation will be assessed according to the method of determining the preservation of the performance of microcircuits by measuring deviations in volt-ampere characteristics before and after irradiation. The threshold value ΔU, which is characteristic of critical malfunctions of the microcircuits, will be selected as 0.1 V. Deviation of the volt-ampere characteristic above the threshold value leads to deterioration of the microcircuit and its further failure.

2. Results and discussion

Table 1 shows the initial data of the test coatings that were used to test the absorption efficiency. The thickness of the protective coatings was 10 μm. As can be seen from the data presented in Table 1, by changing the synthesis conditions, in particular the applied potential difference, it is possible to control the phase composition of the synthesized coatings to obtain both single-phase coatings consisting of copper or $CuBi_2O_4$ and a mixed composition. At the same time, the change in phase composition leads to an increase in the density of the coatings, as a result of the dominance of the $CuBi_2O_4$ phase and an increase in the degree of structural ordering (degree of crystallinity). However, in the case where the $CuBi_2O_4$ phases in the coating composition become larger, an increase in grain size is observed, and thereby a decrease in dislocation density.

Table 1 - Initial sample data.

Conditions for obtaining	Phase composition, phase ratio	Average crystallite size, nm	Density, g/cm^3	Crystallinity degree, %	Dislocation density, 10^{11} cm^{-2}
1.5 V	Cu – FCC – 100 %	73.5	9.17	81.2	0.185
1.6 V	Cu – FCC – 75 % $CuBi_2O_4$ – HCP – 25 %	78.3	11.42	85.3	0.163
1.75 V	Cu – FCC – 25 % $CuBi_2O_4$ – HCP – 75 %	84.5	12.44	88.3	0.141
2.0 V	$CuBi_2O_4$ – HCP – 100 %	96.3	12.48	89.7	0.108

To assess the effect of phase composition and crystal structure on shielding efficiency, Xe^{22+} ions with an energy of 230 MeV and fluences of $1x10^{13}$-10^{15} ion/cm^2 were selected as ionizing radiation. Evaluation of efficiency of radiation damage shielding caused by ionizing radiation was carried out according to the method of determining serviceability of microcircuits by measuring deviations of volt-ampere characteristics before and after irradiation. The threshold value ΔU, which is characteristic of critical malfunctions of the microcircuits, was selected as 0.1 V. Deviation of the volt-ampere characteristic above the threshold value leads to deterioration of the microcircuit and its further failure. Figure 1 shows experimental data of ΔU value change depending on irradiation dose for all tested coating samples.

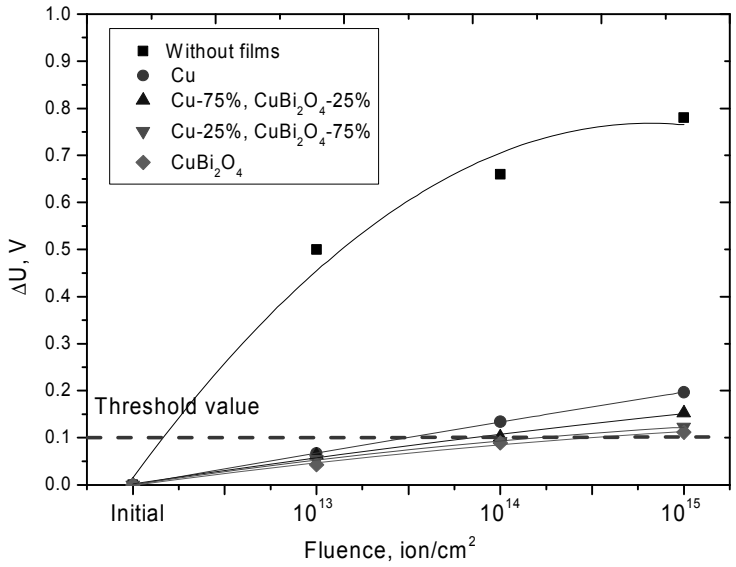

Fig.1. Data on changes in the value of ΔU depending on the radiation dose

As can be seen from the presented data, at a radiation dose of 1013 ion/cm^2, all the tested protective coatings show a high level of absorption of radiation damage, and the deviation ΔU does not exceed 0.05-0.06 V. However, an increase in the radiation dose leads to a significant change in the behavior of ΔU for the studied coatings. For coatings with a crystalline structure characteristic of copper, as well as with a large content of the Cu-FCC phase in the structure, a decrease in absorption efficiency is observed, and an increase in ΔU value that exceeds the threshold value. Further increase of irradiation dose results in deviation of ΔU value being more than 0.15-0.17 V, which indicates sharp decrease of absorption capacity of coatings and deterioration of protection degree.

For coatings dominated by the $CuBi_2O_4$ phase, as well as single-phase coatings based on $CuBi_2O_4$, the deviation of ΔU is significantly lower than for copper coatings, indicating a higher degree of resistance to radiation damage and a high degree of absorption of radiation damage. Figure 2 shows a graph for evaluating the efficiency of reducing radiation damage at maximum irradiation fluence, which was calculated as a result of a comparative analysis with the deviation of the ΔU value for microcircuits without protective coatings.

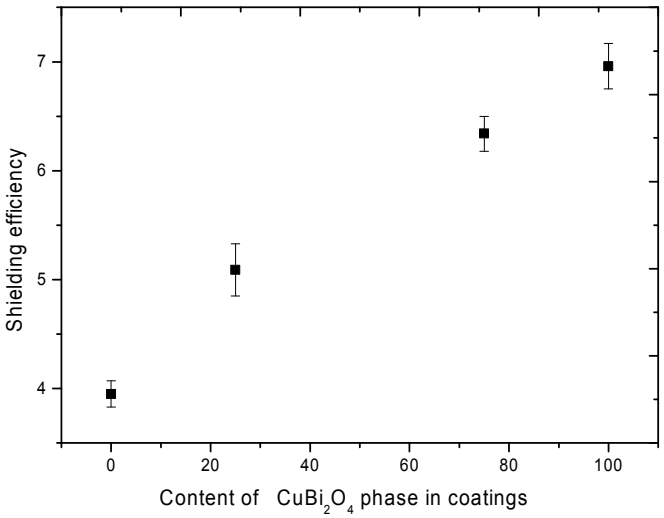

Fig.2. Graph of radiation damage reduction efficiency assessment at maximum radiation fluence.

As can be seen from the data presented, coatings based on $CuBi_2O_4$ for which the value of the shielding efficiency was 6.96 are most effective. The increase in shielding efficiency for coatings is $CuBi_2O_4$ associated with high radiation resistance to radiation damage, as well as resistance of the crystal structure to degradation and amorphization as a result of irradiation. Figure 3 shows the data of changes in the value of

the degree of structural ordering as a result of irradiation, as well as an estimate of the change in grain sizes and dislocation density (see Figure 4).

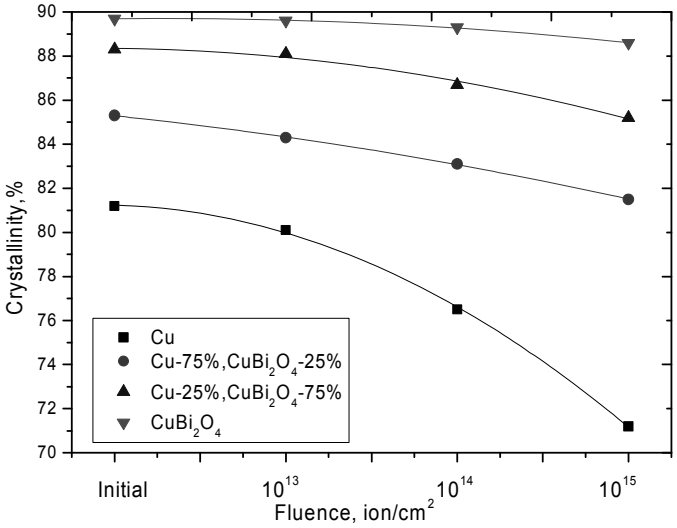

Fig.3. Dynamics of changes in the degree of crystallinity of the coatings under study depending on the radiation dose

As can be seen from the data presented, the greatest decrease in crystallinity is observed for copper coatings, for which amorphization of the structure at maximum irradiation fluence was more than 12 %, while for coatings based on $CuBi_2O_4$, the value of amorphization didn't exceed 1.2 % of the initial value. A high degree of amorphization for copper coatings leads to disordering of the crystal structure, large deformations of the crystal lattice, crushing of crystallites and an increase in dislocation density. According to the presented dependences, the change in the grain size for coatings containing CuBi2O4 with an increase in the radiation dose is less pronounced than for copper coatings. At the same time, an increase in the radiation dose leads to the processes of grain fragmentation, thereby increasing the dislocation density of defects.

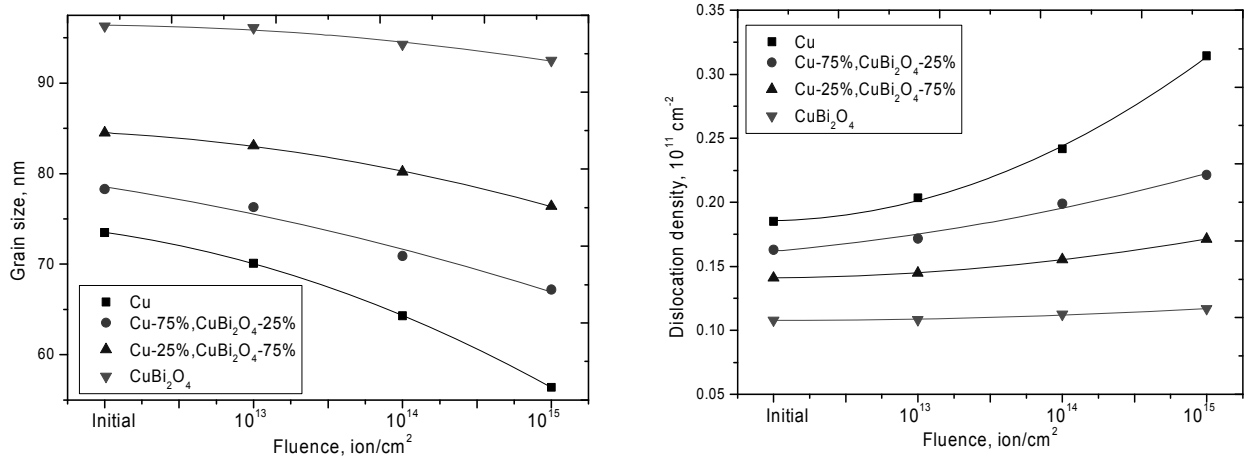

a b

Fig.4. Graphs of changes in structural parameters: a) Change of grain size depending on radiation dose; b) Change of dislocation density depending on radiation dose.

Thus, during the study, it was found that a change in the crystal structure, including the phase composition of synthesized coatings, leads to an increase in the efficiency of shielding ionizing radiation, as well as a decrease in the degree of amorphization of coatings as a result of the accumulation of radiation damage. The amorphization and crushing of grains at high radiation doses leads to a decrease in the shielding efficiency, as well as an increase in the deviation ΔU. It has been found that coatings based on $CuBi_2O_4$ have

the best radiation resistance to degradation and amorphization, as well as the efficiency of shielding from ionizing radiation.

Conclusion

During the study, it was found that a change in the crystal structure, including the phase composition of the synthesized coatings. This change leads to an increase in the shielding efficiency of ionizing radiation, as well as a decrease in the degree of amorphization of coatings as a result of the accumulation of radiation damage. Amorphization and fragmentation of grains at high radiation doses leads to a decrease in the shielding efficiency, as well as an increase in the value of the deviation ΔU. It was found that the best radiation resistance to degradation and amorphization, as well as the efficiency of shielding from ionizing radiation, is possessed by $CuBi_2O_4$-based coatings. In the future, studies to compare the shielding efficiency of synthesized coatings with commercial analogues based on silicon carbide, titanium nitride, aluminum nitride and tungsten oxide will be carried out.

REFERENCES

1 Sayyed M. I. et al. Physical, structural, optical and gamma radiation shielding properties of borate glasses containing heavy metals (Bi2O3/MoO3). *Journal of Non-Crystalline Solids*, 2019, Vol.507, pp. 30 – 37.

2 Ryskulov A. E. et al. The effect of Ni12+ heavy ion irradiation on the optical and structural properties of BeO ceramics. *Ceramics International,* 2020, Vol. 46(4), pp. 4065 – 4070.

3 Kurudirek M. Heavy metal borate glasses: potential use for radiation shielding. *Journal of Alloys and Compounds,* 2017, Vol. 727, pp. 1227 – 1236.

4 Kumar A. et al. Physical, structural, optical and gamma ray shielding behavior of (20+ x) PbO–10 BaO–10 Na2O–10 MgO–(50-x) B2O3 glasses. *Physica B: Condensed Matter*, 2019, Vol. 552, pp. 110 – 118.

5 Kozlovskiy A. et al. Structure and corrosion properties of thin TiO2 films obtained by magnetron sputtering. *Vacuum,* 2019*,* Vol. 164, pp. 224 – 232.

6 Zdorovets M. V. and Kozlovskiy A. L. Argon ion irradiation effect on Zn nanotubes. *Journal of Materials Science: Materials in Electronics,* 2018, Vol. 29(5), pp. 3621 – 3630.

7 Raghuvanshi S. et al. Dual control on structure and magnetic properties of Mg ferrite: role of swift heavy ion irradiation. *Journal of Magnetism and Magnetic Materials,* 2019, Vol. 471, pp. 521 – 528.

8 Kozlovskiy A. et al. Investigation of the influence of irradiation with Fe+ 7 ions on structural properties of AlN ceramics. *Materials Research Express*, 2018, Vol. 5(6), pp. 065502.

9 Mirzayev Matlab N. et al. Thermophysical behavior of boron nitride and boron trioxide ceramics compounds with high energy electron fluence and swift heavy ion irradiated. *Journal of Alloys and Compounds,* 2020, Vol. 834, pp.155119.

10 Rammah Y. S., et al. FTIR, electronic polarizability and shielding parameters of B2O3 glasses doped with SnO2. *Applied Physics A*, 2018, Vol. 124(9), p. 650.

11 Kozlovskiy A. et al. Optical and structural properties of AlN ceramics irradiated with heavy ions. *Optical Materials,* 2019, Vol. 91, pp. 130 – 137.

12 Kozlovskiy A. et al. Dynamics of changes in structural properties of AlN ceramics after Xe+ 22 ion irradiation. *Vacuum,* 2018, Vol. 155, pp. 412 – 422.

13 Kozlovskiy A. L. et al. Radiation resistance of thin TiN films as a result of irradiation with low-energy Kr14+ ions. *Ceramics International*, 2020, Vol. 46(6), pp. 7970 – 7976.

14 Tunhuma S. M. et al. Defects in swift heavy ion irradiated n-4H-SiC. *Nuclear Instruments and Methods in Physics Research Section B: Beam Interactions with Materials and Atoms*, 2019, Vol. 460, pp. 119 – 124.

15 Zdorovets M.V., Kurlov A.S. and Kozlovskiy A. L. Radiation defects upon irradiation with Kr14+ ions of TaC0. 81 ceramics. *Surface and Coatings Technology*, 2020, Vol. 386, pp. 125499.

16 Tinishbaeva K. et al. Implantation of low-energy Ni 12+ ions to change structural and strength characteristics of ceramics based on SiC. *Journal of Materials Science: Materials in Electronics*, 2020. Vol. 31(3), pp. 2246 – 2256.

17 Zdorovets M. V., Kozlovskiy A. L. The effect of lithium doping on the ferroelectric properties of LST ceramics. *Ceramics International*, 2020, Vol. 46(10), pp. 14548 – 14557.

18 Tekin H. O. et al. The investigation of gamma-ray and neutron shielding parameters of Na_2O-CaO-P2O5-SiO_2 bioactive glasses using MCNPX code. *Results in Physics*, 2019, Vol. 12, pp. 1797 – 1804.

19 Rammah Y. S. et al. Optical properties and gamma-shielding features of bismuth borate glasses. *Applied Physics A,* 2018, Vol. 124(12), pp. 832.

20 Chung Cheng-Kai et al. Thermodynamic and structural evolution of mechanically milled and swift heavy ion irradiated Er2Ti2O7 pyrochlore. *Acta Materialia*, 2019, Vol. 181, pp. 309-317.

21 Shlimas D. I., Zdorovets M. V. and Kozlovskiy A. L. Synthesis and resistance to helium swelling of Li 2 TiO 3 ceramics. *Journal of Materials Science: Materials in Electronics,* 2020, Vol. 31(15), pp. 12903-12912.

.

22 Tekin H. O. et al. Characterization of SiO_2–PbO–CdO–Ga_2O_3 glasses for comprehensive nuclear shielding performance: Alpha, proton, gamma, neutron radiation. *Ceramics International*, 2019, Vol. 45(15), pp. 19206 – 19222.

23 Gladkikh T. et al. Changes in optical and structural properties of AlN after irradiation with C2+ ions of 40 keV. *Vacuum*, 2019, Vol. 161, pp. 103 – 110.

24 Kumar Ashok. Gamma ray shielding properties of PbO-Li2O-B2O3 glasses. *Radiation Physics and Chemistry,* 2017, Vol. 136, pp. 50 – 53.

25 Kozlovskiy A. et al. Influence of He-ion irradiation of ceramic AlN. *Vacuum,* 2019, Vol. 163, pp. 45 – 51.

26 Rammah Y. S. et al. Synthesis, physical, structural and shielding properties of newly developed B 2 O 3–ZnO–PbO–Fe_2 O_3 glasses using Geant4 code and WinXCOM program. *Applied Physics A,* 2019, Vol. 125(8), p. 523.

27 Gaikwad D. K. et al. Gamma ray shielding properties of TeO_2-ZnF_2-As2O3-$Sm2O_3$ glasses. *Journal of Alloys and Compound,* 2018, Vol. 765, pp. 451 – 458.

28 Kozlovskiy A. L., Zdorovets M. V. Synthesis, structural, strength and corrosion properties of thin films of the type CuX (X= Bi, Mg, Ni). *Journal of Materials Science: Materials in Electronics*, 2019, Vol. 30(12), pp. 11819 – 11832.

29 Kadyrzhanov K. K. et al. Research of the shielding effect and radiation resistance of composite $CuBi_2$ O_4 films as well as their practical applications. *Journal of Materials Science: Materials in Electronics,* 2020, Vol. 31(14), pp. 11729-11740.

Article accepted for publication 24.10.2020

DOI 10.31489/2020No2/25-30

UDC: 621.785

NITROGENING HYDRAULIC CYLINDER RODS

Yurov V.M.[1], Guchenko S.A.[1], Salkeeva A.K.[2], Kusenova A.S.[2]

[1] E.A. Buketov Karaganda University, Karaganda, Kazakhstan, exciton@list.ru

[2]Karaganda Technical University, Karaganda, Kazakhstan, salkeeva58@mail.ru

The paper considers the method of ion-plasma nitriding of polished rods of hydraulic cylinders. With ion nitriding, the surface hardening of parts is most pronounced. This is due to the fact that the surface layer of the part does not exceed 20 nm, that is, it is a nanostructure. In this nanostructure, nitrogen diffusion processes are significantly different from bulk ones. The size effects in the nanostructure lead to the fact that the "classical" Fick equations do not work in the layer, and the diffusion of nitrogen in this layer depends logarithmically on the properties of the steel. It was theoretically found that diffusion in a nanoplate depends both on the material of the plate through the diffusion coefficient of the bulk sample D_0 and on the size factor α. In the classical case, there is no such dependence.

Keywords: nitriding, detail, surface layer, nanostructure, diffusion, nitrogen, size factor, steel.

Introduction

The surface is the most important component of metal parts and it is necessary to control its condition at all stages of the part's life cycle - during its production, operation and repair [1]. The surface layer of metal parts can be considered as a part of a solid, which includes its constituent molecules, atoms, protons, neutrons, electrons, vacancies, dislocations and other components, each of which has energy [2].

The surface of metal parts plays a special role in increasing their strength by the method of thermochemical action. The basis for such a functional impact is [3]:

- cementation (filling the surface layer with carbon);
- nitriding (filling the surface layer with nitrogen);
- nitrocarburizing or cyanidation (filling the surface layer with carbon and nitrogen simultaneously);
- diffusion metallization (filling the surface layer with various metals).

We will consider the strengthening of 35HGSA steels using ion nitriding [4]. It follows from the analysis of the literature that during ion nitriding, the surface hardening of parts and tools is most clearly manifested, which are constantly used in all industrialized countries instead of the usual methods of chemical-thermal treatment, which is often environmentally harmful.

1. Experimental technique

Ion-plasma nitriding was carried out on an NNV 6.6-I1 setup equipped with a plasma source with a hot cathode "PINK" [5], developed by ISE SB RAS (Fig.1). Plasma generator "PINK" can be installed on any of the three flanges of the NNV 6.6-I1 chamber. On the flange 6 there are two current leads 3 for heating the cathode 2. The hollow electrode 1 is also installed on the flange 6. The direct-heated cathode is made of tungsten. The plasma generator is powered by a combined inverter power supply with a heating current adjustment range of 10-150 A and an ion current of 10-100 A.

Under the influence of an external magnetic field, the trajectory of electrons emitted from the heated cathode is bent. Electrons move along a cylindrical spiral, which increases their path to the anode, thereby increasing the efficiency of gas ionization. By changing the filament current, and hence the emission of electrons from the hot cathode, one can easily regulate the discharge current from tens to hundreds of amperes at a combustion voltage of several tens of volts. Such a discharge is classified as a non-self-sustaining hot-cathode arc discharge without a cathode spot. This arc discharge will make it possible to generate low-temperature plasma in volumes ($\geq$0.1 m^3) with a concentration of $n_e \sim 10^9$–10^{11} cm^{-3} and a uniformity of ± 15% of the average value.

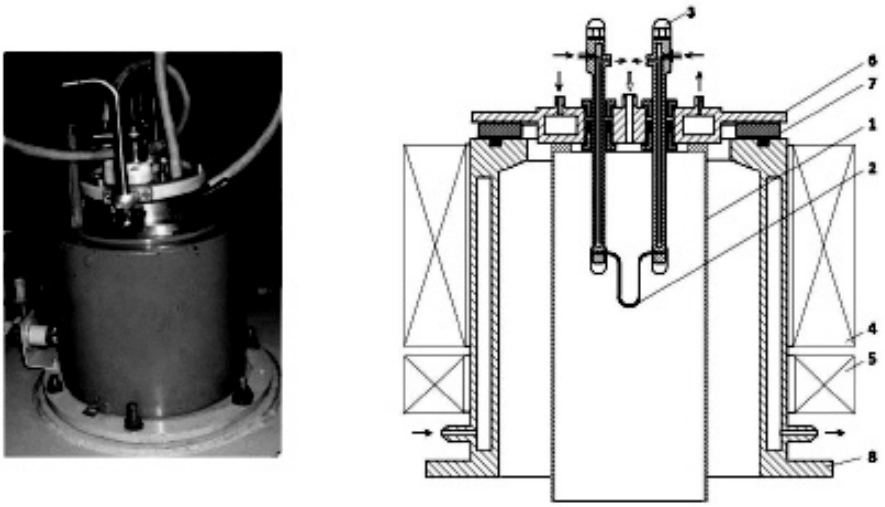

a) b)

Fig.1. Appearance (a) and schematic diagram (b) of the plasma source "PINK" [5].
1 - cathode cavity; 2 - hot tungsten cathode; 3 - electric input; 4 - stabilizing coil; 5 - focusing coil; 6 - water-cooled flange; 7 - insulator; 8 - water-cooled housing.

2. Technological mode of the nitriding process.

Preliminary preparation:

1. Degreasing of stocks with Nefras S2-80/120.
2. Cleaning and polishing of 35HGSA rods in the bath of the EPP-40 electrolytic-plasma polishing unit, with the following parameters: the composition of the polishing solution -5% aqueous solution of ammonium sulfate; solution temperature – 85 °C; cathode-anode voltage 300 V, current 40 A; processing time 5 min.
3. After unloading from the EPP-40 bath, the stocks are washed with running water and treated with steam using a steam jet device UPS 4.3-geyser.
4. After steam-jet cleaning, the rods are wiped with coarse calico moistened with alcohol and placed in a drying oven for drying and preheating to 150 °C.

3. The process of ion-plasma nitriding.

1. Prepared rods are installed in the vacuum chamber of the NNV 6.6-I1 installation (Fig. 2 a) using special equipment in the center of the rotating table (Fig. 2 b).
2. A foreline evacuation of the installation chamber is carried out to a pressure of 1 Pa (time is about 15 min.).
3. Further evacuation of the chamber is carried out by a high-vacuum diffusion pump to a pressure of $5*10^{-3}$Pa. (time 20-25 min.).
4. Then, argon is injected into the chamber through the gas leak and with the help of the BUEN electromagnetic leak control unit the pressure in the chamber is maintained at $2*10^{-1}$ Pa.
5. For the process of ionic cleaning and heating, a plasma source with a heated PINK cathode is switched on, a heating current of 120 A and an ion current of 5 A are set.
6. The block of the reference voltage is turned on and the bias voltage of -1000 V is applied to the parts. To eliminate the formation of micro arcs on parts, the reference voltage unit operates in a pulsed mode with a frequency of 25 kHz and a duty cycle of 80%.
7. The table rotation drive is switched on and the speed is set to 5 rpm.
8. Within 5-7 minutes, the PINK ion current is gradually brought to 45-50 A, while the heating of the rods is monitored using a Smotrich 7 pyrometer focused on the part through the viewing window of the chamber.
9. When the temperature reaches 450 °C (time 20-25 min.), Nitrogen of special purity is admitted into the chamber through a parallel gas main, using the RRG-10 flow meter (nitrogen flow rate is set at 2 l/min.), The pressure is maintained at the level of $1.8\text{-}2.2*10^{-1}$ Pa. Thus, the regime of ion-plasma nitriding of parts

in an argon-nitrogen gas mixture is established. Further, throughout the entire process, the temperature of the products is controlled, if necessary, adjusting the PINC current and the reference voltage.

a) b)

Fig. 2. Vacuum chamber of the NNV 6.6-I1 installation (a) and the satellite of the rotating table (b)

The nitriding process lasts 3 hours, after which the products are allowed to cool in a vacuum chamber for an hour and unloaded. The stocks before and after nitriding are shown in Fig. 3.

a) b)

Fig.3. Stocks 35HGSA before (260 HV) (a) and after (820 HV) (b) nitriding

The results of measurements of the microhardness of the hammer surface using an HV-1000 microhardness tester with a load on the indenter of 1 kg gave the following results: before nitriding about 260 HV, after about 820 HV (Fig. 3).

4. Discussion of the experimental results.

4.1. Surface layer thickness.

In the introduction, we emphasized that the surface plays an important role in nitriding. In [5], we showed that for the dimensional dependence of a certain physical property of a solid A(r), the following relations can be used:

$$\begin{aligned} A(r) &= A_0 \cdot \left(1 - \frac{d}{r}\right), r >> d \\ A(r) &= A_0 \cdot \left(1 - \frac{d}{d+r}\right), r \le d. \end{aligned}, \quad (1)$$

.

The parameter d(nm), which we identify with the surface layer of an atomically smooth crystal, is related to the surface tension σ by the formula:

$$d = \frac{2\sigma\upsilon}{RT}, \tag{2}$$

Here σ is the surface tension of a massive sample (J/m^2); υ – molar (atomic) volume (cm^3/mol); R – gas constant (J/kg K); T is temperature (K).

It was shown in [5] that the following relation is fulfilled with high accuracy:

$$\sigma = 0.7 \cdot 10^{-3} \cdot T_m, . \tag{3}$$

where T_m is the melting point of the solid (K). The ratio is fulfilled for all metals and for other crystalline compounds. If we substitute it in (2), then at $T = T_m$ we get:

$$d(I) = 0.17 \cdot 10^{-9} \upsilon . \tag{4}$$

Equation (4) shows that the thickness of the surface layer d(I) is determined by one fundamental parameter - the molar (atomic) volume of the element (υ = M/ρ, M is the molar mass (g/mol), ρ is the density (g/cm^3)), which periodically changes in accordance with the table D.I. Mendeleev. The d(II) layer extends approximately to the size d(II) ≈ 10d = d_∞, where the bulk phase begins. Dimensional properties begin from this size. By nanomaterials it is customary to mean materials, the main structural elements of which do not exceed the nanotechnological boundary of ~ 100 nm, at least in one direction. Table 1 shows the d(I) and d(II) values of some metals and alloys.

Table 1 - Thickness of the surface layer of metals and alloys

Steel, alloy	M, g/mol	ρ, g/cm^3	d(I), nm	d(II), nm
35HGSA	52.60	7.85	1.14	11.4
HG65MB	72.78	8.90	1.39	13.1
$W_{90}/Ni_6/Cu_4$	171.66	17.10	1.71	17.1
W_{50}/Cu_{50}	123.75	11.85	1.78	17.8

The thickness of the surface layer of metals and alloys d(I) and d(II) does not exceed 2 and 20 nm, that is, it is a nanostructure, where it has been experimentally shown that diffusion processes are significantly different from bulk [6, 7]. This especially affects the nitriding process of the metal rods studied by us [8].

4.2. Diffusion in a metal plate of nanometer thickness.

All manuals on the calculation of diffusion in thin coatings of space and aviation technology proceed from the classical Fick's equations, where the diffusion coefficient is considered a constant value [9]. As we have shown above, when the thickness of the metal film is less than 20 nm, dimensional effects begin to affect its physical properties. Let us consider the problem of diffusion in an unbounded plate of thickness δ. For simplicity and comparison, we restrict ourselves to the stationary case. Then the diffusion equation will have the form:

$$\frac{d}{dx}\left(Д(x)\frac{dc}{dx} \right) = 0. \tag{5}$$

In the classical case, D(x) = const, and in ours - $D = D_0(1-\alpha/\alpha+x)$. Here the size factor is denoted by α so as not to be confused with the differentiation sign. Taking into account the size effect (5) is reduced to the form:

$$\frac{x}{x+\alpha}\frac{dc}{dx} = \frac{C_1}{Д_0}. \tag{6}$$

Here C_1 is the constant of integration. The solution to equation (6) has the form:

$$c(x) = \frac{C_1}{Д_0}(x + \alpha \ln x) + C_2. \tag{7}$$

If in (5) D(x) = const, then we have the classical solution of the problem for an unbounded plate:

$$c(x) = C_1 x + C_2. \tag{8}$$

In contrast to the classical problem, a logarithmic term appears in equation (7). This leads to a divergence at the origin. Therefore, the boundary conditions must be set not at x = 0, but at $x=\lambda_{dB}$ - the de Broglie wavelength of electrons. Only in this case the classical Fick equations make sense.

It is also important that, according to (7), diffusion in a nanoplate depends both on the material of the plate through the diffusion coefficient of the bulk sample D_0 and on the size factor α. This leads to a difference in diffusion in the nanostructure [6, 7]. In the classical case, there is no such dependence.

4.3. The first boundary value problem for diffusion in a nanometer-thick wafer.

To solve (7), the first boundary value problem will look like this:

$$c(x)|_{x=\lambda_{dB}} = \frac{C_1}{Д_0}(Д_{dB} + \alpha \ln Д_{dB}) + C_2 = c_1,$$

$$c(x)|_{x=\delta} = \frac{C_1}{Д_0}(\delta + \alpha \ln \delta) + C_2 = c_2. \quad (9)$$

The general solution (9) (neglecting the de Broglie wave) will have the form:

$$c(x) = \frac{(c_1 - c_2)}{\delta} \cdot (x + d \ln x) + c_1. \quad (10)$$

The general solution to the classical problem is:

$$c^1(x) = \frac{c_2 - c_1}{\delta} x + c_1. \quad (11)$$

Comparison of (10) and (11) shows that diffusion in a nanometer-thick wafer differs significantly from a bulk sample. The difference between c(x) and $c^1(x)$ at x = d = δ is:

$$c(x) - c^1(x) = (c_1 - c_2) \cdot \ln d. \quad (12)$$

4.4. Diffusion of nitrogen in metals and alloys.

The diffusion mobility of nitrogen will be proportional to the thickness of the surface layer d. This value is associated with the crystal structure of the metal and, mainly, with its porosity. The existing nomenclature, adopted by the International Union of Theoretical and Applied Chemistry IUPAC, distinguishes three categories of pore size depending on their diameter: microporous < 2 nm, mesoporous 2-50 nm, and macroporous > 50 nm [10]. An important characteristic of a metal is the degree of its porosity P, defined as:

$$P = 1 - \rho_{Me} / \rho_K, \quad (13)$$

where ρ_{Me} is the density of the porous metal (Me), ρ_K is the density of the single crystal.

If we substitute equation (13) into equation (4), we get [11]:

$$d(I)_K = d(I)_{Me} / (1 - P). \quad (14)$$

Typical porosity is 40-70%, and with supercritical drying it reaches 95%. Equation (14) yields the following table 2.

Table 2 - Thickness of the surface layer of the rod 35HGSA at various values of porosity

P, %	40	50	60	70	80	90
$d(I)_K$, nm	1.9	2.28	2.85	3.80	5.7	11.4
$d(II)_K$, nm	19.0	22.8	28.5	38.0	57.0	114.0

Table 1 show that an increase in steel porosity leads to a noticeable increase in its surface layer thickness and an increase in the diffusion mobility of nitrogen. This steel can be obtained using powder metallurgy. In powder metallurgy, an important role is played by diffusion processes that ensure the formation of the structure of powder materials, especially in the production of alloys from a multicomponent mixture. When a homogeneous structure is obtained, the technological parameters of sintering should facilitate the diffusion homogenization of the alloy. In order to accelerate this process, it is necessary to

.

create conditions for the most active types of diffusion to occur. In [12], the main regularities of the influence of the degree of porosity and the temperature of tests on the processes of local destruction (initiation of microcracks) - resistance to micro-cleavage and resistance of a crack to its development - of powder alloy steels were established. It is shown that there is a significant difference in the behavior of powder steel from ordinary steels in brittle fracture, which consists in an increase in the resistance to micro-spalling with a decrease in the test temperature.

Conclusion

It is shown that the thickness of the surface layer of the steel of the rods turns out to be less than 20 nm and dimensional effects begin to affect its physical properties, that is, it is a nanostructure. Dimensional effects in this layer cause the "classical" Fick equations to fail in the layer. For the first time, we considered the problem of one-dimensional diffusion in the case when the coefficient depends on the coordinate. The analytical solution of the first boundary value problem showed that diffusion in a nanometer-thick wafer differs significantly from a bulk sample. The accuracy of solving this problem is determined by the de Broglie wave, that is, on the order of (0.01-0.001) nm for metals and alloys. The solution to this problem showed that the diffusion mobility of nitrogen will be proportional to the thickness of the surface layer d. This value is associated with the crystal structure of the metal and, mainly, with its porosity. In our work, we have shown that an increase in the porosity of steel leads to a noticeable increase in its thickness of the surface layer and an increase in the diffusion mobility of nitrogen. Such steel can be obtained by powder metallurgy and used for the above rods.

Acknowledgements

This work was supported by the Ministry of Education and Science of the Republic of Kazakhstan.
Grants No. 0118PK000063 and No. Ф.0781.

REFERENCES

1 Yurov V.M., Oleshko V.S. *The impact of the environment on the contact potential difference of metal machine parts. Eurasian Physical Technical Journal*, 2019. Vol. 16. № 1 (31). C. 99-108.

2 Makeeva O.V., Oleshko V.S., Fedorov A.V., Yurov V.M. *Development of a device for determining work electron output. Eurasian Physical Technical Journal*, 2020, Vol.17, No.1 (33). – P. 127-131.

3 Voroshnin L.G., Mendeleeva O.L., Smetkin V.A. *Theory and technology of chemical heat treatment.* – Minsk, New knowledge, 2010, 304 p.

4 Berlin E.V., Koval N.N., Seidman L.A. Plasma chemical heat treatment of the surface of steel parts. Moscow, Technosphere, 2012, 464 p.

5 Yurov V.M. The thickness of the surface layer of atomically smooth crystals. *Physicochemical aspects of the study of clusters, nanostructures and nanomaterials,* 2019, No.11, pp. 389 – 397.

6 Divinsky S.V., Zakharov S.M., Shmatko O.A. Grain-boundary diffusion and segregation in sintered nanocrystalline materials with a hierarchical structure. *Uspekhi fiziki metallov*, 2006, Vol. 7, pp. 1 – 39. [in Russian]

7 Dokukin S.A., Kolesnikov S.V., Saletsky A.M. Diffusion of atomic dimers during the formation of a surface alloy Pt / Cu (111) // VMU, Series 3. Physics. Astronomy, 2019, No. 4. - P. 46–51.

8 Sharifova E.G., Silina O.V., Makarova K.V. Analysis of literature data on the study of ways to intensify the nitriding process. *Master`s journal*, 2015, No. 2, pp. 60 – 65.

9 Bekman I.N. *Higher mathematics: the mathematical apparatus of diffusion*. Moscow, Yurayt Publishing House, 2017, 459 p. [in Russian]

10 Korotcenkov G. *Porous Silicon: From Formation to Application: Formation and Properties*, CRC Press, 2015, Part l, 423 p.

11 Yurov V.M. The thickness of the surface layer of porous silicon. *Bulletin of al Farabi KazNU. Physics*, 2020, No. 1(72), pp. 60 – 66.

12 Volokonsky M.V., Mishin V.M. Influence of porosity and lowering of the test temperature on the characteristics of local fracture of powder alloy steels . *International Journal of Experimental Education,* 2015, No. 4-2, pp. 441 - 442.

Article accepted for publication 24.10.2020

DOI 10.31489/2020No2/31-38

UDC: 621.793-036:678

COMPOSITION AND STRUCTURE OF COMPOSITE COATINGS BASED ON METAL OXIDES AND POLYTETRAFLUOROETHYLENEDEPOSITED UNDER CONDITIONS OF ELECTRON-INITIATED ENDOTHERMIC PROCESSES

Surzhikov A.P.[1], Chicherina N.V.[1], Rogachev A.V.[2], Yarmolenko M.A.[2], Rudenkov A.S.[2], Rogachev A.A.[3], Wang Jicheng[4]

[1] National Research Tomsk Polytechnic University, Tomsk, Russia, surzhikov@tpu.ru

[2]FranciskSkorina Gomel State University, Gomel, Belarus, rogachevav@mail.ru

[3]Institute of Chemistry of New Materials of the National Academy of Sciences of Belarus, Minsk, Belarus

[4]Jiangnan University,Wuxi, China

In this article features of physicochemical processes initiated by the low-energy electron flow between the components of the target based on nitrates of metals and metals, their influence on the kinetics of the formation of volatile products, the chemical composition and structure of the deposited coatings are established. When electrons act on a mixture of aluminum nitrate and dispersed aluminum, zinc oxide coatings containing zinc nanorods are formed. The impact of the electron flow on a mechanical mixture of powders of iron nitrate and dispersed aluminum is accompanied by explosive evaporation of the target, and a large number of microdroplet formations deposited at the final stage of exothermic reactions in the surface layers of the target are fixed on the surface of the coating containing oxides and metal nanoparticles. The features of the structure and chemical composition of coatings deposited from the volatile products of electron beam dispersion of a mechanical mixture of polytetrafluoroethylene, iron nitrate, and aluminum are determined. It is shown that under such conditions of generation of the gas phase, coatings are formed consisting of a polymer matrix and containing particles of oxide, a free metal, and a certain amount of the initial undecomposed salt. The result of exothermic reactions in the crucible is partial defluorination and increased defectiveness of the molecular structure of the fluoroplastic matrix.

*Keywords:*spectral analysis, signal, sensor, process, characteristic

Introduction

Synthesis of nanocomposite coatings based on polymers, metal clusters and their oxides is promising in the production of LEDs, solar cells, piezoelectric transducers [1], gas sensors [2], optical filters. The search for new technological methods of deposition of composite metal-containing coatings is an urgent task of physics and technology of thin-film systems [3, 4]. In recent years, plasmochemical methods of deposition of polymer coatings and surface modification have been actively developed, which are based on processes for creating an active gas phase containing polymerizable molecular fragments [5-8]. The methods are characterized by high efficiency, versatility (there are practically no restrictions on the selection of individual components of the composite coating), a large set of technological techniques for changing the composition, structure and properties of the formed materials, which allows the synthesis of complex thin film systems, the formation of which by other methods is impossible or requires the implementation of a multi-stage technologically complex application process [9-12].

Thus, when using an electron stream to generate a gas phase, polymer-polymer, metal-polymer, polymer-oxide systems are formed, characterized by high mechanical, physical and chemical properties [13-15]. At the same time, the flow of electrons during its action on the target material has a complex effect on the ongoing processes. In addition to the thermal effect on the target, which leads to dissociation of complex compounds, their evaporation or dispersion, radiation activation of chemical processes, synthesis of new compounds, which, being on the surface of the target, change the conditions for generating the gas phase, its composition and activity, are possible. The most significant effect of these processes is on targets containing

complex organic, including high molecular weight or inorganic compounds. It is worth noting that the action of electrons on the polymer target produces a stream of secondary electrons, which also have an initiating effect on dispersion products in the gas phase [16-18].

The main objective of the present work is to establish the influence of exothermic processes that occur under the influence of a low-energy electron flow in a vacuum on mechanical mixtures based on metal nitrate and aluminum, polytetrafluoroethylene (PTFE) on the kinetics of the formation of volatile products, the composition and structure of the resulting layers.

1. Experiment procedure

Coatings were precipitated from the gas phase generated by exposing the original target to an electron stream with an energy of 800-1600 eV and a density of 0.01-0.03 (A/cm^2) [19]. Process of sedimentation of coatings was made with an initial pressure of residual gases in the vacuum unit($\approx 4 \cdot 10^{-3}$ Pas). Powders of nine-water iron (III) nitrate ($Fe(NO_3)_3 \cdot 9H_2O$), dispersed aluminum, PTFE were used as the target material. The targets were manufactured by thoroughly mixing various powders in an agate mortar. A composite target based on PTFE and a mixture of dispersed aluminum with iron nitrate was made in two steps. In the first step, the inorganic components were mixed. In the second step, PTFE was added to the mortar with the prepared mixture of inorganic powders in small portions and mixed thoroughly with a pestle. The weight ratio of organic to inorganic components was 1:1.

The substrates during the sedimentation of the layers were quartz plates (during spectroscopic measurements in the ultraviolet and visible regions), NaCl plates (during infrared (IR) spectroscopic (IKspectroscopic studies), silicon single crystal plates(during atomic force microscopy (AFM) and scanning electron microscopy (SEM) studies). The substrate temperature at sedimentation was as follows: 25°C.

Annealing of the formed coatings was carried out in air at a temperature of 250°C for 60 minutes. In some cases, annealing was performed at 500°C.The IR spectroscopic studies were conducted on Fourier's IR spectrophotometer Vertex-37 (Bruker).UV-View spectroscopic studies were conducted using a Cary-50 spectrophotometer (Varian). The band gap width was determined by the method used in [20] based on the analysis of the optical absorption spectra.The study of morphology, distribution of chemical elements on the surface of thin coatings was carried out using an electron microscope (SEM, Quanta200F) with EDAX microanalysis.

2. Results and discussion

At the first stage the features of electronic dispersion of target containing dispersed zinc and zinc nitrate are determined. It has been found that the use of such a target makes it possible to form continuous coatings based on zinc oxide. The interplane distance of the coating applied using the composite target is 0.281 nm, which is in good accordance with ZnO (1010) [21].

The effect of the electron flux on the target is accompanied by a dazzlingly white glow indicating a high temperature in the electron exposure zone. A zinc oxide sublimation process was identified as the main reason for the formation of the thin coating ZnO. It is worth noting that the sublimation temperature of the ZnO is 1800°C and cannot be achieved in the dispersion zone using a low energy electron flow, as well as due to the decomposition energy of the nitrate (endothermic reaction). In addition to the marked dazzling white glow in the dispersion zone, the high temperature was indicated by the presence of metallic zinc nanoparticles in the precipitated thin layer. As is known, the melting point of zinc exceeds 400°C. Thus, a high temperature is achieved in the target electron exposure zone due to the exothermic reactions between the target components initiated by the thermal radiation electron beam. The analysis shows that chemical processes with the formation of zinc oxide in two stages are most likely:

1 $Zn(NO_3)_2 \cdot 6H_2O + 5Zn = Zn(NO_2)_2 + 2ZnO + 3Zn$ (residue) $+ 6H_2O\uparrow + Q$,

where Q is moderate heating.

2 $Zn(NO_2)_2 + 2ZnO + 3Zn = 6ZnO + N_2\uparrow + Q$ where Q is intensive heating.

Further, the features of electron-beam dispersion of copper and iron nitrates were considered. It has been established that the process of water salts is characterized by the presence of two characteristic periods. The first is the melting of salt in crystallization water, followed by the splitting of water molecules from the salt. In the vacuum chamber, the process of separating water molecules is accompanied by a monotonous

increase in pressure in the vacuum chamber, without any noticeable changes in the readings of the quartz thickness meter. The second is the intensive formation of the gas phase by products of thermal radiation decomposition of metal salts. According to IR spectroscopic analysis, the gas phase in the second period of electron beam dispersion of nitrates forms salt molecules that are intensively evaporated by an electron flow.

Heating of formed copper nitrate coating is accompanied by formation of copper oxide coating. The result is expected because the thermal degradation reaction of anhydrous copper nitrate can be recorded as follows:

$2Cu(NO_3)_2 = 2CuO + 4NO_2\uparrow + O_2\uparrow$

Electron beam dispersion of ninety-water iron (III) nitrate has features. The effect of the electron stream on the salt is accompanied by the melting of the salt in crystallization water and its intensive transition to the gas phase. In contrast to zinc nitrate no intense plasma glow was recorded at a late stage of electron beam impact on powder $Fe(NO_3)_3 \cdot 9H_2O$. The IR spectrum of the formed coating coincides with the IR spectrum of the original iron salt powder. Annealing of the formed coatings is accompanied by salt decomposition to form iron oxide. The band gap width (E_g) for the Fe_2O_3, determined by extrapolation of the dependence $(Dh\nu)^2$on the photon energy, is 2.2-2.4 (eV) (Figure 1).

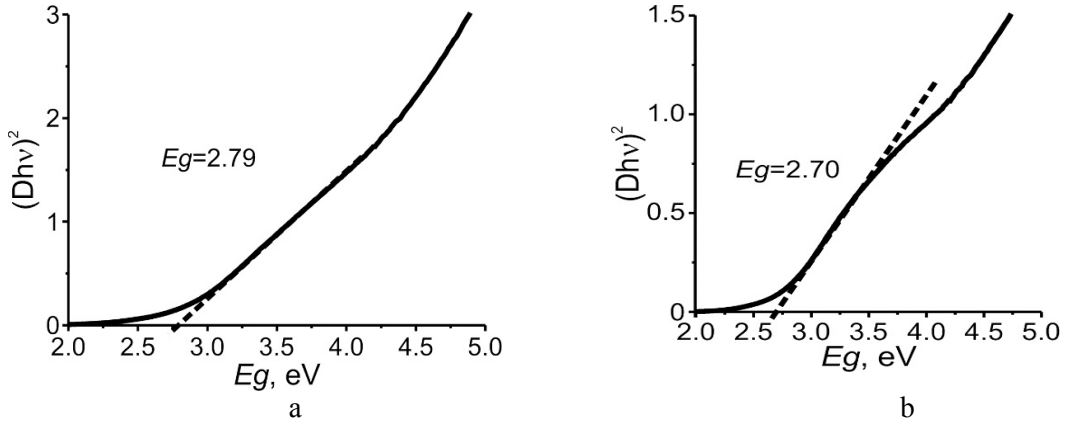

Fig.1. Dependence $(Dh\nu)^2$ on photon energy for $Fe(NO_3)_3 \cdot 9H_2O$ coatings annealed at: a) 250°C; b) 500°C

For Fe_2O_3 nanoparticles the Eg value can significantly exceed the specified interval of values [22, 23]. Thus, work [11] considers the effect of annealing on the size of nanoparticles Fe_2O_3 and the value of the band gap. It is noted that the size of Fe2O3 particles increases with an increase in the annealing temperature, the electron transition energies approach the value known for a bulk material of 2.2 eV: a decrease in the width of the gap zone from 3.51 to 2.76 eV occurs. Thus, on the basis of $Fe(NO_3)_3 \cdot 9H_2O$ with increase in temperature of annealing the increase in the size of nanoparticles of oxide of iron can be one of the reasons of reduction of E_g of coatings.

As in the case of zinc nitrate, to eliminate or reduce the effect of salt melting, it is proposed to use a mechanical mixture of iron nitrate powders and aluminum powder. It is noted that the preliminary thorough mixing of salt and aluminum powder can significantly level the process of salt melting. This is due to chemical interactions between the components in the mixing step. Indirectly, this is indicated by the fact that when mixed, the powder becomes brown due to the formation of iron oxide. The thermal radiation effect of the electron stream should be accompanied by decomposition of nitrate to oxide to form a finely dispersed mixture of iron oxide and aluminum. At the same time, the heat generated as a result of the reaction will be responsible for the intensive formation of a gas-phase stream of dispersion products.

However, preliminary studies of electron beam dispersion of the mixture of salt and aluminum showed the absence of exothermic reactions. The main reasons are the low energy of the electron flow and insufficient mechanical contact between the target components. The absence of contact under vacuum conditions prevents the chemical interaction between salt and aluminum powder. It should be noted that in aluminum powder, aluminum is protected from interaction with the environment by fat additives. Thus, in order to conduct chemical interactions between salt and aluminum, it is necessary to achieve good mechanical contact and destroy the protective film. The destruction of the fat film is easily effected by a low energy electron flux. Good mechanical contact was achieved by thoroughly mixing the target components in diethyl ether. The short effect of the electron flow in a vacuum on the mechanical mixture prepared in this

way initiates a violent chemical reaction resulting in explosive evaporation of the target material.Peculiarities of morphology of deposited coatings and their chemical composition are established. Figure 2 shows the IR spectra of coatings based on iron nitrate and aluminum powder formed as a result of the implementation of such an interaction.

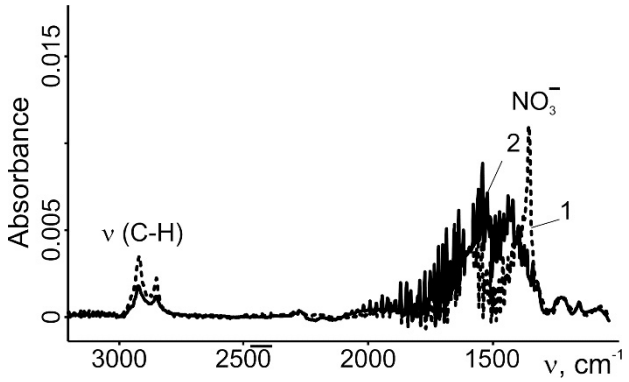

Fig.2. IR spectra of the coating based on $Fe(NO_3)_3 \cdot 9H_2O$ and aluminum powders:
1 –without heat treatment; 2 – heat treatment 250°C, 1hour.

Faintly noticeable absorption bands are recorded in the spectrum due to the presence of C-H and NO_3 groups in the thin layer [13]. Thus, the high reaction temperature and explosive nature of the reaction initiate rapid decomposition of the salt. There is practically no undissolved salt in the formed reaction product stream. Thermal treatment of the coating is accompanied by complete decomposition of iron nitrate (Fig.2). Figure 3 shows the results of SEM studies of coatings formed under conditions of exothermic interaction between iron nitrate and aluminum. On surface of the formed layer there is a large number of microdrops, indicating the explosive nature of the application (Fig.3,a). The coating itself is solid and defect-free (Fig.3, b). Droplet formation occurs at the final stage of exothermic interaction in the target. Chemical analysis of various microdroplets shows a high content of aluminum in them, while the lower defect-free layer (analysis was carried out at various points) is characterized by a high content of iron (Table 1).

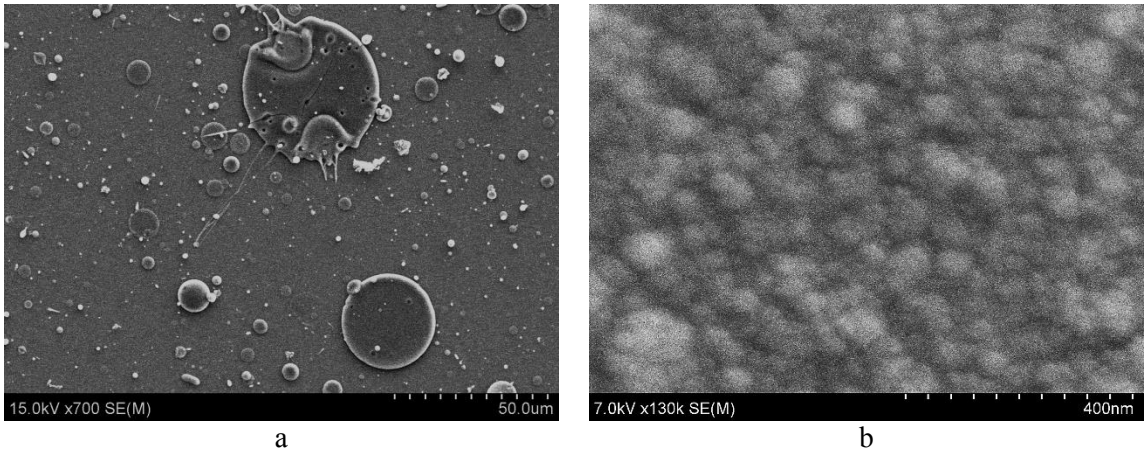

a b

Fig.3. Results of SEM studies of coatings based on $Fe(NO_3)_3 \cdot 9H_2O$ and aluminum powder

Table 1 - Chemical composition of thin layer

Objecttobeanalyzed	Fe	Al	O
	at. %		
Microdrop1	22.05	30.57	47.38
Microdrop2	11.62	35.78	52.60
Microdrop3	1.36	41.01	57.63
Bottomsolidlayer	50.21	21.96	27.83

Analysis of the chemical composition of the thin layer indicates incomplete metal oxidation; metal nanoparticles are present in the coating along with iron and aluminum oxides.

3. Formation of coatings based on iron oxide, aluminium and PTFE

It has been found that exposure of mechanical mixtures containing polymers such as polyethylene, polyurethane to electron flow in vacuum causes melting of the target polymer component, and the resulting melt prevents direct contact of the salt and aluminum particles and, accordingly, chemical interaction. During electron beam dispersion of PTFE, the formation of a viscous-flowing state of the polymer is not observed and contact of iron and aluminum nitrate particles is maintained. The kinetic features of the electron beam dispersion process of organo-inorganic targets are shown in Figure 4.

The effect of electron flow on the composite target is accompanied by an increase in pressure in the vacuum chamber. At the same time, there is a long induction period during which the quartz thickness meter does not record the deposition of the coating. The increase in pressure during the induction period is due to the formation of the gas phase by low molecular weight non-condensing compounds at room temperature. These compounds are the products of salt decomposition: water molecules, nitric acid. Subsequently, there is a local exothermic interaction of inorganic compounds. On the kinetic curve of pressure change, characteristic peaks appear, indicated in Figure 4, b. Bright flashes are visually fixed on the target surface, accompanied by local blackening of the target.

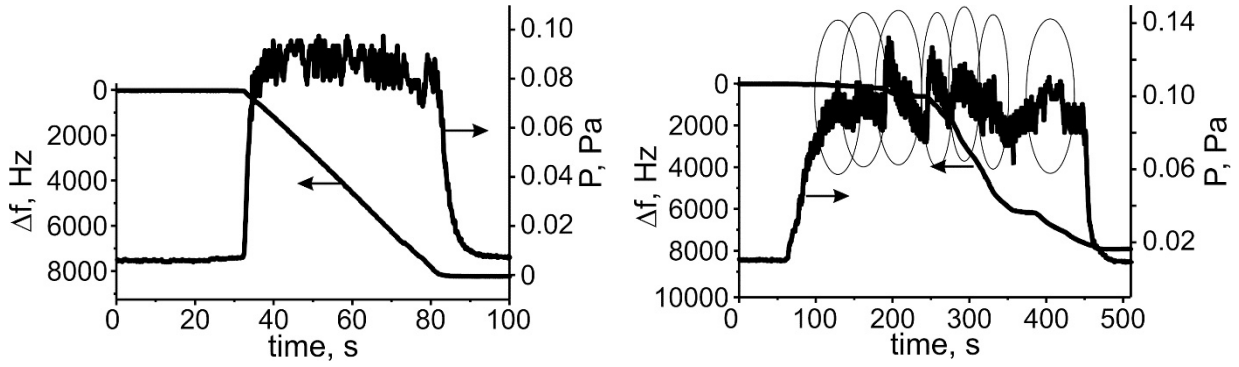

Fig.4. Kinetics of electron beam dispersion of PTFE (a) and mixture $Fe(NO_3)_3 \cdot 9H_2O$+Al+PTFE (b)

A noticeable amount of the starting salt is present in the formed thin composite layer. In the IR spectrum of the coating, in addition to the absorption bands characteristic of PTFE, the absorption of NO_3 and OH groups is recorded (Figure 5).

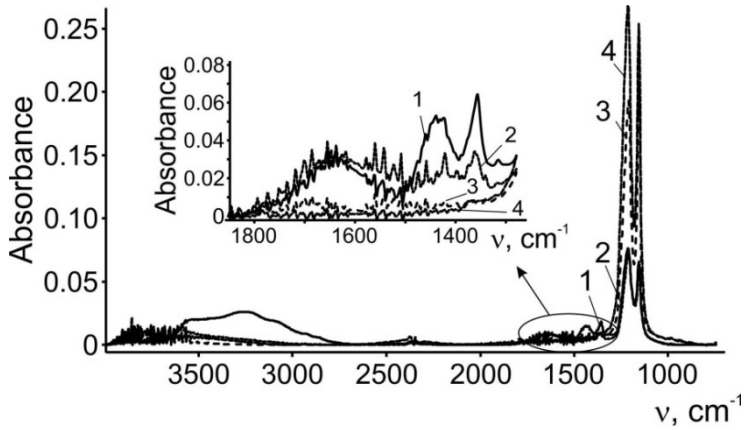

Fig.5. IR spectra of $Fe(NO_3)_3 \cdot 9H_2O$+Al+PTFE coatings: without heat treatment (1), $Fe(NO_3)_3 \cdot 9H_2O$+Al +PTFE coatings after heat treatment (2), PTFE coatings without heat treatment (3), PTFE coatings after heat treatment (4)

Valence vibrations of OH groups are manifested in the range of 3600-2800 cm^{-1}, deformation - near 1640 cm^{-1} [13]. The presence of water molecules in the thin layer is due to the non-deposited salt intensively sorbing atmospheric moisture. Annealing is accompanied by salt decomposition and desorption of adsorbed moisture.The effect of inorganic components and the generated heat flux on the molecular structure of PTFE was judged by absorption bands at 638 and 625 cm^{-1}. The strip at 625 cm^{-1} is referred to a defective structure, and the strip at 638 cm^{-1} is associated with the presence of a regular spiral [13]. The analysis was carried out after heat treatment of the formed coatings. For the composite coating, the ratio of D_{638}/D_{625} corresponds to 1.40 and for the PTFE thin layer to 1.84. The consequence of exothermic reactions is a predicted increase in the defect of the molecular structure of the fluoroplastic matrix.

The morphology of the composite layer in comparison with the morphology of PTFE is more "loose" and porous, there is a significant number of small drop-like formations that form larger surface structures (Figure 6). It can be assumed that the deposition of the composite layer, unlike the PTFE single-component coating, occurs under conditions of insufficiently high density of active fragments of PTFE macromolecules and their increased adsorption activity. It should be noted that thermal effect in vacuum on PTFE is accompanied by generation of a chemically inactive monomer. Activation of the monomer requires additional physical influence: treatment with an electron flow, discharge plasma, etc. The results of atomic force microscopy (AFM) studies indicate a significant effect of thermal effects on the morphology of the deposited layer.

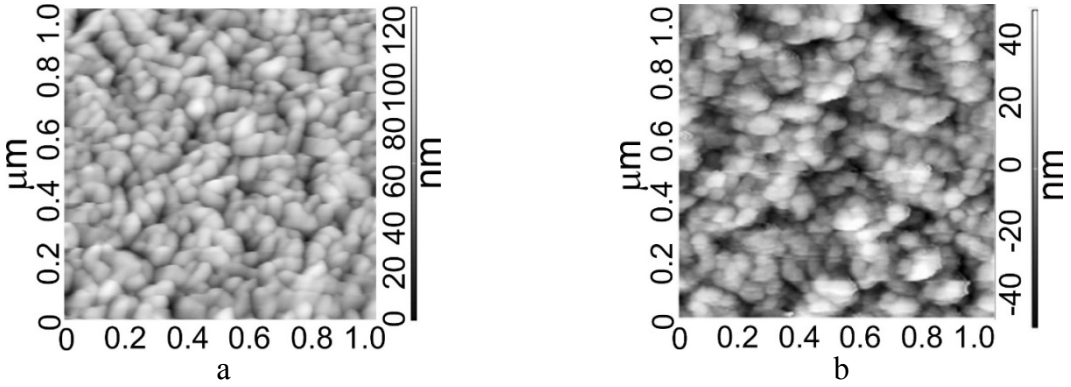

Fig.6. AFM images of coatings obtained by dispersing PTFE (a) and $Fe(NO_3)_3 \cdot 9H_2O$+Al + PTFE (b)

It should be noted that the deposited coating composition is non-uniform in thickness. That is why during its annealing with the help of SEM, a discontinuity was established, the presence of local areas, the formation of which can be explained by the decomposition of iron nitrate, the vapors of which are present in volatile dispersion products (Figure 7).

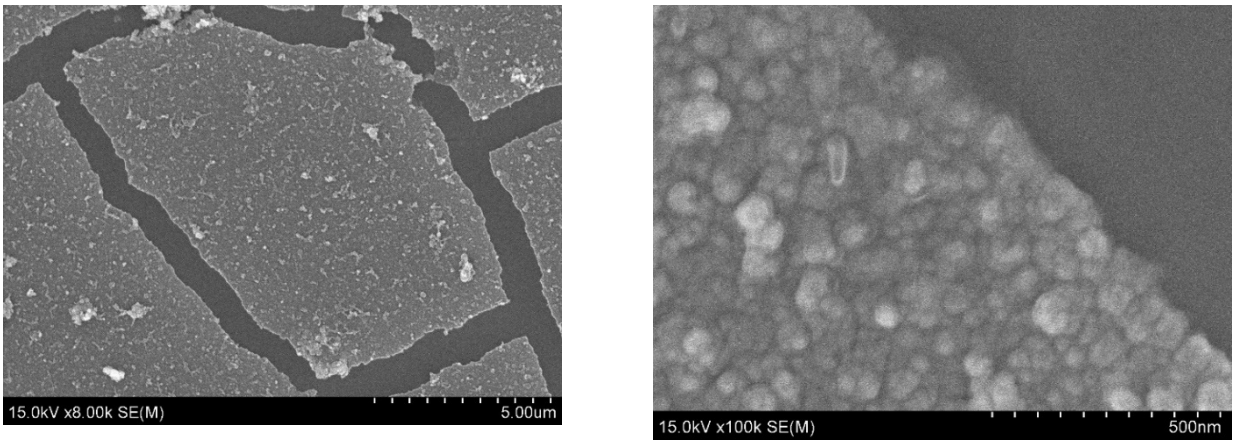

Fig.7.SEM image of coating based on $Fe(NO_3)_3 \cdot 9H_2O$ +Al+PTFE subjected to heat treatment with different zoom

High heterogeneity of deposited coatings is confirmed by the results of their chemical analysis (Table 2). Large droplets (Fig. 8) on the surface of the coating are the result of melting and evaporation of aluminum powder. Dispersion of the composite target is accompanied by defluorination processes of the organic component. If in the starting polymer the ratio of carbon atoms to fluorine is 1:2, so in the coating it is approximately the same or the number of fluorine atoms is less, which is possible when cluster carbon structures are formed in the coating volume, or when forming macromolecules of the form $[-C = CF-]_n$.

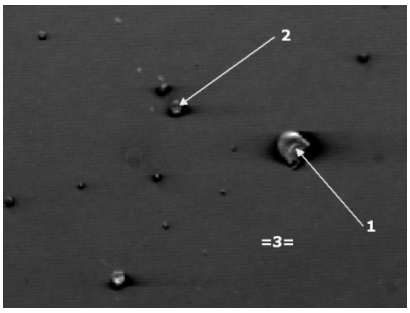

Fig. 8.SEM image of coating based on $Fe(NO_3)_3 \cdot 9H_2O$ +Al+PTFE

Table 2 - Chemical composition of composite coating areas

Object to be analyzed	Fe	Al	O	C	F
	at. %				
1	3.31	13.90	4.31	35.50	42.98
2	14.46	12.52	14.22	30.23	28.56
3	4.14	8.51	11.15	45.26	30.94

According to the chemical analysis, a certain fraction of the metal in the thin layer is not present in the oxidized state. The results are consistent with UV-Type spectroscopy data: the value of the band gap cannot be determined based on electronic spectra. This indicates a low concentration of oxide in the organic layer.

Conclusion

Peculiarities of electron-beam dispersion of mechanical mixtures based on aluminium, copper, iron and dispersed aluminium nitrate are considered. Under the influence of low-energy electrons on a mixture of aluminum nitrate and dispersed aluminum, the formation of zinc oxide coatings containing zinc nanosupples was established, which indicates a significant effect of exothermic reactions between the target components on the formation of volatile products and their chemical composition of the deposited coatings. It is noted that the effect of electron flow on the mechanical mixture of iron nitrate powders and dispersed aluminum is accompanied by explosive evaporation of the target. A large number of microdroplet formations deposited at the final stage of exothermic interaction in the target are fixed on the surface of the thin layer. Chemical analysis of the lower defect-free layer showed a high iron content (more than 50 at%), the formation of a coating containing metal oxides and nanoparticles.

The principle possibility of sedimentation of polymer coatings containing oxides, metal nanoclusters is established by electron-beam dispersion of mechanical mixtures under conditions of exothermic processes in the target. It has been shown that by dispersing the mechanical mixture of PTFE, iron nitrate, iron nitrate and aluminum nitrate, coatings are formed consisting of a polymer matrix and containing particles of oxide, free metal and a certain amount of the original non-deposited salt. The consequence of exothermic reactions in the crucible is partial deflection and increased defects in the molecular structure of the fluoroplastic matrix.

Acknowledgements

The work was carried out with the financial support of the Ministry of Education of the Republic of Belarusas a task 2.4.04 "Development of physical and chemical foundations of methods for activation of gas phase generation processes using exothermic and endothermic reacting chemicals" and the research is carried out at Tomsk Polytechnic University within the framework of Tomsk Polytechnic University Competitiveness Enhancement Program grant.

REFERENCES

1 Bryanskikh T.V., Kokourov D.V. Energy efficiency of electric furnaces with movable floor in firing of vermiculite concentrates of different size groups. *Refractories and Industrial Ceramics*, 2017, Vol. 58, pp. 368–373.

2 Zhuravlev V.A., Naiden E.P., Minin R.V., Itin V.I., Suslyaev V.I., Korovin E.Yu. Radiation-thermal synthesis of W-type hexaferrites. *IOP onference Series: Materials Science and Engineering*. 2015, Vol. 81, Article number 012003. https://doi.org/10.1088/1757-899X/81/1/012003.

3 Santamaria A., Faleschini F., Giacomello G., Brunelli K., Pasetto M. Dimensional stability of electric arc furnace slag in civil engineering applications. *Journal. of Cleaner Production*. 2018, Vol. 205, pp. 599-609.

4 Sharipov M.Z., Mirzhonova N.N., Hayitov D.E. Effect of inhomogeneous radially directed mechanical stresses on the domain structure of a FeBO3 single crystal. *Eurasian phys. tech. j.* 2019, Vol.16, No.1, pp. 35 – 41.

5 Surzhikov A.P., Malyshev A.V., Lysenko E.N., Vlasov V.A., Sokolovskiy A.N. Structural, electromagnetic, and dielectric properties of lithium-zinc ferrite ceramics sintered by pulsed electron beam heating. *Ceramics International.* 2017, Vol. 43, No. 13, pp. 9778-9782. DOI**:** 10.1016/j.ceramint.2017.04.155

6 Yarmolenko M.A. Plasma-chemical modification of sealing rubber products based on nitrile butadiene rubber: structure and antifriction properties of surface layers, Extended abstract of D.Ph. thesis, Gomel, *Institute of Mechanics of Metal-Polymer Systems named after V. A. Bely of the National Academy of Sciences of Belarus*. 2006, 24 p.

7 Patil U.V., Rout C.S., Late D.J. Impedimetric humidity sensor based on α-Fe_2O_3 nanoparticles. *Advanced Device Materials*. 2015, Vol. 3, pp. 88–92.

8 Shkarin A.V., Zhabrova G.M., Topor N.D., KushnarevM.Ya. Thermal stability and chemical transformations of oxalates. *Bulletin of the Tomsk Institute named after C.M.Kirov* 1969, Vol. 199, pp. 105 – 111.

9 Kolesnikov V.N. Forms of carbon formed during thermolysis of formates of metals of the iron subgroup. *Bulletin of the Kharkov National University*. 2011, Vol. 976, No 20, pp. 247 – 253.

10 Myagkov V.G., Zhigalov V.S., Bykova L.E., Maltsev V.K. Self-propagating high-temperature synthesis and solid-phase reactions in two-layer thin films. *Technical Physics Journal.* 1998, Vol. 68, pp. 58 – 62.

11 Myagkov V.G., Bykova L.E., Bondarenko G.N. Self-propagating high-temperature synthesis and formation of quasicrystals in two-layer Al / Mn thin films. *Journal of Experimental and Theoretical Physics Letters*. 1998, Vol. 68, pp. 121 – 124.

12 Yarmolenko M.A., Rogachev A.A., Luchnikov P.A., Rogachev A.V., Hong Jang Xian. *Micro- and nanocomposite polymer coatings deposited from the active gas phase*. Radiotekhnika, Moscow, 2016, 424 p.

13 Surzhikov A.P., Peshev V.V., Pritulov A.M., Gyngazov S.A. Grain-boundary diffusion of oxygen in polycrystalline ferrites. *Russian Physics Journal.* 1999, Vol. 42, No. 5, pp. 490-495. DOI: 10.1007/BF02508222

14 Investigation of structural properties of electron-beam deposition of zinc oxide coatings doped with copper *Surfaces and Interfaces.* 2017. Vol. 6, pp. 24 – 32.

15 Kharlamova M.V., Sapoletova N.A., Eliseev A.A, Lukashin A.V. Optical properties of γ-iron oxide nanoparticles in a mesoporous silicon oxide matrix. *Journal of Experimental and Theoretical Physics Letters*. 2008, Vol. 34, No 7, pp. 36 – 43.

16 Gutnik V.A., Khalipova O.S., Kuznetsova S.A. Gutnik, V.A. The effect of salicylic acid on the properties of Fe_2O_3 films obtained from a film-forming solution based on iron (III) chloride. *Bulletin of Tomsk State University. Chemistry.* 2015, No 2, pp. 76–86.

17 Rogachev A.V., Yarmolenko M.A., Rogachev A.A., Gorbachev D.L., Zhou B. Chemical composition, morphology and optical properties of zinc sulfide coatings deposited by low-energy electron beam evaporation. *Applied Surface Science.* 2014, Vol. 303, pp. 23-29.

18 Barman B., Sarma K.C. Luminescence properties of ZnS quantum dots embedded in polymer matrix. *Chalcogenide Letters*. 2011, Vol. 8, No 3, pp. 171 – 176.

19 Karipbayev Zh., Alpyssova G., Mussakhanov D., et al. Time-resolved luminescence excited with N_2 laser of YAG:CE Ceramics formed by electron beam assisted synthesis. *Eurasian Physical Technical Journal*. 2020, Vol.17, pp. 73-76. https://doi.org/10.31489/2020NO1/73-76.

20 Dekhant I. Infrared spectroscopy of polymers. Khimiya, Moscow, 1972, 472 p. [in Russian]

21 Surzhikov A.P., Frangulyan T.S., Ghyngazov S.A., Lisenko E.N., Galtseva O.V. Physics of magnetic phenomena: Investigation of electroconductivity of lithium pentaferrite. *Russian Physics Journal*. 2006, Vol. 49, No. 5, pp. 506 – 510. DOI**:** 10.1007/s11182-006-0133-6

22 Ridgley D.H., Lessoff H., Childress J.V. Effects of Lithium and Oxygen Losses on Magnetic and Crystallographic Properties of Spinel Lithium Ferrite. *Journal of the American Ceramic Society.* 1971, Vol.53, pp. 304 – 311. https://doi.org/10.1111/j.1151-2916.1970.tb12113.x.

23 Mazen S.A., Abu-Elsaad N.I. Structural, magnetic and electrical properties of the lithium ferrite obtained by ball milling and heat treatment. *Applied Nanoscience.* 2015, Vol. 5, pp. 105 – 114. https://doi.org/10.1007/s13204-014-0297-2.

Article accepted for publication 19.10.2020

DOI 10.31489/2020No2/39-44

UDC 530.1; 538.97; 539.216.1; 539.216.2; 539.23

WIDTH OF ENERGY BAND GAP OF NANOPOROUS SEMICONDUCTOR FILMS

Zhanabaev Z.Zh., Ikramova S.B., Tileu A.O.,Turlykozhaeva D.A.

al-Farabi Kazakh National University, Almaty, Kazakhstan, zhanabaev.zeinulla@list.ru

The aim of this work is to experimentally clarify the reasons for the appearance of jumps in the current and memory of semiconductor nanoporous structures.Porous nanostructures were obtained by electrochemical etching. The current-voltage characteristics of the samples were measured for porous silicon and on thin films of a chalcogenide glassy semiconductor. The existence of jump-like switching and current hysteresis in porous silicon nanofilms under laser illumination is shown experimentally.A connection between the switching voltage values and the dependence of the band gap on the porosity of nanofilms is found. These results make it possible to construct a theory of current switching and its hysteresis based on the concepts of the theory of second-order phase transitions.

Keywords: porous silicon, energy band gap, current-voltage, electrochemical etching, laser, chaos.

Introduction

Porous silicon (PS) is a special composite material consisting of pores and silicon crystals. It has a wide range of applications due to the variety of arrangement of surface atoms. The high tunability of porous silicon is determined by many properties, such as dielectric constant [1,2], bandgap [3], etc. The results of work [4-5] showed that porous silicon has a wider energy bandgap $\left(E_g\right)$ than solid silicon has. This is explained by the fact that more intense recombination of electron-hole pairs occurs in quantum porous nanostructures and their energy band gaps become larger [6]. In many studies, the band gap is determined through the optical properties (transmission, reflection, absorption) of porous silicon.

The results of work [7, 8] showed that the radiation intensity of PS increases with an increase in the percentage of porosity since it is proportional to the number of re-emitted photons. The band gap increased as the concentration of mobile charge carriers in the remaining silicon structure of PS decreased. In this case, the porosity was more than 60%. Energy band gap increments E_g in porous silicon are determined from the condition of quantum confinement; therefore, the average size of nanocrystallites is a very important parameter of porous silicon [9, 10]. It is also noted in [11, 12] that with a decrease in the diameter of a porous silicon nanocrystal, E_g increases. This is because a decrease in the nanocrystal diameter leads to an increase in the porosity value. In [13] for calculating, the value E_g for Si is calculated by the empiricalpseudo-potential method. It is indicated that the calculation results are in good agreement with other experimental and theoretical results. A linear increase in the bandgap from 1.4 to 1.88 eV with an increase in porosity of PS films in the range of 27–88% was also noted. This is explained by the arrangement of atoms, mechanical behavior, and quantum confinement of carriers in PS microcrystallites, causing an expansion of the Si bandgap.

In [14], an estimate of the electron energy (E_g) relative to the valence band of bulk Si for nanostructures of oxidized porous silicon was presented. The photoluminescence spectra are explained based on traprelated transitions. For samples with high porosity, double peaks appeared in the PL spectra. One of these peaks remained constant at ~ 730 nm, while the other was blue-shifted with increasing current density. The PS nanostructure was modeled as an array of regular hexagonal pores, and the average value E_g was estimated at 1.67 eV.

.

The values E_g of the zones of n-type and p-type porous silicon layers are larger than $E_g = 1.11$ eV [15]. In the range of porosity (50–76%), theenergy bandgap of porous p-type silicon (1.80–2.00 eV),measured by the optical method,is higher than that of the porous n-type silicon layer (1.70–1.86 eV). For the same porosity, the values E_g for p-PSi is always higher than the values E_g obtained for the n-PSi layer. The values E_g were identified through the transmission spectrum also in [16-17]. From a brief review of the state of the art, it follows that it is important and necessary to study the energy bandwidth of nanoporous semiconductors since it largely depends on the degree of porosity of nanostructures. For example, with an increase in porosity, the values E_g increase, the electrical conductivity of nanostructured films changes. Experimental studies currently cover a narrow range of parameters without establishing a universal dependence on their nanoscale structure. More detailed studies are needed to significantly optimize the methodology for experimental studies of nanomaterials to reduce the cost of developing appropriate new technologies.

The aim of this work is to experimentally study dependence of the electrical conductivity of semiconductor nanoporous structures, and effect of the degree of porosity on the value of energy band gap.

1. Experimental setup and measurement procedure

Dependence of the energy bandwidth of nanostructured semiconductors on their porosity was investigated experimentally on the surface of porous silicon grown by electrochemical etching. The original silicon was monocrystalline silicon with a p-n + - junction, where n + is a layer, is a diffusion layer with a gradient distribution of phosphorus impurities with a concentration of up to 10^{20} cm^{-3} with a gradual decrease in impurity to the p-n junction boundary. In the future, the n-layer will be used as a working surface for the formation of porous silicon. The effect of porosity on the conditions of silicon electrochemical etching is investigated.

The thickness of p - silicon is 350 μm with an initial resistivity of 10 Ohm·cm, the thickness of the n-layer is about 500 nm, the surface of the n-layer is mirror-polished. Before electrochemical etching, the silicon surface was etched in a 10% solution of hydrofluoric acid to remove phosphor silicate glass, thoroughly washed in isopropyl alcohol using an ultrasonic device, and dried.

An electrolyte was used to obtain porous silicon in an HF: ethanol solution in a 1: 1 ratio. The anodic etching was performed in a mode of different current density and anodization time in a specially prepared fluoroplastic cell, and during each etching, the porous silicon layer was thoroughly washed in deionized water and dried.After anodic etching, porous nano- and microcrystalline structures with expanded porous spaces are formed on the surface of crystalline silicon. With an increase in the anodization current density, the porous spaces expand with a decrease in the diameters of silicon clusters. Structural images of nanofilms (Figure 1) were obtained by scanning electron microscopy (SEM) ULTRA 55 FE-SEM (Carl Zeiss).

The porosity was measured by gravimetric weighing. Weighing determined the masses of the sample before anodizing (m_1), after anodizing (m_2), and after removing the porous silicon layer in a 2% KOH medium (m_3). Formula

$$\eta(\%) = \frac{m_1 - m_2}{m_1 - m_3} \times 100\% \quad (1)$$

was used.

The experiments on the current-voltage characteristic (CVC) of nanoporous semiconductors were also carried out in the air with laser illumination (infrared laser wavelength λ = 630 nm, ħω = 0.5 eV). An n-Si layer with crystal orientation (100) was used as the studied sample. Porous silicon samples with a thickness of 350 μm (p-type), 500 nm (n-type) were obtained by electrochemical etching. The voltage, current density, and taring time were 10 V and 50 mA / cm^2, 3 min, respectively. Metal contacts applied to the n-layer and porous surface (Figure 2) make it possible to obtain the current-voltage characteristic of porous silicon. A voltage was applied to the PC film in the range from 0 V to 2 V with a step of 0.1 V using the Two-Wire Current-Voltage Analyzer of the Ni ELVIS II + universal station.

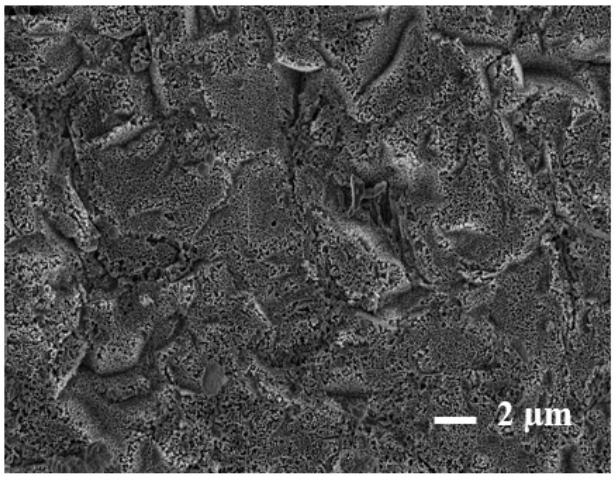

Fig. 1. SEM images of porous silicon layers: top view.

The I – V characteristics of the samples were measured on the NI ELVIS II + educational platform (Figure 2), which uses instruments developed in the LabVIEW software environment on a specially designed prototype board. The main characteristics of the platform: operating current range is ± 40 mA, the voltage range is from -10 V to 10 V.

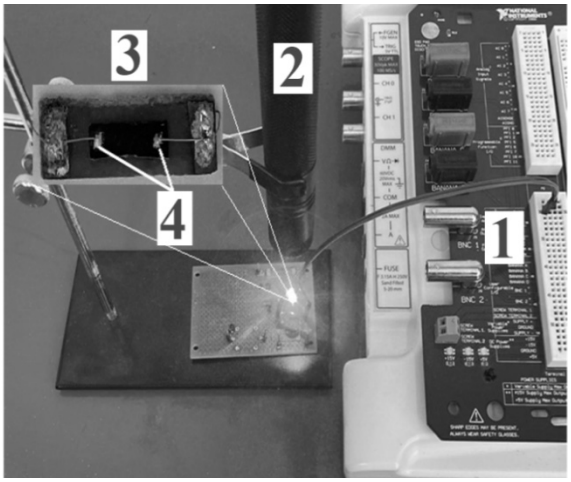

Fig. 2. General view of the installation for measuring the electrical properties of samples:
1- NI ELVIS II^{+} platform, 2- infrared laser λ =630 nm, 3-PS films, 4- contacts.

2. Electrical conductivity of porous semiconductor nanofilms

Changes in current versus voltage (VAC) for porous silicon were obtained in natural light (Figure 3) and under laser illumination. The measurements were repeated at regular intervals. Without laser illumination of nanofilms, a jump-like change in current is not observed. Currenthysteresisoccurs.

The reverse current is greater in value than that of the original measurement in the forward direction. This can be explained by a change in the polarization of nanostructures due to the directional action of the primary current.At voltage values of the order of E_g and higher (for crystalline silicon $E_g = 1.12$ eV), currentswitching is observed (Figure 4).At voltage values of the order of E_g and higher (for crystalline silicon $E_g = 1.12$ eV), current switching is observed (Figure 4).

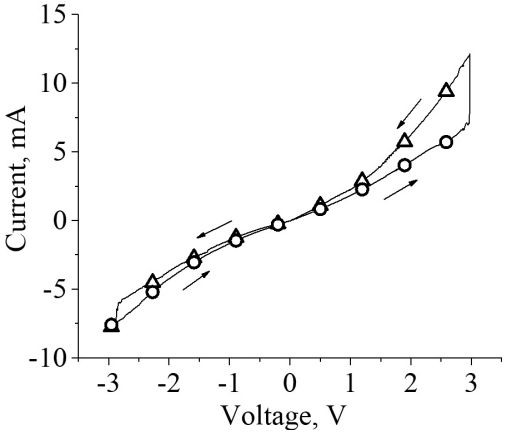

Fig. 3. Current-voltage characteristic of porous silicon in natural light.
Measurements in forward (Δ) and reverse (○) directions.

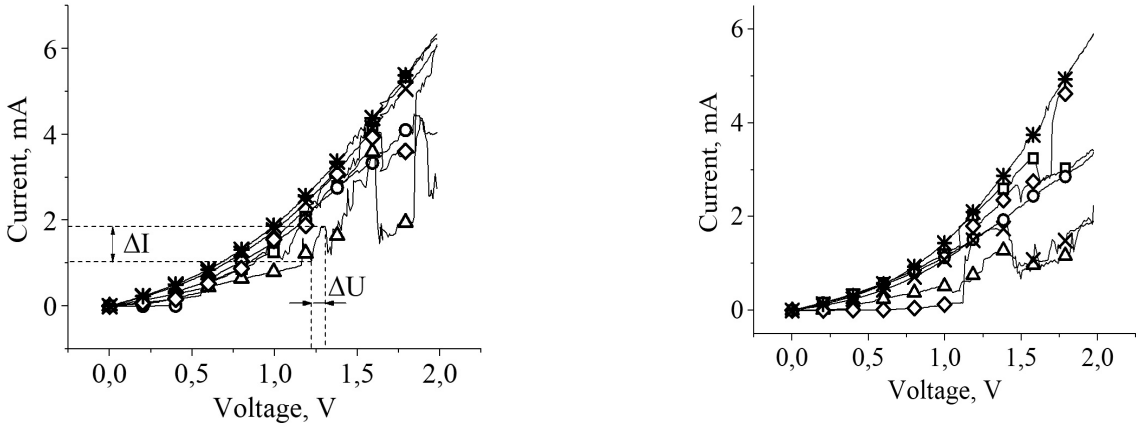

a) measurements at times t_0 b)after 24 hours

Fig. 4. Volt - ampere characteristics of porous Si at different time moments under laser illumination of the film.
t_0 : t_0=0, t=t_0+nτ, τ=2 min., n: □- 0,○- 2, Δ- 4, x- 6, ◊- 8, *- 10.

The standard deviations were determined by the formulas

$$x = U/U_{\max}, \sigma_x = \sqrt{\left(\langle x^2\rangle - \left(\langle x\rangle^2\right)\right)}, y = I/I_{\max}, \sigma_y = \sqrt{\left(\langle y^2\rangle - \left(\langle y\rangle^2\right)\right)}, \quad (2)$$

where $\langle U^2\rangle = \frac{1}{N}\sum_{i=1}^{N} U_i^2$, $N = 200$ and are presented in Figure 5.

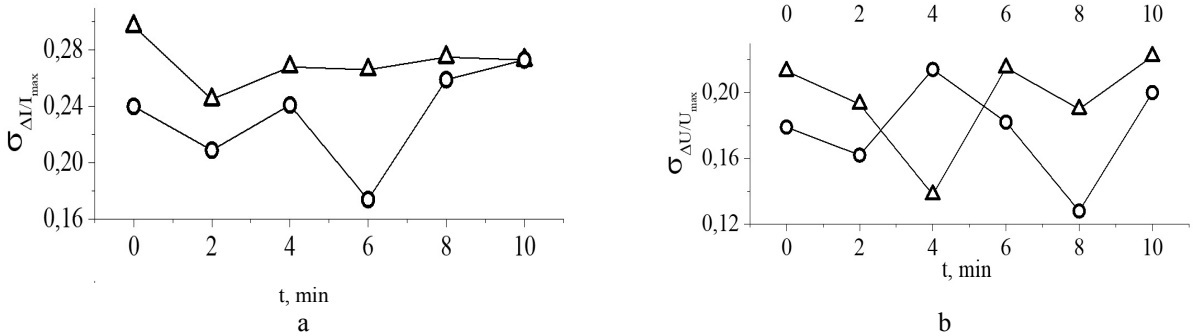

a b

Fig.5. Changes in the relative standard deviation of current (a) and voltage (b) over the time sequence of measurements.

Under laser radiation on nanoporous silicon films, current switching in the region $V \sim E_g$ and current hysteresis are also observed. Over time, the hysteresis loop narrows (Figure 6).

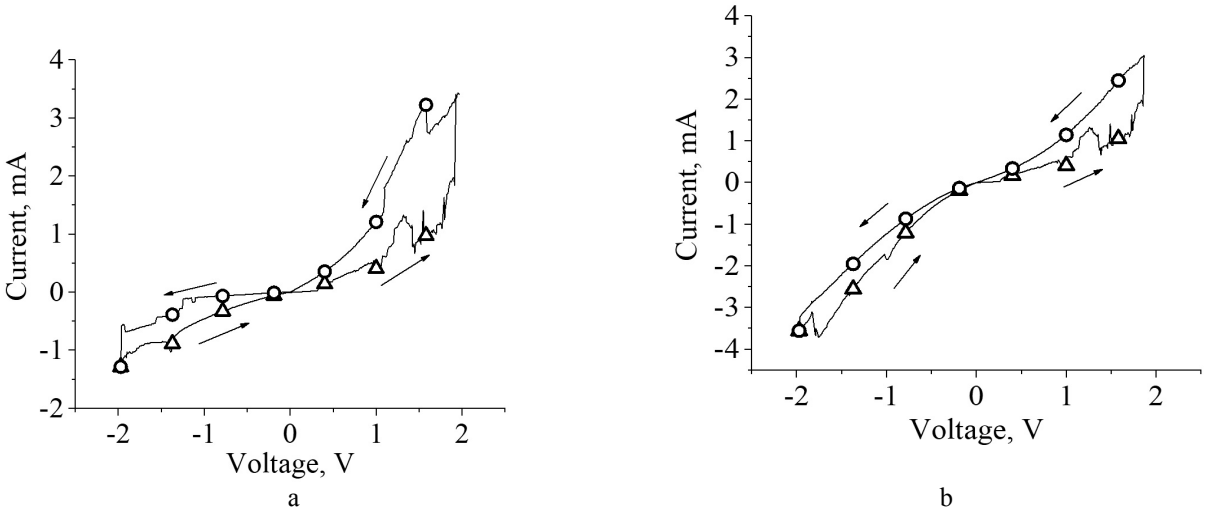

Fig.6. Current-voltage characteristic of porous silicon under laser illumination:
a) $-t_0$, b) $– t_0$+2 min. Δ – live measurements, ○ – 2 in the opposite direction.

GST - thin films of a chalcogenide glassy semiconductor of the Ge (germanium) -Sb (antimony) -Te (tellurium) system of composition $Ge_2Sb_2Te_2$, modified with a bismuth impurity. Chalcogenide glassy semiconductors (CGS) have some unique properties and phenomena, such as switching and memory effects, photo structural transformations, and a weak effect of impurities on electronic properties, which have no analogs in crystal materials. The switching effect is observed in thin CGS films and is associated with a reversible stepwise decrease in the CGS resistance in the absence of laser illumination (Figure 7).In Fig.7 $L(mm)$ – is the distances between the contacts correspond to the numbering of the curves: 1 - 5.

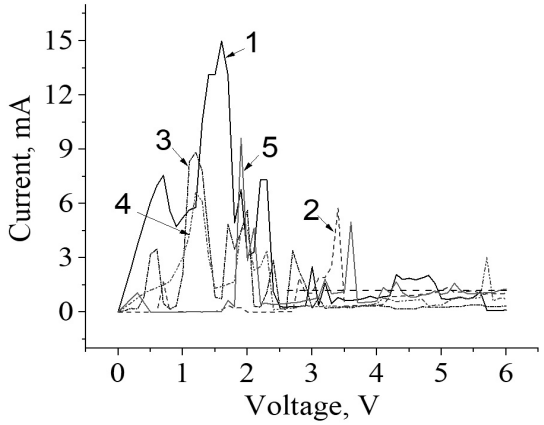

Fig.7. Current-voltage characteristics of GST in natural light.

However, GST films are opaque, non-porous; therefore, their direct use for photovoltaic and gas sensor applications is difficult.

Conclusion

Porous silicon structures with different diameters are formed by the method of electrochemical anodizing. The current-voltage characteristic of porous silicon has been measured in natural light and under laser radiation. At voltage values of the order of E_g and higher (for crystalline silicon $E_g = 1.12$ eV), switching is observed in the form of an abrupt increase in the current strength. It was found that with an increase in porosity, the width of the energetically forbidden zone of porous silicon increases within

$\eta \leq 0.8$ This effect is nonlinear since a decrease in E_g should be observed at $\eta \to 1$. Measurements of the electrical characteristics of a non-porous crystal indicate the dependence of E_g on the distance between contacts. This fact points to general physical laws between pyroelectrics and nanoporous semiconductors.

REFERENCES

1 Sun C. Q., Sun X. W., Tay B. K., Lau S. P., Huang H., Li S. Dielectric suppression and its effect on photoabsorption of nanometric semiconductors. *Journal of Physics D: Applied Physics*, 2001, Vol. 34, No. 15, pp. 2359.

2 Pan L. K., Huang H. T., Sun C.Q. Dielectric relaxation and transition of porous silicon.*Journal of applied physics*, 2003, Vol. 94, No. 4, pp. 2695-2700.

3 Pan L. K., Sun C. Q. Coordination imperfection enhanced electron-phonon interaction. *Journal of applied physics*, 2004, Vol. 95, No. 7, pp. 3819-3821.

4 Canham LT. Silicon quantum wire array fabrication by electrochemical and chemical dissolution of wafers.*Applied physics letters*, 1990, Vol. 57, No. 10, pp. 1046-1048.

5 Hybersen MS. Absorption and emission of light in nanoscale silicon structures.*Physical review letters*. 1994, Vol. 72, No. 10, pp. 1514.

6 Amri C., OuertaniR., HamdiA., et al. Effect of porous layer engineered with acid vapor etching on optical properties of solid silicon nanowire arrays. *Materials & Design*, 2016, Vol. 111, pp. 394-404.

7 Al-Douri Y., Badi N., Voon C. H. Etching time effect on optical properties of porous silicon for solar cells fabrication.*Optik*, 2017, Vol. 147, pp. 343-349.

8 Abd Rahim A. F., Hashim M. R., Ali N. K.High sensitivity of palladium on porous silicon MSM photodetector.*Physica B: Condensed Matter*, 2011, Vol. 406, No. 4, pp. 1034-1037.

9 Andersen O.K., Veje E. Experimental study of the energy-band structure of porous silicon.*Physical review B*, 1996, Vol. 53, No. 23, pp. 15643-15651.

10 Wolkin M.V., Jorne J., Fauchet P.M., Allan G., Delerue C. Electronic States and Luminescence in Porous Silicon Quantum Dots. *Phys. Rev. Letters*, 1999, Vol. 82, No. 1, pp. 197-200.

11Gaburro Z., Daldossoh N., &Pavesi L. Porous Silicon.*Reference Module in Materials Science and Materials Engineering*, 2016, doi:10.1016/b978-0-12-803581-8.01134-6.

12Praveenkumar S. et al.An experimental study of optoelectronic properties of porous silicon for solar cell application.*Optik*, 2019, Vol. 178, pp. 216-223.

13 Al-Douri Y., Ahmed N.M., Bouarissa N., Bouhemadou A. Investigated optical and elastic properties of Porous silicon: Theoretical study. *Materials & Design*, 2011, Vol. 32, No. 7, pp. 4088-4093.

14 Das M. M. et al. Estimation of oxide related electron trap energy of porous silicon nanostructures. *Materials Chemistry and Physics*, 2010, Vol. 119, No. 3, pp. 524-528.

15 Sheng C. K. et al. Characterization of thermal, optical and carrier transport properties of porous silicon using the photoacoustic technique. *Physica B: Condensed Matter*, 2008, Vol. 403, No. 17. pp. 2634-2638.

16 Zhang T. T. et al. Cr-doped $BaSnO_3$nanoporous thin films with tunable band gap via a facile colloidal solution route. *Chemical Physics*, 2019, Vol. 522. pp. 91-98.

17 Mergen Ö. B., Arda E. Determination of Optical Band Gap Energies of CS/MWCNT Bio-nanocomposites by Tauc and ASF Methods. *Synthetic Metals*, 2020, Vol. 269, pp. 116539.

Article accepted for publication 03.12.2020

DOI 10.31489/2020No2/45-54

UDC 678.6/7+544.23.057+544.25.057

HYDROPHOBIZATION OF PET TRACK-ETCHED MEMBRANES FOR DIRECT CONTACT MEMBRANE DISTILLATION OF LIQUID RADIOACTIVE WASTES

Yeszhanov A.B.[1,2], Dosmagambetova S.S.[2]

[1]Institute of Nuclear Physic of the Republic of Kazakhstan, Almaty, Kazakhstan, a.yeszhanov@inp.kz

[2]L.N.Gumilyov Eurasian National University, Astana, Kazakhstan

This article provides the results of liquid low-level radioactive wastes treatment by direct contact membrane distillation using polyethylene terephthalate hydrophobic track-etched membranes. The hydrophobization of track-etched membranes was carried out by UV-induced graft polymerization of triethoxyvinylsilane with styrene and coating with fluorine-containing silanes. Hydrophobic membranes were investigated by scanning electron microscope, Fourier-transform infrared spectroscopy, contact anglemeasurements, and liquid entry pressure analysis. Prepared membranes were tested in treatment of liquid low-level radioactive wastes by membrane distillation. The influence of pore sizes on water flux and rejection degree was studied. Rejection degree was evaluated by conductometry and atomic emission method. Decontamination factors evaluated by gamma-ray spectroscopy for ^{60}Co, ^{137}Cs, and ^{241}Am are 85.4, 1900 and 5.4 for membranes modified with polystyrene and triethoxyvinylsilanewith pore diameters of 142 nm; 85.0, 1462 and 4 for membranes modified with perfluorododecyltrichlorosilanewith pore diameters of 150 nm respectively.

Keywords: UV-induced graft polymerization, track-etched membranes, direct contact membrane distillation, hydrophobization, fluorine-containing silanes, radioactive waste treatment

Introduction

One of the main problems determining the existence and further development of nuclear energy is the solution of the problem of collecting and concentrating radioactive waste [1]. Environmental disasters at the Chernobyl nuclear power plant, Fukushima Daiichi and the problems of former nuclear test sites have led to the focus of attention all over the world on the treatment and concentration of low-level liquid radioactive waste (LLLRW). LLLRW canbe concentrated and solidified with cement, glass and bitumen [2]. Various methods for the separation of liquid radioactive solutions are known, such as plasma processesand sorption [3]. One of the most promising method are also membrane separation. Among membrane methods, ultrafiltration, reverse osmosis and electrodialysis [4] have found their application. Currently, a promising method of direct contact membrane distillation (MD) has been used for the separation and purification of low-level liquid radioactive waste. The advantages of MD are low energy consumption, low operating temperature, over-pressure is not required. Drawback of this process is the short lifetime of the membranes due to gradual surface fouling and poor performance. Despite this, MD is widely used for the desalination of seawater and groundwater, wastewater and natural water treatment from heavy metals [5–7].

The membranes used for the MD process are imposed following requirements: hydrophobicity, high porosity, water impermeability, chemical and mechanical stability, uniform pore size distribution. Hydrophobicity of the membrane surface prevents wetting and provides good separation characteristics. The wetting contact angle allows estimating the hydrophobicity and hydrophilicity of membrane surface. A water contact angle above 90° is required for the treatment of salty aqueous solutions with MD [8].

Various types of polymers for example, polytetrafluoroethylene (PTFE), polyamide (PA), polypropylene (PP) are used in MD due to their hydrophobic nature and thermal stability [9–11]. However, these types of membranes also have their drawbacks such as poor productivity, high cost, fouling of the hydrophobic surface, which led to reducing water purification. Thus, searching for new type membranes for MD is an important task. Recently, track-etched membranes (TeMs) are started to use in the process of MD [12–14]. Regular geometry of the pores with the ability to control their amount per unit area and excellent distribution of pore sizes together with low thickness and tortuosity make track-etched membranes (TeMs)

attractive for application in precise separation methods. The most frequently used track-etched membranes are based on poly(ethylene terephthalate) (PET). A unique feature of TeMs is the control of the number of pores per unit area, which significantly expands fields of applicationin sensing [15], catalysis, lithium-ion batteries, template synthesis of nanostructures [16–20]. As mentioned above, for membrane distillation it is important that the membrane has hydrophobic properties. However, PET TeMs has medium-hydrophobic properties, and for application in MD process, the membranes should have the water-repellent properties. The most common method of hydrophobization is to cover the surface by hydrophobic layer. Previously obtained hydrophobic PET TeMs by covalent bonding of silicon monomers such as dichlorodimethylsilane [21] and UV-induced graft polymerization of TEVS in presents of acrylic acid and N-vinylimidazole [22] were used for concentration of juices desalination by DCMD.

In this paper, UV-graft polymerization of styrene and triethoxyvinylsilane (TEVS) on the surface of PET TeMsand covalent binding of perfluorododecyltrichlorosilane (PFDTS) in an *o*-xylene solution.TeMs with a narrow pores size distribution and not tortuous channels will be tested in MD of LLLRW solutions. These properties of TeMs led to high salt and radioactive isotopes rejection degree.

1. Experimental part

Sodium hydroxide, N,N-dimethylformamide, benzophenone, sodium chloride, trichloromethane, TEVS, styrene, PFDTS were purchased from Sigma-Aldrich. Deionized water (18.2MΩ) obtained by water purification system Akvilon D-301 used in all experiments. Purification of monomers from inhibitors was carried out by passing through a column filled with alumina oxide.Samples of TeMsin size 10 x 15 were prepared by irradiation with $^{84}Kr^{15+}$ ions with an energy of 1.75 MeV/nucleon and ion fluence of $1 \cdot 10^8$ ion/cm^2, using the DC-60 accelerator in Astana branch of Nuclear Physics Institute. Then membranes were photosensitized for 30 min from each side and were chemically treated in 2.2 M NaOH at certain time to obtain membranes with different pores. Prepared membranes were dried and kept between paper sheets.

In order to increase hydrophobic properties of PET TeMs, two methods of surface modification were considered in comparison. First, modification of PET TeMs was carried out by UV-induced grafting of styrene and TEVS. PET samples were immersed in N,N-dimethylformamide 5% benzophenone solution. After that, samples were put into chloroform solutions of the 10-20% styrene and TEVS concentration with various ratios. The UV-irradiation was carried out for 60 min under UV lamp OSRAM Ultra Vitalux E27. After irradiation, samples were washed first in chloroform, and then in hot water to remove ungraftedhomopolymers, dried and weighed to calculate the grafting degree.

The second method was achieved by immersing membranes into *o*-xylene solution of PFDTS at different concentration range and time (1-24h). After that, membranes were washed *o*-xylene and dried.

The surface morphology of pristine and modified PET TeMs was examined using JSM-7500F scanning electron microscope (SEM) (JEOL, Japan).Agilent Cary 600 Series FTIR Spectrometer with ATR accessory was used to record FTIR spectra to study different chemical groups appeared after modification. Scan range: 400 to 4000 cm^{-1}, resolution 4.0 cm^{-1}. Spectral analysis was conducted by using Agilent Resolution Pro. Each sample was measured 32 scans at the room temperature. The gas flow rate was measured at a pressure drop of 20kPa. The contact angle (CA) of the pristine and modified PET TeMs was measured goniometrically using the static drop method using Digital Microscope with 1000x magnification. Measurements were taken from different points of the polymer and the average result was calculated.

Liquid Entry Pressure (LEP) was determined by using deionized water flow measurements according to recommendations described in [23,24]. A round sample with the radius of 1.25 cm was compressed inside the hermetically-sealed chamber, and a test was run with air at gradually increasing pressure. The LEP was recorded as the pressure corresponding to the point of initial passage of flow through the membrane using capillary with the diameter of 0.7 mm. According to the recommendation, the LEP should be >2.5 bar for a successful application in MD [23].

The mechanism of the process and DCMD rig was described earlier in the papers. The permeate flux was measured by weighing. LLLRW samples obtained from WWR-K research nuclear reactor (Almaty, Kazakhstan) were tested. The degree of salt rejection was calculated by the change in conductivity that was measured using Hanna Instruments HI2030-01. OPTIMA-8000 ICP-Optical Emission Spectroscopy (the spectral range is 165-900 nm with resolution of < 0.009 nm at 200 nm) was used to estimate elemental content of solutions before and after MD. Gamma-ray spectroscopy Canberra GM1520 with semiconductor Ge detector and the energy range (25 - 3000) keV was used to estimate activity of radioisotopes.

2. Results and Discussion

First, hydrophobization of PET TeMswas carried out by UV-induced graft polymerization two monomers – styrene and TEVS. Chloroform was used as a solvent for UV photo-induced graft polymerization due to its high ability to dissolve monomers and transparency in the UV region. Effect of hydrophobization of different parameters such as concentration of monomers in solvent (10-30%), percentage ratio of monomers (50:50; 10:90; 90:10; 30:70; 70:30) and grafting time was studied (Figure 1).

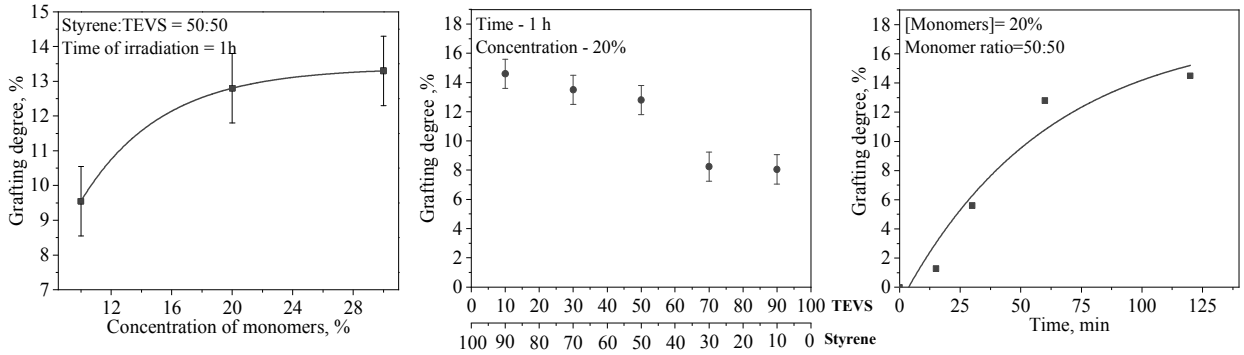

a b c

Fig.1. The degree of grafting of styrene and TEVS to the surface of PET TeMs with various concentration (a) and monomer ratios (b) and time (c)

Due to the high ability of styrene for polymerization in comparison to TEVS, it can be noted that with an increase in the concentration of styrene leads to an increase in the degree of grafting, while an increase in the concentration of TEVS leads to a decrease in the concentration.The effect of the degree of grafting on different ratios of monomers is shown in Figure 1b.A significant increase in the concentration of the monomer mixture from 10% to 20% leads to a significant increase in the grafting degree, however, a further concentration increase only slightly with increases in the grafting degree.Thus, as can be seen from Figure 1a, an increase in the concentration of monomers above 20% is not effective.

Figure 1c shows exponential relationship of grafting degree with time at constant concentration of monomer 20% and monomer ratio 50:50. Grafting degree reaches 12.8% after 60 min and 14.5% after 120 min of grafting. An increase in the time of grafting from 60 to 120 minutes lead to an insignificant increase in the degree of grafting, thus, the optimal time is 1 hour.

The second method of hydrophobization is based on the soaking of PET TeMs in a solution of *o*-xylene with PFDTS. The principle of the interaction of PFDTS with *o*-xylene is the high hydrolysis ability of the Si-Cl bond, which is able to easily interact with the surface of PET TeMs. Figure 2a shows the dependence of the concentration of PFDTS on the value of the CA. As can be seen, at an optimal monomer concentration of 20 mM the CA reaches a maximum value.

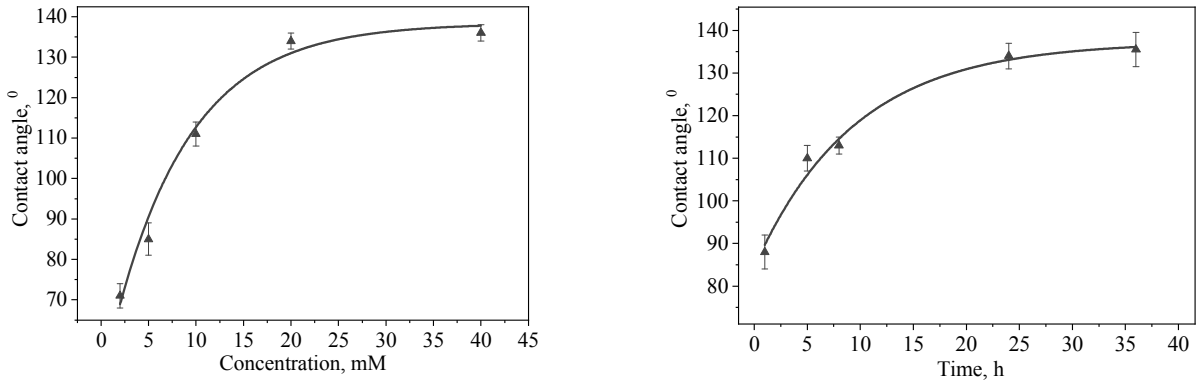

a b

Fig.2. Contact angle of modified PET TeMs at various concentration of PFDTS (a) and reaction time (b) (pore diameter of initial PET TeMs is 200 nm)

A further increase in concentration does not lead to a significant change in the CA. The dependence of the holding time in the reaction on the CA was considered. The results are shown in Figure 2b. The largest CA (134°) was reached after 24 hours. A further increase in time did not significantly affect the value of the CA. Characteristics of hydrophobized PET TeMs by PFDTS are presented in Table 1.

Table 1 - Characteristics of hydrophobized PET TeMs by PFDTS

Sample	Contact angle, °	Effective pore size, nm	Pore size (from SEM analysis), nm	LEP, MPa
Initial PET TeMs	56	198±5	220±8	0.12
PET TeMs – PFDTS	134	148±6	174±4	>0.43

To evaluate the hydrophobic properties of prepared samples, the method of contact angle measurements was used. The measurements of CA were carried out from different places of the sample and the average value was calculated. Images of droplets are shown in Figure 3.

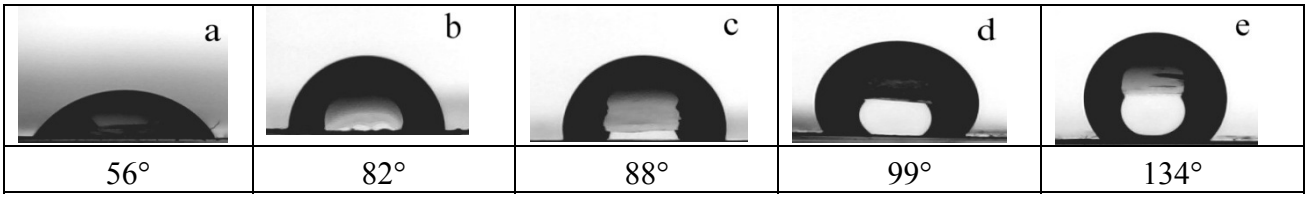

Fig.3. CA for initial PET TeMs (a), PET TeMs-g-Styrene-TEVS (70:30) (b), PET TeMs-g-Styrene-TEVS (90:10) (c), PET TeMs-g-Styrene-TEVS (50:50) (d), PET TeMs – PFDTS (e)

It can be seen, the contact wetting angle of the initial PET TeMs increases significantly from 56 to 99° for PET TeMs-g-Styrene-TEVS with monomer ratio (70:30), (90:10), (50:50) and to 134° for PET TeMs – PFDTS respectively.As it can be seen from Table 2, contact angle is dependent on the degree of grafting and on the concentration of monomer and their ratio. Along with that, the pore diameter of the membrane also significantly affects contact angle and LEP. With an increase in the pore diameter from 142 to 287 nm, the value of the capillary effect exceeds the surface tension force of a water droplet. It is also confirmed a decrease in LEP with an increase in pore diameter. However, according to the recommendation, the LEP should be >2.5 bar for a successful application in MD. The use of a membrane with a pore diameter of 287 nm may lead to liquid slipping. Thus, according to the above given results, the optimal conditions for the modification of PET TeMs with pore sizes 150-250 nm by UV-induced graft polymerization of styrene and TEVS leading to maximum hydrophobization of membranes (99°) with preservation of the pore structure are: grafting time 60 min, total monomer concentration 20% and monomer ratio of 50:50.

Table 2 - Contact angle and pore sizes of PET TeMs-g-PS-TEVS in various concentration and ratios (time is constant – 1h)

Sample and monomer ratio	Concentration of monomer, %	Contact angle, °	Pore size (SEM analysis), nm	Effective pore size, nm	Liquid Entry Pressure (LEP), MPa	Grafting degree, %
PET TeMs	-	56	220±20	208±6	-	-
PS-TEVS (50:50)	20	99	206±21	200±6	0.34	13
PS-TEVS (90:10)	20	82	211±21	203±7	0.13	8
PS-TEVS (70:30)	20	85	200±21	193±7	0.14	14
PS-TEVS (50:50)*	20	87	287±25	283±6	0.13	14
PS-TEVS(50:50)**	20	92	242±27	235±6	0.25	13
PS-TEVS (50:50)***	20	99	142±12	131±6	0.39	12

** - PET TeMs with pore size of 300 nm; **- PET TeMs with pore size of 250 nm, *** - PET TeMs with pore size of 150nm*

According to Table 2, the liquid entry pressure (LEP) decreases significantly with increasing in pore diameters. When membranes with a large pore diameter (~ 300 nm) are used, concentrate breakthrough occurs, i.e., the filtration process is observed instead ofmembrane distillation. As a result, the value of conductivity and productivity increases significantly. Thus, the developed method of hydrophobization can be applied to PET TeMs with pore sizes up to 200 nm, at which optimal values on the degree of salt rejection and productivity are observed.

The characterization of pore sizes before and after modification, as well as the morphology of PET TeMs surfaces was carried out by SEM analysis.Microphotographs of the pristine PET TeMs surface and modified at different ratios are shown in Figure 4.From Figure 4 it is noticeable that there is a slight narrowing of the pore diameter of PET TeMs, while the pore structure remains unchanged.

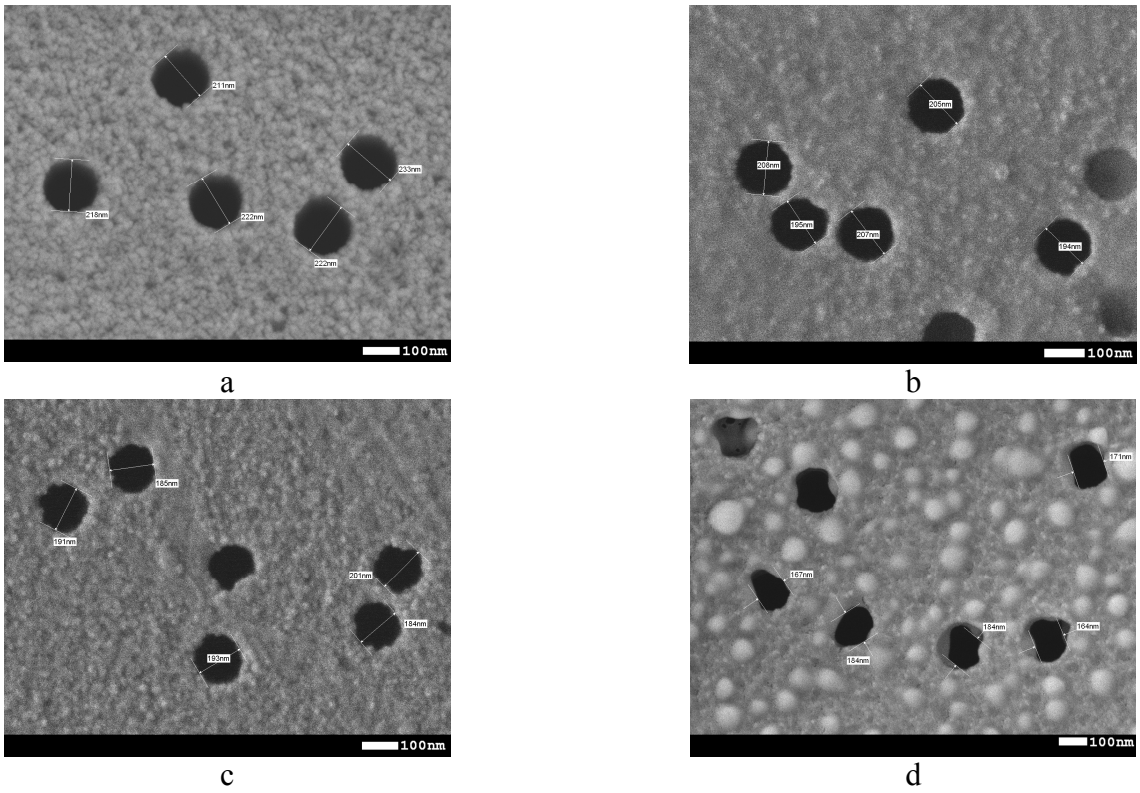

Fig.4. SEM images of PET TeMs surfaces before (a) and after grafting at different ratios of monomers styreneand TEVS 50:50 (b), 70:30 (c), and PET TeMs – PFDTS (d)

Table 3 - Average pore diameter of pristine and modified PET TeMs

Sample and monomer ratio	Average pore diameter, nm
Pristine PET TeMs	221±8
PS-TEVS (50:50)	202±7
PS-TEVS (70:30)	191±7
PET TeMs – PFDTS	174±8

To confirm graft polymerization and detect the presence of chemical group vibrations come from TEVS and PS in modified PET TeMs, FTIR-ATR analysis was performed. FTIR-ATR spectra of initial and grafted PET TeMs are shown in Figure 5. Typical FTIR-ATR spectrum of initial PET TeMs consist of main absorption peaks at 2972 cm^{-1} (aromatic C-H), 2910 cm^{-1} (aliphatic C-H), 1715 cm^{-1} (C=O), 1471 cm^{-1} (CH_2 bending), 1410 cm^{-1} (ring CH in plane bending), 1341 cm^{-1} (CH_2 wagging), 1238 cm^{-1} (C(=O)-O stretching), 1018 cm^{-1} (ring CCC bending), 970 cm^{-1} (O-CH_2 stretching), 847 cm^{-1} (ring CC stretching). The presence of grafted TEVS is established by Si-O-Si and Si-CH_3 vibrations at 1180-1110, 761 cm^{-1}, respectively.

Moreover, peak at 3300-3600 cm^{-1} was detected with low intensity that is corresponding to OH. OH-groups can come from hydrolysis of Si-OC_2H_5 groups.Covalent bonding of PFDTS led to appearance of new peaks at 1060, 1127 cm^{-1}, as well as peaks of low intensity at 577, 602 and 628 cm^{-1} related to the C-F bond.

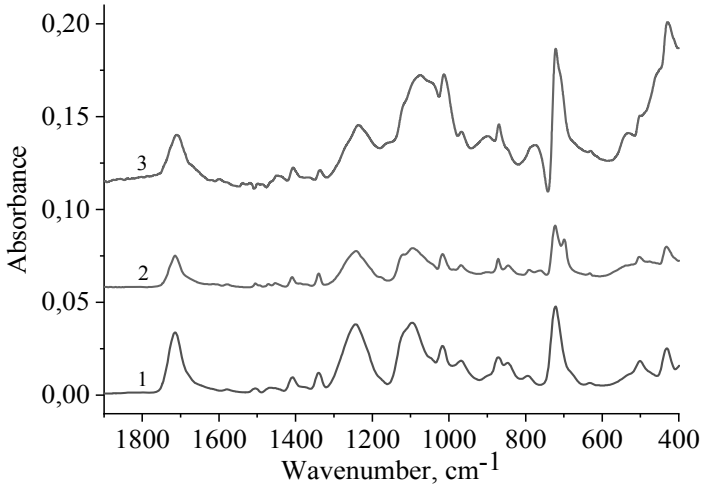

Fig.5. FTIR-ATR spectra of 1–PET TeMs, 2 – PET TeMs-g-PS-TEVS (50:50), 3– PET TeMs – PFDTS

Thus, optimal parameters to obtain membranes with the highest CA and maintaining pore structure for PET TeMs-g-PS-TEVS are 20% monomer concentration at monomer ratio 50:50 during 1h and for PET TeMs – PFDTS are 20mM monomer concentration in *o*-xylene solution during 24h.

Membrane distillation of liquid low-level radioactive wastes

Membrane distillation of LLLRW with hydrophobic PET TeMs-g-PS-TEVS with different pore sizes (142, 206, 242 and 287 nm) and hydrophobic PET TeMs – PFDTS with pore sizes (150, 200 and 250 nm)obtained at optimal parameters was performed in direct contact mode with temperature control. LLLRW was purchased from Research Nuclear Reactor WWR-K (Almaty, Kazakhstan). LLLRW consist of different ions such as Na, Mg, K, Fe, Ca, Al, Sb, Sr, Mo, Cs measured by atomic emission method (Table 3) and consist of radioisotopes ^{60}Co, ^{137}Cs and ^{241}Am with different activity measured using Gamma Ray Spectrometer. In DCMD experiment, hydrophobic PET TeMs were used to evaluate water fluxes and decontamination factor (D) efficiency of LLLRW depends on pore diameter. Decontamination factor (D) was calculated according by the equation:

$$D = \frac{a_f}{a_p}, \quad (1)$$

where a_f and a_p are specific activities of the feed and the permeate respectively.

Removal efficiency of wastes was primarily evaluated by electrical conductivity, which can be also used for overall efficiency of DCMD for metal ions rejections since the main component of the waste sample is Na and K which are highly sensitive to changes in conductivity with changing concentration. Results are presented in Figure 6a. PET TeMS-g-PS-TEVS with pore diameters of 142, 206 and 242 nm showed minor changes in conductivity during MD, whereas using membranes with a pore diameter of 287 nm leads to a significant increase in conductivity from 214 to 2238 μS/cm. Degrees of salt rejection for the hydrophobized PET TeMs-g-PS-TEVS with pore diameter of 142, 206 and 242 nm are 99.2 %, 96.8% and 86.9% respectively.

Figure 6b shows us increasing average water fluxes from 810 g/m^2h for the PET TeMs-g-PS-TEVS with 142 nm pore diameter to 1584 g/m^2h for the membrane with 242 nm pore diameter. It should be noted that according to analysis of conductivity (degree of salt rejection is around 5%), high flux of membranes with pore sizes of 287 nm is due to wetting the channels and filtration through occurs.

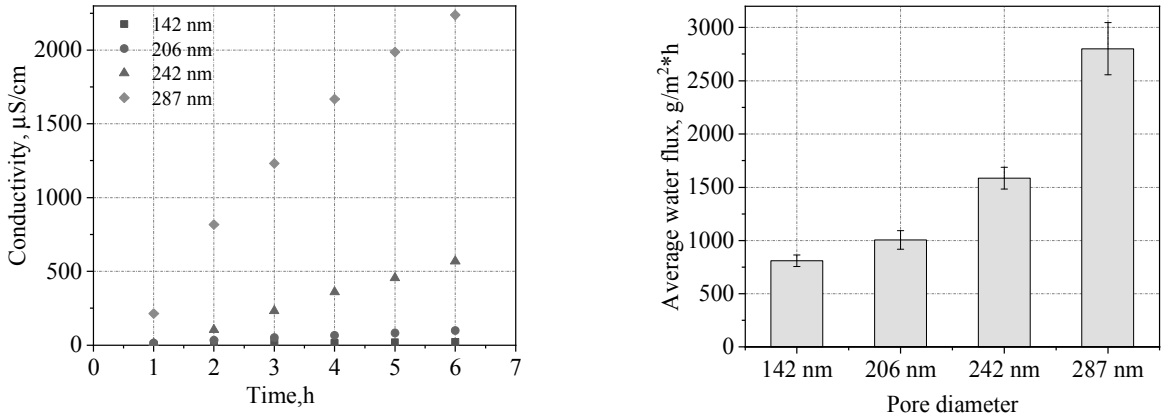

Fig.6. Electrical conductivity (a) and MD water flux (b) during continuous DCMD tests using hydrophobized PET TeMs-g-PS-TEVS with different pores for radioactive waste solution

Electrical conductivity and water flux results of PET TeMs – PFDTS after DCMD are showed in Figure 7a, b. For hydrophobic PET TeMs – PFDTSwith pore sizes of 150, 200 nm is a slight increase in conductivity, however, with pore sizes of 250 nm, the conductivity sharply increases from 6 to 184 µS/cm. Degrees of salt rejection for the PET TeMs – PFDTS with pore diameter of 150, 200 and 250 nm are 98.7%, 97.3% and 79.2% respectively. Figure 6b shows us increasing average water fluxes from 520g/m^{2}h for the PET TeMs – PFDTS with pore diameter 150 nm to 1240g/m^{2}h for the membrane with 250 nm pore diameter.

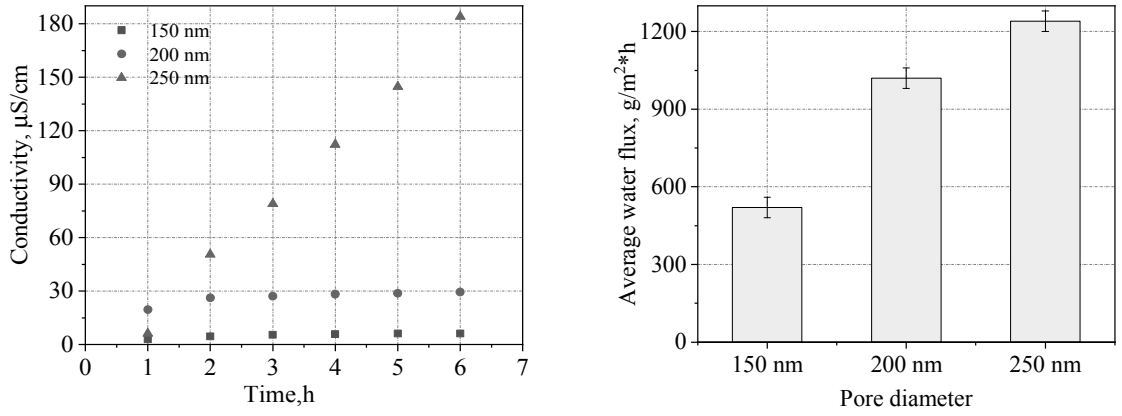

Fig.7. Electrical conductivity (a) and MD water flux (b) during continuous DCMD tests using hydrophobized PET TeMs– PFDTS with different pores for radioactive waste solution

Chemical composition of the waste sample and degree of rejection after DCMD process using hydrophobic PET TeMs are presented in Table 3,4. According to Table 3,4all degree of rejection were more than 94%, most of them are close to 100%. For comparison, hydrophobic PET TeMS – PFDTS with different pore diameter was used. Variations in ion concentration are caused by different salt concentration in feed solution. Decrease in the degree of salt rejection with an increase in the pore radius is associated with a decrease in the LEP (as it seen in Table 1,2). The higher the LEP, the lower the probability of liquid passing through the pores of the membranes.

Results on decontamination factors of radioisotopes are presented in Table 5,6. PET TeMs-g-PS-TEVS with pore diameters of 142 and 242 nm showed decontamination factor for ^{60}Co of >85.4, for ^{137}Cs of >1900 and 42, for ^{241}Am of 5 and >7 respectively. PET TeMs – PFDTS with pore size of 150 and 250 nm showed decontamination factor ^{60}Co >85.4 and 34.2, for ^{137}Cs of 1462 and 815.5, for ^{241}Am of 4 and > 2.6 respectively. It should be noted that in most cases data received was below detection limit. The decrease in

the decontamination factor with an increase in the pore diameter is associated with a decrease in the LEP and the contact angle.

Table 4 - Chemical composition of the waste sample and the effluent after DCMD process using hydrophobic PET TeMs-g-PS-TEVS with different pore diameter

Element	Concentration in the feed, μg/l	Concentration in the permeate (PET TeMs-g-PS-TEVS, d=242 nm), μg/l, (degree of rejection, %)	Concentration in the permeate (PET TeMs-g-PS-TEVS, d=206 nm), μg/l, (degree of rejection, %)	Concentration in the permeate (PET TeMs-g-PS-TEVS, d=142 nm), μg/l, (degree of rejection, %)
Cs (σ=±26%)	304	7.13 (97.7%)	1.18 (99.6%)	0.34 (99.9%)
Mo (σ=±15%)	458	4.14 (99.1%)	<0.3 (99.9%)	<0.3 (99.9%)
Sr (σ=±15%)	136	<0,5 (99.6%)	<0.5 (99.6%)	<0.5 (99.6%)
Sb (σ=±15%)	46.3	0.68 (98.5%)	<0.3 (99.4%)	<0.3 (99.4%)
Al (σ=±16%)	660	<12 (98.1%)	<3 (99.5%)	<3 (99.5%)
Ca (σ=±16%)	1780	96.1 (94.6%)	84.2 (95.2%)	18.6 (99.0%)
Fe (σ=±10%)	383	<2.4(99.4%)	<0.6 (99.8%)	<0.6 (99.8%)
K (σ=±15%)	249 200	1523 (99.4%)	236 (99.9%)	54.6 (99.9%)
Mg (σ=±15%)	1046	<4 (99.6%)	2.36 (99.8%)	<1 (99.9%)
Na (σ=±15%)	4 710 000	103 (99.9%)	17.6 (99.9%)	1.87 (99.9%)

Table 5 - Chemical composition of the waste solution and the effluent after DCMD process using hydrophobic PET TeMs – PFDTS with different pore diameter

Element	Concentration in the feed, μg/l	Concentration in the permeate (PET TeMs-PFDTS, d=250 nm), μg/l	Concentration in the permeate (PET TeMs-PFDTS, d=200 nm), μg/l	Concentration in the permeate (PET TeMs-PFDTS, d=150 nm), μg/l
Cs (σ=±26%)	304	6.82 (98.2%)	3.26 (98.9%)	0.85 (99.8%)
Mo (σ=±15%)	458	3.90 (99.1%)	1.82 (99.6%)	<0.3 (99.9%)
Sr (σ=±15%)	136	1.08 (99.2%)	<0.5 (99.6%)	<0.5 (99.6%)
Sb (σ=±15%)	46.3	0.73 (98.4%)	<0.3 (99.3%)	<0.3 (99.3%)
Al (σ=±16%)	660	<12 (98.1%)	<6 (99.1%)	<3 (99.5%)
Ca (σ=±16%)	1780	89.1 (95.0%)	55.6 (96.8%)	33.3 (98.1%)
Fe (σ=±10%)	383	<2.4 (99.3%)	<1.2 (99.7%)	<0.6(99.8%)
K (σ=±15%)	249 200	1 568(99.3%)	838 (99.7%)	215 (99.9%)
Mg (σ=±15%)	1046	<4 (99.6%)	<2 (99.8%)	<2 (99.8%)
Na (σ=±15%)	4 710 000	56 100 (98.8%)	31 800 (99.3%)	7 770 (99.8%)

Table 6 - Radioisotope composition of feed waste solution and permeate solution after DCMD process using hydrophobic PET TeMs-g-PS-TEVS with different pore diameter

Radioisotope	Activity of the feed (Bq/kg)	Activity of the permeate (PET TeMs-g-PS-TEVS, d=142 nm), (Bq/kg)	Decontamination factor (D)	Activity of the permeate (PET TeMs-g-PS-TEVS, d=242 nm) (Bq/kg)	Decontamination factor (D)
^{60}Co	85.4±6.1	<1.0	>85	<1.0	>85
^{137}Cs	1900±27	<1.0	>1900	45.8±1.8	42
^{241}Am	<2.2	<0.41	5	<0.32	>7

Table7 - Radioisotope composition of feed waste solution and permeate solution after DCMD process using hydrophobic PET TeMs – PFDTS with different pore diameter

Radioisotope	Activity of the feed (Bq/kg)	Activity of the permeate (PET TeMs– PFDTS, d=150 nm) (Bq/kg)	Decontamination factor (D)	Activity in the permeate (PET TeMs– PFDTS, d=250 nm) (Bq/kg)	Decontamination factor D
^{60}Co	85.4±6.1	<1.0	>85	2.5±1.1	34.2
^{137}Cs	1900±27	<1.3	>1462	2.33	815.5
^{241}Am	<2.2	<0.55	>4	<0.86	>2.6

The results obtained in terms of the factor of decontamination of radionuclides, the degree of purification from salt and productivity exceed previously published works in some parameters. The authors [25]used commercial polypropylene membranes, which showed a lower water flux about 700 g/m^2·h. However, the salt rejection of radioactive waste of such elements as ^{60}Co, ^{90}Sr, ^{137}Cswas achieved more than 98%. The value of the decontamination factor of radionuclides varied within 10^5-10^6.FeiJia and others [26,27] have conducted research on the purification of ^{60}Co and ^{137}Sr by vacuum membrane distillation with hollow fiber polypropylene membrane. The salt rejection was over 99%, and the permeate water flux reached about 6200 g/m^2·h.However, in these works there are some disadvantages associated with the need for a reduced pressure of approximately (0.1-1 atm), as well as the high cost of hollow fiber membranes.

Based on the obtained results, methods of hydrophobization of PET TeMs showed good performance. The most preferred type of modification for membrane distillation is PET TeMs-g-PS-TEVS, due to high performance and efficiency in treatment of LLLRW. Using of TeMs with a narrow pores size distribution allows us to achieve better purification from radioactive wastes.

Conclusion

In this research,two simple and effective methods of hydrophobization of PET track-etched membranes by UV-graft polymerization of styrene with TEVS (at optimal conditions of 20% monomer concentration at monomer ratio 50:50 during 60 min) and covalent binding of PFDTS were considered and applied in treatment of liquid low-level radioactive wastes. Prepared membranes were characterized by FTIR, SEM, LEP and goniometric analysis to evaluate hydrophobic properties of the membranes. DCMD was controlled by gravimetric and conductometricanalysis. The effect of membrane pore diameter on water flux and rejection degree was studied. Elemental content of the solutions were evaluatedby gamma-ray spectroscopy and atomic emission method. Modified in two different ways PET TeMs showed an excellent degree of salt rejection of main elements of LLLRW such as Cs, Mo, Sr, Sb, Al, Ca, Fe, K, Mg and Na, decontamination factor for ^{60}Co, ^{137}Cs, and ^{241}Am – >85, >1900 and 5 respectively when using modified membrane with average pore diameters of 142 nm (average water flux for this membrane is 810 g/m^{2}h).

Maximum average permeate flux of 2800 g/m^2·hwere achieved using PET TeMs-g-PS-TEVS, however degree of salt rejection and decontamination factor are not sufficient due to the fact that modified membranes with large pore diameters have lower LEP and contact angle. The optimum ratio between water flux and efficiency of salt rejection is achieved using 142 nm pore radius of the membranes. For the first time track-etched membranes were studied in membrane distillation of liquid low-level radioactive wastes. The use of track-etched membranes with a narrow pores size distribution and not tortuous channels allows us to achieve better purification from radioactive wastes in comparison with hollow-fiber membranes.

Acknowledgments

The work was done within the project of the Ministry of Education and Science of the Republic of Kazakhstan titled "Preparation of track-etched membranes with specified properties for membrane distillation and forward osmosis" (grant No AP05132110).

REFERENCES

1 Zakrzewska-Trznadel G. Advances in membrane technologies for the treatment of liquid radioactive waste. *Desalination*.2013, Vol. 321, pp. 119–130.

2 Mijnendonckx K., Van Gompel A., Coninx I., Bleyen N., Leys N. Water-soluble bitumen degradation products

can fuel nitrate reduction from non-radioactive bituminized waste. *Appl. Geochemistry*. 2020, Vol. 114, pp. 104525.

3 Osmanlioglu A.E. Treatment of radioactive liquid waste by sorption on natural zeolite in Turkey. *J. Hazard. Mater.*2006, Vol. 137, pp. 332–335.

4 InoueH., KagoshimaM., Yamasaki M., Honda Y. Radioactive iodine waste treatment using electrodialysis with an anion exchange paper membrane. *Appl. Radiat. Isot.*2004, Vol. 61, pp. 1189–1193.

5 AttiaH., Alexander S., Wright C.J., Hilal N. Superhydrophobic electrospun membrane for heavy metals removal by air gap membrane distillation (AGMD). *Desalination*.2017,Vol. 420, pp. 318–329.

6 Quist-Jensen C.A., Macedonio F., Horbez D., Drioli E. Reclamation of sodium sulfate from industrial wastewater by using membrane distillation and membrane crystallization.*Desalination*.2017, Vol. 401, pp. 112–119.

7 Naidu G., Jeong S., Johir M.A.H., et al. Rubidium extraction from seawater brine by an integrated membrane distillation-selective sorption system. *Water Res.*2017, Vol. 123, pp. 321–331.

8 AnA.K., Guo J., Lee E.-J., JeongS., ZhaoY., Wang Z., Leiknes T. PDMS/PVDF hybrid electrospun membrane with superhydrophobic property and drop impact dynamics for dyeing wastewater treatment using membrane distillation. *J. Memb. Sci.*2017, Vol. 525, pp. 57–67.

9 An A.K., Guo J., Jeong S., Lee E.-J., et al. High flux and antifouling properties of negatively charged membrane for dyeing wastewater treatment by membrane distillation. *Water Res*.2016, Vol. 103, pp. 362–371.

10 Shirazi M.M.A., Kargari A.,Tabatabaei M. Evaluation of commercial PTFE membranes in desalination by direct contact membrane distillation.*Chem. Eng. Process. Process Intensif.*2014, Vol. 76, pp. 16–25.

11 KhayetM. Membranes and theoretical modeling of membrane distillation: A review. Adv. *Colloid Interface Sci.*2011, Vol. 164, pp. 56–88.

12 Gancarz I., Bryjak M., Kujawski J., Wolska J., Kujawa J., KujawskiW. Plasma deposited fluorinated films on porous membranes. *Mater. Chem. Phys.*2015, Vol. 151, pp. 233–242.

13 ZdorovetsM.V., YeszhanovA.B., KorolkovI.V., GüvenO., DosmagambetovaS.S., ShlimasD.I., ZhatkanbayevaZ.K., ZhidkovI.S., KharkinP.V., GluchshenkoV.N., etal. Liquid low-level radioactive wastes treatment by using hydrophobized track-etched membranes. *Prog. Nucl. Energy.* 2020, Vol. 118, pp. 1–9.

14 KorolkovI.V., YeszhanovA.B., ZdorovetsM.V., GorinY.G., GüvenO., DosmagambetovaS.S., KhlebnikovN.A., SerkovK.V., KrasnopyorovaM.V., MiltsO.S., etal. Modification of PET ion track membranes for membrane distillation of low-level liquid radioactive wastes and salt solutions. *Sep. Purif. Technol.*2019,Vol.227, pp. 1–9.

15 ZdorovetsM.V., Korolkov I.V., Yeszhanov A.B., Gorin Y.G. Functionalization of PET track-etched membranes by UV-induced graft (co)polymerization for detection of heavy metal ions in water. *Polymers* (Basel).2019, Vol. 11, pp. 1–16.

16 BorgekovD., Mashentseva A., Kislitsin S., Kozlovskiy A., Russakova A., ZdorovetsM. Temperature Dependent Catalytic Activity of Ag/PET Ion-Track Membranes Composites. *Acta Physica Polonica.* 2015, Vol. 128, pp. 871–875.

17 Mashentseva A.A., ZdorovetsM.V., Borgekov D.B. Impact of testing temperature on the structure and catalytic properties of au nanotubes composites. *Bull. Chem. React. Eng. & Catal.*2018, Vol. 13, pp. 405–411.

18 MashentsevaA.A., Zdorovets M.V. Catalytic Activity of Composite Track-Etched Membranes Based on Copper Nanotubes in Flow and Static Modes. *Pet. Chem.*2019, Vol. 59, pp. 552–557.

19 Mashentseva A.A., Kozlovskiy A.L., Zdorovets M.V. Influence of deposition temperature on the structure and catalytic properties of the copper nanotubes composite membranes. *Mater. Res. Express.* 2018, Vol. 5, pp. 1–14.

20 Shumskaya A., Bundyukova V., Kozlovskiy A., Zdorovets M., KadyrzhanovK., KalkabayG., Kaniukov E. Evolution of morphology, structure, and magnetic parameters of Ni nanotubes with growth in pores of a PET template. *J. Magn. Magn. Mater.*2020, Vol. 497, pp. 1–5.

21 Korolkov I.V., Yeszhanov A.B., Gorin Y.G., Zdorovets M.V., Khlebnikov N.A., SerkovK.V. Hydrophobization of PET track-etched membranes for direct contact membrane distillation. *Mater. Res. Express.* 2018, Vol. 5, pp. 1–13.

22 Korolkov I.V., Gorin, Y.G., Yeszhanov A.B., Kozlovskiy A.L., Zdorovets M.V. Preparation of PET track-etched membranes for membrane distillation by photo-induced graft polymerization. *Mater. Chem. Phys.*2018, Vol. 205, pp. 55–63.

23 Eykens L., De Sitter K., Dotremont C., Pinoy L., Van der Bruggen B. Membrane synthesis for membrane distillation. *A review. Sep. Purif. Technol.*2017, Vol. 182, pp. 36–51.

24 Chamani H., Yazgan-Birgi P., Matsuura T., et al. CFD-based genetic programming model for liquid entry pressure estimation of hydrophobic membranes. *Desalination.* 2020, Vol. 476, pp. 1–10.

25 Wen X., Li F., Zhao X. Removal of nuclides and boron from highly saline radioactive wastewater by direct contact membrane distillation. *Desalination.*2016, Vol. 394, pp. 101–107.

26 Jia F., Yin Y., Wang J. Removal of cobalt ions from simulated radioactive wastewater by vacuum membrane distillation. *Prog. Nucl. Energy*. 2018, Vol. 103, pp. 20–27.

27 Jia F., Li J., Wang J., SunY. Removal of strontium ions from simulated radioactive wastewater by vacuum membrane distillation. *Ann. Nucl. Energy.* 2017, Vol. 103, pp. 363–368.

Article accepted for publication 03.12.2020

DOI 10.31489/2020No2/55-60

UDC 535.215; 539.23; 535.3; 535.3; 538.9

INVESTIGATION OF OPTICAL AND ELECTROPHYSICAL CHARACTERISTICS OF COMPOSITE FILMS NIO/PEDOT:PSS

Aimukhanov A.K.[1], Zeinidenov A.K.[1], Omarbekova G.I.[1], Plotnikova I.V.[2]

[1]E. A. Buketov Karaganda University, Karaganda, 100028, Kazakhstan, gulnur_130983@mail.ru
[2] National Research Tomsk Polytechnic University, Tomsk, Russia

This work presents the results of a study of the morphological, optical, and electrophysical parameters of Nickel Oxide/poly(3,4-ethylenedioxythiophene) polystyrene sulfonate (NiO/PEDOT:PSS) composite films. It is shown that an increase in the speed of rotation of the substrate leads to a decrease in the surface roughness of NiO films. As the surface roughness of the Nickel oxide decreases, the roughness of the PEDOT:PSS film also decreases. Increasing the speed of rotation of the substrate leads to a decrease in the optical density of the absorption spectra of NiO films, as well of composite films NiO/PEDOT:PSS. It was found that changes in the morphology of NiO/PEDOT:PSS composite films contribute to the rapid transport of injected holes to the external electrode and reduce the probability of reverse recombination.

Keywords: nickel oxide (NiO), PEDOT:PSS, composite film, surface morphology, optical and impedance spectroscopy.

Introduction

Among inorganic hole transport layers (HTL), nickel oxide (NiO) is of considerable interest and has been extensively studied as a selective electrode for PSCs [1, 2]. Nickel Oxide is a well-known semiconductor material with hole conductivity, which has excellent properties: it is thermally and chemically stable, has a wide band gap of 3.6-4.0 eV, providing optical transparency, and is not an expensive material whose films can be obtained by various physical and chemical synthesis methods. Like many oxides, it has a non-stoichiometric composition due to the formation of point defects: Nickel vacancies and interstitial oxygen, which form shallow acceptor levels and contribute p-type conductivity.

NiO-based PSCs usually have a p-i-n structure (inverted structure) [1, 2]. In NiO-based PSCs, they are used as compact NiO layers (c-NiO) so are the mesoporous layers of NiO (mp-NiO). Planar PSCs have a simpler design than mesoporous ones. However, in both types of PSCs, an important role is played by the c-NiO layer, which extracts holes from the active layer, transports them to the TCO anode, and blocks the active layer from contacting the cathode. To further increase the efficiency and stability of NiO-based PSCs, it is necessary to optimize the synthesis of compact NiO films, as well as optimize the processes of modifying the structure and surface of NiO through doping and other modification methods.

One of the disadvantages of using the HTL layer of PEDOT:PSSis the degradation of organic solar cells due to the highly acidic nature of PSS [3]. As a result, the interface between ITO and PEDOT:PSS becomes unstable, and an undesirable chemical reaction occurs. To solve this problem, this paper proposes the use of an HTL NiO layer between ITO and PEDOT:PSS that will block unwanted degradation of ITO. For this purpose, the present paper presents the results of the study of the optical and electrophysical characteristics of composite films NiO/PEDOT:PSS.

Experimental methods

Production of Nickel oxide films on the ITO surface was carried out as follows [4]: Nickel nitrate hexahydrate [$Ni(NO_3)_2$ $6H_2O$] weighing m=145mg (LLC «Polihrom») was dissolved in a volume of ethylene glycol V=1 ml. Monoethanolamine (5 μkl) was added to the resulting solution. The solution was mixed at room temperature for 16 hours and then kept for 24 hours at room temperature. NiO films were obtained by centrifugation (SPIN150i, Semiconductor Production System). To change the film thickness, the substrate rotation speed was changed from 1500 rpm to 2500 rpm. After that, the film was annealed for 10 minutes at

100°C, and then annealed to a temperature of 350°C at a rate of 10°C/min. Ito-based substrates were prepared according to the method [5].

For obtaining the composite films of NiO/PEDOT:PSS solution was used PEDOT:PSS (1%, Ossila Al4083). Before applying the solution of PEDOT:PSS was filtered through a 0.45 micrometer filter. Films of PEDOT:PSS were obtained on the NiO film by centrifugation at a speed of 4000 rpm. After film of PEDOT:PSS on the surface of NiO annealed in air atmosphere at a temperature of 120°C for 15 min.

The surface topography of the samples was studied using the JSPM -5400 atomic force microscope (ASM) JSPM-5400 (JEOL, Japan). A special modular program for analyzing scanning probe microscopy data (Win SPMII Data-ProcessingSoftware) was used to process images obtained on the ASM. Surface morphology, roughness of NiO films, and composite NiO/PEDOT:PSS films were analyzed from ASM images. Images of the film surface were obtained using the semi-contact scanning method. The absorption spectra of the studied samples were recorded using a CM-2203 Solar spectrofluorometer. The impedance spectra were measured using a potentiostat-galvanostat P45X in the impedance mode on the installation described in detail in [6].

Results and discussion

Images of the surface morphology of NiO films obtained at different speeds of rotation of the substrate are shown in figure 1. From figure 1, it can be seen that the NiO film obtained at the substrate rotation speed of 1500 rpm /min has a granular structure, the surface roughness is 7,44 nm. As the substrate rotation speed increases, the film surface roughness decreases (figures 1, b and 1, c).

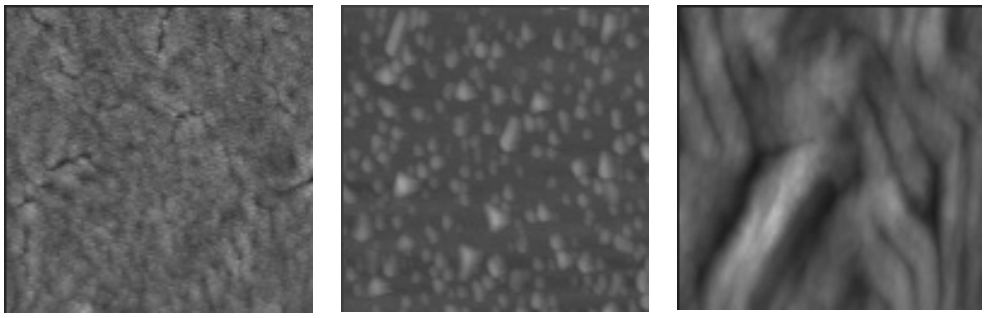

a b c

Fig.1. Images of the surface morphology of NiO films:
a) – NiO – 1500 rpm /min; b) – NiO – 2000 rpm /min; c) – NiO – 2500 rpm /min.

The roughness of the film at the speed of rotation of the substrate 2000 rpm/min is 5.19 nm, and at 2500 rpm is 3.51 nm. Table 1 shows the roughness values of NiO films obtained at different speeds of rotation of the substrate. After that, PEDOT:PSS films were applied to the surface of the NiO films by spincoating. Figure 2 shows images of the surface morphology of PEDOT:PSS films on the NiO surface. The figure shows that the PEDOT:PSS film on the surface of the NiO film obtained at a rotation speed of 1500rpm/min has an inhomogeneous surface structure with a roughness of 5.56 nm.

Table 1- Surface roughnessof NiO films with different rotation speeds

Sample	R_a, nm
NiO – 1500 rpm /min	7.44
NiO – 2000 rpm /min	5.19
NiO – 2500 rpm /min	3.51

As can be seen from the figure, when the surface roughness of the Nickel oxide film decreases, the roughness of the PEDOT:PSS film also decreases (figure 2, b). Further reduction in the roughness of the NiO film also leads to a reduction in the roughness of the PEDOT:PSS film (figure 2, c). PEDOT film roughness PEDOT:PSSon the surface of NiO films are shown in table 2.

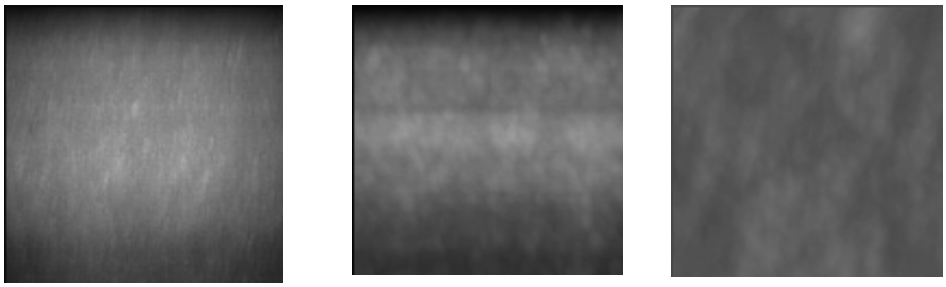

a b c

Fig.2. Images of the surface morphology of NiO/PEDOT:PSS films:
a) – NiO – 1500 rpm/min /PEDOT:PSS; b) – NiO – 2000 rpm/min /PEDOT:PSS;
c) – NiO – 2500 rpm/min / PEbOT:PSS.

Table 2 - The surface roughness of the films, the NiO/PEDOT:PSS

Sample	R_a, nm
NiO - 1500 rpm/min / PEDOT:PSS	5.56
NiO – 2000 rpm/min /PEDOT:PSS	4.92
NiO – 2500 rpm/min /PEDOT:PSS	1.15

Figure 3 shows the absorption spectra of NiO films obtained at different speeds of rotation of the substrate: 1500 rpm, 2000 rpm, 2500 rpm.

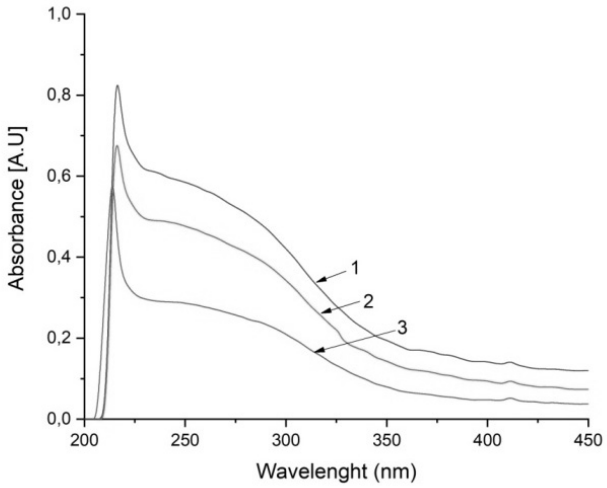

Fig.3. Absorption spectra of NiO films:
1 – NiO – 1500 rpm/min; 2 – NiO – 2000 rpm/min; 3 – NiO – 2500 rpm/min.

The absorption spectrum has two peaks at 216 nm and 237 nm. The figure shows that the optical density of the absorption spectra of NiO films decreases as the substrate rotation speed increases. The positions of the maxima of the absorption spectrum do not change. Table 3 shows the characteristics of the absorption spectra of NiO films. The decrease in the optical density in the absorption spectra with an increase in the rotation speed of the substrates is associated with a decrease in the thickness of the NiO films.

Table 3 - Characteristics of the absorption spectra of NiO films

Sample	D1, (λ =216 nm)	D2, (λ =237 nm)
NiO – 1500 rpm/min	0.82	0.60
NiO –2000 rpm/min	0.67	0.49
NiO –2500 rpm/min	0.56	0.29

.

Figure 4 shows the absorption spectra of NiO/PEDOT:PSS composite films. The absorption spectrum of the films has two max at 216 nm and 237 nm.

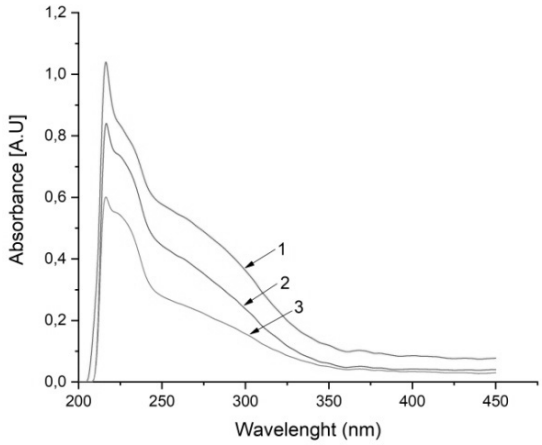

Fig.4. Absorption spectra of films: NiO/PEDOT:PSS:
1 – NiO - 1500 rpm /min/PEDOT:PSS; 2 – NiO – 2000 rpm /min/PEDOT:PSS;
3 – NiO – 2500 rpm /min/PEDOT:PSS.

Due to the small thickness of the PEDOT:PSS film compared to the NiO film, no absorption bands of PEDOT:PSS are observed in the absorption spectrum, except for an increase in the optical density. Reducing the thickness of the NiO film leads to a decrease in the optical density of the absorption spectrum of the composite film. However, it should be noted that the absorption of the composite film remains high compared to the NiO film. The characteristics of the absorption spectra of NiO/PEDOT:PSS composite films areshown in table 4.

Table 4 - Characteristics of the absorption spectra of films NiO/PEDOT: PSS

Sample	D1, (λ =21 nm)	D2, (λ =222 nm)
NiO - 1500 rpm/min / PEDOT:PSS	1.03	0.85
NiO – 2000 rpm/min / PEDOT:PSS	0.83	0.74
NiO – 2500 rpm/min /PEDOT:PSS	0.59	0.55

The impedance spectra were measured using a potentiostat-galvanostat P45X in the impedance mode. For this purpose, an aluminum electrode with a thickness of 200 nm was applied to the surface of the films in a vacuum at a pressure of 10^{-5} Torr on the CY-1700x- spc-2 spray plant (Zhengzhou CY Scientific Instruments Co., Ltd). Fitting of the impedance spectra was performed using the EIS-analyzer software package. The analysis of the impedance measurement results was carried out according to the diffusion-recombination model and the equivalent circuit shown in figure 5 was used for the fitting. The figure shows the following parameters for obtaining a hodograph of semiconductor films: R1 and R2 are the resistances corresponding to R_h and R_{ext}; CPE1 is a constant phase element, which is an equivalent component of an electrical circuit that simulates the behavior of a double layer, but is an imperfect capacitor.

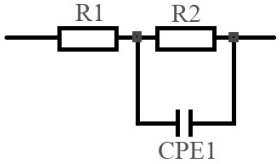

Fig.5. Equivalent electrical circuit

Light impedance spectra of the cells of the structure ITO/PEDOT:PSS/Al and ITO/ NiO/PEDOT:PSS/Al on voltage -500 mV and frequencies from 100 kHz to 0.5 Hz is shown in figure 6. Fitting of impedance spectra was performed using the software package EIS–analyzer, it was calculated the basic charge transport properties of the films (table 5), where: k_{eff} is the effective rate of extraction of charge carriers from PEDOT:PSS or NiO/PEDOT:PSS, τ_{eff} is effective time of flight of charge carriers through PEDOT: PSS or NiO/ PEDOT:PSS, R_h-resistance of the film PEDOT:PSS or NiO/PEDOT:PSS, Rext – resistance of transfer of charge carriers at the border PEDOT:PSS/electrode or NiO/PEDOT:PSS/electrode associated with the extraction of charge carriers with PEDOT:PSS or NiO/PEDOT: PSS.

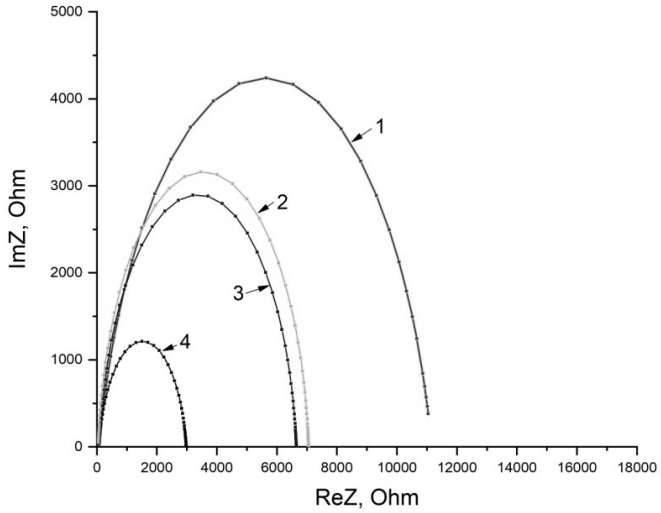

Fig.5. Light impedance spectra of NiO/PEDOT: PSS films with voltage parameters of -500 mV and frequency from 100 kHz to 0.5 Hz: 1 – PEDOT: PSS; 2 – NiO - 1500 rpm /min/ PEDOT:PSS; 3 – NiO – 2000 rpm /min/PEDOT:PSS; 4 – NiO – 2500 rpm /min/PEDOT:PSS.

The values of the electrophysical parameters of the films are shown in table 5. As can be seen from the data in table 5, the thickness of the NiO film significantly affects the resistance of the NiO/PEDOT:PSS (R_{ext}) film and the resistance of charge carrier transfer at the NiO/PEDOT:PSS/electrode interface (R_{ext}). The resistance of the NiO-1500 rpm/min / PEDOT:PSS film has the highest resistance, and the resistance of the NiO-2000 rpm /min/ PEDOT:PSS film is less than the resistance of the PEDOT:PSS film by about 30%. Nio-2500 rpm/PEDOT:PSSfilm resistance shows the best value. A lower film resistance should improve the solar cell fill factor and generally increase photovoltaic performance

The dynamics is observed in the change in the charge carrier transfer resistance at the interface between PEDOT: PSS/electrode and NiO/PEDOT:PSS /electrode (R_{ext}). The R_{ext} resistance value of the PEDOT:PSS film has the highest value. The resistance of the NiO-1500 rpm/min/PEDOT:PSS and NiO-2000rpm/min/PEDOT:PSS films is significantly less than the R_{ext} resistance of the PEDOT:PSS film. The Rext resistance of the NiO film is 2500 rpm/min/PEDOT: PSS shows the lowest value. The R_{ext} value determines the efficiency of charge carrier recovery from PEDOT:PSS and NiO/PEDOT:PSS films, and the lower the R_{ext}value, the greater the efficiency of charge carrier accumulation and photocurrent of the cell. The values k_{eff} and τ_{eff} characterize the efficiency of charge carrier extraction with PEDOT: PSS,NiO/PEDOT:PSS and the effective time of charge carrier flight in PEDOT:PSS, NiO/PEDOT:PSS. As can be seen from table 5, the NiOfilm significantly affects the PEDOT:PSS film, and there is a positive dynamics in the coefficients k_{eff} and τ_{eff}.

Table 5 - Value of the electrophysical parameters of the film PEDOT:PSS and composite films NiO/PEDOT:PSS

Sample	R_h, Ω	R_{ext}, Ω	k_{eff}, s^{-1}	τ_{eff}, ms
PEDOT:PSS	95.5	11097	46.8	21.36
NiO - 1500 rpm/min /PEDOT:PSS	81.41	6571.2	56.37	17.13
NiO – 2000 rpm/min /PEDOT:PSS	44.17	7016	79.83	12.52
NiO – 2500 rpm/min /PEDOT:PSS	35.49	2917.2	118.12	8.46

The efficiency of charge carrier extraction from NiO – 2500 rpm/min/ PEDOT:PSS films increased approximately twice as compared to the film PEDOT:PSS, and the effective time of charge carrier flight decreased inversely. Holes injected into NiO/PEDOT:PSS diffuse to the electrode, where they recombine with electrons. Fast transport of the injected holes to the external electrode is very important, as this reduces the probability of their reverse recombination.

Conclusion

As a result of research, it was found that the surface roughness of NiO films decreases with increasing substrate rotation speed. It is shown that when the surface roughness of Nickel oxide decreases, the roughness of the PEDOT:PSS film also decreases. It is found that with increasing substrate rotation speed, the optical density of the absorption spectra of NiO films and the absorption of composite NiO/PEDOT:PSS films decreases. It is shown that optimization of the surface structure of NiO//PEDOT:PSS composite films promotes rapid transport of injected holes to the external electrode and reduces the probability of reverse recombination. The results obtained open up the prospect of using NiO//PEDOT:PSS composite films as an HTL Layer of organic solar cells.

REFERENCES

1 Ye S.et al. *Oxide Hole Transport Materials in Inverted Planar Perovskite Solar Cells (Chapter 4): The Future of Semiconductor Oxides in Next-Generation Solar Cells edited by Monica Lira-Cantu*. Elsevier, 2018, pp.117-158.

2 YinX. et al. Nickel Oxide as Efficient Hole Transport Materials for Perovskite Solar Cells. *Sol. RRL*, 2018, Vol.3, pp. 1900001. doi.org/10.1002/solr.201900001

3 Li G., Shrotriya V., Huang J., Yao Y., Moriarty T., Emery K., Yang Y. Highefficiency solution processable polymer photovoltaic cells by self-organization of polymer blends, *Nature Materials*, 2005, Vol.4, pp. 864–868.

4 Jung J., Dong Lim Kim, Sang Hoon Oh, Hyun Jae Kim. Stability enhancement of organic solar cells with solution-processed nickel oxide thin films as hole transport layers. *Solar Energy Materials & Solar Cells,* 2012, Vol.102, pp. 103–108.

5 Kim K., Ihm K., Kim B. Surface Property of Indium Tin Oxide (ITO) After Various Methods of Cleaning. *Acta Physica Polonica A,* 2015, Vol. 127, No. 4, pp.1176 – 1179.

6 Bisquert J., Mora-Sero I., Fabregat-Santiago F. Diffusion–Recombination Impedance Model for Solar Cells with Disorder and Nonlinear Recombination. *Chemelectrochem* , 2014, Vol. 1, Issue 1, pp. 289 – 296.

Article accepted for publication 03.12.2020

DOI 10.31489/2020No2/61-68

UDC 536.24

FRACTAL-STRUCTURAL ANALYSIS OF CONVECTION HEAT TRANSFER IN A TURBULENT MEDIUM

Turmukhambetov A.Zh., Aitmanova K.A., Otegenova S.B.

al-Farabi Kazakh National University, Almaty,Kazakhstan, Akylbek.turmukhambetov@gmail.com

The features of convective heat transfer of bodies in a turbulent environment are considered. The results of experimental research by one of the authors are discussed. Experimental data show that the heat transfer of a spherical body is affected by natural convection, the thermo-physical properties of the medium, the tightness of the flow, the turbulent flow regime, etc. Due to these factors, the formula for calculating convective heat transfer, which includes many experimental constants, becomes cumbersome and inconvenient for practical application. The paper presents the results of applying fractal-structural analysis methods to describe experimental data on convective heat exchange of badly streamlined (cylinder and sphere) bodies in a channel. Quantitative relations are obtained that link the intensity of turbulent heat transfer with the criteria for the degree of self-organization.

Keywords: turbulence, heat transfer, fractal, multifractal, vortex structure, entropy, flow crampedness.

Introduction

Analysis of numerous turbulence models shows their limitations and lack of accuracy. In many cases, to reach agreement with the experiment, the method of fitting using multiple empirical coefficients is used, or various empirical functions are introduced that are not physically justified. This approach may be useful for describing a specific process, but it is not sufficient for developing more or less General methods for solving turbulence problems. There is an opinion about the need for a deeper study of the physics of turbulent exchange to create an adequate theory, which puts turbulence in the category of General physical problems, and the results obtained in this direction are of General scientific significance. To understand the physics of hydrodynamic turbulence, it is important and relevant to conduct a theoretical study based on simple and visual models (for example, fractal and multifractal) of the dynamics of interaction of structural elements – vortices and vortex clusters in gradient flows, paying special attention to convective heat transfer in homogeneous and heterogeneous media, as a possibility of tracking the evolution of turbulent motion. At the same time, it is obvious that the value of any theoretical model depends on the degree of coincidence with the results of well-known or specially designed experiments.

1. Experimental results

Figures 1-3 show data on the average convective heat transfer of a sphere in a constrained flow, which shows a complex dependence of the heat transfer intensity on natural convection, the thermo-physical properties of the medium, and the degree of flow congestion. More than 1000 experiments were carried out to measure the convective heat exchange of a sphere flowing around a viscous liquid flow in a channel with a wide range of changes in the experimental conditions: the degree of flow constraint, the magnitude and direction of natural convection, the directions of heat flow, and the thermo-physical properties of the medium. A description of the experiment and part of the results are presented in [1, 2]. As you know, to date, we have observed the desire of the authors of such studies to present the results of heat exchange in the form of formulas:

$$Nu = aRe^b + cRe^d,$$

where *a, b, c, d* are empirical constants that take into account the above and other similar conditions of experience.

In any case, the dependence of heat transfer on the values of the Reynolds number is clearly shown, which can be represented as:

$$Nu = CRe^n. \quad (1)$$

Obviously, the explicit form of formula (1) depends on the flow mode: laminar or turbulent. In this regard, it should be noted that while some of the experimental results we have studied are known to relate to

the laminar regime, most of them relate to the transient and turbulent flows. Although it is generally assumed that turbulence occurs when the sphere flows around Re ≥ 40, it seems that anisotropic turbulence is observed much earlier. It should be noted that in the case of heat exchange, non-isothermicity is an additional factor that introduces a disturbance in the flow.

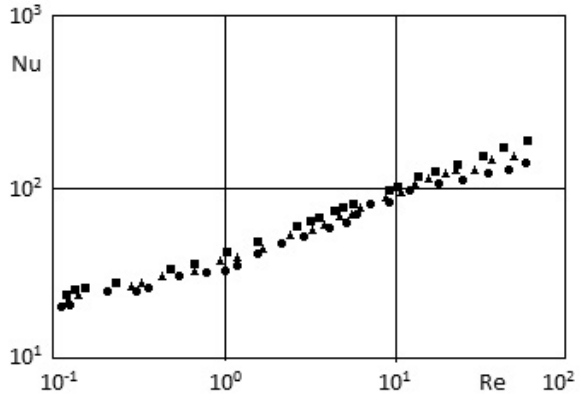

Fig.1. Influence of natural convection on the average heat transfer of the sphere, Pr_f=6120. Designations: • – Gr=13.0; ▲ – Gr=20.0; ■ – Gr=38.0.

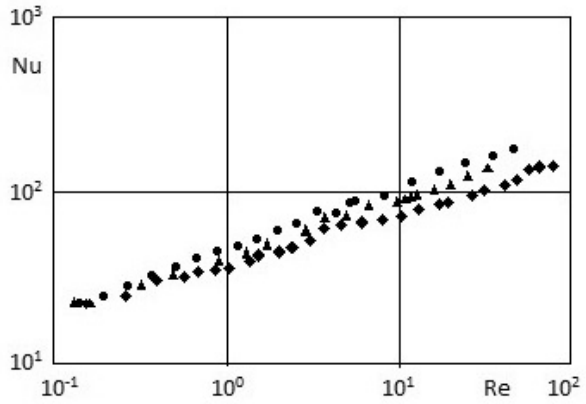

Fig.2. Influence of the thermo-physical properties of the medium on the heat transfer of the sphere. Pr_w/Pr_f=0.20. Designations: • – Pr_f=8680; ▲ – Pr_f=6120; ♦ – Pr_f=3080

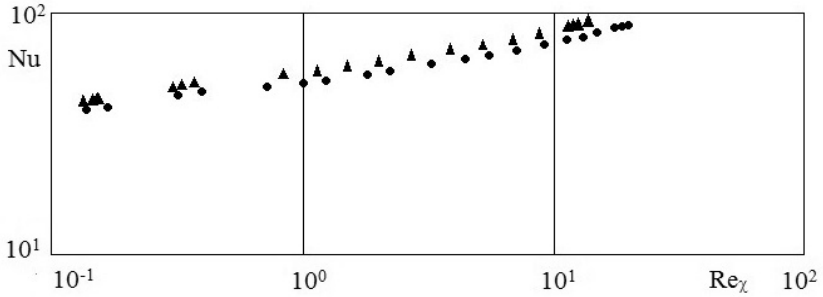

Fig.3. Influence of restricted flow on convective heat transfer of the sphere. Designations: ▲- χ = 0.235; • - 0.148

Thus, as a result of the experiments, systematic data on the hydrodynamic resistance and heat exchange of a sphere in the region of relatively small Reynolds numbers were obtained for the first time. Under the accepted experimental conditions, it was possible to ignore the influence of natural convection already at Re ≥ 10, paying attention to the flow constraint as the main factor leading to inhomogeneity of the turbulent flow. In article, the degree of flow constraint, which determines the spatial scales of complex turbulent eddy formations both on the surface of the body and a track of the body, is calculated as the change in the area of the gap between the surfaces of the streamlined body and the limiting walls of the channel. The geometrical parameters of the problem of fluid flow around a cylinder and a sphere in a channel are shown in Fig. 4.

The degree of crampedness of the flow is expressed by the number $\chi = h/H$, where h and H, respectively, are the characteristic dimensions of the body and channel (in our case, the diameters). Therefore, $0 \le \chi < 1$. Limiting case $\chi = 0$ corresponds to the flow of an unlimited fluid flow around a body. The relative values of the gap area in the midsection sections are defined as

$$\frac{F_{01} - F_1}{F_{01}} = 1 - \chi, \qquad \frac{F_{02} - F_2}{F_{02}} = 1 - \chi^2,$$

where F_{01}, F_{02} – the cross-sectional area of the channel and pipe, F_1, F_2 – the median section area of the respectively cylinder and sphere.

The movement in the gap between the body surface and the channel wall is inhomogeneously turbulent. Therefore, strictly speaking, the structural elements of turbulence are self-affine (not self-similar) multifractals that have different similarity coefficients in the corresponding spatial directions. One of the consequences of this complication of fluid movement in a limited space is that now the effective gap area-the characteristic size of the fluid flow is smaller than both in laminar motion and incomparison with the case of free turbulence. This will lead to an additional increase in the coefficient of hydrodynamic resistance of the body and the intensification of the heat exchange process.

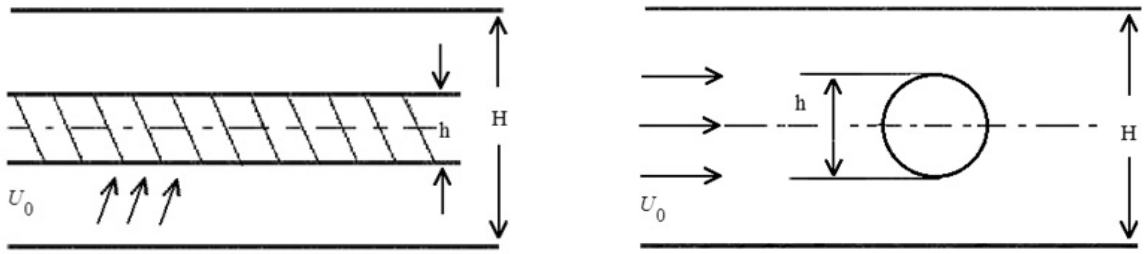

a *b*

Fig.4. Flows diagram of the cylinder in the channel (*a*), and the sphere in the pipe (*b*)

Obtained experimental data on the heat exchange of the sphere in the channel confirm the structurality of the flow even at relatively small Reynolds numbers. For the first time, the natural extension of the known regularities to the region of small Re numbers (up to the obviously laminar regime) allows us to consider our experimental data as test data confirming the provisions of the proposed structural approach to the study of convective heat transfer in a turbulent environment.

2. Theoretical part

Development by Mandelbrot [3] the mathematical concept of a fractal and its applications to the description of the shapes of various objects make it possible to construct models of non-trivial random scale-invariant structures [4, 5]. The application of these models is a new approach to the description of disordered structures in physics. Success in applying fractal models in physics is primarily due to the fact that fractal forms are inherent in a huge number of processes and structures. Especially successful the possibilities of theory fractal are used especially successfully in studies of hydrodynamic turbulence and heat transfer [6-9].

The fractal character of hydrodynamic turbulence follows from the scale-invariant property of turbulence dynamics and from the structure of a strange attractor corresponding to the occurrence of hydrodynamic chaos. The structural and scaling characteristic of the evolution of turbulent vortices allows us to consider them as a fractal object. Moreover, numerous experimental studies show that turbulence, as a combination and result of the interaction of different-scale vortices, is a multifractal characterized by a set of different fractal dimensions. The dimension of the multifractals itself or the generalized dimension D_q is determined by the Renyi formula [4]:

$$D_q = \frac{1}{(q-1)} \lim_{\delta \to 0} \frac{lnN(\delta, q)}{ln(\delta)}, \tag{2}$$

where $-\infty \le q \le +\infty$ – is order of the multifractal moment, $N(\delta, q)$ - is number of vortices.

It is well-known, the multifractality of turbulence is directly related to its intermittency. Representing the characteristic of the dependence of the number of vortices on their size in the form:

$$N(q, \delta) \sim \delta^{-\tau(q)}; \quad \tau(q) = -\lim_{\delta \to 0} \frac{lnN(\delta, q)}{ln\delta}$$

can be received:

$$D_q = \frac{1}{1-q} \tau(q),$$

where $\tau(q)$ – is the intermittency function, which can be determined from the experiment by processing the time series.

.

2.1. Fractal nature of convective heat transfer

Indicators of power dependencies between dimensionless complexes of basic parameters (similarity criteria) can be expressed in terms of fractal characteristics determined by theoretical models of structures (vortices, clusters of particles) of the phenomenon. We present the Nusselt criterion for turbulent heat transfer as:

$$Nu = \frac{\alpha l_0}{\lambda} = \frac{q}{q_0}; \quad \alpha = \frac{q}{\Delta T}; \quad q_0 = \lambda \frac{\Delta T}{l_0}, \tag{3}$$

where α – is the heat transfer coefficient; l_0 – is the characteristic spatial scale; λ – is the thermal conductivity; q, q_0 are the heat flows through the unit surface at the temperature difference ΔT in turbulent and laminar modes.

The q/q_0 ratio is equivalent to the ratio of the effective surface area of turbulent mixing F to its value F_0 in laminar mode. The law of increasing F, which corresponds to the intensification of heat exchange during flow turbulence, according to [10, 11] can be represented in the most general form as power dependence:

$$F = F_0 \left(\frac{\ell_0}{\ell_\nu} \right)^\gamma,$$

and equation (3) goes to the form:

$$Nu = \frac{q}{q_0} = \frac{F}{F_0} = \left(\frac{l_0}{\delta_\nu} \right)^\gamma, \tag{4}$$

where l_0 – the minimum dissipative scale is replaced by δ_ν – the smallest size of self-similar structural elements of turbulence, depending on the kinematic viscosity ν; γ – an indicator determined by a specific scaling model – scale-invariant deformation of the surface of the medium structures.

Considering the well-known estimate $\delta_\nu \sim \nu/U_0$ from formula (4), we obtain

$$Nu = CRe^\gamma, \tag{5}$$

where $Re = l_0 U_0/\nu$ – the Reynolds number make up the characteristic velocity U_0, C is a constant.

Some fixed values of γ can be determined from simple models of scale-invariant deformation of surfaces that restrict liquid volumes. It should be expected that isotropic turbulence actually corresponds to symmetric deformation, and anisotropic turbulence, which is more typical for shifted flows, corresponds to one – sided asymmetric deformation. It is taken into account that model deformations have the properties of turbulent mixing: maximum surface stretching with the smallest number of links, self – similarity of the cascade deformation process-the next deformable surface (generator) must contain parallel elements to the original surface. The value of γ can be found by calculating the fractal (Hausdorff) dimension D of the object obtained after the n-th deformation. By definition

$$D = \lim_{l_n \to 0} \frac{\ln N(l_n)}{\ln 1/l_n}, \quad N(l_n) = F_n / l_n^{d-1},$$

where $N(l_n)$ - is the number of elements required to cover the surface F_n; d - is the topological dimension of the space in which the object with the deformable surface is insirted.

As a result of simple calculations, we find a formula that relates the scaling exponent γ to the fractal dimension D:

$$\gamma = D - d + 1. \tag{6}$$

Substituting the values D in (6) and taking into account that for isotropic and anisotropic deformations d is equal to 3 and 2, respectively, we calculate the founded values: $\gamma : \gamma_0 = 0.7925$ and $\gamma_\perp = 0.4650$. Finding from geometrical consideration index of γprocess scaling should probably be considered as their limit values describing the universal properties of turbulent transport. In particular, γ_0 corresponds to the region of large Reynolds numbers, when almost homogeneous, isotropic (Kolmogorov) turbulence is observed, $\gamma_\perp$ can be used both for large Reynolds numbers, when the anisotropy is caused by local (boundary) conditions (the presence of walls, the second phase, heat transfer, etc.), and for relatively small Re numbers, i.e. in the processes of occurrence and evolution of turbulence. The calculated values of γ_0, $\gamma_\perp$ are close to the well-

known experimental results on heat exchange for developed, isotropic turbulence (n ~ 0.8) and for quasi-regular, large-scale turbulence (n ~ 0.5).

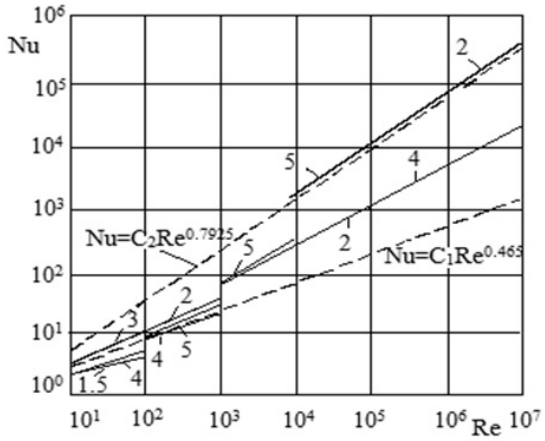

Fig.5. Average cylinder heat transfer. The results are taken from [1]. 1 - dat of J. Ulzamer; 2 - A.A. Zukauskas; 3 - B.Kh. McAdams; 4 - M.A. Mikheev and I.M. Mikheeva; 5 - G. Hilpert

Figure 5 shows a comparison of numerous results of various authors presented in [1] in the form of empirical dependencies with the formula (5) for two limit values γ. As can be seen from the graph, the theoretical dependence (5), covering the lower and upper regions of the values of the number Re, correctly reflects the laws of heat exchange of the cylinder under different flow modes. Therefore, instead of an empirical dependence (1) with an undefined degree n, we propose the formula (5), where the exponent γ is associated with the fractal dimension D. The indexes γ of the dependences degree of turbulent heat transfer can be determined not only by geometric, but also by physical – multi-fractal models connected with information-entropy concepts.

2.2. Multifractal (physical) model of turbulent heat transfer

The movement of turbulent vortices of different scales, their interaction is observed as random alternations of different-scale dynamic characteristics. Therefore, it is necessary to take into account the probabilistic, intermittent nature of turbulent heat transfer. Objects in which the distribution of a measure is described by probabilistic moments of different order (the degree of inter leavability) and the corresponding spectrum of fractal dimensions are called multifractals. In [4], the following is one of the definitions of the multifractal probability measure M:

$$M \sim \delta^{-\alpha} N(q,\delta);\ N(q,\delta) = \sum_i P_i^q \sim \delta^{qD_q} \times \delta^{-D_q} = \delta^{D_q(q-1)} = \delta^{-\tau(q)}, \tag{7}$$

where δ – size of the measure split cell, α – fractal dimension of the cell, $N(q,\delta)$ – number of cells containing the measure, P_i – probability of realization cell number i, q – the order of the multifractal moment, which takes any real value, $\tau(q) = (1-q)D_q$ –interleaving function, D_q – a generalized (multi-fractal) dimension defined by the Renyi formula, which differs from (2) in that instead of $N(q,\delta)$ - the number of vortices, we consider P_i - the probability of their realization:

$$D_q = \frac{1}{q-1} \lim_{\delta \to 0} \frac{\ln \sum_i P_i^q}{\ln \delta}. \tag{8}$$

$N(q, \delta)$ it can also be expressed via local characteristics

$$N(q,\delta) = \sum_i P_i^q \sim \delta^{q\times\alpha} \times \delta^{-f(\alpha)} = \delta^{q\alpha - f(\alpha)}, \tag{9}$$

where $f(\alpha)$ is multifractal spectral function.

From (7) and (9) we obtain an unambiguous cyclic relation between the functions $\tau(q)$ and $f(\alpha)$ via Legendre transformations:

.

$$f(\alpha(q)) = q \times \alpha(q) + \tau(q), \tag{10}$$

where $\alpha(q) = -\frac{d\tau(q)}{dq}$, $q = \frac{df(\alpha)}{d\alpha}$.

In the case of q = 1, there is no interleaving (by definition $\tau(1)=0$) and the chaos structures can be self-similar. If we reveal the uncertainty in (8) that occurs when, $q \to 1$ by decomposing the numerator with a small argument q - 1, we have

$$D_1 = \lim_{\delta \to 0} \frac{\sum_i P_i(\delta) \ln P_i(\delta)}{\ln \delta} = -\lim_{\delta \to 0} \frac{S(\delta)}{\ln \delta} = S; \quad S(\delta) = -\sum_i P_i \ln P_i, \tag{11}$$

where $S(\delta)$ – entropy of splitting a measure into cells, S - is the entropy of a self-similar set that does not depend on splitting.

From formulas (10), (11) follows

$f(\alpha_1) = \alpha_1 = D_1 = S$, $\alpha_1 \equiv \alpha(q = 1)$.

In short, the entropy of a self-similar set is equal to the value of the multifractal spectral function at its fixed point. Information entropy, defined by the second expression (11), according to the generally accepted terminology [12] is the average value of synergetic information I_i, acquired at the construction (destruction) of the structure with probability P_i

$$I_i = -\ln P_i; \qquad \sum P_i = 1.$$

We will represent the probability of realization of structures P as a function of a continuous variable-information I [13]:

$$P(I) = e^{-I}, \qquad \int_0^\infty P(I) dI = 1.$$

The probability $P(I)$ is expressed through the probability density distribution function $f(I)$

$$P(I) = e^{-I} = \int_I^\infty f(I) dI, \tag{12}$$

where the limits of integration correspond to areas of definition $P(I) \geq 0$.

Relation (12) is satisfied by the function

$$f(I) = P(I) = e^{-I}, \quad \int_0^\infty f(I) dI = 1. \tag{13}$$

The probability function of the realization of information $P(I)$ coincides with the probability density function $f(I)$. Precisely information is an integral characteristic of a self-similar system inherent in any of its hierarchical levels: a part contains complete information about the whole. Taking into account (13), information of entropy of self-similar systems we write in the form:

$$S(I) = -\int_I^\infty f(I) \times I dI = (I + 1) e^{-I}.$$

Further, according to [14], any continuous function $g(x)$, describing self-similar properties of dynamic chaos at its fixed point satisfies the functional equation:

$g(x) = \alpha g(g(x / \alpha))$,

where α – is a scaling multiplier. Therefore, as criteria for self-similarity, we take the values of the characteristic functions of probability $P(I)$ and information entropy $S(I)$ at their fixed points:

$$P(I_1) = e^{-I_1} = I_1, \quad I_1 = 0.567, \tag{14}$$

$$S(I_2) = (I_2 + 1) e^{-I_2} = I_2, \quad I_2 = 0.806. \tag{15}$$

Taking into the account the taken results from the formula (5) for the intensity of heat transfer in the developed turbulent regime ($\tau(q = 1) = 0$) we write in the following way:

$$Nu = CRe^{I_2}, \quad (16)$$

where C- is a new constant.

Similarly, for anisotropic turbulence

$$Nu = CRe^{I_1} \quad (17)$$

The numbers I_1, I_2 are extended analogues of the Fibonacci number, which is used in many areas of modern science, and correspond to two extreme cases of describing the conduct of a complex system: informational and entropy. Between statistics and dynamic conditions realizes a informational state (the beginning of structuring and stochastization) , described by a number $I_1=0.567$. The most complex statistical state with internal order is characterized by a number $I_2=0.806$ - the value of entropy, normalized to unit. The numbers I_1, I_2 they can be considered as the minimum values of the fractal dimensions of the set of values of information generated by the system at qualitatively different levels of its evolution. In a broad sense, numbers I_1, I_2 are universal quantitative criteria for qualitative changes in the evolution of open systems of any nature.

3. Discussion

3.1. Influence of flow tightness on average heat exchange.

From the analysis of the data shown in figures 1-3, follows that the main factor affecting the heat exchange of the body in the channel is the tightness of the flow. Obviously, the mechanism of influence of the constraint factor also works in the case of flow around bodies without heat exchange. The study of fractal properties of a constrained turbulent flow provides the following correction for changes in the hydrodynamic resistance of poorly streamlined bodies [15]:

$$Re_\chi = \frac{Re_m}{(1-\chi^j)^{D_i/2}}, \quad (18)$$

where the index «χ» - means that Re is calculated adjusted for tightness; Re_m – the Reynolds number calculated from the maximum speed; $j = 1$ corresponds to a cylinder, $j = 2$ - a sphere; D_i is calculated using the formula (6), where $\gamma_1 = \gamma_\perp = 0.4650$, $\gamma_2 = \gamma_0 = 0.7925$.

Therefore, taking into account (18), formulas (16) and (17) can be given the form:

$$Nu = C\left[\frac{Re_m}{(1-\chi^j)^{D_i/2}}\right]^{I_i}. \quad (19)$$

Figure 6 shows the results of processing experimental data on the heat exchange of the sphere (the experimental conditions and initial data are shown in figure 3). The coincidence of the values of Nu calculated by formula (19), where for a specific case it is accepted: $j = 2$; $D_1 = 2.465$; $I_i = I_1 = 0.567$, confirms the fruitfulness of applying the fractal theory to the study of heat transfer (hence, hydrodynamics) of a body flowing around a constrained flow of a viscous liquid.

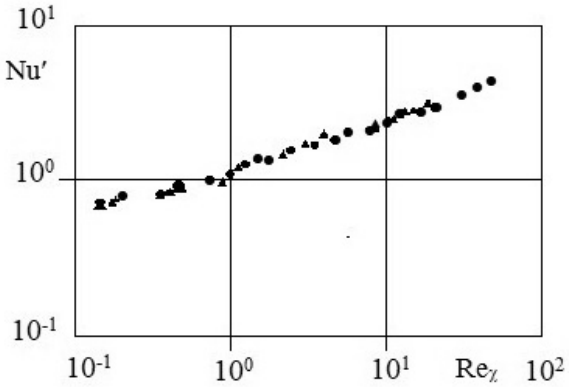

Fig.6. Taking into account the effect of flow constraint on convective heat exchange of the sphere. The designations and conditions of the experiment correspond to fig.3

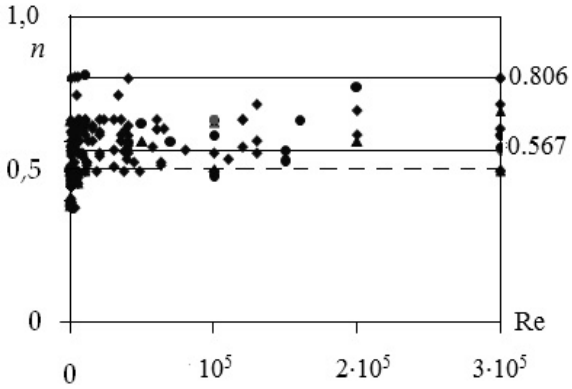

Fig.7. Average heat transfer of bodies in a viscous fluid flow**.** Designations: ♦ – experimental data of various authors for the cylinder [14], • – for the sphere [1].

3.2. Average heat exchange of bodies in a turbulent flow.

The obtained theoretical results are compared with the known experimental data on convective heat exchange of bodies (figure 7). The results of more than 100 publications are analyzed, the main part of which is given in [16]. Experiments cover a wide range of factors (various liquids and gases, sizes and shapes of bodies, the range of changes in the number of Re, research methods, etc.) that affect the course of the heat exchange process and the accuracy of the study itself. At first glance, there is actually a significant spread of the indicator n both in terms of the Reynolds number and for the same value. But this scatter is apparent: if we do not take into account the results for the smallest Reynolds numbers, when the values of $n \le 0.5$ are selected based on the theoretical solution for laminar flow, the remaining data are located in the interval $I_1 \le n \le I_2$.

Conclusions

The given results of an experimental research of the average heat transfer of a sphere in a constrained turbulent flow. Here proposed simplified calculation formulas for heat exchange of bodies in a channel with a smaller number of empirical constants. On the basis of results measurements and theoretical analysis is confirmed the fractal nature of convective heat transfer. Presented a fractal description of the influence of the constraint factor on the convective heat exchange of the body. Set up information-entropy criteria for the degree of self-organization of the heat exchange process. Comparison of the numerical results obtained on the basis of the proposed fractal models with the known experimental data shows their satisfactory agreement. The results discussed complement the known information about heat exchange in a turbulent environment, and can be directly used in technological processes related to flow and heat exchange, in order to control and manage them.

REFERENCES

1 Isataev S.I., Akylbaev Zh.S., Turmukhambetov A.Zh. *Aerohydrodynamics and heat exchange of curved bodies*. Almaty, Gylym, 1996, 437 p. [in Russian]

2 Turmukhambetov A.Zh. Heat Transfer of a sphere in a constrained flow of a viscous liquid. *IFJ*. 2001, Vol. 74, No.3, pp. 161 – 163. [in Russian]

3 Mandelbrot B.B. *Fractals: form, chance and dimension*. San Francisco, 1977, 347 p.

4 Feder E. *Fractals*. Moscow, Mir, 1991, 254 p.

5 Mandelbrot B. *Fractal geometry of nature*. Moscow, 2002, 656 p.

6 Kolesnichenko A.V., Marov M. Ya. *Turbulence and self-organization. Problems of modeling space and natural environments*. Moscow, 2009, 632 p. [in Russian]

7 Kovalnogov V.N., Khakhalev Yu.A. Numerical investigation of effected turbulent flow on the base of pressure fluctuations fractal dimension analysis. *Vector of science of Tolyatti state University*. 2014, No. 3 (29), pp. 62 – 66. [in Russian]

8 Suprun T.T. Heat transfer in the presence of transition induced by wakes of hesitating cylinder. *Eurasian Physical Technical Journal,* 2016 Vol. 13, No. 2(26), pp. 92 – 97.

9 Demenok S.L. *Heat transfer and hydraulic resistance in pipes and channels*. SPB, N-PromByuro, 2012, 285 p. [in Russian]

10 Stern V.. *Elementary structural model of turbulent mixing*. In: Collection of Structural turbulence. Novosibirsk. 1982, 166 p. [in Russian]

11 Zhanabaev Z.Zh. Fractal model of turbulence in a jet. *Izvestia of SB as USSR. Series of technical Sciences*. 1988, Vol. 4, No. 15, pp. 57 - 60. [in Russian]

12 Haken G. *Information and self-organization*. Moscow, Mir, 1991, 240 p.

13 Zhanabaev Z.Zh. *Information properties of self-organizing systems.* Reports of the national Academy of Sciences of the Republic of Kazakhstan, 1996, No. 5, pp. 14 – 19.

14 Shuster G. *Deterministic chaos*. Moscow, Mir, 1988. - 240 p.

15 Turmukhambetov A.Zh. Fractal properties of the constrained turbulent flow. *Bulletin of the NAS RK*. Almaty, 1999, No. 5, pp. 77 – 83. [in Russian]

16 Morgan V.T. The overal convective Heat Transfer from smooth circular cylinders. *Advances in Heat Transfer*. 1975, Vol. 11, pp. 199 – 264.

Article accepted for publication 21.10.2020

DOI 10.31489/2020No2/69-72

UDC 629.5.015.26

DARRIEUS TYPE WIND TURBINE WITH CONTROLLED BLADES

Kayan V., Lebid O.

Institute of Telecommunications and Global Information Space of the National Academy of Sciences of Ukraine, Kyiv, Ukraine, kayan@ua.fm

The results of studies on possibility of increasing efficiency in the use of wind energy and improving the dynamic characteristics of Darrieus wind turbine with straight blades are described. It is shown how the values of torque on the rotor shaft may be optimized by controlling the orientation of the turbine blades relative to the oncoming flow. Control of blades was provided with a cylindrical track of the special form in plan. The track form allowed to establish optimum angle of attack on each site of blade circular trajectory. It allowed to increase power coefficient Cp by 1.5 times and to reduce wind speed at which there is self-start of the wind turbine.

Keywords: Darrieus type wind turbine, controlled blades, torque, power coefficient, tip speed ratio

Introduction

As it is known, all over the world, the technologies have been intensively developed using renewable energy sources, including kinetic energy of wind and water flows [1]. The main types of the wind power units are the wind generators with a horizontal or vertical axis of rotation, the electric generator for converting mechanical energy on the turbine shaft into electric and the tower for the placement of these generators. At present, for utilization of wind energy the horizontal axis wind turbines (HAWT) with capacity from hundreds watts to several megawatts are widely used. The essential components of such wind turbine construction is the vertical tower with height from 10 to 150 meters, the mechanisms for orientation the area of wind turbine rotation perpendicular to the direction of wind flow.

Vertical axis wind turbines (VAWT) do not need special arrangements of orientation relative to the direction of the wind and allow two-bearing turbine mounting system. The electric generator may be placed in the base of the unit, which simplifies its construction. The important advantage of VAWT is the relative simplicity of blades construction and the relatively small area required for the placement of wind turbines [2]. One of the main disadvantage of Darrieus type VAWT with rigidly fixed blades relative to the horizontal crosspieces is a high-speed wind flow, at which there is the self-starting of VAWT to rotate, and large values of the variable mechanical load on the shaft. As it turned out both of these disadvantage can be eliminated by using special methods of control the position of the blades on its circular trajectory.

1. Darrieus type VAWT design with straight controlled blades

When moving in a circular path the blade of VAWT operates in a periodically changing unsteady flow. As the typical wing profiles are used in the construction of blades, the main parameter determining the value and direction of the forces acting on the profile is the angle of attack. The nature of blades movement in the turbine with fixed position of blades is such that the angle of attack becomes supercritical at a very large part of its trajectory [3]. This leads to flow stall and big decrease of the value of the useful component of the aerodynamic forces, so that the blade even brakes wind turbine in some parts of the trajectory.

However, if it is possible to turn the blade in such a manner that the flows are at the optimal angle of attack around of the blade profile, the produced value of torque on the VAWT shaft can be significantly increased. The test of turbine models in water [3-4] and the full-scale prototypes of VAWTs in the air [4-5] have shown considerable increase the power coefficient

$C_p = 2P/\rho V^3 S$,

where P – is capacity of wind turbine, ρ – density of air or water, V – velocity of air or water flow, S – swept area of wind turbine) as well as a significant decrease in the average load on the turbine shaft and its amplitude pulsations [5-6].

The last prototype of the series of the wind turbines was created and tested in 2013-2018 and showed a stable and reliable performance during the tests in the wind tunnel, and the value of coefficient C_p was received equal 0.45. Darrieus type VAWT with straight controlled blades (Fig. 1) had the following parameters: blade length l_{blade} = 1.6 m, the chord length of the blade b = 0.25 m, the profile of the blade is symmetrical NACA 0015, the blade aspect ratio AR = l_{blade}/b = 6.4, radius of blade rotation R = 0.7 m, the average diameter of the control track D = 0.4 m, the VAWT swept area $S = 2Rl_{blade}$ =2.24m^2, the solidity $\sigma = 3b / 2R$ = 0.54. The blades were made of carbon plastic and one blade weighed 2.7kg.

Fig.1. The wind turbine with controlled blades in the wind tunnel

Mechanism for blades control have cylindrical track of the special form in plan and 8 mm thick, placed below the lower crosspieces of the VAWT, on both sides of which three pairs of rollers moved. The pair of rollers connected by special carriages, which are in its turn were pivotally connected to the rods disposed within the lower horizontal crosspieces. Another ends of the rods were pivotally connected to the control axes at the lower end of the blades. The control track was attached to the bottom support rigidly. To determine the shape of the cylindrical track was used computer modeling of the flow around the VAWT. A modified method of discrete vortices was used for modeling. This method based on the model of inviscid incompressible fluid [7]. A variable nature of the flow around blades is a feature of this modification: a flow around blade is unseparated at subcritical angles of attack of blade, at supercritical angles of attack a flow separate on leading edge of blade, as shown in [8].

2. Results and discussions

The used method of computer modeling allows to view the time evolution of the vortex trail behind VAWT and to get instantaneous and integral dynamic characteristics of VAWT. The presence of numerical flow visualization helps to better understand the physics of the processes and identify patterns that cannot be identified solely by instrumental measurements.

The results of numerical visualization of a vortex flow behind VAWT with fixed (*a*) and controlled (*b*) blades at tip speed ratio $\lambda p = 2\pi n R/V$ = 1.2 are shows in Fig.2 (the clockwise-rotating vortices are blue, counterclockwise rotating vortices are red, more intensive vortices are brighter). It can be seen that for VAWT with fixed blades the trail has a pronounced turbulent character that adversely affects the dynamic characteristics of the VAWT. For the VAWT with controlled blades highly visible vortex trail is formed and this trail leads to the improvement of dynamic characteristics of the VAWT. Note that such a marked difference vortex trail occurs precisely at tip speed ratio λp = 1.2, which was selected for controlling track

optimization. By change λp in upward or downward from this value the vortex trail behind the VAWT quickly loses its orderly appearance and the positive effect of the control blades loses also.

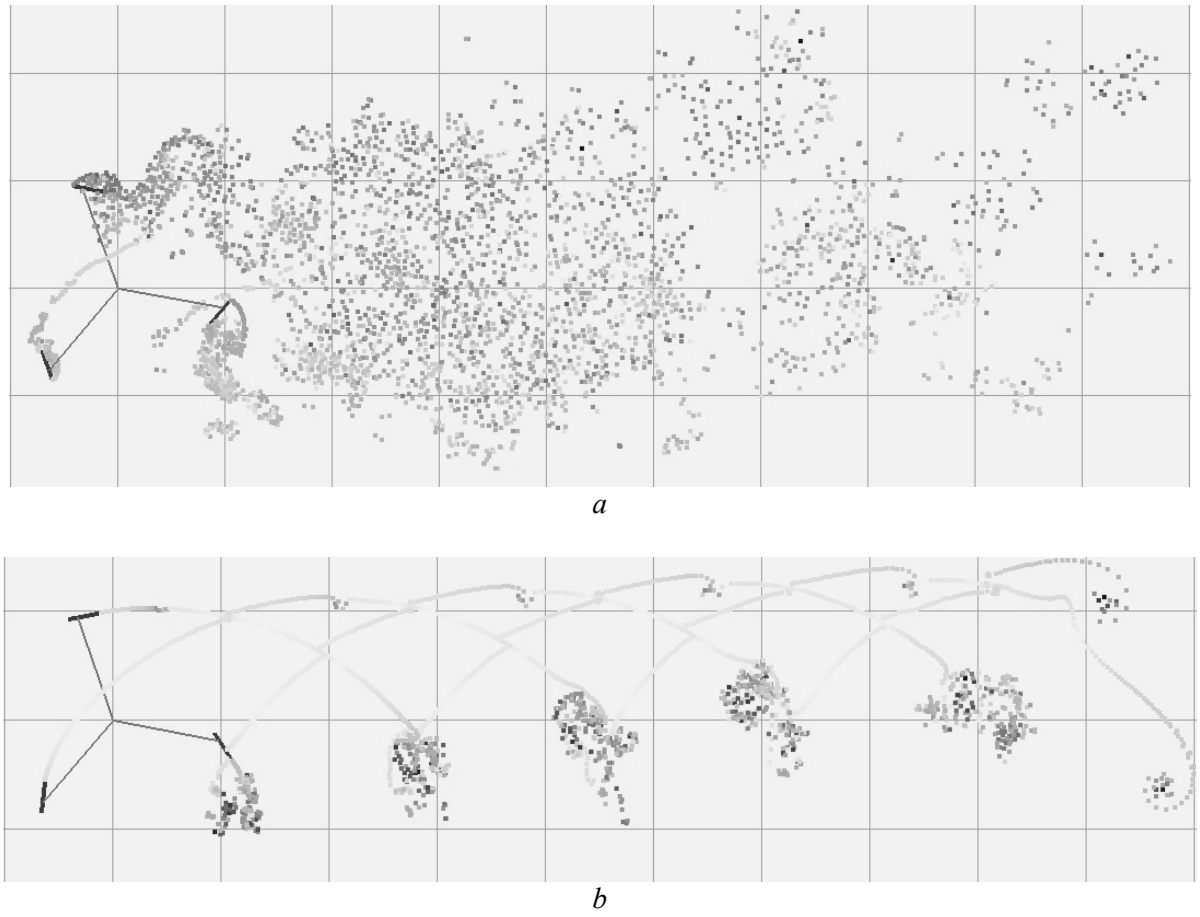

Fig. 2. Numerical visualization of a vortex flow behind VAWT with fixed (*a*) and controled (*b*) blades at tip speed ratio λp = 1.2

The lower end of the turbine shaft went under the floor of the wind tunnel, where on the shaft the disc with the 60-hole for measuring the speed of rotation of VAWT was placed on the shaft, and the shaft through gear box with conic gears connected to the electromagnetic powder brake coupling. The range of brake torque of coupling is 3 ÷ 80 Nm in increments of 2 Nm. Under the initial load on the shaft of 3 Nm (resistance coupling with the power supply disconnected), VAWT self-started when the wind flow velocity in wind tunnel was V = 2.5 ÷ 2.8 m / sec, without load (i.e. the coupling is removed) the VAWT self-started when the wind flow velocity was V = 1.8 ÷ 2 m/sec. Wind flow velocity V was defined by the stationary of wind tunnel equipment with an accuracy of 0.05 m/sec. The same VAWT without control mechanism (i.e. the blades are rigidly fixed to the crosspieces) and without load on the shaft self-started when the wind flow velocity V = 3.5 ÷ 3.8 m / sec. Dependence of the rotation speed of the VAWT $\boldsymbol{n}$ from the useful torque M_{net} on the shaft at various velocity of wind flow V is shown in Fig. 3, *a*. The useful torque M_{net} was set by change of current in electromagnetic brake coupling. The full torque M_{full} created by the wind turbine at rotation in a wind stream was defined as the sum of useful torque M_{net} + drag moments of structural elements of the wind turbine and the braking moment during the control mechanism operation, which defined experimentally at various speeds of turbine rotation without blades when V=0.

The maximum power on shaft was obtained at the lowest rotation speeds of the VAWT. The control of blades allows to get a torque on the shaft almost three times superior than the VAWT with blades rigidly fixed, thus almost twice the speed of rotation decreases (Fig. 3, *a*). This is clearly seen in Fig. 3, *b*, where the maximum of power coefficient C_p of the VAWT with controlled blades obtained by tip speed ratio λp = 1.1, and the maximum of power coefficient C_p of the VAWT with blades which are rigidly fixed obtained by λp =

.

2.1. At the same time the power coefficient Cp_{net} of the VAWT with controlled blades almost 1.5 times higher than the same with rigidly fixed blades.

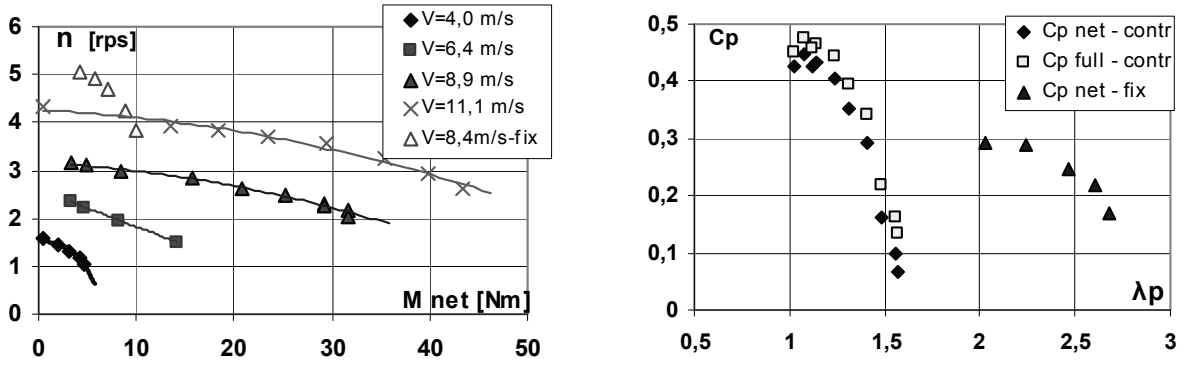

a *b*

Fig. 3. The dependences of the VAWT rotation speed ***n*** from the torque M_{net} on the shaft at various speeds of wind flow V (*a*) and the dependence of the energy coefficient C_p from the value of tip speed ratio λp (*b*) at wind flow V = 9 m / sec ($C_{p-\text{contr}}$–controlled blades, $C_{\text{p}-\text{fix}}$ – fixed blades).

At rigid attachment of blades the angle of the blades placement on the crosspiece was 8°, which agrees with the data obtained at the Institute of McMaster in Canada [9] while purging of the VAWT with sizes l_{blade} x D = 3 x 2.5m (Cp_{full} was received experimentally and was not more than 0.33).

Thus, the use of simple constructive and technological control blades mechanism of the wind turbine with vertical axis allows using it effectively in small (6-8 m/sec) wind speeds, reducing the value of wind load on the wind turbine shaft, and significantly improving the performance characteristics.

Conclusions

The Darrieus type wind turbine with straight controlled blades was designed and was built. The results of turbine tests in wind tunnel approved the efficiency of this turbine as the wind or water energy converter is 1.5 times higher than the best world samples. The electric generator model was composed for wind power unit based on VAWT with controlled blades. The calculated results were compared to experimental results. The mean difference between these results is not higher than 7%.

REFERENCES

1 Sakipova S., Jakovics A. Sail-type wind turbine for autonomous power supply: Possible use in Latvia. *Latvian Journal of Physics and Technical Sciences* No 51(6), 2014, pp. 13-25.

2 Avallone E. A., Baumeister T., Sadegh A. M., Marks Standard Handbook for Mechanical Engineers. 11–th Ed., *McGraw Hill. New York*, 2006, 685p.

3 Kayan V., Dovgy S., Lebid O. Darrieus Water Turbine with Active Control of Blades Prospective Renewable Power Generation Device for Slow Moving Water. *Book of Abstracts of the 6th Conference on Sustainable Development of Energy, Water and Environment Systems*, Dubrovnik, Croatia, 2011, A-217, pp. 376-377.

4 Kayan V., Darrieus Turbine with Controlled Blades: The Perspective Converter of Hydrokinetic Energy. *Open Journal of Renewable Energy and Sustainable Development*, CA, USA, 2014, Vol.1, No.2, pp. 9 – 23.

5 Kayan V., Kochin V., Lebid O., Studying the Performance of Vertical Axis Wind Turbine Models with Control Mechanism of Blades. *Intern. Journal of Fluid Mechanics Research*, USA, 2009, Vol. 36, No. 2, pp. 154 – 165.

6 Kayan V. P., Lebid O. G., Performance optimization of full-scale Darrieus type wind turbine with straight controlled blades. *Applied hydromechanics* (Ukraine), 2010, No. 4, pp. 26 – 35.

7 Cottet G.-H., Koumoutsakos P.D. Vortex Methods: Theory and Practice. *Cambridge U. Press,* 2000, 314p.

8 Gorban I.M., Lebid O.G. Numerical Modeling of the Wing Aerodynamics at Angle-of-Attack at Low Reynolds Numbers. In: Sadovnichiy V. Zgurovsky M. (eds) *Modern Mathematics and Mechanics. Understanding Complex Systems.* Springer, Cham., 2019, pp. 159 – 179.

9 Fiedler A. J., Tullis S., Blade Offset and Pitch Effects on a High Solidity Vertical Axis Wind Turbine. *Wind Engineering*, 2009, Vol. 33, No 3, pp. 237 – 246.

Article accepted for publication 21.10.2020

DOI 10.31489/2020No2/73-77

UDC: 621.311.24

A METHOD FOR INCREASING THE EFFICIENCY OF A WIND TURBINE

Yershina A.K., Sakipova S.E.

[1]Kazakh National Women's Teacher Training University, Almaty, Kazakhstan, 123ainakul.yershina@gmail.com

[2]E.A. Buketov Karaganda University, Karaganda, Kazakhstan, sesaule@mail.ru

The article discusses the possibilities of improving the energy efficiency of wind turbines. A brief analysis of the current state of development of alternative energy, in particular wind energy in Kazakhstan, is considered. The computational study has shown that an increase in the power of a wind - power plant is possible due to the use of a system of simultaneously rotating rotors. A brief description of Bidarrieus-2 wind turbine construction, which can significantly increase the power removed from the wind flow, is given. The possibility of further increasing the efficiency of the Bidarrieus-2 wind turbine by means of a concentrator is discussed. The unique method for the speed controlling of the wind flow with the help of sliding flaps of the guide concentrator in order to improve the performance of the wind turbine at high wind speed is proposed first time.

Keywords: wind power, vertical-axial wind turbine, multy-rotor unit, Bidarrieus-2, wind energy utilization factor.

Introduction

The problems of warming and climate change caused by ever-increasing harmful emissions into the atmosphere have led to a widespread transition from hydrogen energy to the development and implementation of technologies for converting renewable energy sources (RES) [1-5]. Kazakhstan has also made voluntary commitments to reduce harmful carbon emissions to zero by 2050. Our country possesses significant renewable energy resources, which include hydropower, wind and solar energy. The number of renewable energy projects being implemented annually increases.

The highest growth rates of electricity from renewable energy sources excluding large hydroelectric power plants in Kazakhstan were observed in 2011-2016. [1]. Although the growth rates of RES facilities slightly decreased, but continue to grow: by the end of 2017, 58 RES facilities with an installed capacity of 342.3 MW were commissioned, and by the end of 2018, 67 RES facilities with a total installed capacity of 531 MW were in operation, which amounted to an increase in the number by 19% and power by 55% [3]. As of July 1, 2019, 75 renewable energy facilities with a total installed capacity of 683.6 MW were commissioned, of which 16 wind power plants (232 MW), 23 solar photovoltaic plants (250 MW), 34 hydroelectric power plants (200.3 MW) and 2 bioelectric power plants (1.3 MW).

Practice shows that wind energy is the most preferable among the fairly actively introduced renewable energy facilities. Now wind power is one of the fastest-growing renewable energy technologies. Usage is on the rise worldwide, in part because costs are falling.

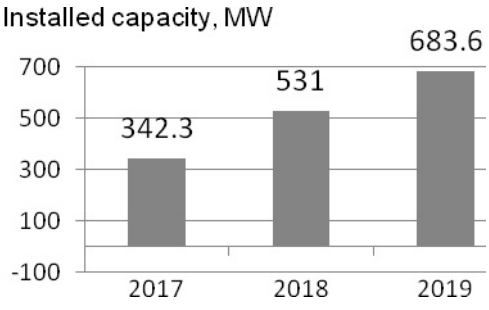

Fig.1. Dynamics of renewable energy facilities in Kazakhstan.

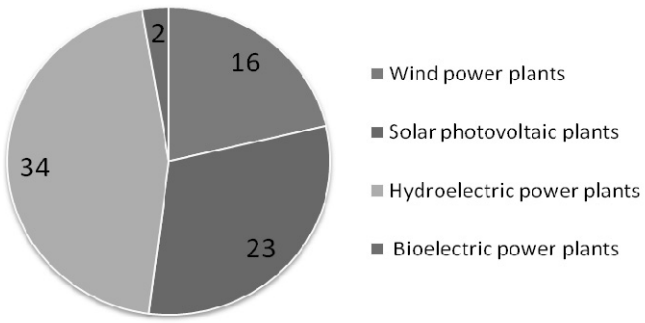

Fig.2. Types of renewable energy facilities in Kazakhstan.

According to [2] the production of wind electricity in 2016 accounted for a 6% of the electricity generated by RES. Wind energy not only in Kazakhstan is actually becoming the basis for both a strategy to reduce greenhouse gas emissions and a rejection of the use of fossil and nuclear energy. According to the official statistical report of the World Wind Energy Association Global Status Report 2020, the total capacity of installed wind turbines in the world reached 651GW by the end of 2019 [3].

Despite the active development of the RES sector in Kazakhstan, there are still problems [4-5]. It should be noted that the emergence and rapid spread of COVID-19, which began in late 2019, turned into a global pandemic by early 2020, leading to a global health and economic crisis. It has also impacted the energy sector around the world. Many parts of the world have strong wind speeds, but the best locations for generating wind power are sometimes remote ones. It is quite possible to solve some problems, for example, training qualified engineering personnel for servicing wind energy facilities, creating a new pricing model in the field of electricity production, etc. But to solve a number of problems, significant capital investments are required from the state and large energy corporations: these include insufficient development of domestic capacities of wind power plants (WPPs), the impossibility of integrating the energy generated by individual WPPs into the general power supply system, and the lack of sufficiently effective technologies for its storage (accumulation). Let us consider some aspects of increasing the efficiency of wind turbines.

1. Energy efficiency of a wind turbine and multy-rotary wind units

It is well known that in the development and creation of any machine an important and main characteristic o f the usefulness of its use is the value of the coefficient of energy conversation efficiency [6-8]. During its operation, it characterizes the ratio of the benefits of using this machine to the required costs: cost, operating costs, operating life, payback, etc. This also applies to the operation of wind power units. Here, the coefficient of energy conversation efficiency of the wind unit is determined by the wind energy utilization factor ξ (WEUF). The higher the ξ value means the more effective the economic and commercial value of the wind turbine. Obviously, the larger the area of the wind wheel swept by the wind, the greater the value of the WEUF should be. Over the past few decades, the scale of wind turbines has increased significantly, this has led to a decrease in the cost of electricity generated [2, 9]. It is necessary to increase the size of the wind turbine in order to reduce the normalized cost of energy. But increasing the power of the turbine by simply increasing the direct dimensions of the blades in practice requires large expenditures for their manufacture, installation and operation. In addition, it is impossible to infinitely increase the size of the blades. Therefore, the researchers propose as an alternative method for solving the problem of increasing the WEUF - to use a system of simultaneously rotating several rotors (two or more), instead of one.

The idea of a multi-rotor installation is not new. At the beginning of 2016, a wind turbine with a capacity of 900 kW was erected at a test site located near Roskilde (Denmark) as part of a research and development project, Fig.3 [9]. This wind turbine, as part of a wind power plant (WPP), was equipped with four V-29-225kW wind turbines with a controlled pitch and a rotor diameter of 29 m. After 2.5-years tests, Vestas company dismantled an experimental 4-rotor wind turbine. The processes of interaction between the wind turbine blades and their effect on the turbine aerodynamics were studied. The influence of multi-rotor speed on the noise level and other wind turbine characteristics were also investigated. The tests carried out by the Danish company confirmed the improvement in the quality of the wind turbine. Preliminary results of studies on a 900-kilowatt wind turbine showed a 1.5% increase in power in relation to annual energy production, compared with a separately rotating rotor [9]. It was found that the 4-rotor version of the installation has the property of a faster leveling of the vortex wake behind the wind generator, which in a real situation means the possibility of installing the turbines at a closer distance relative to each other. Probably it's the result of the overlapping of the perimeters of the rotors, which is equal in area to two perimeters of a single-rotor turbine for the same swept area.

The relevance of this direction of innovation and technology modernization for vertical-axis wind turbines is confirmed by a number of publications [10 - 14]. In [10], the authors studied the dynamics of the vortex flow on the basis of numerical simulations in order to compare the flow characteristics in the wake of a multi-rotor wind turbine with the characteristics of a single rotor turbine. In numerical experiments [10], it was found that the wake of a multi-rotor turbine recovers faster at short distances downwind. In [11], the aerodynamics of a double vertical-axial wind turbine with a deflector is studied. The performance of the system was quantified by aerodynamic tests followed by 3D fluid dynamics simulations. Thus, to meet the

need for increasing power, the creation of multi-rotor wind generators becomes a promising alternative to massive single-rotor wind generators.

a

b

Fig.3. «Vestas» multi-rotor wind farm:
a) main view of a 4-rotor wind turbine; b) experimental wind turbine test farm [9].

In Kazakhstan, combined vertical-axial devices with two coaxially located rotation shafts were first developed more than 20 years ago by a group of scientists [7, 8]. As a result of calculations and tests, three versions of two-rotor wind turbines have been proposed: Darrieus type, Bidarrieus-1, Bidarrieus-2. The most effective is the third version of the Bidarrieus-2 wind turbine, the fundamental feature of which is that its swing is not rectilinear, but L-shaped in the form of two half swings connected to each other on one of the shafts [7, 15]. The uniqueness of this design is that the power taken by two DC electric generators is summed up. For centering, coaxially mounted rotation shafts are separated from each other by support bearings, which makes it possible for their independent rotation: both coordinated in the same direction, and opposite. The rotor blades can be made in the form of NASA symmetrical wing profiles. This design, together with the HBI rotor, allows you to get almost 2 times more streamlined area than a conventional Darrieus windmill. So, the amount of wind energy used by wind turbines with HBI rotor doubles [15].

Laboratory tests and calculations have shown that such a constructive solution significantly increases the value of WEUC, and, accordingly, the practical efficiency and commercial viability of wind turbines [16]. The tests of the laboratory sample and calculations have shown that such a constructive solution significantly increases the value of WEUC, and, accordingly, the practical efficiency and commercial feasibility of wind turbines [7]. The autonomy of the shaft rotation of the carousel type wind turbine allowing energy to transfer each working blade to two different generators, thus increasing the total energy received, i.e. increase the value of the ξ coefficient.

The developed semi-industrial Bidarrieus wind turbine with a 5 kW HBI-rotor showed the need for its placement at a certain height [8, 16]. Outside the surface boundary layer where wind speeds are 2-2.5 times higher than the average wind speed in the surface boundary layer. Due to the cubic dependence of the wind turbine power on wind speed, the location of the wind turbine outside the surface boundary layer (20-30 m) will lead to a several-fold increase in the power of the wind turbine. The torque and power are determined by loading the pulley with calibrated loads mechanically by the friction method [6]. With varying degrees of loading the wind turbine, the number of shaft speed is measured using an electronic tachometer. The speed of the wind turbine is determined by the number of shaft. The torque M created by the wind turbine is determined by the well-known correlation of the theory of similarity:

$$M = m \cdot \frac{\rho V^2}{2} \cdot S \cdot R,$$

where *m* is the dimensionless coefficient of torque, $\frac{\rho V^2}{2}$ is the dynamic pressure of the incoming flow, U is the flow velocity (determined by two calibrated anemometers), ρ is the air density, S is the swept area, R is the radius of the turbine and H is its height.

.

From the calculated values of the torque and speed of the wind turbine, the values of the wind energy utilization coefficients are determined:

$$\xi = m \cdot \chi,$$

where χ is tip speed ratio.

Then, the dependence of ξ on speed for different wind turbine models is built and a comparative analysis of wind turbines is carried out.

2. A method further increasing the efficiency of two-rotor wind turbine using a concentrator.

For the purpose of increase in wind speed operating in a windmill the concentrator of wind energy is offered. In Fig. 4 the design of Bidarrieus-2 with the wind power concentrator is shown in axonometric. As shown in figure 5 the motionless concentrator represents a system of convergent guides located in a uniform fantail around the windmills. To increase the velocity of wind acting on the wind power unit, a concentrator of wind energy is proposed.

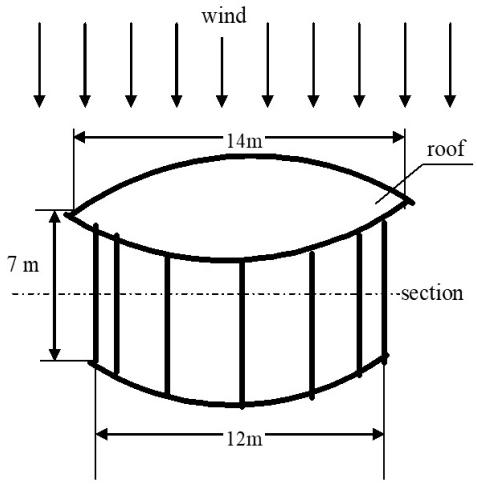

Fig. 4. Wind power concentrator design.

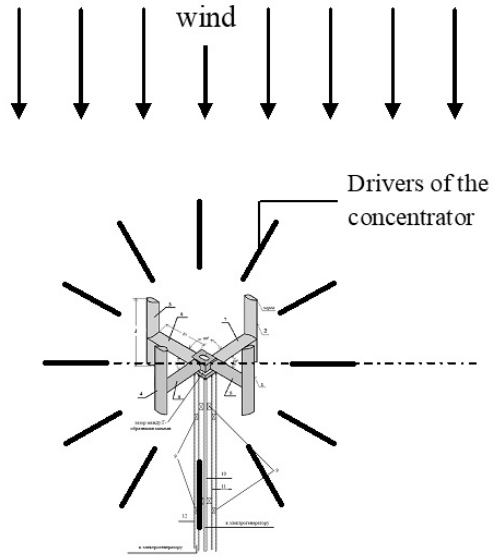

Fig.5. General view of Bidarrieus-2 with wind power concentrators.

A concentrator is a system of converging guides positioned as a uniform fan around wind power units. The sizes of guiding concentrators in this case allow increase more than twice the velocity of wind flow acting on the unit at any direction of wind. For six-meter Bidarrieus-2 the diameter of total area taking into account the concentrator is equal to 14 m. The total height is 7 - 8 meters. All this construction is protected by a roof with a small cone angle [15]. Diameter of this roof is at 1 and 2 meters more than diameter of whole construction. Let's enter acceleration factor of a wind stream in concentrator as the relation

$$\varkappa = \frac{U_1}{U_2},$$

where:

U_1 – speed at the entrance of the wind stream in concentrator,

U_2 – exit speed from concentrator.

The guides of concentrator consist of two flaps which can open as a book. The material of guides must be from dielectrics and must conduct heat well. To the internal side of each flap, tans are pasted which heat the guides and in winter protect the whole construction from wet snow-drift. It's an effective method of additional regulation of speed of a wind stream by means of moving apart flaps concentrator guides. Devices for directing can perform one more function. You can reveal them and regulate the wind speed, which is acting on the wind turbine. The movement of the leaflets is controlled by the axes of rotation like on the "book binding".

Conclusion

Two-rotory Bidarrieus-2 wind turbine was proposed first time in Kazakhstan. A vertical-axis wind turbine is the most promising converter of wind energy, especially in conditions of rapid changes in wind speed and direction. The relevance and necessity of developing this wind turbine is also justified by the fact that its use for generating electricity is beneficial and economical for decentralized regions and in remote places. In addition, the double-rotor wind turbine of the carousel type Bidarrieus-2 has a low rotation speed. This allows it to work at high wind speeds, and the service life is practically unlimited. All this makes it important and necessary to carry out full-scale tests of these WPPs in order to ensure their industrial production in the future.

REFERENCES

1 Development of green energy in Kazakhstan. 19.09.2018. Available at: https://eenergy.media/2018 / 09/19 / razvitie-zelyonoj-energetiki-v-kazahstane /

2 Wind Energy Data. International Renewable Energy Agency (IRENA). Available at: https://irena.org/wind

3 Renewable Energy 2020. Statistical Global Status Report. Available at: https://www.ren21.net/reports/global-statusreport

4 Mukhamadiev IR, et al. Multi-criteria spatial decision-making system to support the development of RES in Kazakhstan. *IEEE Access*, 2019, Vol. 7, pp. 122275 – 122288.

5 Zhunusova G. Zh. et al. Renewable energy in Kazakhstan: challenges and prospects. *International Energy Journal*. 2020, pp. 311 – 324.

6 Bezrukikh P.P. *Ispol'zovanie energii vetra.(Wind power use)*. Moscow, 2008, 196 p. [in Russian]

7 Yershin Sh., Yershina A.K About High efficiency of two-rotor wind power unit Bidarrieus-2. *Eurasian Physical Technical Journal*. 2019, No. 1(31), pp. 82 – 87. DOI 10.31489/2019No1/82-87

8 Yershina A.K., Sakipova S.E., Manatbayev R.K. Some desing featurs of the carousel type wind turbine Bidarrieus. *Eurasian Physical Technical Journal*. 2019, No. 2(32), pp. 63 – 67. DOI: 10.31489 / 2019No2 / 63-67.

9 Eize de Vries. Vestas tests four-rotor concept turbine. 04/20/2016. Available at: www.windpowermonthly.com /article/ 1391775/ exclusive-vestas-tests-four-rotor-concept-turbine

10 Mosfequr Rahman, et al. Numerical and Experimental Investigations on Vertical Axis Wind Turbines of Different Models. *Open Access Library Journal*. 2017, Volume 4, e3273. DOI: 10.4236/oalib.1103273

11 Yichen Jiang, Peidong Zhao, Thorsten Stoesser, Kun Wang, Li Zou. Experimental and numerical study of dual vertical-axis wind turbines with a deflector. *Energy Conversion and Control*. 2020, Vol. 209, pp. 112588. https://doi.org/10.1016/ j.enconman.2020.112588.

12 Ahmedov A., Ebrahimi K. M. Numerical Modelling of an H-type Darrieus Wind Turbine Performance under Turbulent Wind. *American Journal of Energy Research*. **2017**, Vol.5(3), pp. 63 – 78. DOI: 10.12691/ajer-5-3-1

13 Longhuan Du, Ingram, Grant Dominy R. A review of H-Darrieus wind turbine aerodynamic research. *Journal of Mechanical Engineering Science*. 2019, Vol. 233, Issue (23-24), pp.7590-7616.

14 Kayan V.P., Kochin V.A., Lebid O.G. Studying the Performance of Vertical Axis Wind Turbine Models with Blade Control Mechanism. Intern. *Journal of Fluid Mechanics Research*, 2009, Vol.36, Issue 2, pp. 154 – 165.

15 Yershina A.K., Yershin Sh., Yershin Ch.Sh. Manatbaev R.K. *Wind turbine*. Patent KZ. Reg. No. 2016/0337.1. Bul. No. 15. Publ. 04/11/2016.

16 Yershina A.K., Manatbayev R.K., Sakipova S.E., Kalasov N.B. Improving the efficiency of wind turbine. *Proceeding of the 2nd Intern. Scient. Conf. "Alternative Energy Sources, Materials & Technologies (AESMT'19)*, Sofia, Bulgaria. 2019, Vol. 1, pp. 89 – 90.

Article accepted for publication 25.11.2020

DOI 10.31489/2020No2/78-86

UDC 621.577+697.1

THE HEAT PUMP SYSTEM FOR VENTILATION AND AIR CONDITIONING INSIDE THE PRODUCTION AREA WITH AN EXCESSIVE INTERNAL MOISTURE GENERATION

Bezrodny M.K., Misiura T.O.

National Technical University of Ukraine "Igor Sikorsky Kyiv Polytechnic Institute", Kyiv, Ukraine, Sconosciuto.T@gmail.com

The paper studies application feasibility and energy efficiency of the ventilation and air conditioning heat pump system for maintaining comfort conditions inside the production area with an excessive internal moisture generation during the warm season. In this regard, a thermodynamic analysis of a heat pump system with a partial exhaust air recirculation and a variable ratio of fresh outside air was carried out. Numerical analysis was then done to estimate the influence of changes in the environment temperature and relative humidity and the characteristics of the ventilation and air conditioning object on the system parameters. This allowed to determine potential capabilities of this system to maintain comfortable conditions in the production area. It was also shown that the required additional cooling of the supply air at the entrance to the premise for air conditioning demands can be determined by a simple coefficient and its calculation method is provided in the article. The heat pump system of temperature and humidity maintenance has the highest energy efficiency in the zone of relatively low environment temperatures and largely depends on the relative humidity of the outside air. This suggests that the studied system is suitable for application in countries with temperate continental climate.

Keywords: heat pump system, ventilation, air conditioning, refrigeration efficiency, recirculation, comfortable conditions, production area, temperate continental climate.

Introduction

The trend of increasing energy resources costs for final consumers makes it vital and primary to constantly enhance the efficiency of equipment and to find new ways and methods of utilising low-potential energy in order to replace traditional heat sources, which involve the combustion process of expensive and limited fossil fuels [1].

Nowadays systems with heat pumps (HP) are considered to be an alternative energy source for heat supply. They are widely used for ventilation and air conditioning of various objects, among which predominant are those that require maintenance of not only temperature but also humidity conditions indoors due to excessive internal moisture generation [2]. Examples of such objects may be shopping centres, sports facilities as well as production, storage and sorting facilities with required specific technological and comfort conditions. Removal of excess moisture from such premises is normally done with the exhaust ventilation. Maintenance of set parameters (temperature and humidity) of air inside a premise during the warm season can be achieved by supply air pre-treatment in a heat pump system (HPS) [3]. The implementation of HP in such systems has some features, since the dried air after the HP evaporator needs to be heated up to a set temperature at the entrance to a premise, which can be organised in different ways. One of them is by mixing of one air flow cooled down in the HP evaporator with another air flow heated up in the HP condenser [4]. The energy efficiency of such HPS increases due to the partial recirculation of the exhaust air and thus due to the partial utilisation of the cold produced by this HPS. However, the analysis performed in [4] concerns the system operation in terms of premise ventilation only without external and internal entrance of heat, i.e. in conditions without air conditioning.

In this regard, the authors propose and analyse the basic ventilation and air conditioning HPS of the production area with an excessive internal moisture generation during the warm season. To ensure set air parameters indoors and considering the internal heat generation as well as the entrance of heat through enclosing structures a method to calculate the required supply air supercooling was developed. It is shown that the additional cooling of the supply air required for the air conditioning can be determined by a simple coefficient which is proportional to the temperature difference of air outside and inside a premise and which

is defined by the premise constructional properties along with its required air exchange rate and internal heat generation. The thermodynamic analysis of the HPS was carried out taking into account the additional supercooling of the supply air for air conditioning. The purpose of the analysis is to determine air parameters at nodal points of the system and to define conditions under which supply air parameters can be maintained by changing recirculation and fresh air flows. As a result of the study the energy efficiency and HPS operation modes during the warm season were determined depending on the ambient air parameters and the properties of the production area where ventilation and air conditioning are required.

*Purpose and tasks***.** The purpose of the article is the analysis of the ventilation and air conditioning HPS energy efficiency in order to maintain comfort conditions inside the production area with an excessive internal moisture generation during the warm season by using a variable ratio of fresh outside air depending on its parameters.

1. Description of the ventilation and air conditioning HPS and the ventilation air workflow process

A schematic drawing of the ventilation and air conditioning HPS with a partial exhaust air recirculation and a variable ratio of fresh outside air is shown in Fig. 1. The following designations are used: C_{HP} – a heat pump condenser; E_{HP} – a heat pump evaporator; C – a compressor; MC – a mixing chamber; OVAC – an object of ventilation and air conditioning. This HPS was previously designed and studied in work [4]. However, the subject of the current article is to assess operating mode of this HPS not only for ventilation demands but also for air conditioning during the warm season. The system operation principle is as follows: fresh outside air at a temperature t_0, a moisture content d_0 and with a mass flow rate G_0 is supplied to the HP evaporator where it is cooled with a partial water vapour condensation up to a temperature t_{ev} and a moisture content d_{ev}. The exhaust air from the premise at a temperature t_2, a moisture content d_2 and with a mass flow rate G_{tot} is supplied to the HP condenser where it is heated to a temperature t_{ex} at the constant moisture content d_2. Heated exhaust air is then divided into two flows: one flow with a mass flow rate G_0 is discharged into the environment; the second flow is fed to the mixing chamber where it is mixed with the cooled outside air after the HP evaporator. The resulting air mixture (t_1, d_1, G_{tot}) after the mixing chamber is supplied to the production area for ventilation and air conditioning demands (to compensate the entrance of heat through enclosing structures and internal heat generation). The ventilation air workflow process, which indicates different air conditions inside the studied system, can be presented using the *h-d* diagram and it is shown in Fig. 2. Point *O* describes a condition of the ambient air (t_o, h_o) [5].

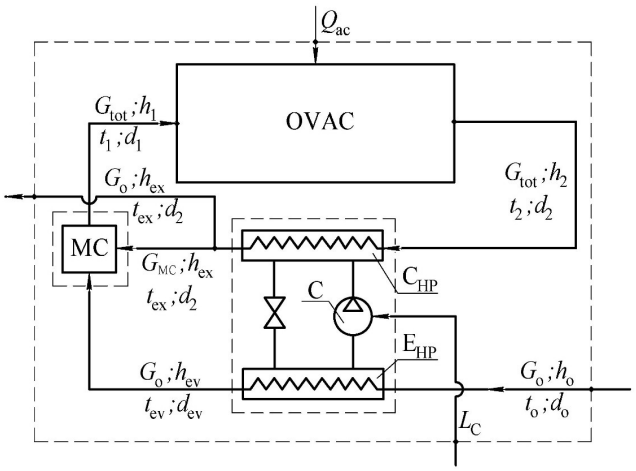

Fig. 1. A general design of the ventilation and air conditioning HPS inside a premise with an excessive internal moisture generation.

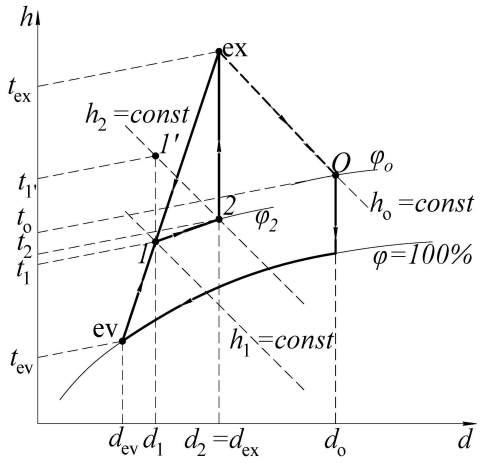

Fig. 2. The ventilation air workflow process inside the studied system presented using the *h-d* diagram.

Point *2* is set according to the required temperature t_2 and the relative humidity φ_2 of the air inside the production area. It is determined as provided by [6] depending on the premise technological purpose. Using the *h-d* diagram h_2 is defined. According to the building standards [6] the value of additional supply air heating Δt_v for the given premise is defined and using the temperature $t_{1'} = t_2 + \Delta t_v$ the point *1′* is obtained on

the line h_2 = const. This point corresponds to the supply air state for ventilation demands only. The process *1'-1* depicts the additional supply air cooling in order to meet air conditioning demands. Air temperature at point *1* on the line $d_{1'}$ = const can be defined based on the relationship between the temperature difference which corresponds to the additional supply air cooling at the entrance to a premise and the temperature difference of air outside and inside the premise, i.e.

$$\Delta t = t_{1'} - t_1 = K(t_0 - t_2),$$

where K is a proportion coefficient that depends on external and internal entrances of heat.

The exhaust air with parameters at point *2* is heated in the HP condenser to a temperature t_{ex} at the constant moisture content d_2. One flow is discharged into the environment and the second flow is mixed with the outside air cooled in the HP evaporator (point ev) creating an air mixture at point *1* with a moisture content $d_{1'} = d_1$ and a temperature t_1 which is then supplied to the production area for ventilation and air conditioning demands. Process *1-2* corresponds to the workflow process of air condition change inside the premise.

2. Determination of the supply air temperature at the premise entrance

The relationship between the additional cooling of the supply air to meet air conditioning demands and the temperature difference of air outside and inside a premise can be estimated in the following way

$$\Delta t = t_{1'} - t_1 = K(t_0 - t_2), \quad (1)$$

where K – a proportion coefficient that depends on external and internal entrances of heat.

The additional cooling of supply air Δt can also be presented as

$$\Delta t = \Delta t_1 + \Delta t_2, \quad (2)$$

where Δt_1, Δt_2, ºC – additional cooling of supply air to compensate external and internal entrances of heat respectively.

Additional cooling Δt_1 can be written by analogy to the equation (1), and Δt_2 can be expressed from the heat energy demands equation for air conditioning (to compensate internal heat generation). Considering this the equation (2) takes form

$$\Delta t = K_1(t_0 - t_2) + \frac{Q_{\text{int}}}{G_{\text{tot}} c_{\text{p}}}, \quad (3)$$

where K_1 – the proportion coefficient which depends on the premise constructional properties and needs to be determined.

Equating expressions (1) and (3) and dividing them by the temperature difference $(t_0 - t_2)$, the following is obtained

$$K = K_1 + K_2, \quad (4)$$

where $$K_2 = \frac{Q_{\text{int}}}{G_{\text{tot}} c_{\text{p}} (t_0 - t_2)}. \quad (5)$$

In order to determine coefficient K_1 the next equations to calculate required heat energy demands for ventilation and air conditioning (to compensate external entrance of heat) should be written down

$$Q_{\text{v}} = G_{\text{tot}}(h_0 - h_1), \quad (6)$$

$$Q_{\text{ac}} = G_{\text{tot}} c_{\text{p}} (t_{1'} - t_1). \quad (7)$$

From equations (6) and (7) considering previously expressed additional cooling Δt_1 the following can be written

$$K_1 = \frac{Q_{\text{ac}}}{Q_{\text{v}}} \frac{(h_0 - h_1)}{c_{\text{p}}(t_0 - t_2)}. \quad (8)$$

On the other hand, the entrance of heat through enclosing structures and heat consumption for ventilation can be defined as:

$$Q_{\text{ac}} = \bar{K} F (t_0 - t_2), \quad (9)$$

$$Q_{\text{v}} = G_{\text{v}}(h_0 - h_1), \tag{10}$$

where $\bar{K}$, W/(m^2·ºC) – an average heat transfer coefficient of production area enclosure structures; F, m^2 – an area of enclosure structures through which heat enters to the production area; G_{v}, kg/s – an air mass flow rate for ventilation system demands.

The air mass flow rate G_{v} can be calculated depending on a production premise volume V_{prem} and an air exchange rate $K_{\text{a.ex}}$, 1/h, using the relationship

$$G_{\text{v}} = \rho_{\text{a}} V_{\text{prem}} \frac{K_{\text{a.ex}}}{3600}, \tag{11}$$

where ρ_{a} – air density.

From equations (9) and (10) considering (11) the expression for $Q_{\text{ac}} / Q_{\text{v}}$ can be defined as

$$\frac{Q_{\text{ac}}}{Q_{\text{v}}} = \frac{3600\bar{K}F(t_0 - t_2)}{\rho_{\text{a}} K_{\text{a.ex}} V_{\text{prem}} (h_0 - h_1)}. \tag{12}$$

Then the expression of the proportion coefficient according to the equation (8) and considering (12) assumes the following form

$$K_1 = \frac{3600\bar{K}F}{\rho_{\text{a}} c_{\text{p}} K_{\text{a.ex}} V_{\text{prem}}}. \tag{13}$$

Thus, the proportion coefficient K in the equation (1) can be predetermined by coefficients K_1 and K_2. These coefficients are determined by geometric and thermophysical characteristics of a building and the air exchange rate which is determined by the functional purpose of the air conditioning object (coefficient K_1) as well as by internal heat generation within the building (coefficient K_2). The supply air temperature t_1 at the entrance to the production area can be derived from the equation (1) respectively.

3. The thermodynamic analysis of the HPS

The thermodynamic analysis of the studied system is performed based on the preliminary determination of its thermodynamic state depending on the initial set indoor air parameters and the change of ambient air parameters. The ventilation and air conditioning system state in turn depends on the yet unknown air parameters at system's nodal points. The unknown parameters of this system are the ratio of the fresh outside air flow rate supplied to the HP evaporator, air temperatures after the HP evaporator and condenser, the value of the system's refrigeration efficiency. The corresponding relationships for these parameters can be determined from the equations of thermal and material balances of both individual elements inside the system and the system as a whole. The fresh outside air enthalpy at the outlet of the HP evaporator can be determined from the thermal balance equation of the mixing chamber which has the following expression

$$G_0 h_{\text{ev}} + G_{\text{MC}} h_{\text{ex}} = G_{\text{tot}} h_1, \tag{14}$$

where G_0, G_{MC}, G_{tot}, kg/s – mass flow rates of the fresh ambient, the heated exhaust and the total air flows; h_{ev}, h_{ex}, h_1, kJ/kg$_{\text{d.a.}}$ – enthalpies of the corresponding air flows.

After dividing left and right parts of the expression (14) by the value G_{tot} it can be written

$$K_0 h_{\text{ev}} + (1 - K_0) h_{\text{ex}} = h_1, \tag{15}$$

where K_0 – the ratio of fresh outside air for ventilation demands.

The enthalpy h_{ev} which is derived from the equation (15) takes form of

$$h_{\text{ev}} = \frac{h_1 - (1 - K_0) h_{\text{ex}}}{K_0}. \tag{16}$$

The fresh outside air moisture content at the outlet of the HP evaporator can be determined from the material balance equation of the moisture content for the whole system which has the following expression

$$G_{\text{tot}}(d_2 - d_1) + G_0 d_0 = G_0 d_2 + G_0 (d_0 - d_{\text{ev}}). \tag{17}$$

.

After dividing left and right parts of the expression (17) by the value G_{tot} and after a few mathematical transformations the following is obtained

$$d_{\text{ev}} = d_0 - \frac{K_0(d_0 - d_2) + (d_2 - d_1)}{K_0}. \quad (18)$$

The air temperature at the outlet of the HP evaporator, t_{ev}, can be determined using the *h-d* diagram for moist air at the intersection point of the curve φ=100% with h_{ev} or d_{ev}.

The HP energy balance equation can be used to determine the ratio of fresh outside air for ventilation demands

$$Q_{\text{c}} = Q_{\text{ev}} + L_{\text{c}}. \quad (19)$$

The components of the equation (19) are defined as follows:

the heat flow from the HP condenser

$$Q_{\text{c}} = G_{\text{tot}}(h_{\text{ex}} - h_2); \quad (20)$$

the heat flow to the HP evaporator

$$Q_{\text{ev}} = G_0(h_0 - h_{\text{ev}}); \quad (21)$$

external electricity expenses for the HP compressor

$$L_{\text{c}} = Q_{\text{ev}} / \varepsilon_{\text{HP}}, \quad (22)$$

where ε_{HP} – the HP refrigeration efficiency.

After a few mathematical transformations, the expression to determine the ratio of fresh outside air for ventilation demands takes form of

$$K_0 = \frac{h_{\text{ex}} - h_2}{h_0 - h_{\text{ev}}} \frac{\varepsilon_{\text{HP}}}{\varepsilon_{\text{HP}} + 1}. \quad (23)$$

The operation efficiency of a HP, which works as a refrigeration machine in the air conditioning mode, in this case can be estimated by the value of the HP refrigeration efficiency

$$\varepsilon_{\text{HP}} = \frac{1}{\frac{273 + t_{\text{ex}} + \Delta t_{\text{c}}}{273 + t_{\text{ev}} - \Delta t_{\text{ev}}} - 1}, \quad (24)$$

where t_{ev} – the fresh outside air temperature at the outlet of the HP evaporator, °C; t_{ex} – the exhaust air temperature at the outlet of the HP condenser, °C; Δt_{ev} – the temperature difference between the outside air flow and the refrigerant at the outlet of the HP evaporator, °C; Δt_{c} – the temperature difference between the refrigerant and the exhaust air flow at the outlet of the HP condenser, °C. Numerical values of temperature differences in the condenser and the evaporator for an air-to-air HP type are given in the literature. According to [7] it is possible to assume that $\Delta t_{\text{c}} = \Delta t_{\text{ev}} = 10$ °C for the HP condenser and the HP evaporator respectively.

The HP refrigeration efficiency in this study is estimated for ideal reversed Carnot cycle which considers only heat irreversibilities inside HP evaporator and condenser due to the existing temperature differences Δt_{ev} and Δt_{c}. Real processes which a working medium undergoes inside a HP are not reviewed for several reasons. First, since a HP operates as a refrigeration machine the temperature difference between its surfaces and the environment is less during the warm season comparing to winter period when a HP works to provide heating demands. With lower heat losses the efficiency of HP operation increases. Second, this assumption was made to compare results with the previous study [4] which was also carried out for ideal refrigeration cycle.

The exhaust air enthalpy at the outlet of the HP condenser can be determined from the thermal balance equation of the whole system which has the following expression including the entrance of heat through enclosing structures

$$G_0 h_0 + L_{\text{c}} + Q_{\text{ac}} = G_0 h_{\text{ex}}. \quad (25)$$

After dividing left and right parts of the expression (25) by the value G_{tot} and considering equation (1) in Q_{ac}, the following can be obtained

$$h_{ex} = h_0 + (h_0 - h_{ev})\frac{1}{\varepsilon_{HP}} + \frac{c_p K(t_0 - t_2)}{K_0}. \quad (26)$$

The air temperature at the outlet of the HP condenser, t_{ex}, can be determined using the *h-d* diagram for moist air at the intersection point of h_{ex} with the moisture content indoors d_2. Enthalpy h_1 can be determined by the following formula for a moist air with enough accuracy [5]

$$h_1 = 1.005t_1 + (2500 + 1.8t_1)d_1. \quad (27)$$

The HP refrigeration efficiency, as well as the HP coefficient of performance (COP), only depends on the operating conditions of the HP itself, i.e. the temperature level of heat transfer processes in the HP evaporator and condenser. Therefore, to characterise the efficiency of the whole HPS it is more appropriate to use a complex value (system refrigeration efficiency), which can be presented in the following way

$$\varepsilon_S = \frac{Q_{cold}}{L_c}, \quad (28)$$

where Q_{cold}, kW – the refrigeration capacity at the entrance to the premise.

It is determined as

$$Q_{cold} = G_{tot}(h_0 - h_1). \quad (29)$$

Considering equations (21), (22) and (29), the expression (28) can be written as follows

$$\varepsilon_S = \frac{\varepsilon_{HP}(h_0 - h_1)}{K_0(h_0 - h_{ev})}. \quad (30)$$

4. Numerical analysis of the HPS for ventilation and air conditioning

Numerical analysis of the HPS for ventilation and air conditioning is done for a typical production area with an excessive internal moisture generation. Roshen Confectionery production workshop in Kyiv region was selected as the prototype [8]. In order to ensure comfortable working conditions the following indoor air parameters were set in the workshop [6]: the premise temperature t_2 = 18 °C; the premise relative humidity φ_2 = 50 %; the additional heating of the supply air for the ventilation purposes Δt_v = 3 °C.

Under the given conditions the air moisture content at the inlet and outlet of the premise was determined. These are the points *1* and *2* respectively on the diagram in Fig. 2: d_1 = 5.3 g/kg$_{d.a.}$ and d_2 = 6.5 g/kg$_{d.a.}$. Numerical analysis using the equations (16), (20), (23), (24), (26), (27) and (30) and the method of successive approximations allows to estimate the influence of changes in the environment temperature and relative humidity and the characteristics of the ventilation and air conditioning object on the system parameters (air temperatures at the outlet of the HP evaporator and condenser (Fig. 3), the ratio of fresh outside air (Fig. 4), the HP refrigeration efficiency (Fig. 5)) and the thermodynamic efficiency of the ventilation and air conditioning system (Fig. 5). The chosen calculation method of analysing HPS in its different conditions consists of iteration cycles in the whole range of atmospheric air parameters and with different building characteristics. Iterations complete when the condition of relative deviation is achieved. In this case we consider two parameters (h_{ev} and K_0) which should have a difference between their values after and before an iteration cycle not exceeding 0.5 % for K_0 and 0.06 % for h_{ev}.

When choosing the value *K*, the following has been assumed. According to the equation (4) and considering (13) for the selected production premise it was calculated that *K* = 0.23 (a proportion coefficient depending on external and internal entrances of heat). The obtained value is correct since ventilation expenses can be several times higher than the corresponding entrance of heat for industrial and public buildings [9]. Therefore, the following values of this coefficient were considered *K* = 0.1; 0.2; 0.3; 0.4; 0.5.

Fig. 3, a-b shows graphical relationships between air flow temperatures at the outlet of the HP condenser and evaporator, the environment temperature and relative humidity and different values of *K* (t_{ex}, $t_{ev} = f(t_0, \varphi_0, K)$). The case when *K* = 0 (plots 11 and 12) corresponds to the absence of air conditioning which was described in work [4]. Temperature t_{ex} is limited by a critical value at which normal operation of the HP condenser is still possible. It is seen that application conditions of this system deteriorate with increasing environment relative humidity. Thus, the application range of this system is from t_0 = 25 °C (φ_0 = 80 %) to t_0 = 33 °C (φ_0 = 40 %). This suggests that this HPS is suitable for application in countries with

temperate continental climate. Temperatures t_{ev} at $t_0 > 25$ °C almost do not depend on environment relative humidity φ_0 and temperature t_0 and average 4 °C. However, the difference between them is greater the lower the values of φ_0 and t_0 are.

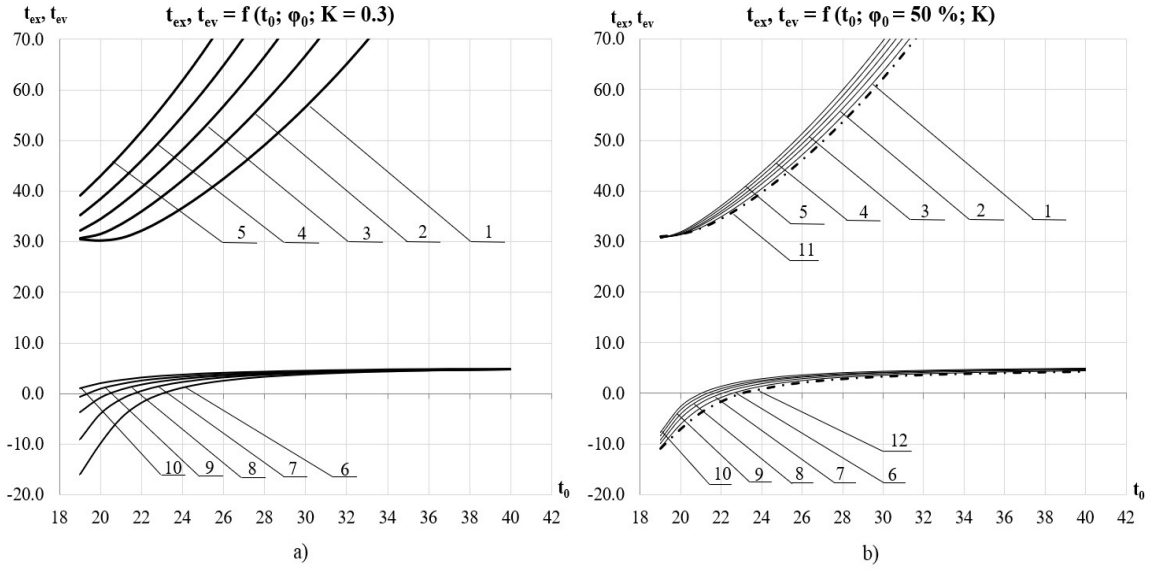

Fig. 3. Graphical relationships between air temperatures at the outlet of the HP condenser and evaporator, the environment temperature and relative humidity and the coefficient K: a) K = 0,3; t_{ex}: 1 – φ_0 = 40 %; 2 – 50 %; 3 – 60 %; 4 – 70 %; 5 – 80 %; t_{ev}: 6 – φ_0 = 40 %; 7 – 50 %; 8 – 60 %; 9 – 70 %; 10 – 80 %; b) φ_0 = 50 %; t_{ex}: 1 – K = 0.1; 2 – 0.2; 3 – 0.3; 4 – 0.4; 5 – 0.5; 11 – 0; t_{ev}: 6 – K = 0.1; 7 – 0.2; 8 – 0.3; 9 – 0.4; 10 – 0.5; 12 – 0.

An important characteristic of this system is the fresh outside air flow rate ratio at the entrance to the system, K_0, which is supplied to the HP evaporator. The corresponding calculated data for the variable fresh air ratio obtained by the equation (23) are shown in Fig. 4. Plot 6 shows HPS that maintains only ventilation demands [4]. As can be seen from the plots, the variable ratio of fresh outside air to fulfill the requirement of maintaining set comfortable air parameters in the premise must vary depending on both the temperature t_0 and the relative humidity φ_0 of the ambient air. At a constant temperature t_0 the need for fresh air increases with the increase of both relative humidity φ_0 and the coefficient K, i.e. entrance of heat to the premise. As φ_0 increases, the enthalpy h_0 increases as well. This leads to an increase of the exhaust air temperature t_{ex} at the outlet of the HP condenser. As a result, a larger ratio of fresh air at higher relative humidity φ_0 is supplied to the mixing chamber. Therefore, the design of HPS for ventilation and air conditioning should be done with the variable fresh air supply, because otherwise the system will not be able to provide required conditions inside the premise depending on changes in environment parameters.

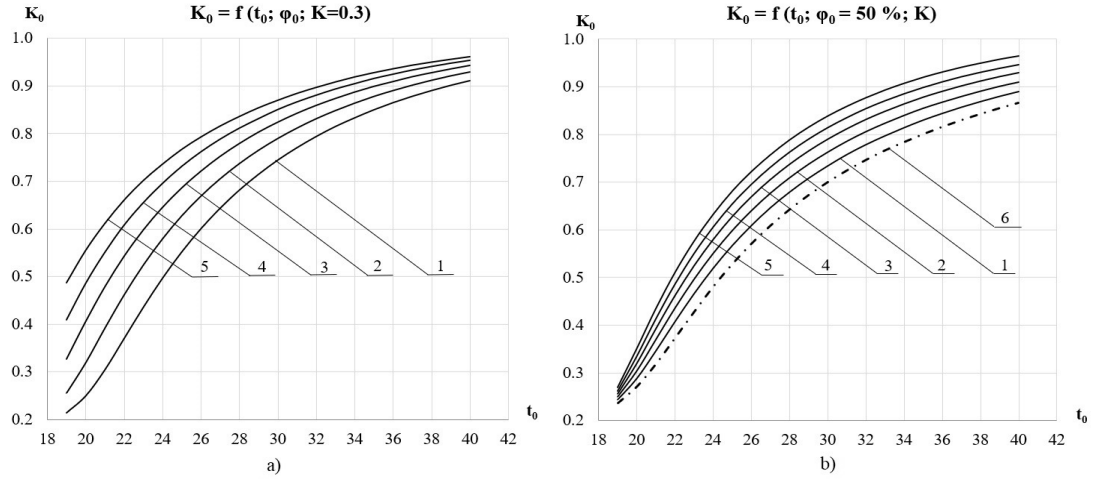

Fig. 4. Graphical relationships between the variable ratio of fresh outside air, the environment parameters and the coefficient K: a) K = 0.3; 1-5 – φ_0 = 40 - 80 %; b) φ_0 = 50 %; 1-5 – K = 0.1 – 0.5; 6 – K = 0.

Based on the numerical analysis of equations (24) and (30) graphical relationships between HP and HPS refrigeration efficiencies, the environment temperature and relative humidity and different values of the coefficient K were obtained ($\varepsilon_{HP}, \varepsilon_S = f(t_0, \varphi_0, K)$) (Fig. 5, a-b). Again plots 11 and 12 are for $K = 0$. The HP refrigeration efficiency is characterised by high values in the range of moderate temperatures $t_0 = 20$ - 30 °C.

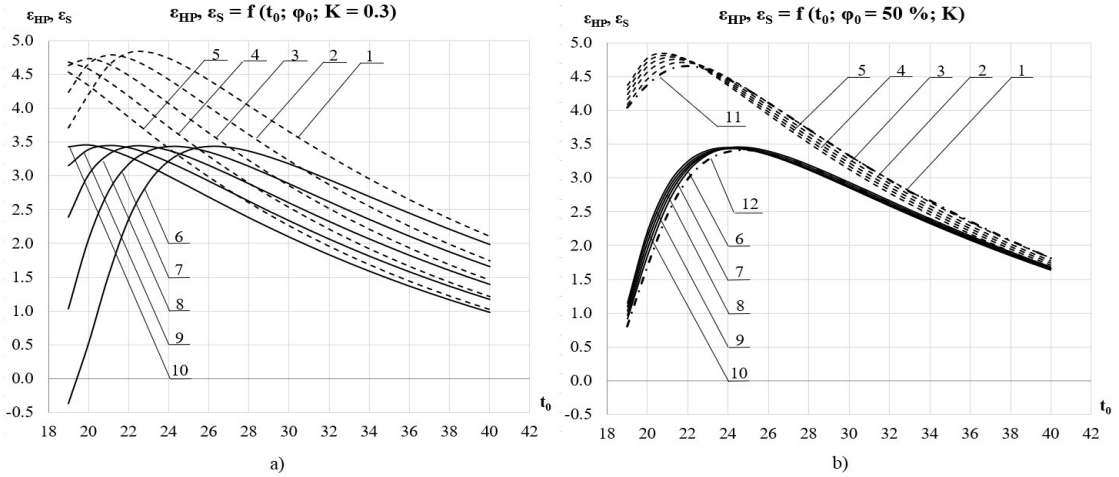

Fig.5. Graphical relationships between HP and HPS refrigeration efficiencies, the environment parameters and the coefficient K: a) $K = 0.3$; ε_{HP} : 1-5 – $\varphi_0 = 40$ - 80 %; ε_S : 6-10 – $\varphi_0 = 40$ - 80 %; b) $\varphi_0 = 50$ %; ε_{HP} : 1-5 – $K = 0.1 - 0.5$; 11 – $K = 0$; ε_S : 6-10 – $K = 0.1 - 0.5$; 12 – $K = 0$.

It decreases significantly with the further growth of t_0 as well as with the increasing relative humidity φ_0. Plots show that the HPS refrigeration efficiency reaches highest values also in the zone of low environment temperatures and largely depends on the relative humidity of the outside air. Values of HP and HPS refrigeration efficiencies do not depend much on the premise properties, i.e. the coefficient K, in the entire temperature range t_0. In general, the studied HPS can have high energy efficiency when it is used in temperate latitudes. It should also be noted that this system, which is designed for operation during the warm season (cooling and drying of fresh outside air), has its limitations. Fig. 6 shows two air workflow processes which indicate different air conditions inside the ventilation and air heating HPS (a) and the ventilation and air conditioning HPS (b). The first process was obtained as a result of the HPS analysis for this object during the cold season. Results of this analysis are presented in [10]. According to them, depending on the relative humidity φ_0, there exists a critical outside air temperature t_0, above which the HPS in the operating mode a) will not be able to provide comfortable conditions in the premise due to the incoming excessive moisture from the environment.

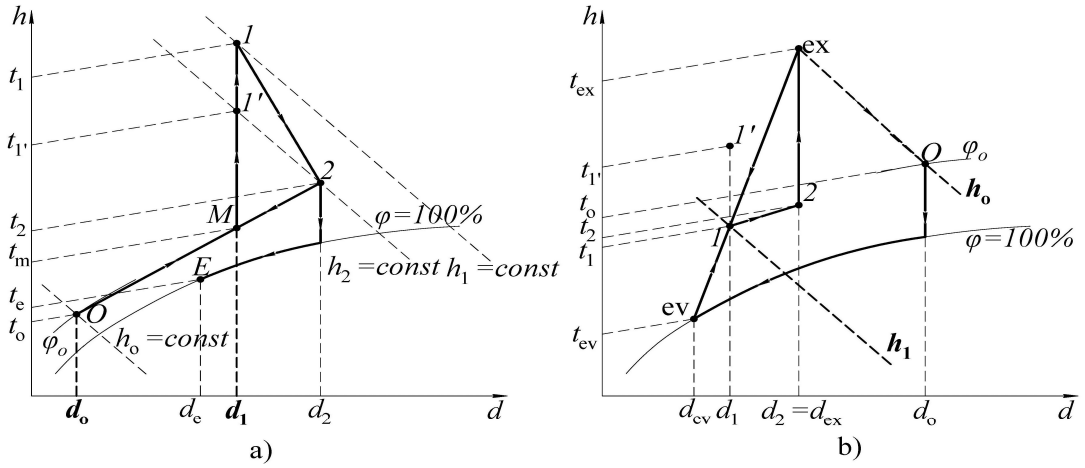

Fig.6. Air workflow processes which indicate different air conditions inside the ventilation and air heating HPS (a) and the ventilation and air conditioning HPS (b).

This situation occurs when the outside air moisture content exceeds the set moisture content of the supply air at point *1*, i.e. $d_0 > d_1 = 5.3$ g/kg$_{d.a}$ (Fig. 6, a). In case of exceeding the outside air temperature limit values a fundamental change of the system is required with its following transition to the air conditioning mode in which the supply air is cooled and drained. The result of this problem solution is the given HPS for ventilation and air conditioning, the working process of which is shown in Fig. 2 and Fig. 6, b. According to Fig. 6, b the boundary condition for this system application will be the situation when the outside air enthalpy becomes lower than the enthalpy of the air mixture at point *1*, i.e. $h_0 < h_1 = 34.7$ kJ/kg$_{d.a}$ (Fig. 6, b).

Conclusions

Efficiency of the studied system comparing to one in work [4] increased due to the presence of air conditioning. This effect occurs because of partial utilisation of generated cold within the system. However, the benefit is only in a range of relatively low outside air temperatures. The higher demands for air conditioning are, the faster air temperatures after HP condenser will reach critical values at which the work of HPS is not recommended.

It is shown that the required additional cooling of the supply air at the entrance to the premise for air conditioning demands can be determined by a simple coefficient *K* which is proportional to the temperature difference of air outside and inside a premise and which is defined by the premise constructional properties along with its required air exchange rate, determined by the functional purpose of the object of ventilation and air conditioning, as well as by the premise internal heat generation. The studied system of ventilation and air conditioning in premises with an excessive internal moisture generation can provide maintenance of the required conditions indoors during the warm season only up to moderate values of outside air parameters, further increase of which is limited by the maximum temperature of the exhaust air after the HP condenser.

The studied system of temperature and humidity maintenance has the highest energy efficiency in the zone of relatively low environment temperatures and largely depends on the relative humidity of the outside air. This suggests that this HPS is suitable for application in countries with temperate continental climate. The results of the study will be used for further scientific work on the improvement of existing heating, ventilation and air conditioning heat pump systems.

REFERENCES

1 Ukraine's new energy strategy until 2035: "security, energy efficiency, competitiveness". Kyiv, Ministry of Energy and Coal Industry of Ukraine, 2017, 53 p.

2 Khrustaliov B. M. *Heat supply and ventilation*. Moscow, ASV, 2007, 784 p.

3 Yu-Yuan Hsieh, et al. A study of heat-pump fresh air exchanger. *Applied Thermal Engineering*, 2018, Vol. 132, No. 5, pp. 708-718.

4 Bezrodny M., et al. Efficiency of heat pump systems of air conditioning for removing excessive moisture. *Archives of Thermodynamics*, 2019, Vol. 40, No. 2, pp. 151-165. DOI: 10.24425/ather.2019.129546

5 Bozhenko M. F. *Heat sources and heat consumers*. Kyiv, NTUU KPI "Politehnika", 2004, 192 p.

6 *State Building Standards of Ukraine DBN B.2.5-67: 2013, "Heating, ventilation and air conditioning"*. Kyiv, Ministry of Regional Development, Construction and Housing of Ukraine, 2013, 149 p.

7 Morozjuk T. V. *The theory of chillers and heat pumps*. Odesa, Studija "Negociant", 2006, 712 p.

8 Bezrodny M., et al. Thermodynamic analysis of the heat pump ventilation system for support of comfort conditions in industrial premises with release of moisture. *NTU "HPI"*, 2018, No. 13, pp. 77-82. DOI: 10.20998/2078-774X.2018.13.14

9 Bezrodny M. K. *Thermodynamic and energy efficiency of heat pump heat supply circuits: monograph*. Kyiv, NTUU KPI "Politehnika", 2016, 272 p.

10 Bezrodny M., Misiura T. The heat pump system for air heating and ventilation inside the production area with an excessive internal moisture generation. *KPI Science News*, 2020, No. 2, pp. 7-16. DOI: 10.20535/kpi-sn.2020.2.205111

Article accepted for publication 07.08.2020

DOI 10.31489/2020No2/87-95

UDC 621.039

DESIGN-BASIS JUSTIFICATION FOR IMPLEMENTING TARGETED ENERGY RELEASE IN TEST OBJECTS OF THE IMPULSE GRAPHITE REACTOR

Vityuk V.A.[1], Vityuk G.A.[1,2], Skakov M.K.[1], Zhagiparova L.K.[1]

[1] National Nuclear Center of the Republic of Kazakhstan, Kurchatov, Kazakhstan
[2] D. Serikbayev East Kazakhstan technical university, Ust-Kamenogorsk, Kazakhstan,
galina-shmeleova@mail.ru

The article presents the approaches and technical solutions applied to assure preset axial and radial distribution of energy release in simulative fuel rods and fuel assemblies in the tests at the impulse graphite reactor. It considers the procedure for the design-basis justification of solutions that provide a given volume distribution of energy release in a test unit. The considerations are based on the example of heterogeneous fuel assemblies with the altitude separation of enriched fuel into two zones by a depleted uranium layer used to reproduce fissile material. The implementation of the procedure and making appropriate technical solutions made it possible to provide a targeted profile of the axial and radial distribution of energy release in a simulative fuel assembly at the design stage of an irradiation device. By the result of study, it is demonstrated that uniform radial energy release and targeted average energy release in upper and lower fission zones of experimental fuel assembly could be obtained at the level of 90.6 W/g (UO_2) and 74 W/g (UO_2), respectively. The measures include profiling of fuel pellets enrichment in fuel rods, using the pellets with an absorber at the zone ends, and a certain altitudinal positioning of the irradiation device in the reactor.

Keywords: Impulse graphite reactor, fuel assembly, energy release, power profile, fissile zone

Introduction

The experimental Justification of workability of nuclear fuel is the significant aspect of the decision making of its using. The complex of activities in this direction (both calculations and experiments) is devoted to the modeling of the fuel behavior in the conditions, which could lead to the progression of emergency mode with the core melting as consequence. The nuclear fuel tests in the research reactors are the most appropriate direct method to receive such experimental information which may be used both for experimental evaluation of fuel roads and fuel assemblies workability and to support the verification process of computer models and codes for corresponding calculations. Only several research nuclear reactors in the world possess the characteristics, which make it possible to carry-out the tests with fuel rods and fuel assemblies destruction. Among them the impulse graphite reactor IGR (National Nuclear Center, Kazakhstan), TRIGA type reactors including ACRR (Sandia Lab., USA), NSRR (Japan atomic energy agency), CABRI (French Commissariat on nuclear energy and alternative energy sources), BR-2 (SCK-CEN, Belgium), TREAT (Idaho lab., USA) and now stopped SCARABEE (France) [1-7].

In fact at present only IGR is actively used for experimental investigations of accidental conditions with the core melting for fuel assemblies with the loading up to 8 kg of UO_2. Many years the experimental programs are successfully implemented at the IGR. At the moment the researches are focused on study of fuel pins and fuel assemblies behavior in severe accident conditions at the fast sodium reactors designed in Japan and France [8-11]. Other reactor designers are interested in such experimental programs realization also [12, 13].

The research thermal neutrons impulse nuclear reactor IGR with a homogeneous uranium-graphite core is a unique source of neutron and gamma radiation with high dynamics of power change. In the IGR reactor, the neutron flux can reach a value of $7 \cdot 10^{16}$ $cm^{-2} \cdot s^{-1}$, which makes possible to run the dynamic tests of fuel rods and fuel assemblies in transient and emergency modes. Implementation of targeted energy release is an important task when testing the simulative fuel rods and fuel assemblies in the IGR reactor. The solution to this problem should assure both the power required by the test conditions and the specific power profile in each volume of the tested structure.

The power level of the tested fuel rods and fuel assemblies during their irradiation in the IGR depends on the parameters of the neutron field in the experimental channel, spatial and material characteristics of the device with fuel rods under irradiation. The spectrum and shape of the neutron field of the reactor themselves strongly depend on a number of factors: core temperature, position of the control rods, configuration and material composition of the irradiation device. In this regard, prior to the active phase of the tests, a complex of auxiliary studies shall be performed; to include calculation and experimental studies aimed at determining the coupling coefficient between the energy parameters of the test object and the reactor, and the nature of its changes during the reactor experiment [14-16]. Based on the auxiliary studies, we determine and analyze a reactor power diagram, which provides specified profile of power change on the test object and integrated energy release in the fuel. Even before that, while designing the irradiation device with fuel rods, solutions should be made providing the targeted volumetric distribution of energy release in the test object.

The requirements to the energy distribution in the fuel rods and fuel assemblies are determined by the test goals. This may include, for example, the need to reconstruct the energy release profile of a fuel assembly in the conditions of its operation in an actual power reactor or providing local bursts of energy release in the specified volumes to simulate transient and emergency processes. In some cases, the customer requires to ensure most uniform profile of the volumetric energy release in a given volume of fuel, for example, to ensure simultaneous melting of a given volume. At the same time, the quality and validity of the technical solutions undertaken to ensure a given energy release largely determines the degree of achievement of the test goal and the value of their results.

The paper discusses the approaches and technical solutions applied during preparation of the tests at the IGR to ensure targeted axial and radial profile of energy release in simulative fuel rods and fuel assemblies, as well as examples of their implementation.

5. The problem of FA energy release profiling during the test preparation at the IGR

5.1 The IGR core

The structure of the IGR reactor is a masonry of graphite blocks assembled into columns, placed in a steel cylindrical body with a helium medium. The graphite blocks of the reactor core are impregnated with an aqueous solution of uranyl nitrate (uranyldinitrate) with uranium concentration of 3.1 g per 1 kg of graphite. The core consists of fixed and moving parts surrounded by side and butt graphite reflectors. The shape of the core is like cubic: its dimensions in the cross-section are 1.400 × 1.400 mm; the height of the movable part of the masonry – 1.463 mm; the height of the fixed part of the masonry is 1.332 mm. The reactor has a central and lateral experimental channels (CEC and LEC), which are equipped with loop water-cooled devices. The reactor is operated and protected by 16 graphite control rods with a gadolinium oxide absorber [15].

5.2 The axial energy release profile

The axial distribution of the neutron flux in an empty CEC of the reactor is presented in Figure 1. The maximum flux corresponds to the center of the reactor core (mark “66.5”). However, as for the center of the core, the flow is not symmetrical since different amounts of reflectors are placed above and below the core. The shape of the neutron flux distribution in the CEC is also affected by the position of the control rods.

Due to the rather small dimensions of the core, any object placed in the CEC significantly affects the configuration of the neutron field. In case of a sufficiently uniform design of the irradiation device with a fuel rod or fuel assembly filled with fuel pellets with the same ^{235}Ucontent, the axial profile of energy release in the fuel cells will, in general, correspond to the profile of the neutron field in an empty CEC (Figure 2) [18]. Taking the above into account, when it is necessary to assure energy release distribution in fuel rods, obeying to the dependence y = k *Cos* x, control may be provided by determining the optimal altitude level of the FA relative to the center of the core.

In this case, power surges will be observed at the ends of the fuel rods due to the increased neutron flux compared to other regions (see Figure 2). The neutrons entering the simulative fuel assembly installed in the CEC from the IGR core are absorbed by the ^{235}U in the FA fuel. The higher the ^{235}U content in a given FA volume, the more neutrons from IGR would be absorbed in this volume. The pellets located close to the fuel rod ends absorb the neutrons coming both from the side and from the ends of the fuel rods. Accordingly, at the ends of fuel rods with relatively high ^{235}U contents, an increase in neutron flux causing nuclear reactions and an increase in energy release would be observed.

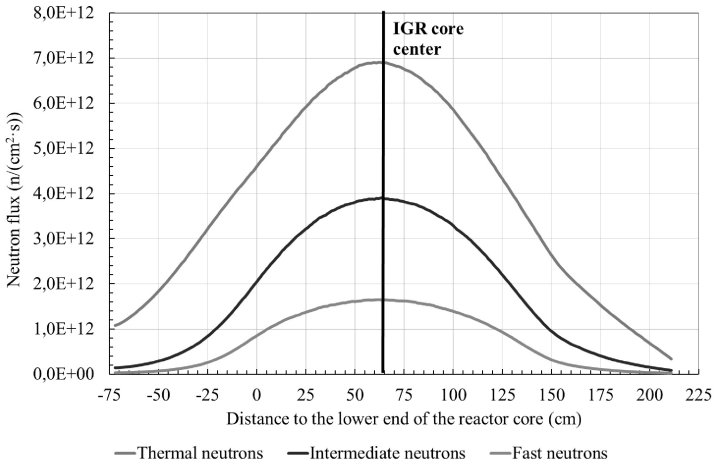

Fig.1. Neutron field parameters in an empty CEC (IGR power – 1MW)

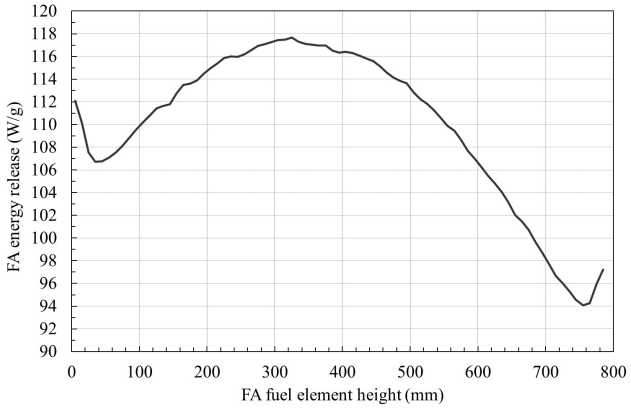

Fig.2. Axial energy release profile in a fuel rod of an irradiation device with a uniform height structure

A similar pattern would be at the junctions of the pellets enriched with ^{235}U and the pellets with depleted uranium. The pellets with ^{235}U content of 0.27%, are often used in experiments for modeling fuel assemblies of fast neutrons containing blanket layers. Sometimes, the term “breeding blanket” is used to name such layers.

5.3 The axial energy release profile

The radial energy release profile in the fuel assemblies during the IGR tests is determined, first of all, by the assembly design. So, if a single-row symmetric arrangement of fuel rods with a uniform ^{235}U content in the pellets throughout the entire fuel assembly volume and a uniform symmetric design of the irradiator device is used, the energy release in the volumes of different fuel rods at the same altitude level would be practically the same. In asymmetric fuel rod arrangement with fuel rods sufficiently close to each other in a single-row fuel assembly, the neutron field in the region of each specific fuel rod is subject to heterogeneous distortion, which depends on the location of the neighboring fuel rods that serve in this case as neutron absorbers generated by the IGR core. Asymmetric single-row arrangement of fuel rods in a FA is the least attractive option for testing and, as a rule, is not used for in-pile experiments due to above-mentioned and other reasons. Nevertheless, the effect can be used, for instance, to set in a particular group of fuel rods of one row with higher or lower energy release values in relation to other fuel rods.

In the case of multi-row FAs, in addition to the described above mutual influence of the fuel rods of the same row, the outer fuel rods would create “shadows” on the fuel rods in the internal rows. The neutron flux from the IGR side on the fuel rods of the inner rows would therefore be lower than that on the fuel rods of the outer rows. Accordingly, in an assembly with a uniformly distributed ^{235}U, the energy release in the outer rows would be greater than that in the inner ones.

6 Examples of achieving a given energy release profile in a fuel assembly

6.1 Test object and test conditions

A heterogeneous fuel assembly of a fast neutron reactor with a triangular lattice of fuel rods is taken as the research object. A fuel assembly contains 37 fuel rods [19] (Figure 3). By height, the fuel column (pellets) is divided into two fission zones (with ^{235}U enrichment of 17%) and a central blanket zone (with ^{235}U content of 0.27 %.). The design choice is conditioned by the fact that the use of fuel assemblies which are heterogeneous in height with separation of highly-enriched fuel into two zones (upper and lower) by a layer of low-enriched fuel designed for the reproduction of fissile material, assures the negative void effect of reactivity in sodium [20]. The blanket in the center of a fuel rod, which in the event of a severe accident in a fast reactor would remain relatively cold, would affect the process of fuel melting and redistribution over the core volume. This factor can help to reduce the possibility of melting for the local masses of highly enriched fuel, and, consequently, reduce the likelihood of repeated criticality in the emergency core. In this regard, tests of the FA in the IGR are considered as a possible direction for studying the behavior of heterogeneous assemblies of future fast neutron reactors with sodium coolant in the conditions of a severe accident [21].

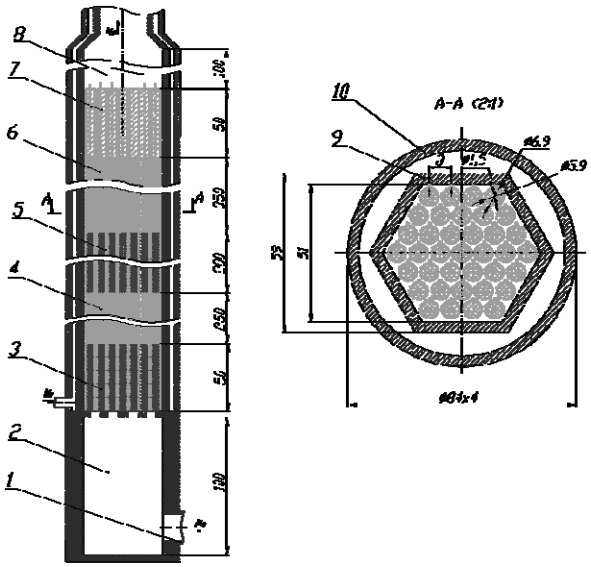

Designations:
1 – sodium mouth,
2 – bottom sodium plenum,
3 – bottom blanket layer (0.27% ^{235}U),
4 – bottom active layer (17 % ^{235}U),
5 – top blanket layer (0.27 % ^{235}U),
6 – top active layer (17 % ^{235}U),
7 – top plug,
8 – top sodium plenum,
9 – hex cover,
10 –cylindrical case

Fig.3. Design of the irradiation device.

With in-pile tests, a number of requirements shall be met in terms of energy distribution in the experimental fuel assembly, that ensure the most complete compliance of the test conditions with the actual conditions for the occurrence and development of an emergency in the reactor under consideration:

1) provide an average energy release in the upper and lower fission zones at the level of 90.6 W/g (UO_2) and 74 W/g (UO_2), respectively;

2) to exclude the possibility of power surges at the butts of the fuel rods, which can lead to local overheating of the fuel;

3) to ensure uniform radial distribution of energy release in the fuel assemblies.

6.2 Calculation Model and Assumptions

In the research, a detailed design model of the IGR reactor was used (Figure 4), protected by the copyright certificate [22]. The design model of the reactor is fully consistent with the real design and considers uneven distribution of uranium concentrations in the core bulk, the relocation of the control rods during startup, the dynamics of the reactor taking into account the uneven heating of individual parts of the masonry. The core, lateral, bottom, top and suspension reflectors of the IGR reactor are modeled by a block structure.

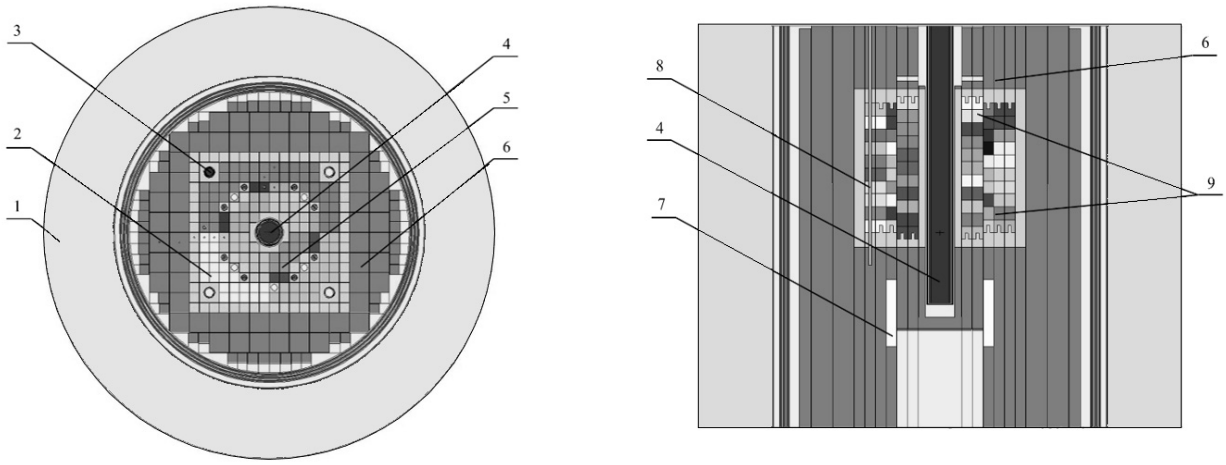

Horizontal cross-section Vertical cross-section

Fig.4. Design model of the IGR reactor: 1 – water tank; 2 – fixed part of the masonry; 3 – LEC; 4 – CEC; 5 – movable masonry; 6 – reflector; 7 – boron cut-off; 8 – control rod; 9 – fuel blocks

The model is combined with irradiation device model containing heterogeneous FA, developed in compliance with all dimensional-material characteristics of the assembly and other structural elements. Figure 5 shows a horizontal cross-section of a combined design model of a device located in the CEC of the IGR reactor.

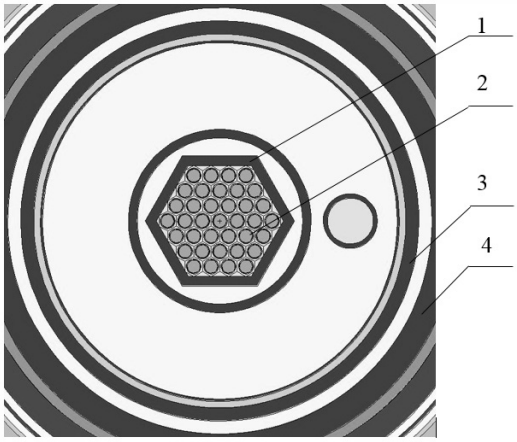

Fig.5. The model of the irradiation device as a part of the integrated calculation model: 1 – FA, 2 – fuel elements, 3 – CEC, 4 – fixed ampoule of the IGR reactor

The device design meets the main dimensional and material characteristics of the structure [1]. The fuel columns of the fuel assemblies are modeled as single rods without chamfers or grooves. All calculations were performed using the MCNP5 [23] calculation code with the ENDF/B-VII library.

6.3 The results of the studies aimed to ensure targeted axial profile

The targeted axial energy release profile was implemented by searching an optimal altitude location of the fuel assemblies in the CEC of the IGR reactor providing the required level and axial distribution of energy release in the fission zones. According to the calculations, the top butt of fuel rod fuel column should be 120 mm above the center of the IGR core. In this case, the average energy release in the upper and lower fission zones, as a whole, corresponds to the required one and comprises 90.6 W/g (UO_2) and 74 W/g (UO_2), respectively (Figure 6).

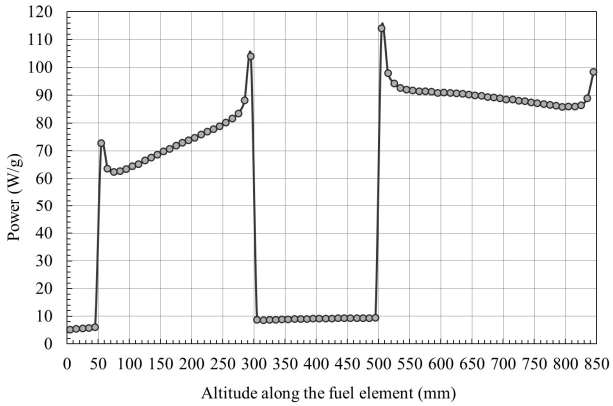

Fig.6. Axial profile of the average power along the fuel rods in the fuel assemblies

Nevertheless, significant power surges are observed at the boundaries of the fission zones due to the increased, in comparison with other regions of the fuel assemblies, neutron flux coming from the IGR. Installation of additional neutron absorbers made of steel rings at corresponding altitude of the experimental device is an option to solve the problem of smoothing the surges. The approach was used in the calculations performed to justify the experiment with a single fuel rod [24]. In the considered case, when the FA section takes up almost the entire volume of the radial section of the experimental cavity, the installation of additional rather massive structural elements is difficult due to the lack of space. To smooth out the peaks, a method is therefore proposed supposing use of pellets with lower enrichment rate or ones made of uranium-gadolinium fuel in the border regions of the fission and breeding zones.

The outcomes of the approach are shown in the graphs of Figure 7: option 1 – one pellet with ^{235}U enrichment rate of 8.25% is installed at each end of the fission zones (Figure 7a); option 2 – one pellet with 8% of Gd_2O_3 is installed at each end of the fission zones, while the fuel enrichment with ^{235}U comprises 8.25% (Figure 7b).

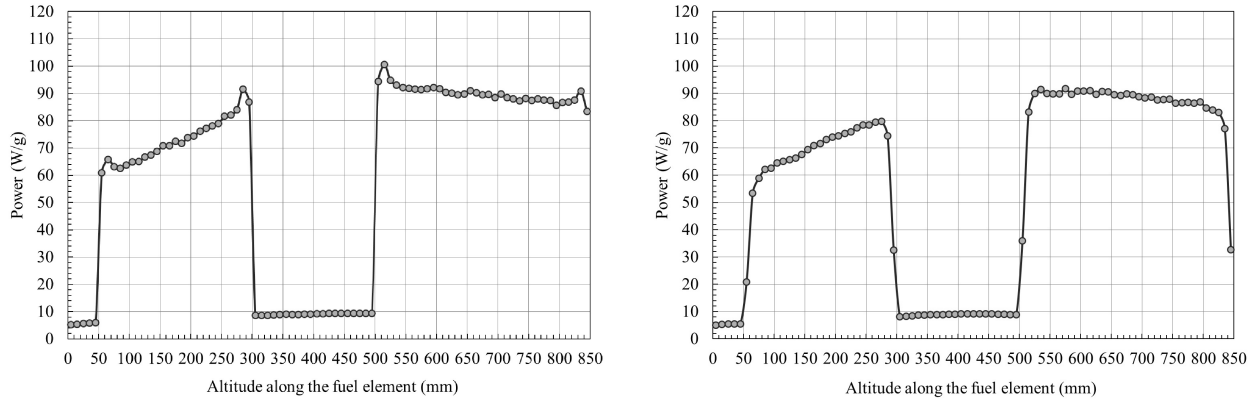

a) option 1 b) option 2

Fig.7. Altitude distribution of energy release in the FAs for the two considered options

As we can see, the approach is acceptable both in the case of low-enriched pellets in the border areas of the fission zones, and for the less enriched pellets made of uranium-gadolinium fuel. Thereby, application of fuel with a burnable absorber is preferable and allows to completely neutralize the local power surges.

6.4 The results of the studies aimed at assuring the targeted radial profile

Calculation results of FA radial profiles in the initial version demonstrated significant (for 2–2.5 times) spread of energy release along the fuel rods in radial direction (Figure 8). Profiling of the ^{235}U content in the fuel rods located on different concentric circles or rows in the fuel assemblies is the most rational solution to assure uniform radial energy release in fuel assemblies. In this case, the ^{235}U content in the fuel rods will increase with approaching to the central vertical axis of a fuel assembly [25].

The coefficient of the relative power non-uniformity in different fuel rod rows is used for a numerical assessment of the non-uniformity rate; the coefficient is determined as:

$$K = \frac{W_{max}}{W_{ave}}, \quad (1)$$

where W_{max} – maximal energy release in the fuel rod rows, relative units; W_{ave} – average energy release in the fuel rod rows, relative units.

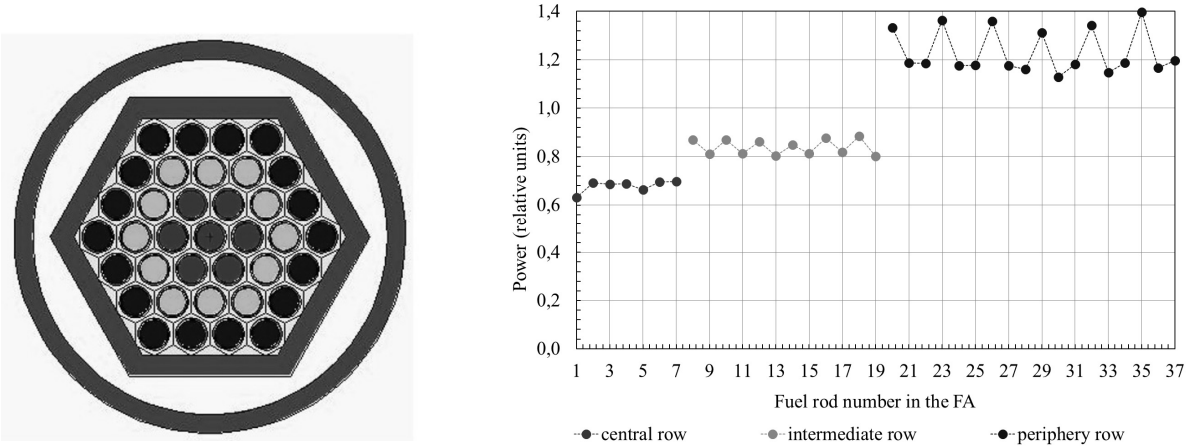

a) fuel rods in FAs b) power distribution in FAs

Fig.8. Power distribution in the fuel rods in FAs: initial version (17% enrichment in the fission zones)

The non-uniformity coefficient (Figure 6) comprised ~ 1.40. In order to reduce the uneven radial power distribution in the FAs, a complex of calculations was performed to choose enrichment profiling for the fuel rods to reduce the radial unevenness of energy release in the simulative fuel assembly (Figure 3). A satisfactory result is achieved for the option with the fuel rods enrichment in the rows 17%, 12.7%, 8.6% (Figure 9). In this case, the coefficient of unevenness is ~ 1.10.

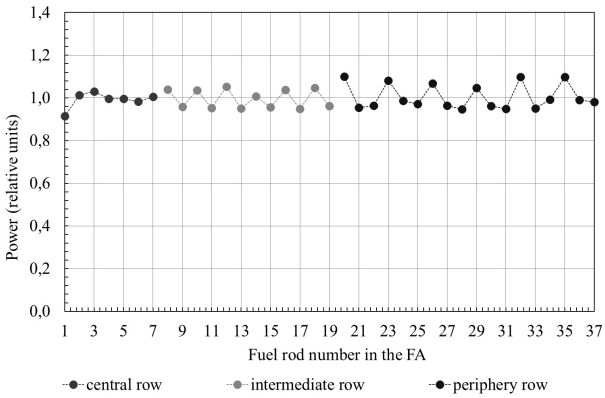

Fig.9. Power distribution in FA with enrichment in fuel rod rows are 17%, 12.7% and 8.6%

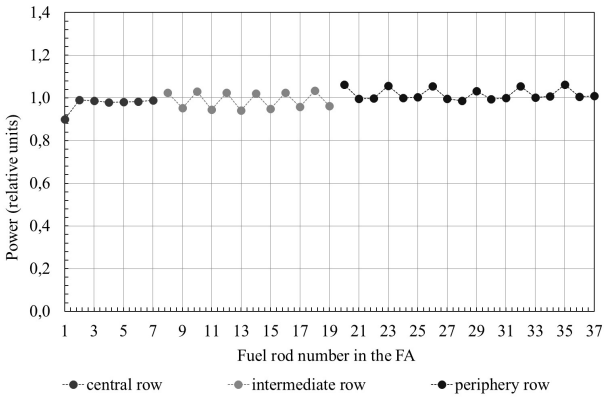

Fig.10. Power distribution in FA with enrichment in fuel rod rows are 17%, 12.7% and 8.94% (enrichment in peripheral row corner fuel rods is 8.25%).

With the power distribution in the FA (Figure 6), a deviation from the average value in the peripheral row is observed. To smooth the power distribution in the peripheral row, we considered an option with reduced enrichment in the corner fuel rods to 8.25% and, simultaneous higher enrichment of remaining fuel rods in the peripheral row to 8.94%. The calculation results are presented in Figure 10. With the power distribution in the fuel rods (Figure 10), the unevenness coefficient is ~ 1.05.

Conclusions

Thus, the presented calculation procedure makes possible to develop and put into practice the technical solutions that assure the targeted profile of the axial and radial distribution of energy release in a simulative fuel assembly. With an example of preparation for testing in heterogeneous FA of the IGR reactor, a set of measures was demonstrated which made possible to provide uniform radial energy release and get targeted average energy release in FA upper and lower fission zones at the level of 90.6 W/g (UO_2) and 74 W/g (UO_2), respectively. The measures include profiling of fuel pellets enrichment in FA rows, use of pellets with an absorber at the zone ends, and a certain altitudinal positioning of the irradiation device in the CEC IGR.

The implemented procedure is applied in preparation for tests of fuel rods and fuel assemblies in the IGR reactor and, along with other organizational and technical measures, ensures the required quality of experimental studies.

Acknowledgments

The work is carried out as part of the scientific and technical program "Development of Atomic Energy in the Republic of Kazakhstan" of the republican budget program "Development of Atomic and Energy Projects" with the support of the Ministry of Energy of the Republic of Kazakhstan.

References

1 Kurchatov I.V., Feinberg S.M., Dollezhal N.A. Pulsed graphite reactor IGR. *Atomic energy.* 1964, Vol. 17, No.6, pp. 463 – 474. [In Russian].

2 Royl P., Breitung W., Fischer E.A., Schumacher G., Gauntt R.O., Wright S.A. Contributions from the ACRR in-pile experiments to the understanding of key phenomena influencing unprotected loss of flow accident simulations in LMFBRs. *Nuclear Engineering and Design.* 1987, Vol. 100, Issue 3, pp. 387 – 408.

3 Amaya M., Udagawa Y., Narukawa T., Mihara T., Taniguchi Y. Behaviors of High-burnup LWR Fuels with Improved Materials under Design-basis Accident Conditions. *Proceedings of Annual Topical Meeting on Reactor Fuel Performance (TopFuel 2018) (Internet)*. Prague, Czech Republic, 2018.

4 Biard B., Chevalier V., Gaillard C., Georgenthum V., et al. Reactivity Initiated Accident transient testing on irradiated fuel rods in PWR conditions: The CABRI International Program. *Annals of Nuclear Energy.* 2020. Vol. 141. 107253.

5 Kalcheva S., Van den Branden G., Van Dyck S., et al. Feasibility studies for simultaneous irradiation of NBSR & MITR fuel elements in the BR2 reactor. *Annals of Nuclear Energy*. 2019, Vol. 127, pp. 303 – 318.

6 Holschuh Th., Woolstenhulme N., Baker B., et al. Transient Reactor Test Facility Advanced Transient Shapes. *Nuclear Technology*. 2019, Vol. 205(10), pp. 1346 – 1353.

7 Bailly J., Tattegrain A., Saroul J. The SCARABEE facility - Its main characteristics and the experimental program. *Nuclear Engineering and Design*. 1980, Vol. 59, Issue 2, pp. 237 – 255.

8 Konishi K., et al. The Result of a wall failure in-pile experiment under the EAGLE project. *Nuclear Engineering and Design.* 2007, Vol. 237(22), pp. 2165 – 2174.

9 Kamiyama K., et al. Experimental studies on the upward fuel-discharge for elimination of severe recriticality during core-disruptive accidents in sodium-cooled fast reactors. *Journal of nuclear science and technology*. 2014, Vol. 51(9), pp. 1114 - 1124.

10 Serre F., Payot F., Suteau C., et al. R&D and Experimental Programs to support the ASTRID Core Assessment in Severe Accidents Conditions. *Proceedings of International Congress on Advances in Nuclear Power Plants (ICAPP*), San Francisco (CA, USA). 2016, Vol. 3, pp. 2173 – 2182.

11 Vityuk G., Vurim A., Skakov M., Pakhnits A. Methods and results of determining the impurity gas amount in ceramic fuel. *Annals of Nuclear Energy*. 2021, Volume 150, 107843.

12 Vityuk G.A., Vurim A.D., Kotov V.M., Vityuk V.A., Zhanbolatov O.M. Calculated studies in support of in-reactor tests of fast reactor fuel elements on fast neutrons. *Bulletin of the National Nuclear Center of the Republic of Kazakhstan*. 2017, Vol. 3, pp. 24 – 31. [In Russian].

13 Vurim A.D., Zhdanov V.S., Zverev V.V., Pivovarov O.S., Kulinich Yu.A. Results of tests of model fuel elements of the BREST-300 reactor in the IGR reactor. *Bulletin of the National Nuclear Center of the Republic of Kazakhstan*. 2000, Vol. 1, pp. 25 – 30.

14 Vityuk V.A., et al. Determination of the parameters for fuel assembly tests in a pulsed graphite reactor. *Atomic Energy*. 2016, Vol. 120, No. 5, pp. 323 – 327.

15 Vityuk V.A., Vurim A.D. Method for determining the energy parameters in pulse reactor experiments. *Annals of Nuclear Energy*. 2019, Vol. 127, pp. 196 – 203.

16 Irkimbekov R.A., Vityuk V.A., et al. About the fuel tests features at the IGR research reactor. *International Conference on Research Reactors: Safe Management and Effective Utilization*. Book of abstracts, International Atomic Energy Agency, Vienna (Austria). November 16–20, 2015, pp.71 – 72.

17 *The complex of the pulse research reactor IGR. Technological regulations: AK.65000.02.104D*. Branch of the IAE RSE NNC RK, Kurchatov. 2014, Ref. No. K-52058. [In Russian].

18 Vityuk V.A., Vurim A.D., Kotov V.M., et al. Development of a model fuel assembly for an emergency study with instant blocking of the coolant flow in a fast neutron reactor. *Bulletin of the National Nuclear Center of the Republic of Kazakhstan*. 2018, Vol. 3 (75), pp.93 – 98. [In Russian].

19 *The ASTRID technological demonstrator. 4th-Generation sodium-cooled fast reactors*. December 2012, Vol. 3, 96 pages.

20 Vurim A.D., Vityuk V.A., Gaydaychuk V.A., et al. Computational-experimental studies in support of the program of in-reactor tests of a model fuel assembly of a promising reactor. *Bulletin of the National Nuclear Center of the Republic of Kazakhstan*. 2015, Vol. 1, pp. 55 – 60. [In Russian].

21 Vurim A.D., Kotov V.M., Irkimbekov R.A., et al. *Computer model of the IGR reactor for stationary neutron-physical calculations*. The Republic of Kazakhstan certificate of authorship. December 27, 2016, No. 2738.

22 Vityuk G.A., Skakov M.K., Vityuk V.A., et al. Implementation of the energy release profile in a heterogeneous fuel element during tests in a pulsed graphite reactor. *KazNITU Bulletin*. 2018, Issue 6, pp. 357 – 364. [In Russian].

23 *MCNP-5.1.40 Monte-Carlo N-Particle Transport Code*. Los Alamos National Laboratory. Los Alamos (New Mexico). April 24, 2003.

24 Vityuk G.A., Vurim A.D., Kotov V.M., et al. Computational studies in support of intra-reactor tests of fuel rods for the fast neutron reactors. *Bulletin of the National Nuclear Center of the Republic of Kazakhstan*. 2017, Vol. 3 (71), pp.24 – 30. [In Russian].

25 Vityuk V.A. et al. Development of a model fuel assembly for investigating an emergency situation with instant blocking of the flow in a fast neutron reactor. *Abstracts of VII Intern. conf. «Semipalatinsk test site. Radiation heritage and prospects for development»*, Kurchatov. September 21-23, 2016, pp. 128 – 129. [In Russian].

Article accepted for publication 25.11.2020

DOI 10.31489/2020No2/96-99

UDC 621.7.537

ELECTRIC PULSE METHOD FOR PRODUCING A SMALL-DISPERSED PRODUCT OF COAL-WATER FUEL

Khassenov A.K.[1], Nussupbekov U.B.[1], Karabekova D.Zh.[1], Stoev M.[2], Bolatbekova M.M.[1]

[1]E.A. Buketov Karaganda University, Karaganda, Kazakhstan, ayanbergen@mail.ru

[2]Neofit Rilski South-West University, Blagoevgrad, Bulgaria

One of the most pressing issues is the effective use of coal combustion in the form of water-coal fuel, which has a number of advantages over layer or pulverized combustion. Coal-water fuel has a number of economic, operational and environmental advantages. The article considers the electric pulse method as a source of obtaining a fine product of coal-water fuel. The proposed method for grinding coal is based on the use of the energy of a pulsed shock wave resulting from a spark electric discharge in a liquid. The parameters of the electric pulse discharge for obtaining the required granulometric composition of the components of coal-water fuel are determined.

Keywords: electric pulse, electrical discharge,coal-water fuel, coal-water suspension, number of discharge, condenser capacity

Introduction

Coal-water fuel (CWF) has great prospects among alternative fuels. It is a liquid mixture of two or more components in different proportions, one of the proportions is a combustible element (coal and brown coal, peat, waste coal, petroleum coke, etc.).The use of water-coal fuel and its subspecies as an energy carrier in the heat power industry has a number of advantages in comparison with other methods of coal preparation and combustion. The main advantage is the reduction of losses during coal transportation, convenience of storage and intra - station movement, and the supply of CWF to the furnaces of power plants. Coal-water fuel is a promising fuel for replacing scarce and expensive fuel oil at energy facilities [1].

In thermal power plants, the efficiency of using coal-water fuel (CWF) significantly depends on its technological parameters: viscosity, sedimentation stability, granulometric composition of the solid phase, and calorific value [1]. The granulometric composition of the solid phase of coal-water fuel is primarily determined by the requirements of consumers. Depending on the use of water-coal fuel, the optimal parameters of solid particles for coal-fired TPP are 250 μm, for fuel-oil TPP 150 μm, for boilers 45 μm, for internal combustion engines 25 μm [2, 3]. The main task of water-coal fuel is coal grinding, which must be solved in the production process. The technology for producing coal-water fuel consists in grinding coal to a fine state and activating components (chemical additives) that are added to increase the fluidity of the water-coal suspension (CWF), prevent stratification and give it stability. For coal grinding, ball and rod mills are used in several stages of dry or wet grinding, which are characterized by multi-stage processing, high metal consumption, high specific energy costs for grinding one ton of coal, low efficiency and significant capital expenditures in the construction of coal-water fuel preparation complexes [4, 5]. In this regard, research work was carried out to obtain coal powder using electric pulse technology. The method for solid fuel grinding is based on the electrohydraulic effect method, which is designed to create shock waves in a liquid medium [6-8]. The peculiarity of the processing method is carried out inside the volume of liquid that is located in an open (closed) vessel, a specially formed pulsed electric (spark, brush and other forms) discharge around the zone of its formation, ultra-high hydraulic pressures arise that can perform useful mechanical work and are accompanied by a complex of physical and chemical phenomena.

The electrohydraulic effect is associated with a relatively slow energy accumulation in the power source and almost instantaneous release in the liquid medium. The main factors of the electro-hydraulic effect are high and ultra-high pulsed hydraulic pressures, which lead to the appearance of shock waves with sound and supersonic speeds. These factors have a variety of physical and chemical effects placed in it on a liquid or

other objects. Thus, shock displacements of liquid that occur during the development and collapse of cavitation cavities can destroy non-metallic materials and cause plastic deformations of metal objects placed near the discharge zone [6].

1. Experimental part

The latest achievements of electronic and high-voltage pulse technology can dramatically reduce the size of electrical elements, significantly increase the reliability of various electrophysical installations. Adaptation to the conditions of electric pulse technologies of electrical equipment mastered in related electrophysical research and technological applications will make it possible to make a technical breakthrough in the production use of electric pulse technologies. The modern element base already opens up prospects for the creation and wide development of EI technologies in special applications with limited productivity. Further improvement of the plants in the direction of increasing their capacity will consistently involve other technological directions of the method in production use [9].

Unlike mechanical crushers, the electrohydraulic unit does not have much moving parts, it is made of ordinary structural steel, so the body practically does not wear out during operation. There is no mechanical contamination of the product with hardware metal, lining material and grinding media. The ability of the method to simply and widely change the nature of dynamic loading allows you to adjust the granulometric composition of the grinding product, to obtain a narrower class of product size than is possible with mechanical grinding. In addition, the electric pulse method has a number of advantages compared to known grinding methods, mainly due to the small dimensions and mobility of the equipment, as well as the absence of restrictions on the strength of the materials being destroyed [10].

The electric pulse installation consists of a power supply-control block, a storage capacitor, an air converter and working channel. The power supply-control unit allows you to control the operating mode of the unit (adjust the power supply current, turn the unit on and off). High-voltage pulse capacitors (rated voltage 100 kV), which perform the function of storing electricity and are designed to operate in a mode in which charges and discharges quickly replace each other, were used as energy storage devices (capacitors). Figure 1 shows a General view of the working channel of the electric pulse unit. A spark pulse discharge is formed in a liquid medium between a rod metal electrode and the base (bottom) of a steel cylindrical vessel.

As a working medium, industrial water was used, which is cost-effective and affordable. After treatment with electric pulse discharges to separate the coal powder from the water, the water mixture was first settled, then the finished product was separated from the water (filtered) and dried at a temperature of 20 ^{0}C.

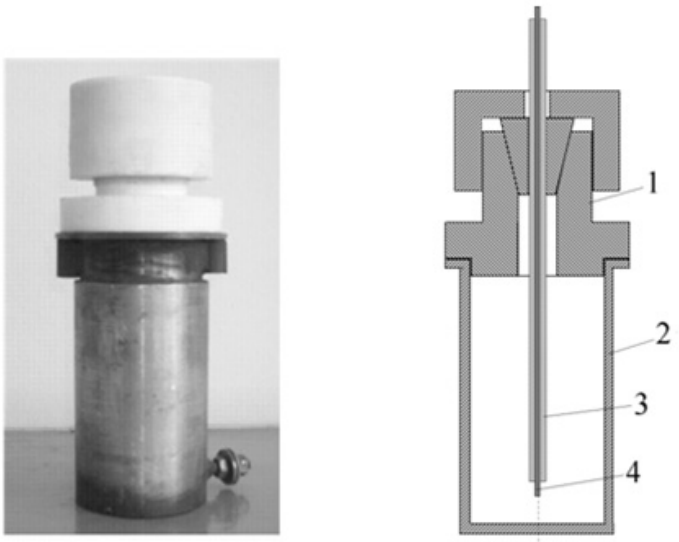

a b

Fig.1. Working channel of the electric pulse installation: a) main view; b) scheme;
1-cover made of fluoroplast, 2 - metal cylindrical container, 3-electrode insulation, 4-metal rod electrode

The capacitance of the capacitor (C) used for grinding raw materials was 0.25 μF and 0.4 μF, the operating voltage of the discharge U = 30 kV and the number of pulse discharges 400, 800, 1200. For carrying out research works, the coal of the Kuznetsk section was used, which is used as a lean additive to

fatty coals. The average diameter of the initial coal fraction was d_0:= 5; 10; 15; 20 mm. Based on the results of processing coal with these parameters of the electric pulse unit, the granulometric composition of the product was determined on standard sieves and powders with a diameter (d) of 150 μm and 250 μm were sorted.

2. Discussion of results

Figure 2 shows the degree of coal grinding depending on the parameters of the electric pulse installation. The results of electric pulse crushing of coal can be seen that increasing the battery capacity of the capacitor (0.25 μF-0.4 μF) and increasing the amount of discharge (from 400 to 1200) the degree of grinding of raw materials increased.

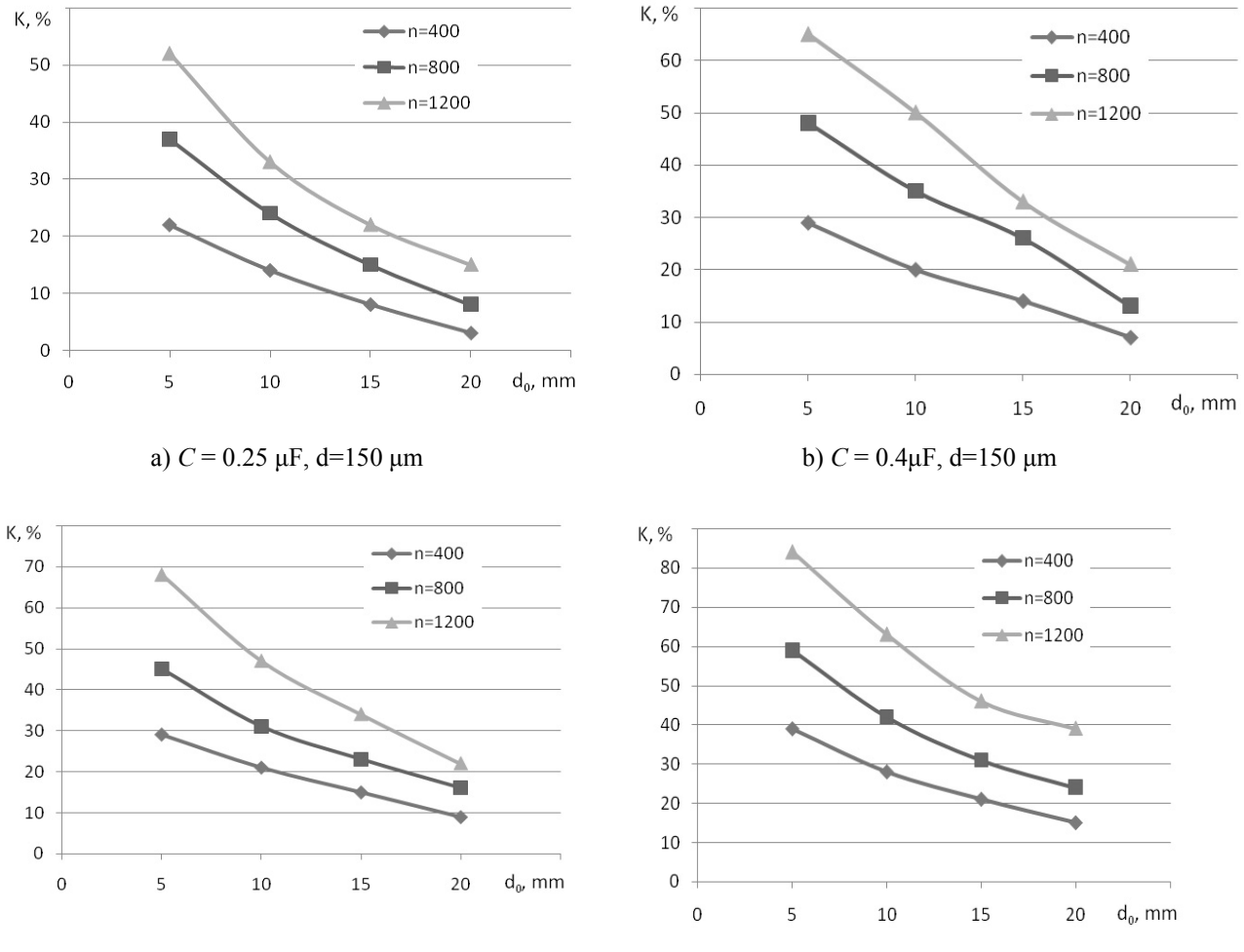

a) C = 0.25 μF, d=150 μm

b) C = 0.4μF, d=150 μm

c) C = 0.25 μF, d=250 μm

d) C = 0.4 μF, d=250 μm

Fig.2. Degree of coal grinding depending on the capacitance of the capacitor and the number of pulse discharges.

The degree of grinding of raw materials in the production of powder with a fraction diameter of 150 microns was the following interval: for coal with a diameter of the initial fraction of 5 mm-20-52%, for 10 mm-14-32 %, for 15 mm-8-22%, for 20 mm-3-15% (figure 2, a). An increase in the degree of grinding of raw materials, depending on the given parameters of the electric pulse unit, was also observed in the production of coal powder with a diameter of 250 microns (figure 2, c).

The data shown in figure 2 are obtained from the average values of experiments repeated many times (5 times) during the treatment of coal by the electric pulse method. After each grinding operation, the diameter of the fraction of the resulting product was determined using the above-mentioned special standard sieves (GOST R 51568-99 (ISO 3310-1-90) laboratory Sieves made of metal wire mesh). From the results obtained, it can be seen that the degree of grinding of raw materials with an initial fraction diameter of 5 mm is higher than that of raw materials with a fraction diameter of 10-20 mm. This is due to the fact that the spark gives

energy to its surface, and therefore, the denser the material surrounds the discharge zone (the more crushed it is), the more efficiently and fully the energy released by the discharge channel is consumed. The main factors affecting the grinding mechanism are the intensity of the pressure wave pulse, its duration, the nature of the energy input in the discharge channel, the total duration of the grinding process, high-speed fluid flows formed as a result of volumetric micro-cavitation.

Conclusion

Research work on coal grinding by electric pulse method was carried out. According to the results of scientific work, a product with a diameter of fractions of 150 μm and 250 μm, necessary for the manufacture of coal-water fuel, was obtained. The results of experimental work have shown that with the number of pulse discharges over 800 and the capacitance of the capacitor Bank of 0.4 UF (while the operating voltage is stable - 30 kV), solid fuel can be crushed to the required size. Currently, electric pulse technologies are used in the processes of cleaning heat exchangers from scale, crushing and grinding of natural ores, as well as processing of solid household waste. Carrying out these studies and implementing their results in enterprises will contribute to technological progress in the industry.

REFERENCES

1 Serant F.A., Tsepenok A.I., Ovchinnikov Yu.V., Lutsenko S.V., Karpov E.G. Preparation of coal-water fuel and its combustion technologies. *Modern science: research, ideas, results, technologies*. 2011, Vol. 1(6), pp. 95-101. [in Russian]

2 Samoylik V.G. Main technological parameters of coal-water fuel. *Dressing of minerals Fig Kopalin.* 2015, Vol. 61 (102), pp. 58-65.

3 Khodakov, G.S. Water-coal suspensions in power engineering. *Heat power engineering*. 2007, Vol. 1, pp. 35-45.

4 Rizun A.R., GolenYu.V., Denisyuk T. D., Kononov V. Yu. Development and implementation of electric discharge process of disintegration of water-coal fuel components. *Science of innovation*. 2009, Vol. 5, Vol. 5. pp. 42-46.

5 Zaydenberg V. E., Trubetskoy K. N., Murko V. I., Nekhoroshikh I. H. *Production and use of water-coal fuel*. 2001. M., Academyofmining Sciences, 176 p.

6 Yutkin L. A. *Electrohydraulic effect and its application in industry: textbook*. 1986, Leningrad, Mashinostroenie, 253 p.

7 Nussupbekov B.R., Khassenov A.K., Karabekova D.Zh., Nussupbekov U.B., Stoev M., Bolatbekova M.M. Coal pulverization by electric pulse method for water-coal fuel. *Bulletin of the University of Karaganda-Physics*. 2019, Vol. 4(96), pp. 80 – 84.

8 Kuritnik I., Nussupbekov B.R., Khassenov A.K., Karabekova D.Zh. Disintegration of copper ores by electric pulses. *Archives of Metallurgy and Materials*. 2015, Vol. 60, 4, pp. 2449-2551.

9 Potokin A. S. Achievements and tasks of improving the electric pulse method of destruction of materials in connection with the assessment of prospects for its application in technologies of mining and processing of mineral raw materials. Intellectual potential of the XXI century: Stages of knowledge. 2011, Vol. 8, pp. 185-189.

10 Kosenkov V. M., Rizun A. R. Determination of the characteristics of pulsed destruction of coal using the Kola method. Electronic processing of materials. 2011, Vol. 2, pp. 100-107.

Article accepted for publication 07.12.2020

DOI 10.31489/2020No2/100-109

UDC 622.784. 622' 17. 22.23.05

TECHNOLOGY AND EQUIPMENT FOR PROCESSING OF LARGE-SIZED VERMICULITE MICAS OF THE KOVDOR DEPOSIT

Nizhegorodov A.I.[1], Gavrilin A.N.[2], Moyzes B.B.[2], Kuvshinov K.A.[2]

[1]Irkutsk National Research Technical University, nastromo_irkutsk@mail.ru
[2]National Research Tomsk Polytechnic University, Tomsk, Russia, mbb@tpu.ru

The development of technology and equipment for the processing of large-sized vermiculite mica obtained from mining waste from the Kovdorsky deposit allows the large-scale vermiculite to be returned to processing industry. This article reviews the aspects of the technology for processing of large-sized mica with dimensions of 20 mm or more. The aim of the research is to study the grinding technology of large-sized vermiculite raw materials by the chopping overall particles, to develop the technological equipment and to study of its operating processes. The object of the research is the operating process of the chopping unit for grinding the large-sized vermiculite raw materials and its design. The methods are based on study of simulated movement of chopped large-sized particles and the determination of the main characteristics of the chipping unit operating process. It was found that the firing of large particles without grinding in chopping units requires a significant increase in firing time, which reduces the productivity of electric furnaces. The time of dropping particles out in the slot of the receiving drums of the chopping unit is determined, based on which the rotation speed of the receiving drums and its operational efficiency are calculated.

Keywords: large-sized vermiculite mica, chopping unit, expanded vermiculite, industrial furnace.

Introduction

The expanded vermiculite has a rare property to enlarge in size when heated and change the original structure from flat mica particles to bulk grains of slit-like structure, while reducing its density by 8...12 times. This property has provided vermiculite with wide application in various areas: production, construction, environmental and other human activities. Vermiculite is under studying still now. The technologies using different fractions of this unique material are developing. The new equipment for the implementation of these technologies [1-15] is being designed as well.

A large-scale study and application of expanded vermiculite began in the second half of the twentieth century in our country, and the industrial development of the world's largest Kovdor phlogopite-vermiculite deposit in the Murmansk region began in 1965 with the development of the main phlogopite deposit located under the vermiculite deposit. To get to phlogopite, a raw material that was more in demand at that time, it was necessary to exhaust vermiculite ores and create several warehouses with different vermiculite contents and a warehouse of vermiculite-sungulite rock.

The processing of vermiculite ores began in 1975, but the processing plant operated only on rich stored and recovered ores. The enrichment technology was based on the use of gravity methods and according to the cadaster of mining waste [16], the extraction of vermiculite was at a low level, which characterizes the very high quality of the tailings sent to the tailing dump.

The material with grain size larger than 20 mm, without being in demand, was discharged into the dry tailings dump without any enrichment. Among the present technologies and equipment, the hammer crushers with cutting blade hammer have got good application perspectives. At the same time, there is a high level of wear of the operating tools. Grinding by other machines (jaw, cone, roller and others) reduces the crushing quality of vermiculite particles. They flake, partially crumble, but doesn't change in overall dimensions significantly. Application of the proposed equipment will not have the mentioned above disadvantages

The issues of improving the technology of processing vermiculite-sungulite conglomerates were reviewed in the article [16]. In a number of other publications, for example [17-20], the issues of returning depleted vermiculite ore and tailings stocks to industrial circulation were considered. This article reviews some aspects of technology and equipment for processing large-sized mica grain ore with dimensions of 20 mm and larger, located in the dumps of dry tailings for the production of expanded vermiculite.

1. Samples and Research Methods

Large-sized row vermiculite mica grains with a vermiculite content of 15...20% by weight [16] is extracted from storage facilities and subjected to gravitational enrichment according to the technology developed at Kovdorslyuda OJSC using slot separators and brought to a target product concentration of 90...95%. Then the resulting material was sent chopping units for grinding to a given size in.

The optimal particle size of vermiculite concentrates depends on the purpose of the expanded product, which is determined by the consumer, but not only by him. JSC "Kovdorslyuda" produced concentrates of size groups KVC-8 and KVC-16, but they were used only in hydroponics, and mainly outside the country, and their firing was a very costly process, since it was carried out in fired furnaces operating on hydrocarbon fuel. Without going into energy calculations, let's try to determine roughly the optimal firing time and the corresponding maximum particle size of the concentrate.

The article [19] describes the research during which the dependence of the calculated time of firing in electric furnaces of concentrates of vermiculite particles of various size groups was set up on the basis of analytical modeling of the layered thermal conductivity of the plates of expanded vermiculite. Vermiculite ore concentrates have a very inhomogeneous particle size, but the distribution of particle sizes approximately obeys the normal distribution of random variables [19]. If a concentrate in a volume of 1 m^3 contains particles with nominal diameters from 1 to 7 mm and more (Figure 1), then the time of their firing to complete expanding will correlate with their sizes.

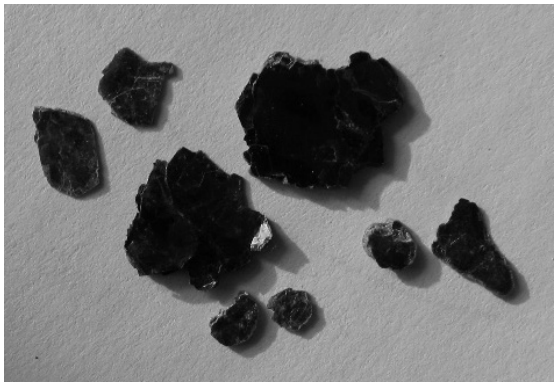

Fig.1. Photo of granulometric heterogeneity of concentrate KVK-4 of the Kovdorskoe field.

The larger the particle, the more time it will take, and the ratio t_{omax}/t_{omin} can reach twelve. Therefore, vermiculite should be fired only after preliminary separation into fractions in order to spend less energy, without overfiring the small particles and not leaving the largest ones unexpanded. This is an accompanying question, but it is closely related to the tasks being solved here.

The study of layered thermal conductivity, based on the principle of equalization of temperatures from the periphery to the center of the plates of expanded vermiculite grains, led to a simple analytical dependence for determining the sufficient duration of firing [19]:

$$t_f = 0.4\frac{d_c^2}{a}, \quad (1)$$

where a is the coefficient of thermal conductivity, m^2/s (a=2.9·10 $^{-6}$ m^2/s [19]); d_c is conditional particle diameter, determined by the formula:

$$d_c = \sqrt{x^2 + y^2},$$

where x and y are the maximum and minimum particle sizes.

According to the formula (1), the values of the time of complete expanding of the vermiculite concentrate particles during firing and the corresponding particle sizes were calculated (Table 1).

Into the analytical dependence (1) does not include the surface temperature of the expended vermiculite grain at the end of the firing process, but the given formula was obtained for a value of 599 ºC, which was roughly determined as optimal for electric furnaces with a heating element temperature of 720...750 ºC. The indicated temperatures were measured during the experimental research of a pilot industrial modular-firing furnace in 2015. Using a pyrometer, we determined the heating temperatures of the surface of expanded

.

grains at the exit from the furnace, with their full and high-quality expanding, which were in the range 586...612 ºC (with an average value of 599 ºC) [19].

Table 1 - Nominal particle diameters and their firing time until full expansion

d_v, [mm]	1.0	2.0	4.0	6.0	8.0	10.0	12.0	14.0	16.0	18.0	20.0
t_o, [s]	0.068	0.27	1.09	2.44	4.34	6.79	9.78	13.31	17.38	21.99	27.15

The other increased temperature conditions with heating of radiant electric heaters over 750 ºC allow to reduce the firing time, but at the same time increase the risk of soot deposit on their surfaces and reduce the reliability of the furnaces. Figure 2 shows the dependence of the firing time on the nominal diameter of the vermiculite concentrate particles, which does not depend on the type of ore from which it is obtained (Kovdorsky, Koksharovsky or Tatarsky concentrates). From the graph analysis it follows that the firing of large-sized concentrates without preliminary grinding of particles with large sizes requires an increase in firing time, which will lead to a decrease in the productivity of electric furnace units. Therefore, Figure 2 shows a graph of the dependence of the firing time on the nominal diameter of a particle with a maximum size of 10 mm.

With the nominal diameter d_c=4 mm, corresponding to the Kovdor concentrate KBC-4, the calculated firing time is 1.086 s (Figure 2). But in the massif, as noted above, there is a large number of particles with sizes of 7...8 mm, therefore, when setting up the furnace unit, the value to is adjusted so that the largest particles are completely swollen. Consequently, the real time to during firing of KBC-4 concentrate should be 3.39 s (Figure 2). The experimental value of the duration of heat treatment in a furnace with a movable base platform [17] during firing KVC-4, at which the highest productivity is achieved, is approximately 3.1 s - point *a* (Figure 2).

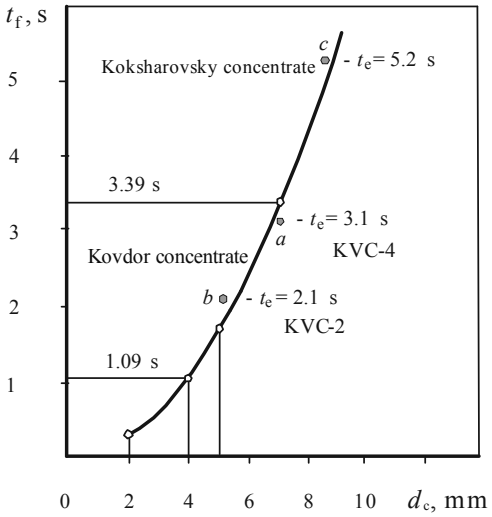

Fig. 2. The dependence of the firing time on the nominal particles diameter of vermiculite concentrate.

For KVC-2 concentrate with d_c=2 mm, the firing time is 0.27 s (Table 1), but the actual calculated t_o, taking into account large particles up to 5 mm, should be 1.78 s. In the experiment, it was equal to about 2.1 s – point *b* (Figure 2). The third experimental point *c* was added during experiments with the Koksharovsky concentrate KBC-4. The size of the maximum particles reached 8.5...9 mm in it. The firing time was 5.2 s (Figure 2). We have already noted above that heat treatment of concentrates without preliminary grinding of large-sized particles is not profitable due to a decrease in productivity and an increase in energy consumption. Therefore, we will proceed to consider the technology and equipment for their preparation and grinding.

2. Technology and equipment for grinding large-sized micas

Concentrates of the Kovdorskoye deposit, the KBC-8 and KBC-16 grades, before they are fired in electric furnaces, must undergo preliminary fractionation, for example, on a drum sieve, at the outlet of which all particles with sizes exceeding 10 mm are collected in a separate bin. This is the preliminary

preparation of raw materials. All other particles that pass through the sieve go to the firing. Large-sized particles of more than 20 mm after gravitational enrichment according to the proven technology using slotted separators, extracted from the dumps, are sent for grinding in chopping units.

Figure 3 shows the of the chopping unit device. It contains a hopper 1, a dispenser 2 with a feed drum 3 and a flow divider of large-sized mica particles 4, made in the form of alternating crossed plates. The dispenser drum is connected to an adjustable gear motor (not shown in Figure 3) and a chain drive with one of the receiving drums, for example, 5, the shaft of which is connected to another receiving drum 6 by a gear drive, which provides their rotation with equal angular velocities ω in opposite directions. The trays 7, leading from the flow divider 4 to the receiving drums, reinforced with stiffening ribs 8, have projections 9 in the lower part and channels 10 (Figure, 4 *a*), inside them. There are longitudinal slots 11 in the drums 5 and 6, and the channels 10 in the projections 9 are parallel to them.

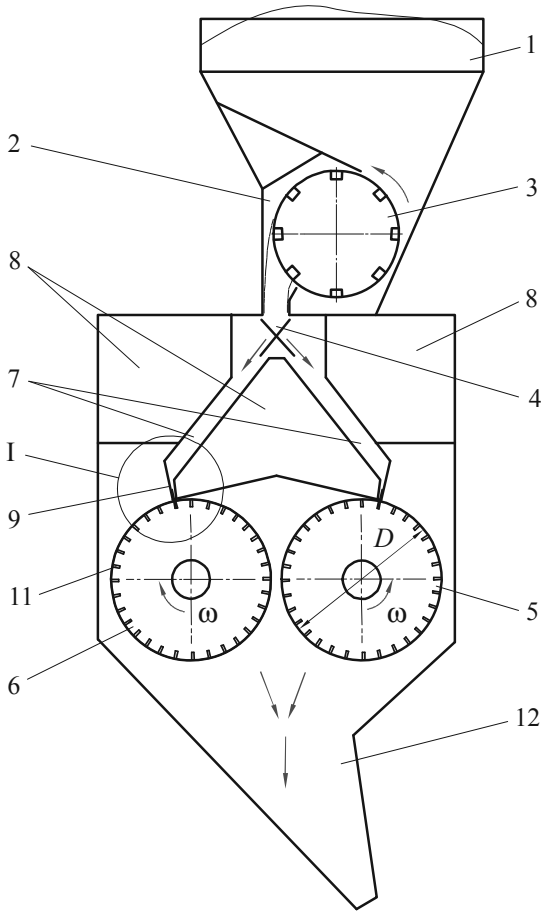

Fig.3. The schematic diagram of the chopping unit.

The drum dispenser delivers the large-sized concentrate to the flow divider, which distributes approximately equally the mica particles along the trays 7. The slots 11 in the receiving drums have a depth of h=10 mm. When large particles of mica come from the flow divider and go down the trays 7, they, being in the channels 10, abut against the surfaces of the rotating drums 5 and 6, and slide along them until they fall out into the nearest slot 11 (Figure 4, *a*).

The receiving drums, turning with a certain angular velocity ω, chop off the particles on the projections 9 of the trays 7 and carry them until they fall out under their own weight into the lower part 12 of the hopper of the chopping unit body. The remainder of the chopped off particle, sliding along the surface of the receiving drum, falls into the next slot and this happens several times on each drum 5 and 6 until all particles are chopped into narrow strips 10 mm wide and length determined by its original size, for example 20...30 or 20...40 mm (Figure 5). Feeding of large particles of mica by the dispenser drum is selected so as to exclude more than two particles from falling into one place in the slot 11 in order to avoid their jamming. The width of these slots is such that two particles can be located in it without jamming. In this case, two particles are chopped off at once. This process of gradual splitting of particles into strips occurs across the entire width of

each of the receiving drums. Stiffening ribs 8, located at an equal pitch one after the other, exclude sagging of the projections 9 during the particles chopping off.

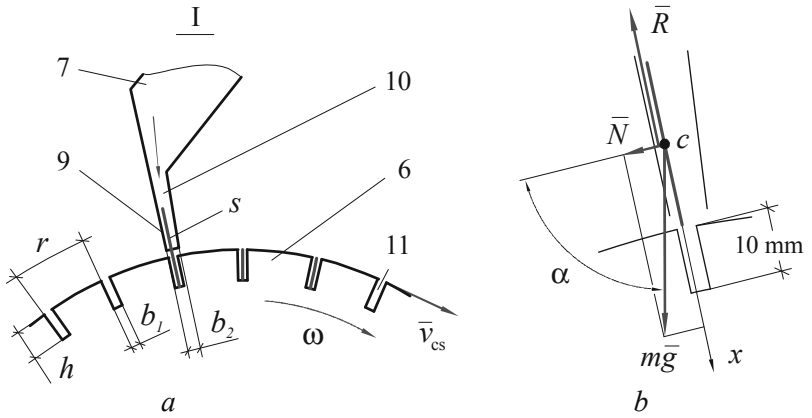

Fig.4. Schemes: *a* – design diagram of the technical characteristics of the unit (fragment I according to Figure 3); *b* – scheme of forces acting on a particle.

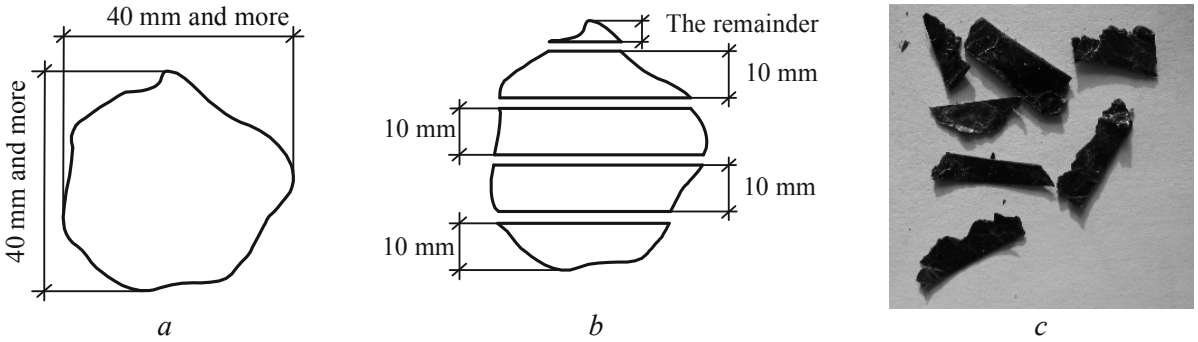

Fig. 5. The shape and size of the particles of large-sized concentrate: *a* – original; *b* – after cutting into strips; *c* – photograph of a chopped particle

The chopping unit provides a gradual reduction of only one particle size to 10 mm, while its other size remains unchanged and equal to 20 mm or more, depending on its initial size (Figure 4). But in order for the chopped particles to expand quickly at a temperature of the heating elements of the furnace of 720...750 ° C, this is enough [19], since the radiant energy, according to the model of the layered thermal diffusivity of vermiculite plates, penetrates from both sides in the transverse direction over a size of 10 mm (by 5 mm left and right).

3. Chopper unit work process theory

Based on the principle of the chopper unit operation, let's determine its technical characteristics, having the following initial data:

- outer diameter of receiving drums 5, 6 (Figure 3) – D=1 m;
- the width of the receiving drums 5,6 (Figure 3) – B=1.25 m;
- the depth of the transverse grooves (Figure 4, *a*) – h=0.01 m;
- width of transverse grooves (Figure 4, *a*) – b_1 = 0.0025 m;
- the width of the channels in the projections of the trays (Figure 4, *a*) – b_2=0.003 m;
- angle of inclination of trays projections to the vertical – 16 °.

The angular speed of rotation ω of the receiving drums can be calculated by considering the dynamics of the process of a mica particle motion at the moment of its falling out of the channel 10 into the transverse groove 11 of the drum 6.

Let's consider the design scheme (Figure, *b*). The *x* axis is directed downward along the surface of the mica plate. The point *c* is the center of gravity of a plate of mass *m*, so its motion when falling out can be described as the motion of a material point *c*.

The differential equation of its motion will be:

$$m\ddot{x} = mg \cdot \sin\alpha - mgf \cdot \cos\alpha, \quad (2)$$

where *f* – is the coefficient of sliding friction of vermiculite mica on steel (for large-sized Kovdor concentrates $f \sim 0.68$ [20]).

Reducing equation (2) by the particle mass, dividing the variables and integrating twice over the time of motion τ, we get:

$$x = 0.5\left(g \cdot \sin\alpha - fg \cdot \cos\alpha\right)\tau^2 + x_0. \quad (3)$$

Since the initial velocity of falls out particle is equal to zero, and in equation (3) the initial coordinate x_0 is zero, then solving the quadratic equation (3) with regard to τ, we obtain the time of motion of the mica plate when falling into the slot of the receiving drum:

$$\tau = \sqrt{\frac{2x}{g \cdot \sin\alpha - fg \cdot \cos\alpha}}. \quad (4)$$

Since the depth of the grooves is h=0.01 m, then the drop-out path is x = 0.01 m, and the angle α is equal to: 90° – 16° = 74°.

Substituting the indicated values and the coefficient of friction into expression (4), we obtain the dropout time or slot filling time:

τ = 0.052 s.

For further modeling of the operating process of the chopping unit, determining the circumferential speed of its receiving drums, and then the angular speed of their rotation, let's make a number of assumptions:

- all mica particles have a thickness of s = 0.001 m;
- all particles have a rectangular shape with a width of e=0.02 m and a surface area equal to the areas of real particles averaged over the conventional diameters d_c;
- in a time τ = 0.052 s, the receiving drum rotates through an angle corresponding to the arc of its circumference, equal to half the width of the groove – 0.5 b_1;
- the particles in the grooves of the drums are arranged in one row tightly to each other.

Let's determine the circumferential v_{cs} and angular ω speed of the receiving drums:

$$v_{cs} = \frac{0.5 \cdot b_1}{\tau} = \frac{0.5 \cdot 0.0025}{0.052} = 0.0241 \text{ m/s}; \quad (5)$$

$$\omega = \frac{v_{cs}}{0.5D} = \frac{0.0241}{0.5 \cdot 0.1} = 0.0482 \text{ rad/s}. \quad (6)$$

Let's determine the speed:

$$n = \frac{30\omega}{\pi} = 0,46 \text{ rpm}. \quad (7)$$

After the particle falls out into the groove, it takes some time for it to jam between the walls of the groove and the channel of the tray, i.e., to select the gaps due to the dimensions b_1 and b_2, which corresponds to the length of the arc:

$\lambda = b_1 + b_2 - s = 0.0025 + 0.003 - 0.001 = 0.0045$ m.

After jamming, the particle is chopped off in a time corresponding to the arc length equal to the mica particle thickness *s*. However, mica has a layered structure, which makes it difficult to shatter, therefore chopping process takes longer to completely separate the severed part from the main particle. To guarantee the results we model this process with time allowance three times longer time then actual chopping time and the length of the drum arc l_a corresponding to this time, equals to:

$l_a = 3s$.

Then the time of one cycle (from the moment the first particle falls out until the second one falls out) will correspond to the circular arc of the receiving drums corresponding to the step of the slots *r*:

$r = \lambda + s + l_a = 0.0045 + 0.001 + 3 \cdot 0.001 = 0.0085$ m.

.

With a drum diameter of 1 m, the ratio of their perimeter L to step r gives the number of chopping cycles k for one drum revolution. For a two-drum chopping unit shown in Figure 3, the total number of chopping cycles will be:

$$k = \frac{2L}{r} = \frac{2\pi D}{r} = \frac{2 \cdot 3.14 \cdot 1}{0,0085} = 739 \cdot$$

Dividing the resulted value by the rotational speed n, we get the number of choppings per minute:

$K = \frac{k}{n} = \frac{739}{0,46} = 1606$ (96390 per hour).

With a drum width of 1.2 m and a conventional particle width of e=0.02 m, 60 rectangular plates with dimensions of 20×10 mm are separated in one chop, and their total number falling into the lower part of the chopping hopper per hour is 5783400 pieces. If the thickness of the plate is 0.001 m, then the volume of all the plates dropped out per hour is:

$V = 5783400 \cdot 0.001 \cdot 0.02 \cdot 0.01 = 1.157$ m^3.

The true density of hydromica is approximately equal to 2300 kg/m^3 [7], so the resulted volume can be converted to mass:

$m = \rho V = 2300 \cdot 1.157 = 2661$ kg.

This value is equal to the theoretical hourly productivity of the chopping unit – 2.66 tons/hour.

Let us write down the formula for the theoretical mass productivity of two drum chopping units in general form (kg/h):

$$P_t = 60 \frac{2\pi BDsd_c}{r \cdot n} \rho, \quad (8)$$

where d_c is the average nominal diameter of a vermiculite mica particle from the bulk of the initial enriched large-size concentrate, m. In this case, the drum rotation frequency n should be determined with the consideration of the formulas (5-7).

If we recalculate the mass productivity for the volumetric (after firing in the furnace) according to the formula (m^3/h):

$P_v = k_e P_t$.

If we take into account the expanding coefficient for large-sized Kovdor concentrates KVC-8, which are closest to that obtained from chopped mica plates, equal to $k_e \sim 10.8$ m^3/t, we obtain an approximate value: P_v=28.7 m^3/h. Taking into account the operational factors that reduce the theoretical productivity by 12...15%, it is possible to determine the actual monthly mass productivity of one unit with the parameters given above:

$P_t = 1630 \ldots 1685$ tn /month.

This will allow loading 27...28 railway open-top wagons with chopped vermiculite concentrate per month.

4. Unit operation as part of a specialized electric furnace

The two-drum unit with considered operational factors is capable of producing, on average, after firing in a furnace, expanded vermiculite about 24.8 m^3/hour. If we reduce the width of the receiving drum to 1 m, and the diameter to 0.9 m, then such a single-drum unit can be built into the dosing system of a three-module electric furnace with a vibrating base platform [17, 18] and process large-size concentrates immediately before firing at the consumer. Focusing on formula (8), we obtain the productivity of such a furnace for expanded vermiculite:

$$\frac{0.5 \cdot 24.8 \cdot 0.9}{1.2} = 9.3 \text{ m}^3 / \text{hour},$$

which roughly corresponds to the performance of an electric furnace with two power technology units (with P_v of 4.5 m^3/h each) and vibrating platforms with forced kinematic excitation (Figure 6) [22].

An industrial furnace consists of two identical energy technology blocks and contains a frame 1, baking trays 2 with movable bases 3, thermally insulated covers 4, electric heaters 5 fixed on the fixing heads 6, rollers 7 located in guides 8 installed transversely to the flow direction of the expanding chopped vermiculite

moving along the base plates. Movable bases are placed obliquely, parallel to each other and one above the other. The furnace also contains a gear motor 9, a drive shaft 10 mounted in bearings 11 with eccentrics mounted on it. The eccentrics are equipped with rolling bearings (in the figure they are covered with movable bases and are not visible), which are rotated on shaft 10 relative to each other by 120 °.

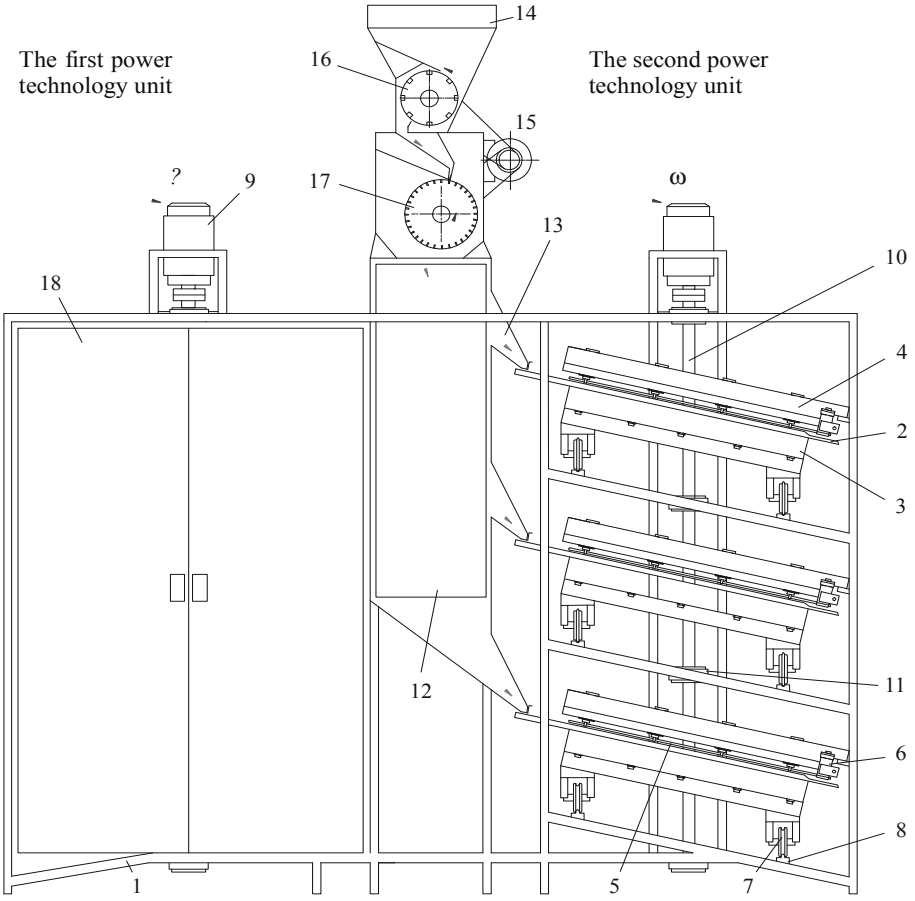

Fig. 6. Industrial furnace consisting of two technological units with a chopping unit built into the raw material dosing system

The hopper 12 for chopped vermiculite concentrate is located in the central part of the furnace and has trays 13 with slide gates installed with gaps above the parts of the base plates 2 protruding on the left. A single-drum chopping unit is installed on the hopper and in this embodiment has a drum dispenser 14 and a drive 15, which is configured so that its transmissions set the rotation of the dispenser drum 16 and the receiving drum 17 with such a ratio of angular velocities at which the excessive supply of concentrate to the chopping unit and wedging of particles in the lateral slots of the drum are eliminated. The furnace is closed on all sides by thermally insulated doors 18, which are conditionally removed on the second power technology unit.

During the operation process, the bearings of the eccentrics, when the shaft 10 rotates with an angular velocity ω, act on the protruding parts of the movable bases 3 and cause their transverse harmonic vibrations with regard to the vermiculite flow with an amplitude *A* equals to the eccentricity value, which is the same for all eccentrics of the drive shaft. In this case, the springs (not shown in the figure) installed on the sides of the movable bases 3 opposite to the eccentrics provide their return movement [23-27]. Under the action of transverse vibrations, the vermiculite concentrate from the hopper 12 through the trays 13 gradually fed onto the protruding parts of the base plates 2 and, moving along their surfaces, enters the thermal field of the electric heaters 5 under the thermally insulated covers 4 and in 3.5...4 under the action of high temperature expands and comes out of the furnace (right and left). The slide gates of the trays 13 provide control of the thickness of the layer exiting the raw material trays 13.

In the electric furnace under consideration, the vibrations of the movable bases are forced by the eccentrics of the drive shaft. Therefore the system does not operate in a resonance mode, which is very sensitive to fluctuations of various factors that affect the stationarity of vibrations and the parameters of

vibration transportation of chopped concentrate along the base plates. For example, if there are changes in the excitation frequency ω, then the amplitude will remain equal to the eccentricity, and this will provide steady fluctuations of the bases 3 and the stationarity of the technological firing process, the duration of firing will not change, there will be no vermiculite expanding or overburning, and the furnace productivity will remain unchanged. Even the contamination of the guide runners 8 with fine vermiculite formed during expanding cannot affect the change in amplitude, since the oscillations are set by the drive shafts 10 and the gear-motors 9 forcibly.

Conclusion

On the basis of the analytical dependence, there were calculated the values of the expanding time of particles of large-sized vermiculite concentrates for the required sizes during firing in electric furnaces with a heater temperature of 720 ... 750 ° C. But these results can be considered as indicative before a study of the process on a physical model is conducted.

Analysis of the graphical dependence correlates with the experimental data and shows that firing large-sized particles without grinding them in chopping units will require a significant increase in firing time, and this will negatively affect the electric furnaces capacity with movable bases. Therefore, the optimal longitudinal size of the obtained particles of chopped vermiculite concentrate is taken to be 10 mm, which is the minimum sufficient, since the radiant energy of the heaters, according to the model of the layered thermal diffusivity of vermiculite plates, penetrates from both sides in the transverse direction, 5 mm from the left and right.

The research of the dynamics of the motion of particles when they fall out into the slot of the receiving drums has shown that the time of this falling is about 0.052 s, including friction. Based on this time and the specified parameters of the design elements of the chopping unit, the angular speed of rotation of the receiving drums and the operating capacity of the two drum unit were calculated. It is equal to 1630...1685 tons/month, which corresponds to a monthly shipment of chopped concentrate in the amount of up to 28 railway open-top wagons per month.

The indicated volumes correspond to 18000...20000 m^3 of expanded vermiculite. The basic two-drum chopping unit is designed for operation at the deposit and processing of large-size concentrates obtained by enrichment from stored and newly obtained vermiculite micas.

It is possible to use its single-drum version with reduced dimensions of the receiving drum and other design elements as a chopping mechanism built into the dosing system of industrial electric furnaces with movable base platforms in the production of expanded vermiculite at the construction industry enterprises. In this case, the consumer buys enriched vermiculite concentrate, consisting of large particles with nominal diameters of 20...40 mm. Such a chopping mechanism is capable of ensuring the operation of a double industrial electric furnace of two energy technology blocks with a capacity of approximately 9.5 m^3/h.

The proposed technical solution has good application perspectives for the processing of particles of large-scale raw materials from other deposits.

Acknowledgments

The research is carried out at Tomsk Polytechnic University within the framework of Tomsk Polytechnic University Competitiveness Enhancement Program grant.

REFERENCES

1 Balima F., Laurence Reinert L., An-Ngoc N., Le Floch S. Effect of the temperature on the structural and textural properties of a compressed K-vermiculite. *Chemical Engineering Science*. 2015, Vol. 134, pp. 555–562.

2 Chen L., Pingxiao Wu P., Chen M., Liu T. Chen L., Pingxiao Wu P., Chen M., Liu T. Preparation and characterization of the eco-friendly chitosan/vermiculite biocomposite with excellent removal capacity for cadmium and lead. *Applied Clay Science*, 2018, Vol. 159, pp. 74–82.

3 Kogal J.E. *Industrial minerals & rocks: commodities, markets, and used*. Littleton, Society for Mining, Metallurgy and Exploration Inc., 2006, 1565 p.

4 Fuks L., Herdzik Koniecko I. Vermiculite as a potential component of the engineered barriers in low and medium level radioactive waste repositories. *Applied Clay Science*, 2018, Vol. 161, pp. 139–150.

5 Cunha Costa J.A., Martinelli A.E., Nascimento R.M., Mendes A.M. Microstructural design and thermal characterization of composite diatomite-vermiculite paraffin-based form-stable PCM for cementitious mortars. *Construction and Building Materials*, 2020, Vol. 232, article number 117167.

6 Tian W., Li Z., Ge Z., Xu D., Zhang K. Self-assembly of vermiculite-polymer composite films with improved mechanical and gas barrier properties. *Applied Clay Science*, 2019, Vol. 180, article number 105198.

7 Hombostel C. *Construction Materials: Types, Uses, and Applications*. New York, John Wiley & Sons Inc., 1991, 878 p.

8 Ruth Hanken B.L., Arimatéia R.R., Farias G.M.G., Agrawal P., T.J.A. de Mélo. Effect of natural and expanded vermiculite clays on the properties of eco-friendly biopolyethylene-vermiculite clay biocomposites. *Composites Part B: Engineering*, 2019, Vol. 175, article number 107184.

9 Kariya J., Ryu J., Kato Y. Development of thermal storage material using vermiculite and calcium hydroxide. *Applied Thermal Engineering*, 2016, Vol. 94, pp. 186–192.

10 Ding F., Gao M., Wang J., Shen T., Zang W. Tuning wettability by controlling the layer charge and structure of organovermiculites. *J. of Industrial and Engineering Chemistry*, 2018, Vol. 57, pp. 304–312.

11 Bryanskikh T.V., Kokourov D.V. Energy efficiency of electric furnaces with movable floor in firing of vermiculite concentrates of different size groups. *Refractories and Industrial Ceramics*, 2017, Vol. 58, pp. 368–373.

12 Mouzdahir Y. et al. Synthesis of nanolayered vermiculite of low density by thermal treatment. *Powder Technol*, 2009, Vol. 189, pp. 2–5.

13 Figueiredo S. The influence of acid treatments over vermiculite based material as adsorbent for cationic textile dyestuffs. *Chemosphere*, 2016, Vol. 153, pp. 115–129.

14 Sofiyev A.H. Review of research on the vibration and buckling of the FGM conical shells. *Composite Structures*. 2019, Vol. 211, pp. 301-317.

15 Mucahit Sutcun. Influence of expanded vermiculite on physical properties and thermal conductivity of clay bricks. *Ceramics In ternational*, 2015, Vol. 41, pp. 2819–2827.

16 Inventory of waste mining and metallurgical production of the Murmansk region [Kadastr otkhodov gorno-metallurgicheskogo proizvodstva Murmanskoj oblasti. Available at: www.murman.ru/ecology/cadastre (accessed 1.10.2020). [in Russian]

17 Nizhegorodov A.I., Gavrilin A.N., Moyzes B.B. Improving the technology for processing sungulite-vermiculite conglomerates. *Bulletin of the Tomsk Polytechnic University. Geo Assets Engineering*, 2019, Vol. 330, No.4, pp 98–109.

18 İşçi S. Intercalation of vermiculite in presence of surfactants. *Applied Clay Science*, 2017, Vol. 146, pp. 7-13.

19 Nizhegorodov A.I., Zvezdin A.V. Transformation of vermiculite energy into mechanical transformation energy during firing in electric furnaces with «zero» module. *Refractories and industrial ceramics*, 2016, Vol. 57, No 3, pp. 239 –245.

20 Nizhegorodov A.I. Experimental determination of friction coefficients of some potentially thermoactive materials, *Stroitelnye materialy*, 2016, Vol. 11, pp. 63–67. [in Russian]

21 Zvezdin A.V., Bryanskikh T.B. Considering adaptation of electrical ovens with unit-type releasing to peculiarities of thermal energization of mineral raw materials. *IOP Conf. Series: Materials Science and Engineering*, 2017, Vol. 168, No 1, article number 012003.

22 Zvezdin A.V., Nizhegorodov A.I. Evaluation of energy efficiency of suspended heating system of electric furnace for heat treatment of bulk materials. *Vestnik Ir GtU*, 2019, Vol. 1, pp. 41–59. [in Russian]

23 Surzhikov A.P., Lysenko E.N., Malyshev A.V., Vlasov V.A., Suslyaev V.I., Zhuravlev V.A., Korovin E.Y., D otsenko O.A. Study of the Radio-Wave Absorbing Properties of a Lithium-Zinc Ferrite Based Composite. *Russian Physics Journal*, 2014, Vol. 57, No. 5, pp. 621-626 DOI:10.1007/s11182-014-0284-9.

24 Surzhikov A.P., Pritulov A.M., Lysenko E.N., Sokolovskii A.N., Vlasov V.A., Vasendina E.A. Influence of solid-phase ferritization method on phase composition of lithium-zinc ferrites with various concentration of zinc. *Journal of Thermal Analysis and Calorimetry*, 2012, Vol. 109, No.1, pp. 63-67. DOI:10.1007/s10973-011-1366-3.

25 Lozano-Lunar A., et al. Safe use of electric arc furnace dust as secondary raw material in self-compacting mortars production. *J. of Cleaner Production*. 2019, Vol. 211, pp. 1375–1388.

26 Santamaria A., Faleschini F., Giacomello G., Brunelli K., Pasetto M. Dimensional stability of electric arc furnace slag in civil engineering applications. *J. of Cleaner Production*. 2018, Vol. 205, pp. 599-609.

27 Xu W., Zhang J., Zhang R. Application of multi-model switching predictive functional control on the temperature system of an electric heating furnace. *ISA Transaction*. 2017, Vol. 68, pp. 287-292.

Article accepted for publication 21.10.2020

.

DOI 10.31489/2020No2/110-115

UDC 621.2.082.18

STATIC INTERACTION OF ROUGH SURFACES UNDER NORMAL FORCE

Khairaliyev S.[1*], Kaishubayeva N.[2], Spitas Ch.[3], Dzhundibayev V.[4]

[1]Intekko Ltd, Nur-Sultan, Kazakhstan, kh.serik@gmail.com

[2] First Wind Power Station, Nur-Sultan, Kazakhstan

[3] Nazarbayev University, School of Engineering, Nur-Sultan, Kazakhstan

[4] L.N. Gumilyov Eurasian National University, Nur-Sultan, Kazakhstan

Modern mechanical engineering designs (and some others) make more and more demands on the development of mathematical models of units in which friction is present. A condition that significantly complicates the study of the properties of a frictional contact is its discreteness with different geometric parameters of two contacting bodies, as a result of which the contact is formed only between a part of the roughness of the rubbing bodies (base and slide). The geometry of the contacting surfaces can most accurately be described by random functions, however, methods for calculating friction nodes based on random functions are very complicated. This work is the initial stage of building a model of contact interaction of two rough bodies with roughness parameters that are different for the two bodies, but constant for each individual body. In addition, the model of contact interaction is considered with a variable force compressing the contacting bodies, in the absence of an external shear force in the contact plane, and this work allows you to check the accuracy of constructing a model of interaction of friction surfaces with a relatively simple scheme of interaction of these surfaces.

Keywords: Rough surface; analytical modelling: static interaction of rough surfaces.

Introduction

At present, reliability, efficiency and environmental friendliness of machines, instruments and devices are increasingly determined by the tribological characteristics of parts and components that work with friction. Frictional resistance absorbs around 20 per cent of world energy consumption [1]. This fact draws interest of engineers and researchers towards tribological phenomena in the design and operation of machines and mechanisms.

In fact, the influence of various phenomenological aspects of friction is still quite challenging to assess and model [2]. It could include macro-, micro- and nanoscale effects such as influence of impurities, adhesion, elastic and plastic deformation and cold welding [2-13]. Descriptions of the various friction phenomena was attempted in numerous studies by considering the surface roughness effect. Surface topography observed in microscopic scale was proved to be extremely rough and of random nature, composed of alternating ledges and hollows of various dimensions referred to as surface heights, or asperities and micro cavities.

A significant contribution to the development of the adhesion-deformation theory of friction was made by I.V. Kragelskii [14], [15] and others in the form of a molecular-mechanical theory. According to this theory, friction is caused both by overcoming the forces of molecular interaction between the contacting surfaces and by the shape change of the relief of the contacting bodies as a result of elastic and plastic deformations of their surface layers. I.V. Kragelskii put forward the idea of the dual (molecular and mechanical) nature of friction. To implement external friction, shear deformations must be concentrated in the thinnest surface layers of rubbing bodies, and these layers must have lower shear strength than the base metal (the rule of a positive gradient of shear resistance).

In this paper, the contact of two rough bodies is considered and the horizontal and vertical forces of interaction are calculated, which are the sums of the set of forces of contact interaction of the roughness of two surfaces; in this work, the horizontal external force is not considered and therefore the sum / integral of the horizontal internal forces arising in each contact should be equal to zero.

1. Normal force model

We will consider the contact of two surfaces at relative rest. As microscopic imaging shows, when two macroscopically flat bodies with microroughness come in contact, the contact occurs at multiple asperities of arbitrary shapes, and varying sizes and heights. The first step in the mechanical contacts analysis is the surface characterization. The knowledge of some statistical surface parameters is very important for the modeling of the surface interaction. As specified in the ASME standards, surface could be defined by waviness and roughness profiles (see Fig. 1) [16]. The first pattern is a real rough surface profile, the second can be the result of imperfect processing and vibrations, the third is the microroughness inherent in the production of the material.

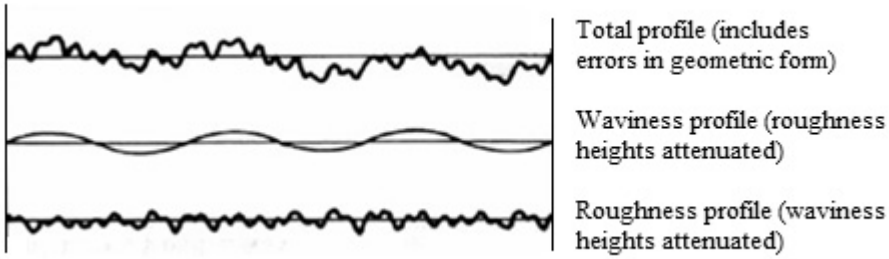

Fig. 1. Schematic diagram of surface characteristics

A detailed description of the surface microgeometry of contact bodies, for the purpose of calculating the contact interaction forces, is not practical or possible; instead a more abstract model description will be used. The main goal of the study is to describe the qualitative aspects of the processes and laws of the formation of frictional forces. For the purposes of this study, the model shown in Fig. 2 can be used, and, as shown below, this scheme allows modeling the basic principles of contact interaction forces.

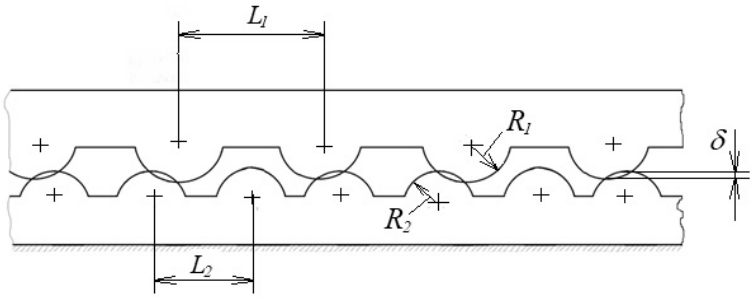

Fig. 2. Two rough contact surfaces (the slider and the base). R_1 and R_2 are micro-roughness radii of the slider and the base, respectively, δ is the overlapping of the pair of contacting micro-asperities in the vertical direction, L_1 and L_2 are period of micro-roughness of the slider and the base.

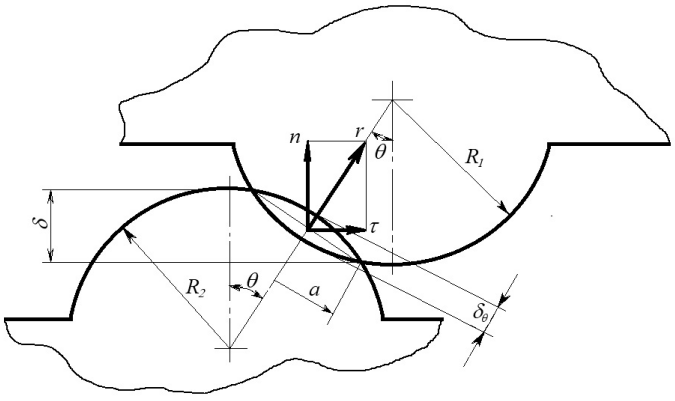

Fig. 3. Mechanical contact model between two asperities

In Fig. 3 the following designations are adopted: r is the contact reaction along the line connecting the centers of the radii of the slide and the base, n and δ_θ are the projections of the force of roughness interaction on the normal and tangent directions, a is the radius of the contact circle of two microroughnesses, θ is the angle between the vertical and the line connecting the centers.

The theory of contact between elastic bodies or Hertz Theory can be used to compute the contact of two spherical micro-asperities. The area of contact between two spheres of radii R_1 and R_2 is the circle of radius:

$$a = \sqrt{R\delta_\theta},$$

where

$$\frac{1}{R} = \frac{1}{R_1} + \frac{1}{R_2}$$

The distribution of normal force in the contact area as a function of distance from the center of the circle r is:

$$p(r) = p_0\left(1 - \frac{r^2}{a^2}\right)^{1/2},$$

where: p_0 is the maximum contact pressure given by

$$p_0 = \frac{3f}{2\pi a^2} = \frac{1}{\pi}\left(\frac{6fE_*^2}{R_2}\right)^{1/3},$$

Where f is the total force of contact interaction between two micro-asperities and

$$\frac{1}{E_*} = \frac{1-\nu_1^2}{E_1} + \frac{1-\nu_2^2}{E_2}.$$

Here E_1 and E_2 are the elastic modules and ν_1, ν_2 are the Poisson's ratios associated with each body.

The area of contact is related to the applied load f by the equation

$$a^3 = \frac{3fR}{4E_*}.$$

The depth of indentation of two spheres (or "overlapping") δ_θ can be calculated as

$$\delta_\theta = \frac{a^2}{R} = \left(\frac{9f^2}{16RE_*^2}\right)^{1/3}.$$

Hence

$$f = c\delta_\theta^{3/2} \quad (1)$$

where:

$$c = \frac{4}{3}R^{1/2}E_*.$$

The following equation can be compiled from consideration of Fig. 3:

$$R_1 + R_2 - \delta = (R_1 + R_2 - \delta_\theta)\cos\theta,$$

and hence:

$$\delta_\theta = \frac{\delta - (R_1 + R_2)(1 - \cos\theta)}{\cos\theta} \quad (2)$$

Substitution of (2) into (1) gives:

$$f = c\frac{[\delta - (R_1 + R_2)(1 - \cos\theta]^{3/2}}{\cos\theta^{3/2}} \quad (3)$$

Current study focuses on the relative sliding of two bodies (as in brakes, clutches, etc.), therefore the friction surfaces of such bodies can be considered as "lapped" and the angle θ cannot be big.

Hence $\cos\theta \approx 1$, $1 - \cos\theta \approx \frac{\theta^2}{2}$ and that simplifies (3):

$$f = c\left[\delta - (R_1 + R_2)\frac{\theta^2}{2}\right]^{3/2} \quad (4)$$

The use of the following symbol

$$\theta_0^2 = \frac{2\delta}{R_1 + R_2}$$

gives

$$f = c_\theta(\theta_0^2 - \theta^2)^{3/2} \quad (5)$$

where

$$c_\theta = c\left(\frac{R_1+R_2}{2}\right)^{3/2}.$$

The simplest way to compute the total force of contact interaction is the integration of (5) over the whole angle θ with apparent assumption of equal probability of any of its values from the interval

$-\theta_L \le \theta \le \theta_L$,

where θ_L is the greatest angle up to which it is assumed that the micro-asperity of the slider opposed to the micro-asperity of the base:

$$\theta_L = \frac{L_1+L_2}{2(R_1+R_2)}, \quad (6)$$

The total force of contact interaction is

$F = \sum_t f_t$,

where the summation of forces of contact interaction is over all pairs of contacting micro-asperities. If we suppose that the number of pair of micro-asperities is big enough then the total force of contact interaction can be calculated by integrating as follows:

$$F = \frac{j_a}{2\theta_L}\int_{-\theta_0}^{\theta_0} f d\theta \quad (7)$$

where j_a is the number of opposing pairs of micro-asperities, $\theta_0$is the angle at which the surface roughness only touch each other and it can be found as:

$$\theta_0 = \sqrt{\frac{2\delta}{R_1+R_2}}. \quad (8)$$

Comparison of (6) and (8) tells that for real surfaces $\theta_0 \ll \theta_L$ and, therefore, only a small fraction of the total number of micro-asperities is in contact. The geometry of the frictional contact can be represented in a simplified form using Fig. 4. Here, all micro-asperities of the base are reduced to one spherical element, and a plurality of micro- asperities of the slider is presented by the gray mass. In contact all micro-roughnesses of the slider are in the range of angle from -θ to θ. It should be emphasized that for relative rest of the friction pair elements, the angle to which contact exists on both sides of the slider microsphere is the same and is equal to $\pm\theta$.

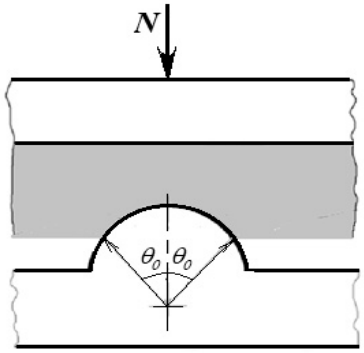

Fig. 4. Reduced model, where all microasperities of the base are reduced to one spherical.

N is a vertical force applied to the slider, θ_0 is maximum contact angle of the slider and base roughness.

The vertical component of *f* (normal contact reaction in a single contact under angle θ to the vertical) and horizontal component (friction force) can be calculated as follows:

$n = f\cos\theta,\ \tau = f\sin\theta.$

As the angle θ is small, the

$$n \approx f\left(1-\frac{\theta^2}{2}\right) \approx f,\quad \tau \approx f\theta,$$

or:

$$n = c_\theta(\theta_0^2-\theta^2)^{3/2},\ \tau = c_\theta(\theta_0^2-\theta^2)^{3/2}\theta. \quad (9)$$

The total value of these forces for all of the contact points may be computed by integrating:

$$N = \frac{j_a c_\theta}{2\theta_L}\int_{-\theta_0}^{\theta_0}(\theta_0^2-\theta^2)^{3/2}\,d\theta, \quad (10)$$

.

$$T = \frac{j_a c_\theta}{2\theta_L} \int_{-\theta_0}^{\theta_0} (\theta_0^2 - \theta^2)^{3/2} \theta d\theta.$$

Taking integrals (10) we finally get:

$$N = \frac{3 j_a c_\theta \pi \theta_0^4}{16 \theta_L}, \tag{11}$$

$$T = 0. \tag{12}$$

In this system there was no external perturbation applied in the horizontal direction and the friction force T equal to zero confirms the correctness of computations above. Equation (11) allows getting a formula for contact stiffness:

$$\delta = \sqrt{\frac{\sqrt{2}(R_1 + R_2)(L_1 + L_2)N}{j_a R_1 R_2 E_*}} \tag{13}$$

The vertical force of contact interaction obtained here (11) is not absolutely accurate. However, this force allows you to see the qualitative side of the contact interaction of rough surfaces and, at the same time, with a qualitative choice of the characteristics of the friction surfaces, it should allow calculating the contact interaction and friction forces with not very large errors.

2. Results and discussion

The vertical force of contact interaction (11) is not absolutely accurate. However, this force allows to see the qualitative side of the contact interaction of rough surfaces and, at the same time, with a qualitative choice of the characteristics of the friction surfaces, it should allow calculating the contact interaction and friction forces with not very large errors. The graph of the contact stiffness having a quadratic parabola in Fig. 5 is based on (13). More accurate theories built using more accurate description of the micro-geometry of surfaces using random functions for the distribution of the surface textures [14], [15], [17] give other power functions in these dependences. However as is evident from (13) obtained functions quite accurately reflect qualitative dependences of the processes in contacts and hence can be used to study the qualitative aspects of the friction processes.

The parameters of the friction system used to construct the graphs shown in Fig. 5 were chosen for the materials considered in [14], [15], [17]. It should be noted that the qualitative aspect of the contact stiffness graphs shown in Fig. 5 has been correspond to the real data used in these books. Our experience in calculations says that in the case of developing a sufficiently high-quality method for choosing the parameters of rough bodies, there is reason to hope for an acceptable quantitative agreement of the calculations with experimental data.

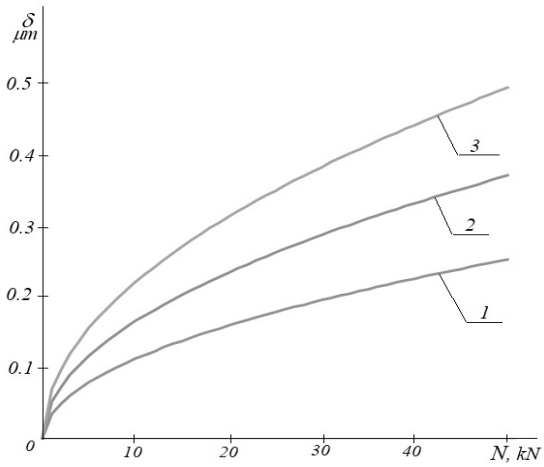

Fig. 5. Graph of contact stiffness (due to the deformation of the micro-roughness)

Table 1. The parameters of the graphs in Fig. 5

Lines on the graph	1	2	3
R_1, m	5.00E-05	1.50E-04	3.00E-04
R_2, m	8.00E-05	2.00E-04	5.00E-04
L_1, m	1.00E-04	3.00E-04	5.00E-04
L_2, m	2.00E-04	6.00E-04	9.00E-04
E^*, Pa	1.067E+11	1.067E+11	1.067E+11
j_a	1.00E+08	5.00E+07	2.00E+07

Thus, the friction pair model considered here can be used to build a qualitative model of the friction force.

Conclusion

This article deals with the static contact of rough surfaces under the action of a normal force on them, but without the action on the considered bodies of a shear force in the contact plane. The consideration of this problem includes the main parameters of the roughness of the contacting surfaces and the mechanical characteristics of the bodies and, of course, the friction force in the conditions under consideration is zero. This condition is verified by integrating the friction forces over all active contacts, and the results obtained here make it possible to accept the considered model for calculating the friction force with stable sliding of bodies relative to each other.

REFERENCES

1 Universiteit van Amsterdam, ScienceDaily, 2018. Friction: Da Vinci revisited. Available at: www.sciencedaily.com/releases/2018/03/180301091836.htm.

2 Popov, V. L., Psakhie, S. G. Numerical simulation methods in tribology. *Tribol. Int*., 2007, No. 40(6), pp. 916–923. DOI: 10.1016/j.triboint.2006.02.020

3 Savencu, O. *Simulations of Dry Friction between Rough Surfaces and Corresponding Nonlinear Problems at Nano and Microscales.* Ph.D. thesis, Cardiff University, Cardiff. 2016, pp. 4-6.

4 Bowden, F. P., Tabor, D. The Area of Contact between Stationary and between Moving Surfaces. *Proceedings of the Royal Society of London. Series A, Mathematical and Physical Sciences*, 1939, Vol. 169, Is. 938, pp. 391-413.

5 Bowden, F. P., Tabor, D. The Friction and Lubrication of Solids. Oxford: Clarendon Press. 1950, pp. 2-3.

6 Kendall, K. *Molecular Adhesion and Its Applications*. The Sticky Universe, Kluwer Academic Publishers. 2001, p.7-8.

7 Archard, J. F. Elastic Deformation and the Laws of Friction. *Proceedings of the Royal Society of London.* 1957, Vol. 243, pp. 190–205. DOI: 10.1098/rspa.1957.0214

8 Johnson, K. L., Kendall, K., Roberts, A.D. Surface Energy and the Contact of Elastic Solids. *Proceedings of the Royal Society of London. Series A, Mathematical and Physical Sciences*. 1971, Vol. 324, Is. 1558, pp. 301–313. DOI: 10.1098/rspa.1971.0141

9 Derjaguin, B. V., Muller, V. M., Toporov, Y. P. Effect of contact deformations on the adhesion of particles. *J.Colloid Interface Sci*. 1975, Vol. 53(2), pp. 314–326. DOI: 10.1016/0021-9797(75)90018-1

10 Ogilvy, J. A. Numerical simulation of friction between contacting rough surfaces *J. Phys. D. Appl. Phys*., 1991, Vol. 24(11), pp. 2098–2109. DOI: 10.1088/0022-3727/24/11/030

11 Maugis, D. Adhesion of spheres: The JKR-DMT transition using a dugdale model. *J. Colloid Interface Sci.,* 1992, Vol. 150(1), pp. 243–269. DOI: 10.1016/0021-9797(92)90285-T

12 McClelland, G. M., Glosli, J. N. *Friction at the Atomic Scale. in Fundamentals of Friction: Macroscopic and Microscopic Processes. NATO ASI Series (Series E: Applied Sciences),* Dordrecht: Spnriger. 1992, 405–425.

13 Tabor, D. Friction. The Present State of Our Understanding. *J. Lubr. Technol.,* 1981, Vol. 103(2), pp. 169–179. DOI: 10.1115/1.3251622

14 Kragelskii, I. V., Dobychin, M. N., and Kombalov V. S. Friction and Wear. Calculation methods. Oxford: Pergamon Press Ltd. 1982, 474 p.

15 Kragelskii I.V. *Friction and Wear*, Elmsford: Pergamon Press, 1982, 420 p.

16 ASME B46.1-2002, 2003, "Surface Texture (Surface Roughness, Waviness, and Lay: An American National Standard," New York: American Society of Mechanical Engineers.

17 Chichinadze A.V., et al. *Basics of tribology*, Moscow, Machinostroenie. 2001, 660 p.

Article accepted for publication 26.10.2020

DOI 10.31489/2020No2/116-122

UDC 538.971:621.039.64

DEUTERIUM TRAPPING IN TUNGSTEN IRRADIATED WITH DEUTERIUM PLASMA AT HIGH TEMPERATURES

Rakhadilov B.K.[1,2*], Skakov M.K.[1,2], Miniazov A.ZH.[2], Zhurerova L.G.[1], Nugumanova A.B.[1], Khassenov A.K.[3], Karabekova D.Zh. [3]

[1]Sarsen Amanzholov East-Kazakhstan State University, Ust-Kamenogorsk, Kazakhstan, *rakhadilovb@mail.ru
[2]National Nuclear Center of the Republic of Kazakhstan, Kurchatov, Kazakhstan
[3] E.A. Buketov Karaganda University, Karaganda, Kazakhstan

This work was attended to the study of the accumulation of deuterium, also to the investigation of the process of capture of deuterium in tungsten samples upon irradiation with a plasma beam. It was shown that after irradiation on the surface, a change in the surface is observed as the development of the relief as a result of non-uniform etching of the surface. The degree of change in the relief and structure of the surface layer of the irradiated samples depends on the irradiation temperature. The accumulation of deuterium tungsten under irradiation with deuterium plasma was studied. The conducted thermal desorption analysis of tungsten samples irradiated with deuterium plasma showed that the tungsten surface is saturated with deuterium. The data obtained by the method of emission spectrometry and thermal desorption spectrometry showed that the majority of the captured deuterium accumulates at a depth under the 7 μm.

Keywords: *deuterium, irradiation, tungsten, a plasma beam.*

Introduction

Tungsten is considered as a priority material for use in the diverter region of the ITER reactor due to such qualities as high melting point and high threshold energy of physical sputtering [1-4]. Today, one of the main requirements for materials in contact with thermonuclear plasma is the reduction of tritium content in these materials [5,6] fluxes of tritium and deuterium. It will be up to 1270 K [7]. It should be noted that the investigation of the tritium inventory. In addition, the study of the accumulation of hydrogen isotopes in tungsten materials when exposed to deuterium plasma is of particular interest for assessing the content of radioactive tritium in reactor elements during the operation of a fusion unit [8-10].

In connection with the foregoing, the purpose of this work is to study the accumulation of deuterium in tungsten materials upon irradiation with deuterium plasma.

1. Materials and methods

99.97% purity tungsten was selected as the object of study in accordance with the objectives. Samples in the form of a cylinder with a diameter of 10 mm and a height of 5 mm, were cut on the EDM machine. Before irradiation, the samples were ground and polished. Tungsten samples were irradiated with a deuterium plasma with an ion energy of 2 keV for 180 min. Samples were irradiated at temperatures of 1273 K (sample W-D-1) and 1773 K (sample W-D-2). During irradiation, the pressure in the chamber was 2×10^{-3} Torr.

Irradiation of samples with hydrogen plasma was carried out on a plasma-beam discharge setup that simulates plasma-surface interactions [11,12]. The plasma beam installation was developed to support the creation and operation of the Kazakhstan Material Tokamak for testing small-scale samples of KTM materials and equipment [13].

The study of the microstructure of tungsten samples before and after irradiation was performed using a JSM-6390 scanning electron microscope. The elemental analysis of the surface layer of irradiated tungsten was determined by the method of optical emission spectrometry on a Glow Discharge Spectrometer HR. The GD-Profiler emission glow discharge spectrometer is designed to determine the mass fraction of elements in solid samples with a pre-polished surface. The surface roughness of tungsten and the depth of craters formed after the study on an atomic emission spectrometer were determined on a Micro Measure 3D Station three-

dimensional contactless profilometer. The accumulation of deuterium in tungsten after irradiation with deuterium plasma was studied by thermal desorption spectrometry using an experimental VIKA unit [14–15]. Experimental installation VIKA allows to conduct experiments on the study of gas emission from various materials by the method of temperature-programmed desorption in the temperature range from 390 K to 1750 K with mass spectrometric recording of the emitted gases. The vacuum working chamber of the VIKA unit is shown in Fig. 1.

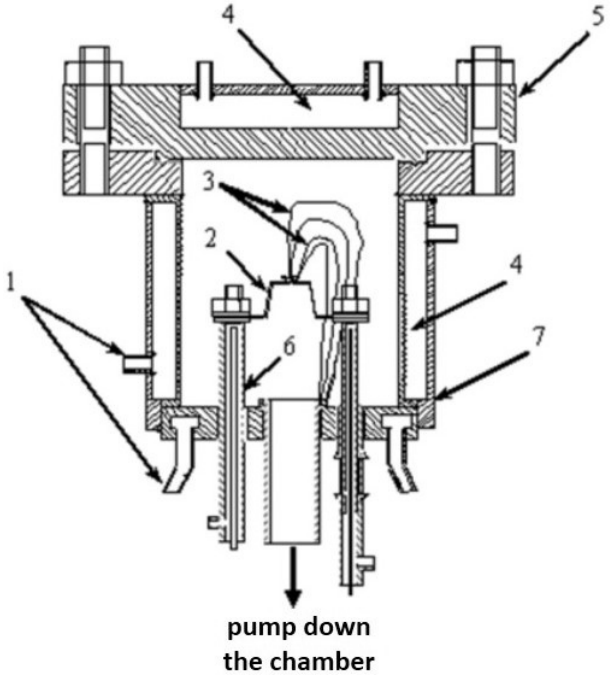

Fig.1. Vacuum working chamber installation VIKA
(1 - water cooling pipes; 2 - tantalum heater with crucible;3 - thermocouples BP; 4 - water cooling circuit; 5 - cover of the vacuum chamber; 6 - current leads; 7 - vacuum chamber housing)

Method of research was concluded in: the cut out sample of irradiated tungsten was degreased, loaded into the crucible of the working chamber of the experimental setup [16]. After that, degassing of the working chamber walls was carried out at a temperature from 473 K to 500 K for two and a half hours with continuous pumping with a vacuum magnetic discharge pump NORD-250 and an EXT 75DX turbomolecular pump. Then the chamber walls were cooled to room temperature, and then an experiment on linear heating of the sample under investigation to a temperature of 1750 K with a heating rate of 15 K/min was carried out, with a constant pumping of the evolved gases from the volume of the working chamber and recording the partial gas pressures in the chamber. The release of H_2 and D_2 molecules was measured with an RGA-100 quadrupole mass spectrometer. During the experiments, the time dependences of changes in the partial pressures of gas in the vacuum chamber of the installation as a result of gas evolution from tungsten samples in the process of linear heating of the studied samples from 390 K to 1500 K were obtained.

2. Results and their discussion

The microstructure of the surface of tungsten before and after irradiation with deuterium plasma you can find in the Fig. 2. It can be seen from the figure that after irradiation, a change in the surface is observed as a development of the relief as a result of non-uniform etching of the surface. The resulting relief consists of chaotically located protrusions and depressions of various shapes. The development of the relief on the surface of tungsten under irradiation, apparently, is due to the sputtering of the surface. Thus, differently oriented crystals are characterized by different sputtering coefficients. In this case, irradiation at T=1773 K leads to the formation of small cracks.

.

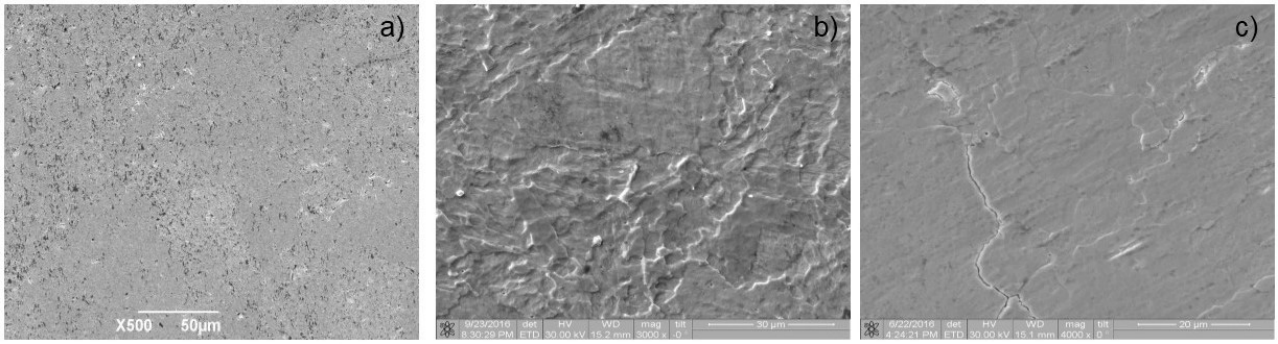

Fig. 2. The microstructure of the surface of tungsten before (a) and after irradiation with hydrogen plasma at T=1273 K (b) and T=1773 K (c)

The surface roughness was measured on an optical profilometer to assess the resulting of relief. It was determined that after irradiation with deuterium plasma the surface roughness changes. For irradiated samples at T=1273 K, the roughness parameter was Ra=0.275 μm, which is several times larger than the original sample. After irradiation at T=1773 K, the roughness was Ra=0.453 μm (Fig.3a-c).

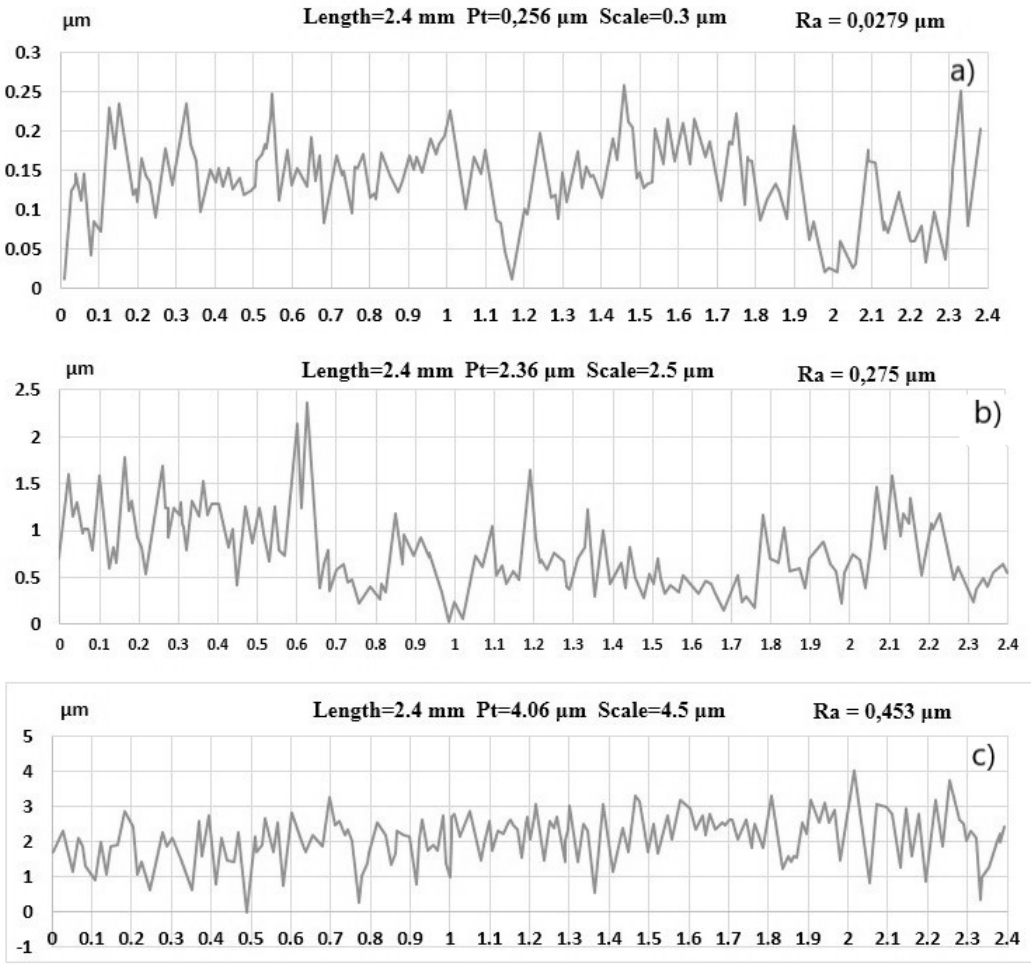

Fig. 3. The results of research on an optical profilometer

Research of the accumulation of gases in samples of tungsten under irradiation were carried out by the method of thermal desorption spectroscopy. Before conducting TDS experiments with the samples of tungsten under investigation, an experiment was carried out on gassing from an empty crucible when it was heated to a temperature of 1750 K at a rate of 15 K/min with a constant pumping out of the vacuum chamber. Fig. 4 shows the characteristic time dependences of the change in the partial pressures of gases in the volume of the working chamber when the crucible is heated.

The common view of gas evolution from an empty crucible presented in Fig. 4 may vary slightly in subsequent experiments, but the nature of gas evolution from an empty crucible remains the same. These dependences of gas evolution allow us to estimate the errors in the interpretation of data obtained during gas emission from the samples under study. From these graphs it can be seen that in the fourth mass (aum 4, corresponding to D_2), no peaks of gas evolution in the region up to 1600 K are observed in which deuterium is always present) from the elements of the design of the working chamber (growth in masses of amu 2 (H_2) and amu 3 (HD)).

Fig. 5 shows the time dependences of the change in the partial pressures of gases in the volume of the working chamber during the TDS experiments with the W-D-1 tungsten sample.

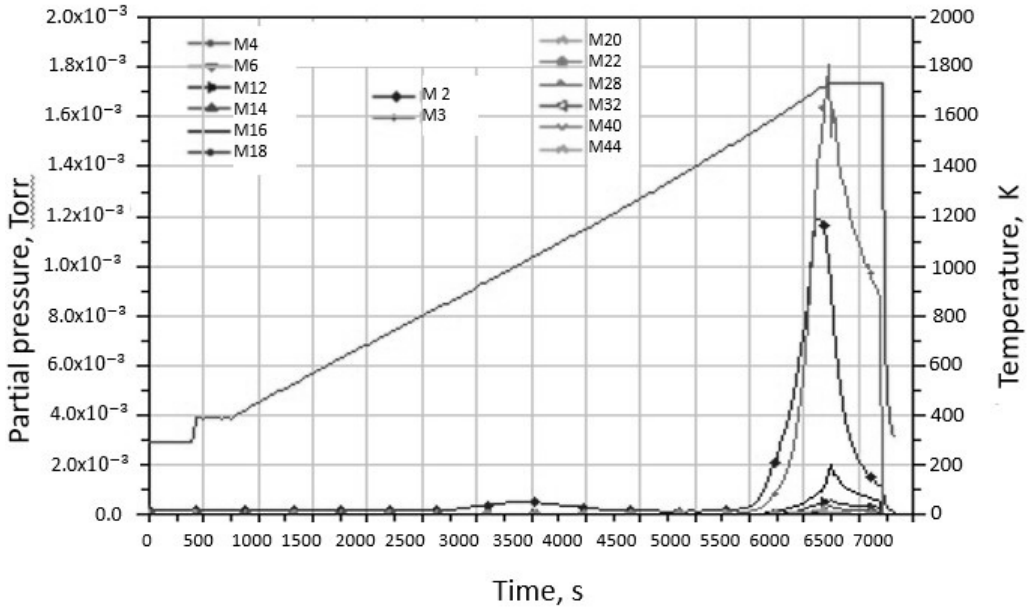

Fig. 4. Gas release from an empty crucible under heartening at a speed of 15 K/min

It can be seen that with a temperature of 1500 K and above, a significant increase in the gas evolution curves for all hydrogen isotopes begins due to separation from the crucible From the gas release graphs that was shown in Figure 4-5. This effect makes it difficult to interpret the results of TDS experiments with the test samples, therefore, further analysis of the results was carried out in the temperature range of samples from 300 K to 1500 K.

Figure 6 shows the temperature dependences of D2 excretion (amount 4) when the empty crucible is heated, samples W-D-1 and W-D-1. On the graph of gas evolution D2 (amount 4) there is a pronounced peak corresponding to the release of D2 from sample WD-1 at a sample temperature of 1223 K. The sample temperature WD-1, at which the maximum deuterium emission occurs, corresponds to the sample temperature the WD-1 sample was saturated on a plasma beam installation (approximately 1223-1273 K). For the W-D-2 sample, it was not possible to fix a noticeable deuterium release due to the high background caused by the release of deuterium from the crucible and the design elements of the vacuum chamber during linear heating.

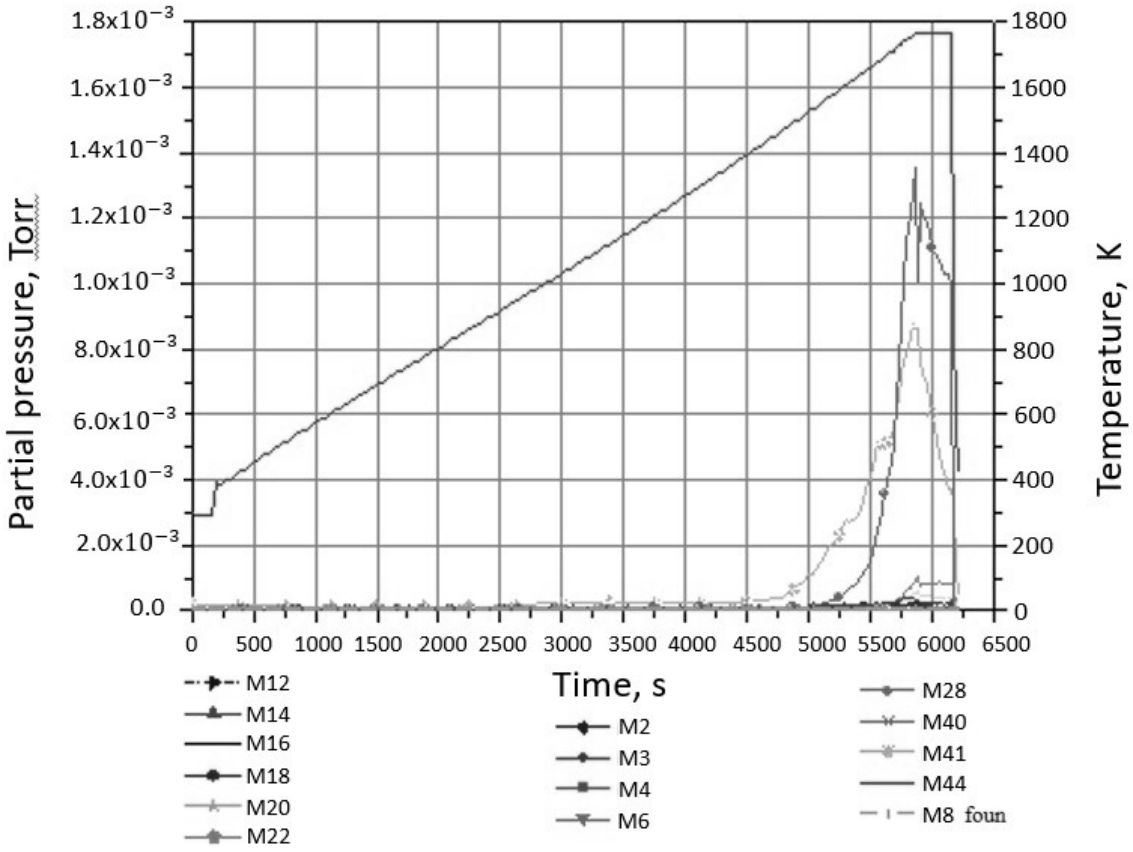

Fig. 5. Gas evolution from a sample of tungsten irradiated with deuterium plasma at T=1273 K (m = 0.4572 g; V = 15 K/min)

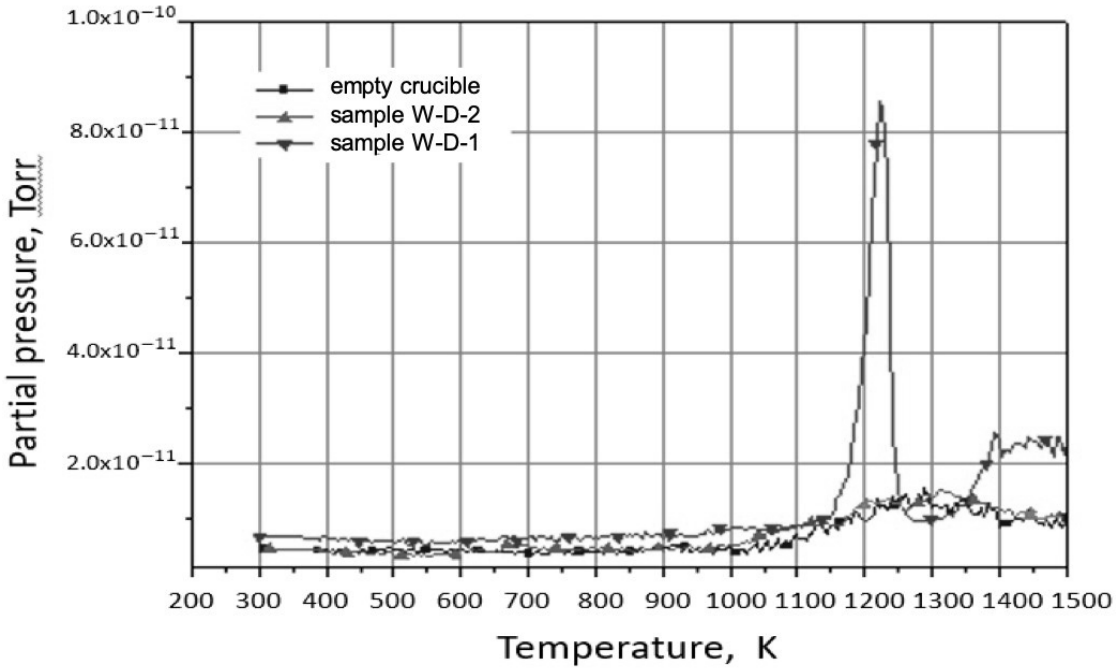

Fig. 6. Dependence of the change in the partial pressure D2 (a.e.m 4) on the sample temperature (crucible) in the working chamber of the experimental setup

Calculated from the obtained TDS dependences of the amount of released deuterium are given in Table 1. The total amount of released deuterium from the sample under study was $4{,}09 \cdot 10^{-11}$ mol despite the high irradiation temperature. The deuterium release peak had the form of a classical diffusion peak and is generally characteristic of the activation energy of deuterium diffusion in a sample with a value in the range from 130 kJ/mol to 200 kJ/mol.

Table 1 - The number of released deuterium from an empty crucible and the samples under study

Calculated data	Empty crucible	Sample, W-D-1
The amount of deuterium released to T=1500 K, mol	$2{,}84 \cdot 10^{-11}$	$6{,}93 \cdot 10^{-11}$
The amount of deuterium released to T=1500 K minus the background due to the heating of the crucible, mol	-	$4{,}09 \cdot 10^{-11}$
The amount of deuterium released to T=1500 K (referred to the mass of the samples)	-	$8{,}95 \cdot 10^{-11}$

Fig. 7 shows the results of a study of tungsten samples W-D-1 and W-D-2, obtained on an optical emission spectrometer. From Fig. 7 it can be seen that a noticeable accumulation of deuterium is observed only in the sample W-D-1. In this case, hydrogen (deuterium) accumulates in the surface layer of the W-D-1 sample to a depth of ~7 μm. At a depth of 0.5-3.0 μm, a pronounced peak is observed, which is associated with the accumulation of deuterium mainly in the near-surface layer. This means that most of the traps in the volume of the material is not active and does not capture deuterium at the irradiation temperature (1273 K). The TDS method showed small amounts of trapped deuterium, since the samples were irradiated at high temperatures. And the method of optical emission spectroscopy, we obtained only the qualitative characteristics of the distribution of deuterium. The data of both methods are consistent with the nature of the temperature dependence. A noticeable accumulation of deuterium is observed at an irradiation temperature of 1273 K. At a temperature of 1773 K, the accumulation is significantly reduced, which is associated with the formation of traps with low binding energy with hydrogen.

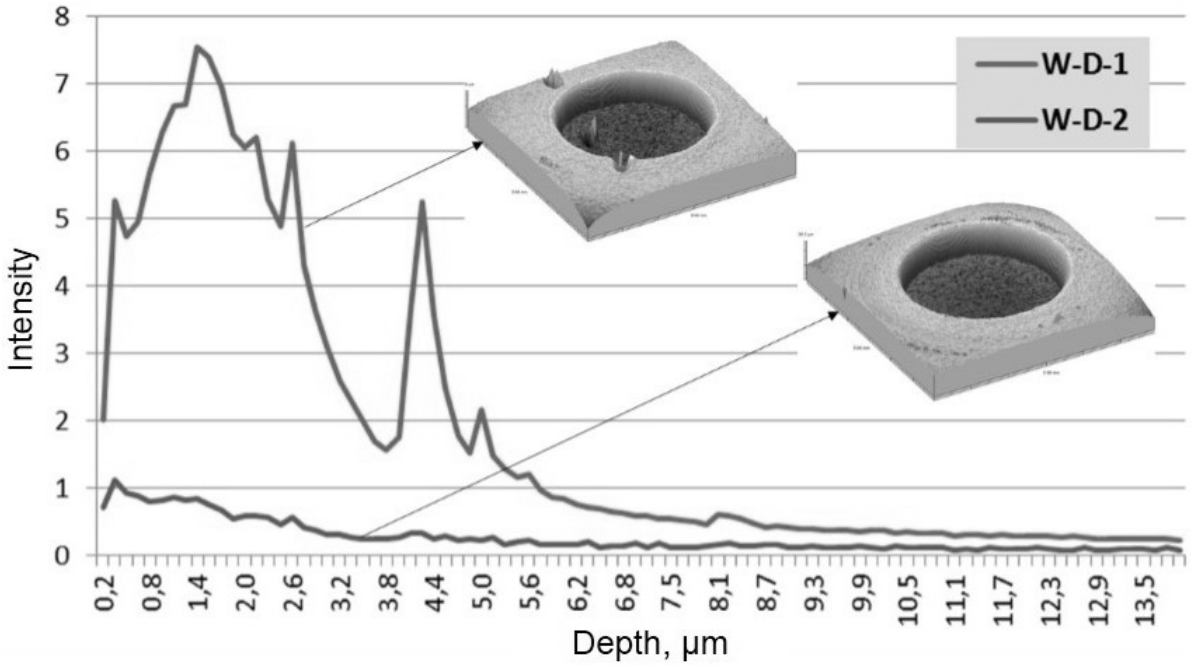

Fig.7. Results obtained on an optical emission spectrometer for W-D-1 tungsten samples

Conclusion

So, it has been established that, upon irradiation of tungsten, a change in the relief is observed as a result of non-uniform etching of the surface. The degree of change in the relief of the surface layer of the irradiated samples depends on the irradiation temperature and at T=1773 K small cracks form on the surface. Thermal desorption analysis showed that samples of tungsten irradiated with deuterium plasma at a temperature of 1273 K accumulate residual deuterium. In samples of tungsten irradiated with deuterium plasma at a temperature of 1773 K, no noticeable release of deuterium could be detected. Comparison of the data obtained by thermal desorption spectrometry and optical emission spectrometry suggests that the structure defect during irradiation leads to the accumulation of deuterium in the surface layer of tungsten, despite the high irradiation temperature.

Acknowledgement

The work has been implemented as part of the grant financing of scientific research by the Committee of Science of the Ministry of Education and Science of the Republic of Kazakhstan (BR05236748).

REFERENCES

1 Pitts R.A., Carpentier S., Escourbiac F., Hirai T., Komarov V., Lisgo S., et al. A full tungsten diverter for ITER: physics issues and design status. *J. Nucl. Mater.*2013, Vol.438, pp. 48 – 56.

2 Philipps V. Tungsten as material for plasma-facing components in fusion devices. *Ibid*, 2011, Vol. 415, pp. 2 – 9.

3 Shimada M., Pitts R., Loarte A., Campbell D.J., Sugihara M., Mukhovatov V., Kukushkin A., Chuyanov V. ITER research plan of plasma–wall interaction. *Ibid*, 2009, Vol. 390 - 391, pp. 282 – 285.

4 Ueda Y., Coenen J.W., Temmerman G. De, Doerner R.P., Linke J., Philipps V., Tsitrone E. Research status and issues of tungsten plasma facing materials for ITER and beyond. *Fusion Eng. Des.,* 2014, Vol.89, pp. 901–906.

5 Federici G., Skinner C. H., Brooks J. N., et al. Plasma-material interactions in current tokamaks and their implications for next step fusion reactors. *Nucl. Fusion*, 2001, Vol.41, pp. 1967 – 2137.

6 Tobita K., Nishio S., Enoeda M., et al. Design study of fusion DEMO plant at JAERI. *Fusion Eng.*, 2006, Vol.81, pp. 1151 – 1158.

7 Gasparyan Yu. M., Golubeva A. V., Mayer M., Pisarev A. A., Roth J., J. Nucl. Mater. 2009, Vol.390-391, pp.606-609.

8 Zinkle S.J., Was G.S. Materials challenges in nuclear energy. *Acta Mater*., 2013, Vol. 61, Iss.3, pp. 735 – 758.

9 Causey R.A., Doerner R., Fraser H., Kolasinski R.D., Smugeresky J., Umstadter K., Williams R. Defects in tungsten responsible for molecular hydrogen isotope retention after exposure to low energy plasmas. *J. Nucl. Mater*. 2009, Vol. 390-391, pp. 717 – 720.

10 Zhao M., Jacob W., Gao L., Manhard A., Dürbeck T., Zhou Z. Deuterium retention behavior of pure and Y2O3-doped tungsten investigated by nuclear reaction analysis and thermal desorption spectroscopy. *Nucl. Mater. Energy*, 2018, Vol. 15, pp. 32 – 42.

11 Tulenbergenov T., Skakov M., Kolodeshnikov A., Zuev V., Rakhadilov B., Sokolov I., Ganovichev D., Miniyazov A., Bukina O. Interaction between nitrogen plasma and tungsten. *Nuclear Materials and Energy*, 2017, Vol.13, pp. 63 – 67.

12 Rahadilov B.K., Skakov M.K., Tulenbergenov T.R. Tungsten surface erosion by hydrogen plasma irradiation. *Key Engineering Materials*, 2017, Vol. 736, pp. 46 – 51.

13 Tazhibayeva I., Kenzhin E., Shestakov V., Chikhray Y., Kulsartov T., Azizov E., Filatov O., Chernov V., J. Material science activities for fusion reactors in Kazakhstan. *Nucl. Mater*. 2009, Vol. 386 - 388, pp. 15 - 18.

14 Kulsartov T., Tazhibaeva I., Ponkratov Y., Gordienko Y., Zaurbekova Z., Baklanov V., Skakov M., Koyanbayev Y., Korovikov A., Chikray Y., Nesterov E. Investigation of hydrogen isotopes interaction with lithium CPS under reactor irradiation. *Fusion Eng. Des*., 2017, Vol. 124, pp. 324 - 327.

15 Skakov M. K., Kurbanbekov Sh. R., Karakozov B. K., Bakhtibaev A. N. ssledovanie mikrostruktury i svoystv absorbtsii-desorbtsii vodoroda splavom na osnove titana. *Vestnik KazNANS*, 2017, Vol. 3-4, pp. 68 – 71. [in Russian].

16 Dyusambaev D.S., Shaimerdenov A.A., Chekushina L.V., Tazhibaeva I.L., Kulsartov T.V., Gordienko Yu.N., Zaurbekova J.A., Koyanbayev E.T., Kukushkin I.M., Kenzhin E.A., Mukanov A.O. Detritiation of different irradiated beryllium grades using high-temperature degassing method. *VAST. Ser. Thermonuclear fusio*n, 2014, Vol.37(2), pp. 27-37. [in Russian].

17 Rahadilov B.K., Skakov M.K., Tulenbergenov T.R., Zhurerova L.G., Kurbanbekov Sh.R. Plasma installation for research of plasma-surface interaction. *Eurasian Physical Technical Journal*, 2019, Vol.16, No.2(32), pp. 36 - 42.

Article accepted for publication 21.10.2020

DOI 10.31489/2020No2/123-127

UDC 004.896

THE OBJECT TRACKING ALGORITHM USING DIMENSIONAL BASED DETECTION FOR PUBLIC STREET ENVIRONMENT

Matveev I. G.[1,3], Karpov K. A.[2,3], Yurchenko A. V.[1], Siemens E.[3]

[1]National Research Tomsk Polytechnic University, Tomsk, Russia, matveev.ivan.gr@gmail.com
[2]Siberian State University of Telecommunications and Information Sciences, Novosibirsk, Russia
[3]Anhalt University of Applied Sciences, Koethen, Germany

The paper proposes an approach to object tracking for public street environments using dimensional based object detection algorithm. Besides the tracking functionality, the proposed algorithm improves the detection accuracy of the dimensional based object detection algorithm. The proposed tracking approach uses detection information obtained from multiple cameras which are structured as a mesh network. Conducted experiments performed in a real-world environment have shown 10 to 40 percent higher detection accuracy that has proved the proposed concept. The tracking algorithm requires negligible computational resources that make the algorithm especially applicable for low-performance Internet of things infrastructure.

Keywords: object tracking, smart city, object detection, street lighting.

Introduction

Different object tracking algorithms are actively used in applications for automatic traffic monitoring, surveillance, and security. Typical purposes of object tracking algorithms are identification of an object in a video scene (e.g. in consecutive video frames) and prediction of possible object locations in the future. The problem of object tracking is extensively researched in the area of computer vision [1–4], however, these algorithms still have a number of limitations: high computational requirements to a processing unit [1], [5] strong dependency of tracking accuracy on image quality (environment illumination, contrast, resolution, etc.) and varying object representation between frames [6]. There are some implementations of tracking algorithms [7,8] which use background subtraction as a detection technique that can be applied on low-performance computational platforms, however, such an approach does not provide object classification functionality as needed e.g. by Smart Lighting applications [9]. For sure, as a low computational power solution, global positioning system (GPS) tracking algorithms can be used instead of computer vision methods [10], however, it makes devices for such tracking more complicated and expensive from hardware point of view.

The proposed algorithm combines the tracking approaches described in the references above to create a new tracking system that includes a computer vision approach and GPS coordinates extraction that can be executed on low-performance hardware in real-time. The tracking method is developed in a frame of the smart city applications, in particular, diverse smart lighting systems aimed at energy saving and lighting pollution reduction via effective control of the street lamps. The decision to switch the lamp on is made depending on object presence in the street. Each lamp of such a system has its (fixed) GPS coordinates, a low-performance computation unit (e.g. Raspberry Pi based), and a low-resolution camera. The camera data is processed by the real-time detection algorithm (DBOD) [11]. This detection algorithm provides to the system a number of object parameters: object class affiliation probability, coordinates of the object in real world coordinate system, and approximate real-world dimensions (height and width) of the object. All the street lamps inform neighbors about the moving objects [12] through a common wireless mesh network. The tracking algorithm in this system improves the detection accuracy of a particular lamp by taking into account the object detection information received from the lamps which have previously detected the object.

1. Tracking algorithm description

The proposed tracking algorithm accumulates the object detection information from multiple nods. The previously obtained information affects a decision about an object class affiliation on an active node.

The following requirements must be satisfied before applying the proposed tracking method:

- the nodes can communicate through a common network;
- a basic object detector outputs the detection result in a form of an object class probability (confidence score);
- GPS coordinates of each particular node are known;
- the route distance between the neighbors is known to the nodes.

When an object has been detected in the street for the first time, the system registers properties of this object (table 1): a unique ID, GPS coordinates, probabilities of class affiliation, estimated real-world dimensions and its velocity. The velocity parameter is calculated based on GPS coordinates and corresponding timestamps (according to the equation 1). These properties are continuously updated after each detection cycle and broadcasted to the mesh network. These parameters are received by the neighboring nodes and stored as a history set for further calculations.

$$v_{12} \approx \frac{R\sqrt{(\theta_2-\theta_1)^2+cos^2\left(\frac{\theta_2-\theta_1}{2}\right)(\varphi_2-\varphi_1)^2}}{t_2-t_1}, \quad (1)$$

where R – the approximate Earth radius; θ, φ – latitude and longitude in radians; t –timestamp.

Table 1 - Data structure of the detected object

Detected object	**Example**
ID (10-byte string)	5b759d52b4
GPS array (latitude, longitude)	[(51.1657442, 12.3555677), … , (53.1453441, 11.1345685)]*
Object width (m)	[0.65, …, 0.33]*
Object height (m)	[1.77, …, 1.85]*
Velocity (km/h)	[3.2, …, 2.5]*
Object class probability	[p_pedestrian=0.7, p_cyclist=0.1, p_vehicle=0.1, noise=0.1]
Timestamp (Unix time)	[1607554893, …, 1607554899]*
*the new value is appended to the array after each detection iteration	

The tracking algorithm proposes solutions for the two most common scenarios of camera installation in the street: with and without overlap of the camera's angles of view (AOV). Decision about applying the concrete scenario depends on the camera's installation scenario which are shown on Fig. 1.

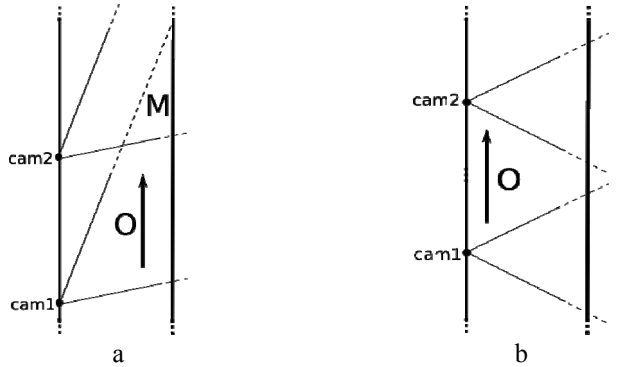

a b

Fig.1. Handover scheme: a) explicit handover; b) implicit handover

In the first scenario (Fig. 1a) the object is observed by both cameras (cam1and cam2) simultaneously, when the object enters the mutual area M between the cameras. If cam2 finds an object which has the same

coordinates as cam1, the object inherits the label assigned by cam1. The transition of the object between cam1 and cam2 is referred to as explicit handover. The properties of the object are recalculated during the handover that leads to cumulative precision growth of the system. The object detection probability is recalculated in the following way [13]:

$$\hat{p} = \frac{\prod_{t=1}^{N} \frac{p_t}{1-p_t}}{1 + \prod_{t=1}^{N} \frac{p_t}{1-p_t}}, \quad (2)$$

where $\hat{p}$ – an updated probability of detection based on probabilities from *N* sources; p_t – a probability of *i-th* source; *N* – a number of sources.

In the second scenario, there is no mutual area between the lamps (Fig1b), therefore the system will try to predict the coordinates and timeframe of an object's appearance in *cam2* AOV based on information obtained from the camera *cam1*. This scenario is referred to as implicit handover. The implicit handover case is error-prone since the object enters the area of uncertainty and can be interpreted as another or new object at the moment of the next detection. To authenticate the object several verifications should be made.

Firstly, the system checks whether the recent value of the dimensional parameter (width and height) belongs to the inter quartile range (IQR) [14] of the object dimensions history set. To calculate a timeframe of expected object appearance in the area of the next camera the IQR of object velocities is used. Having a distance between areas of observations it is possible to calculate the time interval of the object's expected appearance in the area of the neighboring camera.

5. Experimental results

To confirm the effectiveness of the developed tracking algorithm a number of experiments in a real-world street scenario have been conducted. These experiments include movements of *pedestrian*, *cyclist*, and *vehicle* during nighttime. The points of observation have been equipped with Logitech C920 HD cameras which captured images with a resolution of 320x240 pixels. The horizontal AOV of the camera was equal to 40º. The angles of the camera incline varied in the range of 10 – 30º. The height of the camera installation lays in the range of 3.5 – 4.5 m. The tested environment included 6 areas which are shown in Fig. 2.

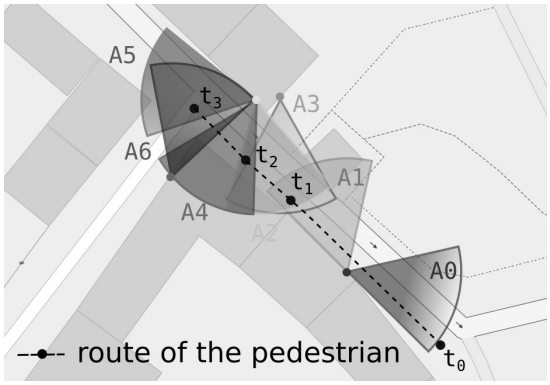

Fig.2. Map of the experiment area

These areas comprise scenarios of explicit and implicit handover shown in Fig.1. So the transition between areas A0 and A1 is an implicit handover case. Transitions between other areas that have mutual regions (A1 – A6) operate explicit handover. Each individual camera detection results are shown in Fig. 3. These images represent a route of the same pedestrian shown in Fig. 2. Image 0 corresponds to the time t_0, images 1-3 have been taken at times t_1, image 4 –t_2, and images 5, 6 – at time t_3.

The detected object is highlighted by a green rectangle and has a class affiliation with corresponding probabilities. The green-colored values are the un-updated probabilities. The probabilities for all objects classes are plotted in Fig.4a. According to this plot, the detection probability does not exceed 0.85. The lowest detection probability is 0.34 that is below the chosen decision threshold [11] and leads to misclassification.

The red-colored values in Fig. 3 are reinforced by previous observations. The updated probabilities are recalculated using equation 2 and plotted in the in Fig. 4b. As can be seen, the cumulative probability update increases the reliability of the system by 10 to 40 percent since the system becomes more rigid to sudden

.

errors. For example, misclassifications that are made by node 1 for the pedestrian class and by node 4.5 for the cyclist class have been corrected using observations history. The curves for the pedestrian and cyclist classes approaching detection probability to value of 1.

Fig.3. The pedestrian movement in the experiment area observed from multiple cameras

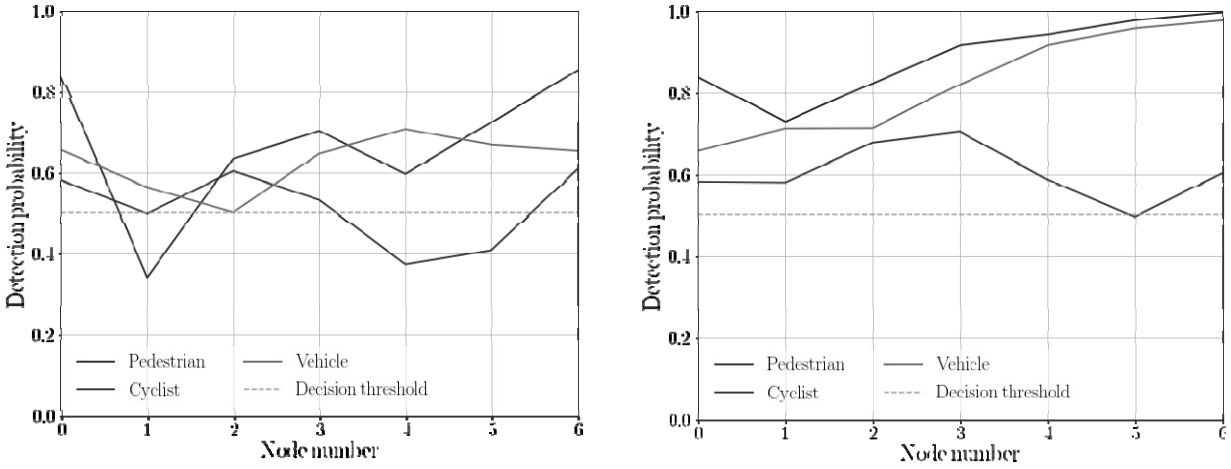

Fig.4. Object class prediction probabilities: a) without cumulative update; b) with cumulative update

Conclusion

The described tracking algorithm covering explicit and implicit handover scenarios has been implemented and tested on a public street of a small town in Germany. The proposed tracking algorithm has increased the overall reliability of the system by 10 to 40 percent. The tracking method workability has been proved by the results of experiments on the setup in a real-world environment. The experiments on low-performance computational equipment have shown negligible extra load of central processing unit (CPU) load of the tracking algorithm. These CPU requirements make possible applying the proposed tracking approach in real-time on low-performance hardware in contrast to existing analogues. These results can be achieved via the nodes communication in a mesh network. In spite of tracking method specifics, the idea of such tracking can be generalized and applied in other scenarios of object tracking.

There is a frame for further investigations and improvements. The behavior of the tracking system should be refined under more complicated object movement scenarios, e.g. high traffic intensity. The important question is finding suitable method for estimating an object geometrical similarity. In the case of implicit handover, the object location prediction mechanism can be improved for a better object identification in areas of uncertainty.

REFERENCES

1 Yilmaz A., Javed O., and Shah M. Object tracking: A survey. *ACM Comput. Surv.*, 2006, Vol. 38, No. 4, pp. 1 – 45. doi: 10.1145/1177352.1177355.

2 Comaniciu D., Ramesh V., and Meer P. Kernel-based object tracking, *IEEE Trans. Pattern Anal. Mach. Intell.*, 2003, Vol. 25, No. 5, pp. 564–577. doi: 10.1109/TPAMI.2003.1195991.

3 Wang Q., Zhang L., Bertinetto L., et al. Fast Online Object Tracking and Segmentation: A Unifying Approach. *Proceedings of 2019 IEEE/CVF Conference on Computer Vision and Pattern Recognition (CVPR)*, Long Beach, USA, 2019, pp. 1328–1338.

4 Xu R., Nikouei S., Chen Y., et al. Real-Time Human Objects Tracking for Smart Surveillance at the Edge. *Proceedings of 2018 IEEE International Conference on Communications (ICC)*, Kansas City, USA, 2018, pp. 1–6, doi: 10.1109/ICC.2018.8422970.

5 Voigtlaender P., Krause M., Osep A., et al. MOTS: Multi-Object Tracking and Segmentation. *Proceedings of 2019 IEEE/CVF Conference on Computer Vision and Pattern Recognition (CVPR)*, Long Beach, USA, 2019, pp. 7942–7951.

6 Philip R., Ram S., Gao X., et al. A comparison of tracking algorithm performance for objects in wide area imagery. *2014 Southwest Symposium on Image Analysis and Interpretation*, San Diego, USA, 2014, pp. 109–112, doi: 10.1109/SSIAI.2014.6806041.

7 Ooi H. L., Bilodeau G. A., and Saunier N., Tracking in Urban Traffic Scenes from Background Subtraction and Object Detection. *Image Analysis and Recognition*, Cham, 2019, Vol. 11662, pp. 195–206, doi: 10.1007/978-3-030-27202-9.

8 Dziri A., Duranton M., and Chapuis R. Real-time multiple objects tracking on Raspberry-Pi-based smart embedded camera. *J. Electron. Imaging*, Vol. 25, No. 4, pp. 1 – 16, 2016, doi: 10.1117/1.JEI.25.4.041005.

9 Zinov S., and Siemens E., The Smart Lighting Concept. *Proceeding of the first Workshop on Problems of Autonomous Power Systems in the Siberian Region,* Koethen, Germany, 2013, pp. 1 – 10.

10 Hewawasam H. S., Ibrahim M. Y., Kahandawa G., et al. Comparative Study on Object Tracking Algorithms for mobile robot Navigation in GPS-denied Environment. *Proceedings of 2019 IEEE International Conference on Industrial Technology (ICIT)*, Melbourne, Australia, 2019, pp. 19–26, doi: 10.1109/ICIT.2019.8754960.

11 Matveev I., Karpov K., Chmielewski I., et al. Fast Object Detection Using Dimensional Based Features for Public Street Environments. *Smart Cities*, Vol. 3, No. 1, 2020, doi: 10.3390/smartcities3010006.

12 Siemens E*., Method for lighting e.g. road, involves switching on the lamp on detection of movement of person, and sending message to neighboring lamps through communication unit*, German Patent No. DE102010049121A1, 2012, 15 p.

13 Satopää V. A, Baron J., Foster D. P., et al. Combining multiple probability predictions using a simple logit model. *Int. J. Forecast.*, Vol. 30, No. 2, pp. 344 – 356, 2014, doi: 10.1016/j.ijforecast.2013.09.009.

14 Zwillinger D., and Kokoska S. *CRC standard probability and statistics tables and formulae*. Crc Press, 1999, 568 p.

Article accepted for publication 20.12.2020

DOI 10.31489/2020No2/128-137

UDC 621.37

PARTICLE SWARM OPTIMIZATION WITH INDIVIDUALLY BIASED PARTICLES FOR RELIABLE AND ROBUST MAXIMUM POWER POINT TRACKING UNDER PARTIAL SHADING CONDITIONS

Baktybekov K.[1, 2], Kurmanbay A.*[1], Sakhanov K.[1], Syzdykov A.[1], Mukhamediyev A.[1]

[1]National Company "Kazakhstan Gharysh Sapary", Nur-Sultan, Kazakhstan, a.kurmanbay.sh@gmail.com

[2]National Research Nuclear University, MEPhI, Moscow, Russia

Efficient power control techniques are an integral part of photovoltaic system design. One of the means of managing power delivery is regulating the duty cycle of the DC to DC converter by various algorithms to operate only at points where power is maximum power point. Search has to be done as fast as possible to minimize power loss, especially under dynamically changing irradiance. The challenge of the task is the nonlinear behavior of the PV system under partial shading conditions. Depending on the size and structure of the photovoltaic panels, PSC creates an immense amount of possible P-V curves with numerous local maximums - requiring an intelligent algorithm for determining the optimal operating point. Existing benchmark maximum power point tracking algorithms cannot handle multiple peaks, and in this paper, we offer an adaptation of particle swarm optimization for the specific task.

Keywords: maximum power point tracking, partial shading, meta-heuristics, particle swarm optimization.

Introduction

Increasing interest in the solar industry and advances in computing capability led to the development of more forward-looking and efficient power control techniques previously ignored due to computational difficulty and challenges in testing. Maximum power point tracking related reliability issues was one of the tasks for solar technology to overcome and opportunity to gain 25-30% additional electrical efficiency [1]. To resolve this matter which might led to more than 70% power loss [2] - a myriad of MPPT procedures with different principles behind - ensuring operation on optimal points was developed [3 - 7]. Some of them owe their functionality to the tested by time control methods history of which links back to many decades if not centuries (calculus-based) [3 - 4]. While there are plenty of products of recent advances in computational science (artificial neural networks (ANN), meta-heuristics, Etc.) [6 - 7] In general, peak finding algorithms for MPPT could be classified into two distinct categories [8]: direct control (DIRC) and soft computing (SC) techniques. If the first mentioned methods use sampling or modulation based active control procedures, the later decides by exploring the performance of the system. DIRC approaches have serious limitations when it has to deal with non - linear behavior of the function and get easily trapped at local maxima. Such a shortcoming is extremely undesirable, as the output of photovoltaic systems shows a high level of non-linearity under non-uniform solar irradiance. Depending on the structure of the PV panel - more than n! (here n number of PV cells) different P-V curves could occur under operating conditions. Hence, MPPT requires a robust algorithm that has a general structure and able to deal with any output of the PV system in a timely manner. When calculus cannot provide means to achieve the desired solution without going through all search space - heuristics are used to obtain a more rapid result.

However, global optimization of function lacking convexity - remains an unsolved mathematical challenge. Monte Carlo based methods in the form of heuristics [9] cannot guarantee an exact solution every time, if at all. Nevertheless, they are proven to be the most superior technique existing today for dealing with non-convexity. One promising SC method is PSO nature-inspired algorithm [10] derived from the social behavior of birds, which relies on swarm intelligence to locate the global optimum. PSO has a beautiful structure that is easy to hybridize for further performance enhancement and adjustment to suit numerous tasks. In this paper, we present an adaptation of PSO to track the maximum power of the PV system. The reliability of the algorithm was extensively tested on various scenarios imitating real-life conditions.

The most common and well-known algorithms for MPPT are Perturb and Observe P&O [3] and Incremental Conductance INC [6] - both of which are direct control methods. The performance of new algorithms is usually compared to well established standard techniques. Furthermore, [11-13] mentioned that modifications done to the PSO should take into account the fundamental principle behind and provide numerical computations. However, under PSC conditions - benchmark MPPT algorithms (INC, P&O) don't function properly without improvements. Therefore, we use basic PSO as a reference to any additions done to the original recipe, and the enhancement procedure is constructed around physical and to a less extent - biological principles. Furthermore, we attempted to preserve the generality of the algorithm and focus on architectural improvements rather than parameter configuration so that procedure developed could be adapted to many other optimization and control procedures.

1. Modeling PV system

The response of the PV panel to varying environmental conditions is an objective function Equation 1 to the PSO algorithm which will sense the I-V and point to the optimal operational voltage by setting the duty cycle of the DC/DC converter Figure 1. Stated differently, the task of the controller is to locate an operational voltage under which the power output of the system is maximized.

$$max_x f(x) \quad \text{subject to} \quad x \in \chi \tag{1}$$

Modeling of the PV system response done as shown in [19] using the basic unit as a single-diode PV cell.

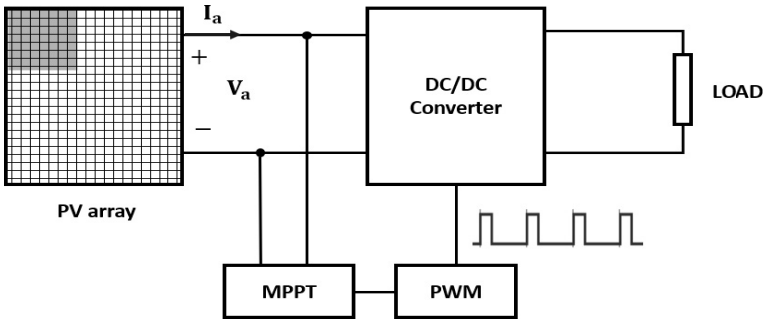

Fig.1. PV system simplified scheme

For more precise and comprehensive models we refer readers to [15]. Further analysis included simulation of the electrical circuitry of PV cells connected in a series-parallel configuration. Results are presented in the Figure 2.

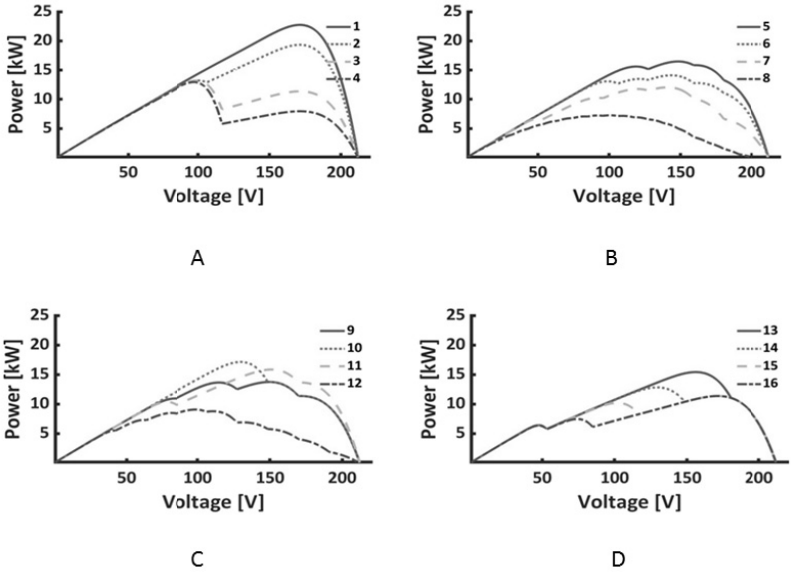

Fig.2. Possible outputs of PV array under PSC (test scenarios for PSO)

They were selected to represent wide variety of multi-modal situations that MPPT algorithm has to deal in real life conditions. Figure 2 A contains 4 curves and 1 curve is the result when the solar panel is not shaded, and the other curves are the result of partial shading. Figures 2 B, 2C and 2 D show the results of partial shading of the solar panel depending on the shading location on the panel. The number of possible peaks dictated by the number of PV elements connected, and takes place due to cells going out of operation range in a non- synchronous manner. Similarly to PSC conditions, non-uniform temperature also causes such peaks. A Significant reduction in electrical efficiency could take place if the MPPT algorithm gets trapped in one of the local maxima Figure 2. Test scenarios represent the output of 20 x 20 solar array connected in a series-parallel connection.

In a brief summary of characterizing the P - V curves of an (n x n) array, at most (n - 1) local maxima could be observed. Depending on temperature and irradiance non-uniformity, peaks might shift in any direction - making it hard to derive straightforward algorithms for MPPT. Although not always correct, what works for complex cases should operate well for more ordinary ones. Therefore, we selected a relatively big array to test the peak finding algorithm and extract difficulties it might face. As will be seen in the preceding sections, some PSC conditions cause more challenges for the MPPT algorithm rather than others. Therefore, to prove its validity - modeling and extraction of as many cases as possible stands extremely important. In most of the MPPT literature - the algorithm is tested on a relatively small array size where it might successfully determine the correct peak among few. However, the functionality of the algorithm can not be proven if not tested in extreme cases. Furthermore, in our testing's, we found that with increasing numbers of peaks, the complexity of tasks for algorithm rises as well.

2. Original PSO structure

Since the introduction to the scientific world, PSO found application in various engineering problems, and many modifications were offered by researchers. Before introducing our recipe, we go through a very brief review of the original PSO structure. Here our goal is to decompose the components of the algorithm for further analysis and adaptation to MPPT. PSO search for optimal solution by moving through search space with certain velocity as described in Equation 2 - 3:

$$v_i^{k+1} = wv_i^k + c_1 r_1 (P_{best} - x_i^k) + c_2 r_2 (G_{best} - x_i^k) \quad (2)$$

$$x_i^{k+1} = x_i^k + v_i^{k+1}, \quad (3)$$

where: w – inertia; v^k - velocity of the i-th particle at iteration k; c_1 - cognitive acceleration constant; x^k_i - position of the i-th particle at iteration k; c_2 - social acceleration constant; P_{best} - best solution obtained so far by the particle; r_1, r_2 - random number in the range of [0, 1]; G_{best} - best solution obtained so far by the swarm

Algorithm 1 Original Particle Swarm Optimization

1: Initialize Particle population $\{ x_i \}, i \in [1, N]$
2: Initialize velocity of each particle $\{ v_i \}, i \in [1, N]$
3: Initialize the best-so-far position of each individual:, $i \in [1, N]$
4: Define Topology (**GBEST** topology)
5: Define social & cognitive acceleration constraints.
6: Define limits of velocity and position
7: While (k < maximum iteration set) Iterate
through equations 2 - 3

2.1. Damped mass spring system analogy

Heuristic methods are inspired either by nature or physics [9]. In other words optimization problem is described as physical system where ground state needs to be found or as a biological system where fittest individuals needs to be described. For instance one of the most powerful technique in the arsenal of heuristic optimization tools simulated annealing [16] (SA) is imitation of physical process - cooling, while genetic

algorithms are derived from theory of evolution. Therefore, fundamental knowledge behind algorithm is a key for understanding it and altering it's behavior according to our needs. It was noticed that mechanics of particle movements could be described by stochastic damped mass spring system [17], which at each iteration has a center of oscillation around point Equation 4:

$$o_i^k = \frac{c_1 p_i^k + c_2 g_i^k}{c_1 + c_2} \quad (4)$$

We modify PSO according to this underlying physical principle and control exploration and exploitation characteristics of the algorithm which will be suitable for our problem.

2.2. Convergence analysis

Continuing on an assumption of stochastic damped mass spring analogy convergence analysis of the algorithm [12,13],[17], Etc. could be accomplished from control theory. Where stability of linear system could be confirmed if it lies within the first order stability region: Equation 5.

$$\{(\omega, \varphi) : |\omega| < 1, 0 < \varphi < 2(\omega + 1)\} , \quad (5)$$

where $\varphi = \frac{c_1 + c_2}{2}$

This knowledge allows to fine-tune parameters of the algorithm with guaranteed convergence and enhances understanding of the search mechanics. Furthermore, the concept of "center of mass" - opens doors to a more intelligent particle movement across search space and could be exploited to regulate the position and velocity of the particles.

2.3 Challenges in PSO algorithm

2.3.1. Premature convergence

In some instances due to limitation of search procedure, a feasible solution is not reachable, and Monte Carlo based methods converge on sub-optimal points. The exploration mechanism of the algorithm ensures that enough points were explored in the search space to conclude. However, in an extremely large search space for the algorithm, to converge it has to rely on collected information and execute decisions. Tricky entropy barriers or so-called golf-hole landscapes are known to cause challenges for heuristic techniques. In the case of PSO ensuring diversity of solutions is controlled by cognitive acceleration while the social coefficient assures exploitation. However, this is not only parameters that influence the mechanics of the particle movement, the architecture of the algorithm could be altered for additional enhancements. The problem of premature convergence is one of the primary directions in the research of PSO and an enormous number of solutions are offered in the literature by various researchers: swarms running on parallel [18],[7], introducing predators to the model [19], inserting invisible walls in search space [20], enforcing diversity [21,22] Etc. Ensuring the reliability and reproducibility of the control stands even more valuable when an algorithm is used in the engineering problem. Therefore, our main focus during this research is to test means of achieving a reliably functioning PSO and techniques which could enhance exploration characteristics of the PSO while preserving speed.

2.3.2. Complexity

Most of the benchmark algorithms (DIRC) used for the MPPT are simple and easy to realize. While for PSO - parameter selection needs to be accomplished for balanced exploration and exploitation. The task is usually achieved by another algorithm and optimization problem on its own. In literature, examples of training PSO by PSO or other Evolutionary algorithms to perform specific optimization tasks at an optimal time. However, such an option doesn't work for MPPT, as was mentioned before more than n! possible outcomes of the PV system need control. Therefore, promoting a necessity to preserve - general structure of algorithm, to find the peak of many possible outputs of the PV panels.

In addition to it, extra complexity of PSO is its architecture, which is harder to optimize rather than parameters. Population size, velocity and position limiting rules, information exchange policies, and many other details that make the algorithm very flexible with the vast capability and adaptability also make it complex to optimize.

.

3.PSO adaptation to MPPT

3.1.Particle initialization & landscape meshing.

The starting position of particles is known to affect the convergence of the PSO [18]. For instance, initialization using Voronoi tessellation reported improving the performance of the algorithm in terms of finding better solutions [23]. In the original PSO, particles are initialized randomly across the search space [10]. Thus, however, occasionally cause unwanted grouping of the particles in a specific section of the landscape, therefore, trap them in local minima or maxima. It is especially evident when fewer particles used. While more particles, in general, lead to an increase in reliability, it comes with a cost of calculation time. To avoid particle trapping into local maxima due to initialization, we decided to come up with a procedure that manually distributes particles uniformly. Although various methods of position initialization exist, we decided to stick on the simplest segmentation inspired by meshing in the field of numerical computations or cells of cellular automata.

Uniform initialization procedure - for the search space in the range of [0,X] each particle out of N is randomly initialized at the range of [0,X/N] , [X/N, 2X/N] ,etc. (2D example is shown in Figure 4) This is could be considered as (Manual enhancement to search) as particles are forced to be distributed across the search space, while in random initialization they might get stuck in specific region if the start was unlucky enough.

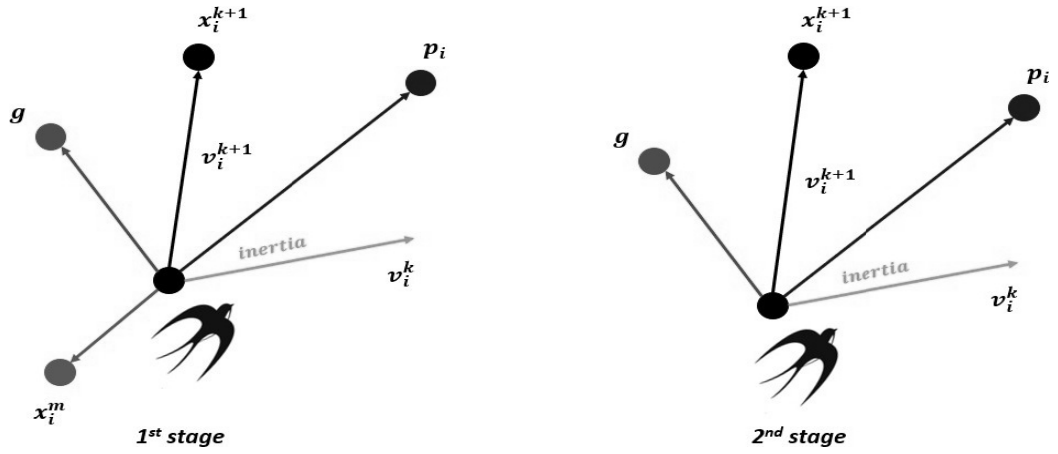

Fig.3. Visualization of the particle movement

Such an initialization could be effectively used further for creating diversity and warrant a uniform search of the landscape. Midpoints of segments, if utilized as an additional component - would give each particle an individuality bias. It will urge them to investigate the initialized section with higher probability - therefore, study its surroundings before converging on a specific spot. Equation 6:

$$v_i^{k+1} = wv_i^k + c_1 r_1 (P_{best} - x_i^k) + c_2 r_2 (G_{best} - x_i^k) + c_3 r_3 (X_i^m - x_i^k) , \quad (6)$$

where: c_3 - acceleration constant; r_3 - random number in the range of [0, 1]; X^m - midpoint of the initialization section of the particle.

Now after initialization the new center of oscillation at each iteration shifts to:

$$o_i^k = \frac{c_1 p_i^k + c_2 g_i^k + c_3 x_m^i}{c_1 + c_2 + c_3} \quad (7)$$

Our attempts could be compared to the stud like operator in genetic algorithms [24]. An additional term is not rare in PSO design - fully informed PSO [25] influenced by a neighborhood, and a global solution is known for delivering better results. Furthermore, [22] term introduced to push away particles from the best position produced additional diversity to the search. Our extension dedicated to enforcing uniform exploration of the search space. It also prevents unnecessary over-exploration of a specific region - which might lead to premature results and waste time. Put differently - it is a term that corresponds to the learning

of the swarm members about the landscape they are exploring and prioritizing the search space after necessary information was collected. Therefore, leaving behind unsuccessful search regions only after enough exploration. c_3 could be described by condition to segment the PSO into two distinct stages or phases where its behavior reshapes:

$$c_3 = \begin{cases} c_3, & if\ k < j \\ 0, & otherwise \end{cases} \tag{8}$$

During the first phase, we limit the dynamic range of particles by $\boldsymbol{X_m^i}$, but with one eye in the global best solution. In the following stage, when enough information about the landscape was acquired - particles recombine in one segment to merge efforts and look nearby the best solution to possibly improve the result. Stability and convergence analysis is an essential part of the algorithm. However, for the initial stage — when the particles set to explore — we don't have to arrange acceleration parameters necessarily according to the condition in Equation 5. In contrast, configure them to warrant uniform and unbiased exploration.

The introduction of the new$_m$term makes it possible to prioritize search space according to obtained results, and change the center of oscillation to particles located in low priority regions. Nevertheless to not make algorithm too complex for our application we didn't implement hierarchy or introduce diversity control mechanism to regulate c_3 or $\boldsymbol{X_m^i}$ like in [33-34] rather used $\boldsymbol{j}$ = 18 as a 18 iterations invested on reliability. Depending on function which will be optimized number might vary, while for our case starting from $\boldsymbol{j}$ = 15 we observed no failure. This is roughly the size of the tested array or # of possible peaks. c_3 was set to $c_3 = c_1 + c_2$. Although different interpretations of the biological principle behind PSO exists - the analogy between human communal activity, the social behavior of the birds, theory of evolution, Etc. We justify our additional term on the fact that no matter what will be the eventual destination of biological life, in the initial stage - it is bounded to the geography it was born and start exploring from what is reachable. In other words, diversity in nature is preserved by geographical fact as well.

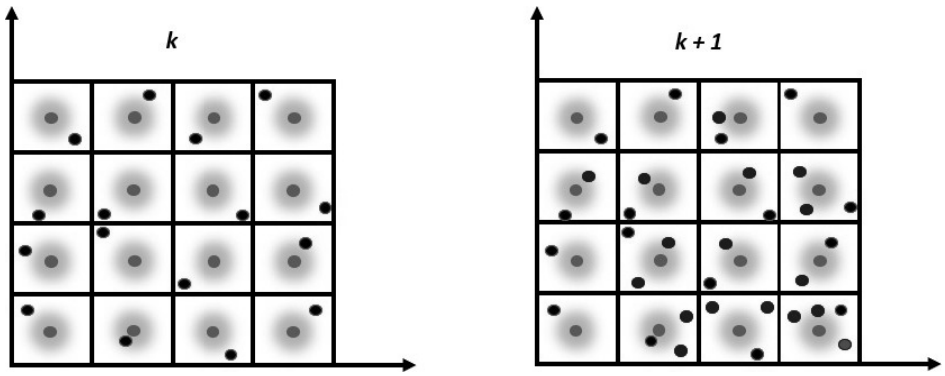

Fig.4. Visual representation of segmented initialization and dynamics of particle movement.

Moreover, the complex behavior of biological life forms probably cannot be comprehensibly described by two terms. Therefore, supplemental information ensuring the permanent diverse attitude of each element seems a reasonable addition to us. This discussion on biological analogy is just our interpretation and hypotheses. We leave the scientific explanation for social and biology experts.

3.2. Velocity Initialization & Limiting

The velocity of the particles, just like their position - could be initialized randomly or at specific values. How it is regulated during the simulation is more critical. In the first studies of the PSO [10], it was reported that without velocity limiting particles could jump out from the boundaries of the search space. Therefore, to control the dynamic range of each swarm member, their velocities limited by the Equation 9.

$$If \quad |v_i| > v_{\{max\}},\ v_i = \frac{v_i v_{\{max\}}}{|v_i|} \tag{9}$$

For our recipe we went by rule of thumb and v_{max} for the first stage was to jump at most 15% of the search space and for the second stage 25%.

.

3.3. Adjusting Inertia

Another important parameters of the PSO algorithm is inertia. The importance of inertia to the convergence rate are reported by many researchers. Limiting the inertia according to certain rule might result in faster convergence.

However, reduced velocity could trap the particles in local maximum as their velocity would be too low to escape local maxima as search progress. In this section several inertia update rules are presented:

Constant value could be used to control the inertia by [26] Setting inertia a constant value is simple solution.

Linear - control of the inertia could result in reduced convergence time [27]. Usually upper and lower bounds of inertia w_{min} and w_{max} are set to [0.4, 0.9]

$$w^k = w_{max} - \frac{k(w_{max} - w_{min})}{k_{max}} \tag{10}$$

Similar to the linear, exponential control of the inertia was experimented in [11] to accelerate convergence.

$$w^k = w_{min} + (w_{max} - w_{min}) \exp\left(-3\left(\frac{k}{k_{max}}\right)^2\right) \tag{11}$$

Inertia update rule [10] which regulates particle movement according to explored distance are shown in Equation 12 & Equation 13. Significant gain in speed could be obtained by online regulation of inertia.

$$w'^k = w_{max} - (w_{max} - w_{min}) \frac{d_{max} + d_{min} - d_{mean}^{k-1}}{d_{max}} \tag{12}$$

$$w^k = \frac{w_{min}}{2} + r\, w'^k \tag{13}$$

Here d is voltages which were tested to locate GM and r is random number in the range of [0, 1]. Benefit of exploiting statistics of visited points is getting rid of need to determine maximum number of iterations which is required for other methods.

3.4. Acceleration constants (social, cognitive)

As mentioned before, tuning acceleration constants (parameter configuration) is done to improve the performance of the PSO to accomplish a specific task. However, due to a wide range of outputs from the PV system - calibrating the acceleration constant seems quite a difficult task if even possible. Therefore, we rely more on the improvement of the algorithm architecture and preserve its generality (the ability to deal with a variety of functions). Upon recommendations in literature we selected c_1 and c_2 as (1.5 & 2.05)

3.5. Topology Selection

Information exchange policies between particles of a swarm exhibits a substantial consequence on the mechanics of their movement, so, to the algorithm performance. Topology modifications result in vastly varying results. It was observed in very first experiments on cellular automata by von Neumann that information exchange between cells can lead to the vast diversity of results.

In the case of PSO particles, this is no exception - topology receives important purpose in algorithm functionality. For instance, two completely independent swarms could run on parallel due to complete isolation (absence of communication) Figure 5b. A myriad of arrangements for information exchange exists. Some of them force particles to explore by delaying propagation of information [18] Figure 5c. However, our goal is to locate a global maximum within the least amount of trials possible. For this reason, large swarms don't suit our purpose. In our adaptation - the number of particles was limited to as small as three, and we followed the original information exchange structure Figure 5a GBEST topology.

Algorithm 2 Modified PSO

1: Initialize Particle population *(In uniform sections N = 3)* $\{ x_i \}, i \in [1, N]$
2: Initialize velocity of each particle $\{ v_i \}, i \in [1, N]$
3: Initialize the best-so-far position of each individual:, $i \in [1, N]$
4: Define Topology (**GBEST** topology)
5: Define social & cognitive acceleration constraints.
6: Define limits of velocity and position *(For stages 1 & 2)* .
7: While (k < maximum iteration set)
1st Phase:
Iterate through equations 6 - 3
Set: w = 0.72
2nd Phase:
Iterate through equations 2 - 3
Adaptive inertia update

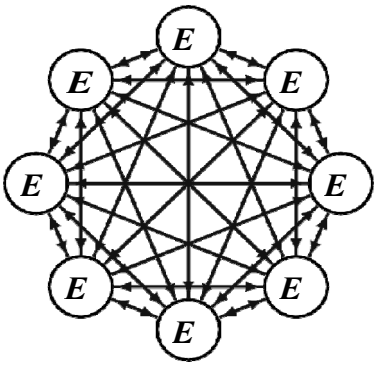

(a) Information exchange in **GBEST** topology

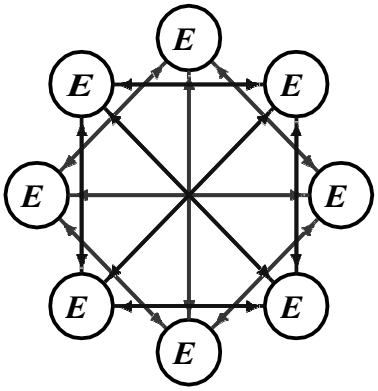

(b) Swarms running on parallel in **GBEST** topology

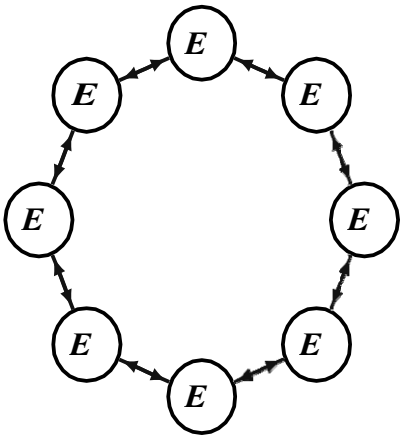

(c) RING (**IBEST**) topology

Fig.5. Visualization of various PSO topology *(here E is particle)*

4.Simulations

To our surprise - steps (# of attempts by particles in total, till global best was found) required by the modified version of the algorithm didn't differ considerably from the offered test scenarios. Examining the literature, we found that similar results were observed by. Meshing the landscape offers reliability close to the exact solution even for a population size of 3 as we received no failures for 1000 runs for all test scenarios.

The additional term cannot guarantee a uniform exploration of the search space. But adds a probability to explore the region where particles are initialized and contribute to the final answer.

In Table 1 results of numerical experiments were we compare original PSO with linear and adaptive inertia update to the modified version are presented. Uniform initialization was implemented only for the later to point on its importance. Our interpretation of convergence is when all particles are within 1 % range of GM. Failure is counted if voltage at GM differs from the real GM more than 1 %. However, all the failures we detected ended up converging in wrong peak. Every optimization problem needs adjustments of some kind [28], and there is no optimization algorithm which could effectively tackle every single problem [29]. However, for MPPT controller we did our best to preserve the generality of the algorithm to deal with wide variety of PV system outputs.

Table 1 - Simulation results (here **PSO1** - is original PSO with linear inertia, **PSO2** - is PSO with adaptive inertia, PSO3 - is modified PSO)

Test cases	**PSO1**	**PSO2**	**PSO3**	**PSO1**	**PSO2**	**PSO3**
	Fails for 1000 runs			Expected convergence		
1	0	0	0	194.39	42.56	73.01
2	0	6	0	196.70	41.91	72.92
3	155	183	0	213.39	42.28	95.63
4	106	108	0	216.70	42.42	86.53
5	0	30	0	198.08	38.14	72.18
6	0	36	0	195.02	39.18	72.08
7	0	32	0	197.80	40.35	72.92
8	1	35	0	206.54	42.60	75.37
9	14	340	0	193.67	41.16	83.17
10	0	0	0	204.15	40.11	72.64
11	1	14	0	192.07	39.06	72.81
12	1	5	0	213.60	42.22	75.77
13	0	4	0	197.91	40.76	72.78
14	5	40	0	210.90	39.23	73.22
15	103	239	0	193.24	39.86	74.74
16	9	67	0	194.51	42.63	73.44

Conclusion

Although adding extra parameter and segmenting the algorithm increases the undesirable complexity of the initial structure. The measure is inevitable as the exploration and exploitation stages require different mechanics of the particle movement across search space. Including a constant term that vanishes after some period when enough information was collected showed good reliability even with a population size of 3 particles. It could be considered as meshing the objective function prior to calculation. Our adaptation of PSO demonstrated superior characteristics in terms of reliability and showed good speed. As further research, it will be interesting to see if PSO could be hybridized with machine learning algorithms to enhance its intelligence more significantly. Most biological creatures, if not all - exhibit learning features and utilize the information they collected over time to improve the quality of the process they are performing. While PSO uses comprehensibly only from several points, and the vast majority of the data it collected remains unused. Our attempts to manually guiding the exploration quality of PSO show the necessity of another component for the algorithm to learn from the past search and avoid stagnation and inefficient exploration.

Acknowledgements

The following work was supported by the Ministry of the Education of the Republic of Kazakhstan.
Grant № BR05336483

REFERENCES

1 Petrone G., Spagnuolo G., Teodorescu R. Reliability issues in photovoltaic power processing systems. *IEEE Transactions on Industrial Electronics*, 2008, Vol. 55, no. 7, pp. 2569–2580.

2 Bruendlinger R., Bletterie B., Milde M. Maximum power point tracking performance under partially shaded pv array conditions. *Proc. of the 21st Eur. Photovolt. Sol. Energy Conf., Berlin, Germany*, 2006, pp. 2157–2160.

3 Abdelsalam A. K., Massoud A. M., Ahmed S. High-performance adaptive perturb and observe mppt technique for photovoltaic-based microgrids. *IEEE Transactions on Power Electronics*, 2011, Vol. 26, No. 4, pp. 1010-1021.

4 Tey K. S. and Mekhilef S. Modified incremental conductance algorithm for photovoltaic system under partial shading conditions and load variation. *IEEE Transactions on Industrial Electronics*, 2014, Vol. 61, No. 10, pp. 5384–5392.

5 Koutroulis E., Blaabjerg F. A new technique for tracking the global maximum power point of pv arrays operating under partial-shading conditions. *IEEE Journal of Photovoltaics*, 2012, Vol. 2, No. 2, pp. 184-190.

6 Seyedmahmoudian M., Mekhilef S., Rahmani R. Maximum power point tracking of partial shaded photovoltaic array using an evolutionary algorithm: A particle swarm optimization technique. *Journal of Renewable and Sustainable Energy*, 2014, Vol. 6, No. 2, pp. 023102. https://doi.org/10.1063/1.4868025

7 Mao M., Duan Q., Zhang L., Chen H. Maximum power point tracking for cascaded pv-converter modules using two-stage particle swarm optimization. *Nature Scientific Reports*, 2017, pp. 9381. DOI: 10.1038/s41598-017-08009-7

8 Verma D., Nema S., Shandilya A. M. Comprehensive analysis of maximum power point tracking techniques in solar photovoltaic systems under uniform insolation and partial shaded condition. *Journal of Renewable and Sustainable Energy*, 2015, vol. 7, No. 042701. 042701. DOI: 10.1063/1.4926844

9 Salamon P., Sibani P., Frost R. *Facts, Conjectures, and Improvements for Simulated Annealing*. Society for Industrial and Applied Mathematics, 2002, 127 p.

10 Kennedy J., Eberhart R.C. Particle swarm optimization. *IEEE international conference on neural networks. IEEE, Piscataway, NJ, USA,* 1995, Vol. IV, pp. 1942–1948.

11 Fernandez-Martinez J., Garcia-Gonzalo E. Particle swarm optimisation: time for uniformisation. *Int. J. Computing Science and Mathematics,* 2013,Vol. 4(1), pp. 16 – 33. DOI: 10.1504/IJCSM.2013.054671

12 Trelea I. C. The particle swarm optimization algorithm: convergence analysis and parameter selection. *Information Processing Letters*, 2003, no. 85, pp. 317–325.

13 Zheng Y., Ma L., Zhang L. On the convergence analysis and parameter selection in particle swarm optimization. *Proceedings of the 2nd Intern. Conference on Machine Learning and Cybernetics,* Wan, 2003, pp. 2 – 5.

14 Kurmanbay A., Baktybekov K., Sakhanov K., Syzdykov A., Mukhamediyev A. Optimization of series-parallel connection of pv array to mitigate negative influence of partial shading conditions. *IOP Conf. Series: Materials Science and Engineering* 2020, 868 012001. DOI: 10.1088/1757-899X/868/1/012001

15 King D., Boyson W., et al. *Photovoltaic array performance model.* Sandia National Laboratories, 2004, 43 p.

16 Kirkpatrick S., et al. Optimization by simulated annealing. *Science*, 1983, Vol. 220, No. 4598. pp. 671-680.

17 Fernandez-Martínez J., Garcia-Gonzalo E. The pso family: deduction, stochastic analysis and comparison. *Swarm Intell 3,* 2009, No. 245, pp. 273. https://doi.org/10.1007/s11721-009-0034-8

18 Chen S., Montgomery J. Selection strategies for initial positions and initial velocities in multi- optima particle swarms. *Genetic and Evolutionary Computation Conference.* Dublin, Ireland, 2011, pp. 53 – 60.

19 Higashitani M., Ishigame A., Yasuda K. Particle swarm optimization considering the concept of predator-prey behavior. *IEEE Congress on Evolutionary Computation*, 2006. DOI: 10.1109/CEC.2006.1688341

20 Mikki S., Kishk A. Improved particle swarm optimization technique using hard boundary conditions. *Microw Opt Technol Lett*, 2005, Vol. 46, No. 5, pp. 422–426.

21 Riget J., Vesterstrøm J.S. *A diversity-guided particle swarm optimizer – the ARPSO. T*ech. rep., EVA Life Project Group, 2002.

22 Chowdhury S., Tong W., Messac A., Zhang J. A mixed-discrete particle swarm optimization algorithm with explicit diversity-preservation. *Struct Multidisc Optim*, 2012, vol. 47, pp. 367–388.

23 . Richards M., Ventura D. Choosing a starting configuration for particle swarm optimization. *Proceeding of the 2004 IEEE Intern. Joint Conference on neural networks,* Budapest, Hungary, 2004, pp. 2309–2312.

24 Khatib W., et al. *The studga: A mini revolution?* in Parallel Problem Solving from Nature. 2006, pp. 683-691.

25 Eiben A., BackT., Schoenauer M., Schwefel H. Parallel Problem Solving from Nature - PPSN V. *Proceedings of the 5th International Conference., Amsterdam, The Netherlands, September 27-30*, Springer, 1998. Available at: www.springer.com/gp/book/9783540650782

26 Simon D. *Evolutionary Optimization Algorithms Biologically-Inspired and Population-Based Ap- proaches to Computer Intelligence*. John Wiley & Sons, Inc., 2013, 685 p.

27 Clerc M., Poli R. *Stagnation analysis in particle swarm optimization or what happens when nothing happens. T*ech. rep., Department of Computer Science University of Essex, 2006, 15 p.

28 Shi Y.H. and Eberhart R.C. Parameter Selection in Particle Swarm Optimization. *Proceedings of the 7th International Conference on Evolutionary Programming VII*. 1998, pp. 591 – 600.

29 Konak A., Coitb D., Smithc A.E. Multi-objective optimization using genetic algorithms: A tutorial. *Reliability Engineering and System Safety*, 2006, Vol. 91, pp. 992–1007.

30 Wolpert D., Macready W. No free lunch theorems for optimization. *IEEE Transactions on Evolutionary Computation,* 1997, Vol. 1, No. 1, pp. 67–82.

Article accepted for publication 21.10.2020

DOI 10.31489/2020No2/138-145

UDC 616.874

ANALYSIS OF THE APPLICABILITY OF PHYSICAL MODELS TO DESCRIBE DENSIFICATION OF LITHIUM FERRITE COMPACTS DURING SINTERING IN THE FIELD OF INTENSE ELECTRON BEAM

Surzhikov A.P.[1], Lysenko E.N.[1], Malyshev A.V.[1], Kassymov S.S.[2]

[1]Tomsk Polytechnic University, Tomsk, Russia, lysenkoen@tpu.ru
[2] E.A. Buketov Karaganda University, Karaganda, Kazakhstan

The paper analyzes the possibility of describing the accelerated sintering of lithium-titanium compacts under high-power radiation effects in terms of classical physical models developed by Kuczynski and Johnson based on the kinetic analysis of ferrite compact densification. LiTi ferrites synthesized by ceramic technology in laboratory conditions were investigated. The first portion of the compacts was sintered in air in thermal ovens at 900–1100°C for 30 minutes at a heating rate of 900 °C/min. The second portion of the compacts was sintered in a similar mode but using a radiation-thermal method: the exposure to pulsed electron beam with energy of 1.5–2.0 MeV using the ILU-6 accelerator. The geometrical dimensions of the compacts were measured before and after sintering to determine shrinkage. Mathematical approximation of the experimental shrinkage data showed the discrepancy of both models to describe sintering of LiTi ferrite samples both under thermal sintering conditions and radiation-thermal effect.

Keywords: lithium ferrite, radiation-thermal sintering, shrinkage, kinetic analysis

Introduction

Diffusion-controlled solid-phase reactions form the basis of many physicochemical processes [1-4]. At the same time, interactions in the solid phase are among the slowest reactions, since the limiting reaction stage in most cases is related to the diffusive mass transfer of components through the layer of reaction products, and to the crossing of the activation barriers that separate the phases of heterogeneous systems [5-7]. Classical methods used to accelerate solid-phase reactions associated with increased temperature are naturally limited due to the thermal stability of materials [8-11]. Therefore, the development of methods to further increase the efficiency of solid-phase reactions is inevitably associated with unconventional methods used to supply energy to the reacting systems. The most promising method of stimulating solid-phase processes is the effect of high-current fluxes of ionizing radiation [12-22]. The advantages of this method are the selectivity of local overheating of phase boundaries, inertia-free heating, the ionizing effect and increased diffusion permeability of the medium due to defect formation.

In radiation materials science, accelerated electron fluxes are most widely used variety of ionizing radiation [23, 24]. This is due firstly to the progress in accelerator technology and relatively small, but powerful electron accelerators. Secondly, electron beams exhibit convenient geometrical parameters, easy to control irradiation mode, and do not induce radioactivity, they are cheaper compared to other sources of ionizing radiation, and highly efficient in conversion of electricity into electron beam energy [25-28].

The first studies that addressed solid-phase transformations in inorganic materials performed using high-temperature electron irradiation, which featured higher reaction rates, improved product quality, and reduced temperature of the processes, were investigations oxide under these specific conditions conducted for the synthesis of europium [29] and lithium ferrite compacts [30]. In [31], the authors report data on the effect of the high-power electron beam on solid-state inorganic synthesis occurring in a number of systems. It is shown that the magnitude of the effect depends on the following factors: the nature of the system, temperature and dose rate. Similar effects were found during the synthesis of a number of complex oxides in [32]. These effects were also used in current studies in sintering of MnZn ferrite [33, 34] and radiation-thermal synthesis of lithium-substituted ferrites [35-37].

During sintering of powder compacts of oxide systems (including ferrite ones), the radiation effect is characterized by increased speed of compact densification, especially at initial stages of sintering. However,

despite a large number of studies, the mechanism of the radiation intensification of sintering processes remains unclear. There are dispersed opinions on the mechanisms of the radiation activity of the processes: from overheating of grain boundaries and grain surfaces, which provides inter particle slip, to diffusion processes enhanced by the generation of non-equilibrium vacancies.

From the above, it can be seen that there are no objective assumptions to choose an adequate model of radiation sintering. The efficiency of radiation used to control solid-phase reactions depends crucially on the depth of understanding of the mechanism of its effect on the nature of the processes. The most common point of view on the mechanism of radiation acceleration of solid phase sintering implies a radiation-stimulated increase in the mobility of diffusing particles. However, a priori use of these ideas to interpret the effects of radiation-thermal sintering is inappropriate, since the diffusion mechanisms of mass transfer are not the only ones occurring during compact sintering. Therefore, this study analyzes the possibility of describing accelerated sintering of lithium-titanium compacts under powerful radiation effects by classical physical models based on the kinetic analysis of ferrite compact densification.

1. Experiment

The study explores mainly lithium-titanium ferrite powders synthesized from a mechanical mixture of oxides and carbonates containing (weight %): Li_2CO_3 – 11.2; TiO_2 – 18.65; ZnO – 7.6; $MnCO_3$ – 2.74; the rest is Fe_2O_3. The components are weighed as specified and then ground and mixed for 1 hour using a vibration grinding mill with distilled water previously added to the mixture in a mixture-water ratio (by weight) equal to 1:2. After treatment in the vibration grinding mill, the mixture is dried at 80 °C at normal atmospheric pressure for 24 hours and then rubbed through a 0.7 mesh sieve. Distilled water is added to the resulting powder in the amount of 10% of the powder weight, and then it is briquetted. The briquettes are heated in thermal furnaces at a rate of 200°C/h up to 900°C, held at this temperature for 6 hours and cooled to room temperature, after which they are crushed, ground and sieved through a 0.9 mesh sieve.

After re-grinding in the vibration grinding mill for 45 minutes, Bi_2O_3 dissolved in concentrated nitric acid in suspension (0.22 weight %) is added to the powder and mixed in the ball mill for 4 hours. The quality of the powder is determined using the method developed by us. To prepare the powder compact, 10% solution of polyvinyl alcohol is added to the synthesized mixture in the amount of 12 weight % of the mixture, and the resulting mixture is alternately rubbed through 0.7 and 0.45 mesh sieves. To study the sintering processes, the compact samples are made by cold single-action compaction in the form of pellets (15 mm in diameter and 2 mm thick). The compaction pressure is typically chosen experimentally for each specific ferrite composition according to the determined dependence of the volume density (ρ) of the samples on the compaction pressure (*P*) (Fig. 1).

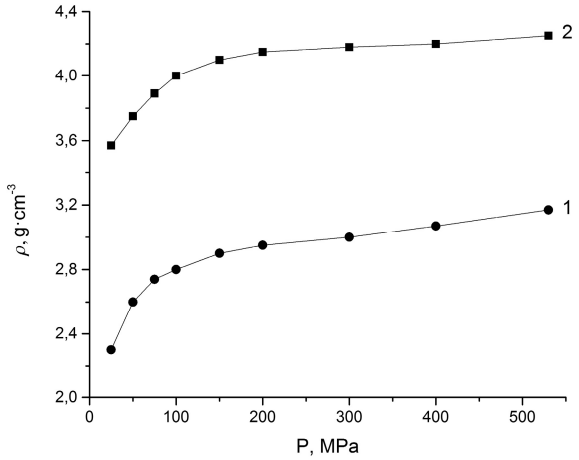

Fig.1. Dependence of the density of ferrite compacts on compaction pressure: 1) raw samples; 2) sintered samples

The compaction pressure varies within 25–500 MPa. The compacts are sintered in the thermal furnace at 900–1100°C for 30 minutes in air at a heating rate of 900°C/min. High speed is achieved by placing the compact samples into the furnace heated to a predetermined point. As follows from Fig. 1, the dependence of the density of the sintered samples on compaction pressure is similar to the dependence of densification of

raw samples (curves 1, 2). It is established that at pressures below 40 MPa the compacts exhibit low density, and at pressures above 250 MPa, the samples have cracks and delamination (over-compaction phenomenon).

Thus, the most optimal compaction pressure to provide an acceptable density of both raw and sintered samples is in the range of 110–200 MPa. The study employed the following pressing mode: P = 130 MPa, the holding time of the material under pressure is 1 min; and two modes of compact sintering: radiation-thermal (*RT*) and thermal (*T*) modes. *RT*-sintering was carried out by irradiation of the compacts by the pulsed electron beam with energy of 1.5–2.0 MeV at the ILU-6 accelerator developed at the Institute of Nuclear Physics (SB, Novosibirsk, Russia) [38]. The beam current in pulse was 0.5–0.9 A, the duration of irradiation pulse was 500 μs, the pulse repetition rate was 5–50 Hz, and the heating rate of the compacts was 1000°C/min. The samples were irradiated in a lightweight fireclay box with a bottom 15 mm thick. The side of the box exposed to irradiation was covered with a radiation-transparent protector with a mass thickness of 0.1 g/cm. The temperature was measured using a check sample placed in close proximity to the compacts sintered.

T-sintering was carried out in a preheated chamber electric furnace, which provided a heating rate comparable to the rate of radiation heating. The sintering cell design and temperature control technique are similar to those used in *RT*-sintering. Both sintering modes were carried out in the air. To date, a large number of sintering theories have been advanced at the atomic level. We used the model representations by Kuczynski [39] and Johnson [40] to perform the analysis. Kuczynski's theory in its simplest and clearest form contains fundamental principles underlying most of the sintering models. Johnson's theory takes into account a number of additional significant factors, such as coexistence of several types of mass transfer (volume and grain boundary diffusion, transfer through the gas phase) and change in the geometric dimension of grains during sintering.

2. Results and Discussion

2.1. Kuczynski's model

According to this model, the interpenetration of powder grains (the initial phase of densification) is carried out through the mass transfer by the mechanism of volume (*V*) or grain boundary (*GB*) diffusion [24–27]. In volume diffusion, the densification kinetics is described by the equation:

$$\left(\frac{\Delta L}{L}\right)_V = \frac{(31\gamma V D_V/RT)^{2/5}\tau^{2/5}}{4a^{6/5}}\tau^{2/5}. \quad (1)$$

According to the mechanism of grain boundary diffusion, the kinetics takes the form:

$$\left(\frac{\Delta L}{L}\right)_{GB} = \frac{(96\gamma\delta V D_{GB}/RT)^{1/3}\tau^{1/3}}{4a^{4/3}}\tau^{1/3}. \quad (2)$$

In (1) and (2): $\Delta L/L$ is linear shrinkage; a is the radius of spherical grains; γ is the coefficient of surface tension; V is the material molar volume; δ is the grain boundary width; D_V and D_{GB} are coefficients of volume and grain boundary diffusion, respectively; T is sintering temperature; τ is sintering time. Mathematical approximations in (1) and (2) limit the applicability of these expressions to $\Delta L/L \approx 6$ %.

The experimental results were processed as follows. The diameters of the sintered samples were measured, and the kinetic dependences of diameters in the time interval of 0–400 s were constructed for all sintering modes, in which the diameter linear shrinkage did not exceed 10%. After compaction, the diameters of all samples were similar and equaled 15.05 mm. This value d_0 was taken as L_0. The intermediate values of diameters with respect to the diameters measured were taken from the constructed dependences $d = f(\tau)$ to calculate linear shrinkage $\Delta L/L = \Delta d/d$.

Figures 2 and 3 show dependences plotted in double logarithmic coordinates: $\Delta d/d = f(\tau)$ for thermal (line 1) and radiation-thermal (line 2) sintering modes. The dependencies are straight lines. This indicates the exponential functional dependence of shrinkage on sintering time [39]. Using the least squares method, the densification dependences were approximated by exponential functions:

$$\frac{\Delta d}{d_0} = A\tau^n, \quad (3)$$

where A is the temperature dependent constant; n is the sintering mode dependent exponent.

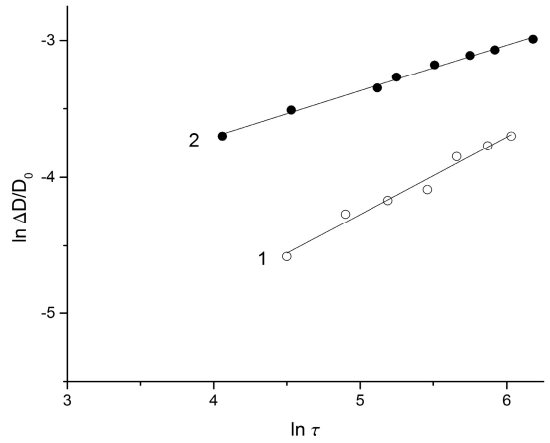

Fig.2. Dependence of linear shrinkage on time of sintering at 900 °C: 1) *T*-sintering; 2) *RT*-sintering.

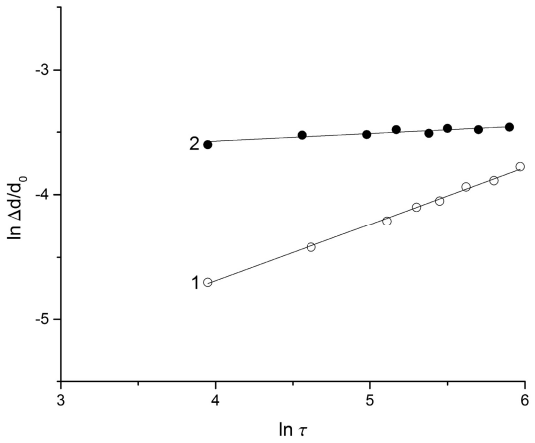

Fig.3. Dependence of linear shrinkage on time of sintering at 1000 °C: 1) *T*-sintering; 2) *RT*-sintering.

Table 1 presents the numerical values of the exponential function parameters for both sintering modes in the temperature range of 900–1100°C.As can be seen, the Kuczynski's model does not satisfy the experimental results despite the exponential dependence of the initial densification. This follows from the fact that the exponent, which characterizes the mechanism of mass transfer to the contact area, monotonously changes with temperature. This may be due to a continuous change in the mechanism of mass transfer (when the temperature changes), which contradicts the theory of Kuczynski.

Table 1 - Parameters of exponential functions (3)

Sintering temperature, °C	Sintering mode			
	Thermal		Radiation-thermal	
	n	*A*	*n*	*A*
900	1.11	$5.4\cdot10^{-5}$	0.38	$5.7\cdot10^{-3}$
950	0.61	$1.4\cdot10^{-3}$	0.31	$1.1\cdot10^{-2}$
1000	0.51	$3.4\cdot10^{-3}$	0.18	$3.5\cdot10^{-2}$
1050	0.28	$1.8\cdot10^{-2}$	0.14	$4.7\cdot10^{-2}$
1100	0.46	$0.7\cdot10^{-2}$	0.09	$6.7\cdot10^{-2}$

It should be noted that the correspondence of the parameter *n* to any sintering mechanism depends on the contact geometry. However, this correspondence should not depend on temperature. In this regard, we can conclude that the mechanism of sintering LiTi ferrites does not satisfy the Kuczynski's model.

2.2. Johnson's model

Johnson's model assumes that mass transfer, which leads to material densification, is performed through diffusion in the volume and along the grain boundary. For the case of sintering the compact from spheres of similar diameter, in which the number of contacts per sphere does not depend on time, the relationship between the linear shrinkage rate $V = \frac{d}{d_0}(\Delta L/L)$and the current contact geometry is expressed by equation [40]:

$$\frac{X^3 R}{X+R} V = \frac{2\gamma\Omega D_V S}{\pi k T a^3 X} + \frac{4\gamma\Omega D_{GB}}{kTa^4}, \quad (4)$$

where $X = x/a$ is relative neck radius; Ω is atomic volume; R is theminimum radius of the neck surface curvature divided by the sphere radius; S is the neck surface area divided by a^2; x is the inner radius of the spherical contact neck; a is the radius of spherical grains. Knowing $\Delta d/d$ and X, the values of R and S can be calculated by the equations:

$$R = \frac{(\Delta d/d)^2 - 2(\Delta d/d) + X^2}{2(1-X)},$$

$$S = 4\pi R[Q(1+R)cosQ - RsinQ],$$

where $Q = sin^{-1}\left[\left(1-(\Delta d/d)\right)/(1+R)\right]$.

When graphically depicting the left side of equation (4) depending on S/X, the coefficients of volume diffusion and diffusion along the grain boundaries can be calculated from the slope of curves and their intersections.

Equation (4) can be greatly simplified if we confine to the analysis of the initial stages of isothermal densification. In this case, the relative neck radius $X=x/a$ can be expressed analytically through linear shrinkage ($\Delta d/d$):

$$\frac{\Delta d}{d} = \left(\frac{x}{2S}\right)^2, X = \frac{x}{a} = 2\sqrt{\Delta d/d}\,. \tag{5}$$

Thus, to apply equation (4) with the approximation (5), it is necessary to know the kinetic dependences of shrinkage $y=f(\tau)$ of the average grain size $\bar{a}=f(\tau)$ only. The approximation limits the range of changes $\Delta d/d$ to 10%. Microstructural analysis of ferrite samples sintered in thermal and radiation modes at 1100°C was performed to determine the kinetic changes in the grain size. The measurement results are presented in Figure 4. It can be seen that recrystallization growth of grains becomes evident at τ>1800 s in both sintering modes. That is, at the initial stages of isothermal sintering, changes in grain sizes can be neglected and a = const in (4). The processing of experimental data according to equation (4) was carried out as follows. The kinetic dependencies of the initial densification were approximated by exponential functions (3) with the parameters given in Table 1. The shrinkage derivatives for the sintering time range of 0–400 s (60 s steps) were calculated by differentiation (3). Then, according to (5), X was calculated and the values of S, R, Q were determined for each point of time.

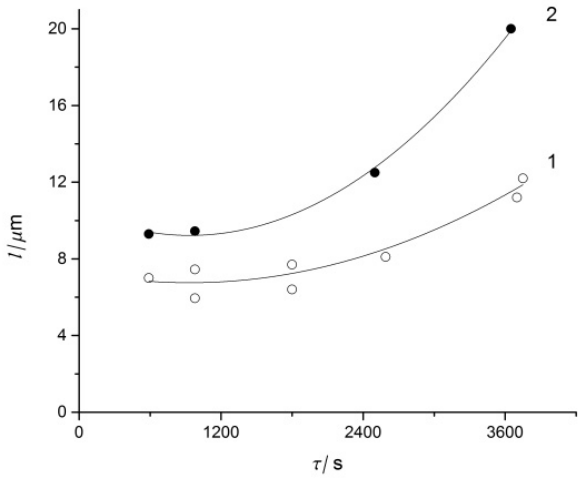

Fig.4. Dependence of the average grain size on time of sintering at 1100 °C: 1) *T*-sintering; 2) *RT*-sintering.

The function graphs were plotted taking $TRX^3\frac{d(\Delta d/d)}{d\tau}/(X+R)$in (4) as a function and S/X as an argument. Some graphs are presented in Figures 5 and 6. According to (4), in case the Johnson's model is valid, the curves should be obtained in given coordinates, the slope of which is proportional to the volume diffusion coefficient D_V, and the intercept in the ordinate axis is proportional to the boundary diffusion coefficient D_{GB}.

However, the experimental curves behave arbitrarily depending on the sintering mode and temperature. In particular, the curves obtained show either non-linearity (Fig. 5, curve 1 and Fig. 6, curve 2) or negative values of the intercepts in the ordinate axis (Fig. 5, curve 1 and Fig. 6, curves 1, 2). Nonlinearity of the curves contradicts equation (4). Negative values of the slope and intercepts indicate negative diffusion coefficients, which has no physical sense.

Thus, the analysis of the experimental results within the Johnson's model shows inefficiency of this model for describing the sintering process of LiTi ferrite samples under both thermal sintering and radiation-thermal exposure.

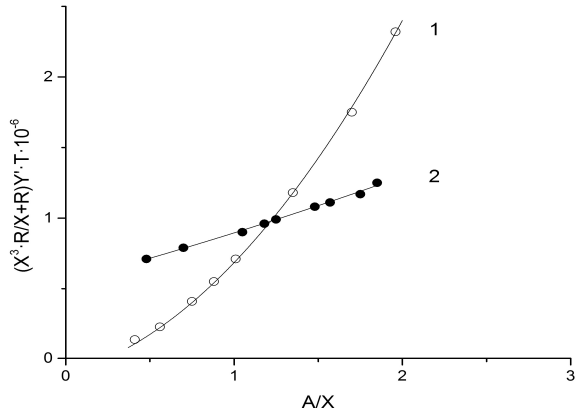

Fig.5. Dependence of densification on geometric characteristics of the grains at 900 °C: 1) *T*-sintering; 2) *RT*-sintering.

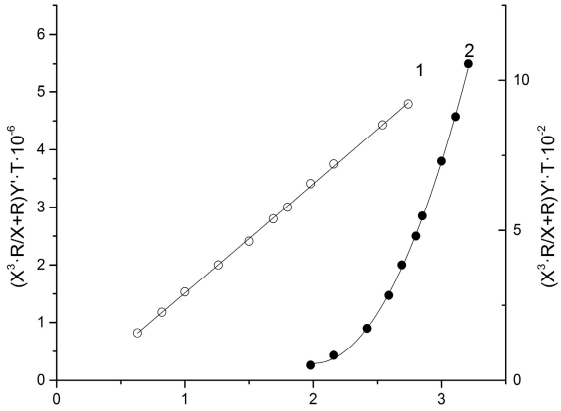

Fig.6. Dependence of densification on geometric characteristics of the grains at 1000 °C: 1) *T*-sintering; 2) *RT*-sintering.

Conclusion

Classical physical models cannot be apparently used to describe the kinetics of ferrite compact densification due to the infeasibility of simplifying assumption (simple geometric shapes of powder grains, equal grain size, etc.). In this regard, the current stage of development of physics of sintering does not allow the description of the processes of electron-beam sintering of ferrite ceramics using physical models, and the phenomenological approach is preferable. This approach, in particular, will allow aquantitative comparison of radiation and thermal sintering modes to identify their features and to interpret these in terms of some hypotheses.

Acknowledgements

This research was supported by the Ministry of Education and Science of the Russian Federation in part of the "Science" program. The experiments on equipment and participation in the scientific conference were funded from Tomsk Polytechnic University Competitiveness Enhancement Program grant.

REFERENCES

1 Surzhikov A.P., Pritulov A.M., Lysenko E.N., Sokolovskii A.N.,Vlasov V.A., Vasendina E.A. Influence of solid-phase ferritization method on phase composition of lithium-zinc ferrites with various concentration of zinc. *Journal of Thermal Analysis and Calorimetry*. 2012, Vol. 109, pp. 63 – 67. https://doi.org/10.1007/s10973-011-1366-3.

2 Surzhikov A.P., Lysenko E.N., Malyshev A.V., Pritulov A.M., Kazakovskaya O.G. Influence of mechanical activation of initial reagents on synthesis of lithium ferrite. *Russian Physics Journal*. 2012, Vol. 55, №.6, pp. 672 – 677. https://doi.org/10.1007/s11182-012-9865-7.

3 Sharma P., Uniyal P. Investigating thermal and kinetic parameters of lithium titanate formation by solid-state method. *Journal of Thermal Analysis and Calorimetry*. 2017, Vol.128, pp. 875 – 882. https://doi.org/10.1007/s10973-016-5977-6.

4 Sun Yu, Wan Zhipeng, Hu Lianxi, Wu Binghua, Deng Taiqing. Characterization on Solid Phase Diffusion Reaction Behavior and Diffusion Reaction Kinetic of Ti/Al. *Rare Metal Materials and Engineering*.2017,Vol. 46, pp. 2080 - 2086. https://doi.org/10.1016/S1875-5372(17)30183-2.

5 Durgadsimi S.U., Chougule S.S., Kharabe R.G., Mathad S.N., Rendale M.K. Solid-state synthesis and structural features of $Li_{0.5}Ni_{0.75-x/2}Fe_2O_4$ ferrites. *International Journal of Self-Propagating High-temperature Synthesis*. 2019, Vol. 28, pp. 71-73. https://doi.org/10.3103/S1061386219010060.

6 Cook W., Manley M. Raman characterization of □- and □-$LiFe_5O_8$ prepared through a solid-state reaction pathway. *Journal of Solid State Chemistry*. 2010, Vol.183, pp. 322 □□326. doi.org/10.1016/j.jssc.2009.11.011.

7 Berbenni V., Marini A., Matteazzi P., et al. Solid-state formation of lithium ferrites from mechanically activated Li_2CO_3 – Fe_2O_3 mixtures. *Journal of the European Ceramic Society*. 2003, Vol.23, pp. 527 – 536. https://doi.org/10.1016/S0955-2219(02)00150-4.

8 Rakshit S.K., Parida S.C., Naik Y.P., Venugopal V. Thermodynamic studies on lithium ferrites. *Journal of Solid State Chemistry*. 2011,Vol.184, pp. 1186 – 1194. https://doi.org/10.1016/j.jssc.2011.03.033.

9 El-Shobaky G.A., Ibrahim A.A. Solid-solid interactions between ferric oxide and lithium carbonate and the thermal stability of the lithium ferrites produced. *Thermochimica Acta*. 1987,Vol.118, pp. 151–158. https://doi.org/10.1016/0040-6031(87)80079-5.

10 Senyut V.T. Study of synergistic effect of mechanical activation and high pressure and high temperature sintering on the structure of the material based on boron nitride. *Eurasian Physical Technical Journal*. 2020, Vol.17, pp. 19-25. https://doi.org/10.31489/2020NO1/19-25.

11 Gundlach E.M., Gallagher P.K. Thermogravimetric determination of the oxygen non-stoichiometry in $Ni_{0.563}Zn_{0.188}Fe_{2.25}O_{4+}$ and $Ni_{0.375}Zn_{0.375}Fe_{2.25}$ O_{4+}. *Thermochimica Acta*. 1998, Vol.318, pp. 15 – 20. https://doi.org/10.1016/S0040-6031(98)00324-4.

12 Ancharova U.V., Mikhailenko M.A., Tolochko B.P., et al. Synthesis and Staging of the Phase Formation for Strontium Ferrites in Thermal and Radiation Thermal Reactions. *IOP Conference Series: Materials Science and Engineering*. 2015, Vol. 81, Article number 012122. https://doi.org/10.1088/1757-899X/81/1/012122.

13 Zhuravlev V.A., Naiden E.P., Minin R.V., et al. Radiation-thermal synthesis of W-type hexaferrites. *IOP onference Series: Materials Science and Engineering*. 2015, Vol. 81, 012003. https://doi.org/10.1088/1757-899X/81/1/012003.

14 Oane M., Toader D., Iacob N., Ticos C.M. Thermal phenomena induced in a small tungsten sample during irradiation with a few MeV electron beam: Experiment versus simulations. *Nuclear Instruments and Methods in Physics Research Section B: Beam Interactions with Materials and Atoms*. 2014, Vol. 337, pp. 17 – 20. https://doi.org/10.1016/j.nimb.2014.07.012.

15 Karipbayev Zh., Alpyssova G., Mussakhanov D., Lisitsyn V., Kukenova A., Tulegenova A. Time-resolved luminescence excited with N_2 laser of YAG: CE Ceramics formed by electron beam assisted synthesis. *Eurasian Physical Technical Journal*. 2020, Vol.17, pp. 73 – 76. https://doi.org/10.31489/2020NO1/73-76.

16 Vasoya N.H., Vanpariya L.H., Sakariya P.N., Timbadiya M.D., Pathak T.K., Lakhani V.K., Modi K.B. Synthesis of nanostructured material by mechanical milling and study on structural property modifications in $Ni_{0.5}Zn_{0.5}Fe_2O_4$. *Ceram. Int.* 2010, Vol.36, pp. 947 – 954. https://doi.org/10.1016/j.ceramint.2009.10.024.

17 Jiang W., Wang L., Wang X. Studies on surface topography and mechanical properties of TiN coating irradiated by high current pulsed electron beam, *Nucl. Instr. Meth. Phys. Res.Sect. B* 2018, Vol.436, pp. 63 – 67.

18 Kavanlooee M., Hashemi B., Maleki-Ghaleh H., Kavanlooee J. Effect of annealing on phase evolution, microstructure, and magnetic properties of nanocrystalline ball-milled LiZnTi ferrite, *J. Electronic materials*. 2012, Vol.41, pp. 3082 – 3086. https://doi.org/10.1007/s11664-012-2235-y

19 Naiden E.P., Minin R.V., Itin V.I., Zhuravlev V.A. Influence of Radiation-Thermal Treatment on the Phase Composition and *Structural Parame*ters of the SHS Product Based on W-Type Hexaferrite, *Russ. Phys. J.* 2013, Vol. 56, pp. 674 – 680.https://doi.org/10.1007/s11182-013-0084-7

20 Šepelák V., Wibmann S., Becker K.D. Magnetism of nanostructured mechanically activated and mechanosynthesized spinel ferrites, *J. Magn. Magn. Mat.* 1999, Vol. 203, pp. 135 – 137. https://doi.org/10.1016/S0304-8853(99)00248-6

21 Ivanov A.S., Maznev V.P., Ovchinnikov V.P., Svinin M.P., TolstunN.G. Present State of Works on Development of Electron Accelerators for Energy Consuming Processes at Efremov Research Institute. Prospects and Challenges in Application of Radiation for Treating Exhaust Gases, Warsaw, 2007.

22 Shirvanedeh H.I., Douk H.S., Farhood B. Improving and optimizing the structure of a cylindrical ionization chamber for radiation protection dosimetry: Guard electrode and chamber wall. *Radiation Physics and Chemistry*, 2019, Vol.163, pp. 45 – 51. https://doi.org/10.1016/j.radphyschem.2019.04.058

23 Matsuyama S., Ishii K., Fujisawa M., et al. Upgrading of the 4.5 MV Dynamitron accelerator at Tohoku University for microbeam and nanobeam applications. *Nucl. Instr. Meth. B*. 2009, Vol. 267, pp. 2060 – 2064. https://doi.org/10.1016/j.nimb.2009.03.028.

24 Lisitsyn V.,Lisitsyna L.,DauletbekovaA., et al. Luminescence of the tungsten-activated MgF_2 ceramics synthesized under the electron beam. *Nucl. Instr. Meth. B*. 2018, Vol.435, pp. 263 – 267. doi.org/10.1016/j.nimb.2017.11.012.

25 Salimov R.A., Cherepkov V.G., Golubenko J.I., et al. High power electron accelerators of ELV-series: status, development, applications. *Radiation Physics and Chemistry*. 2000, Vol. 57, pp. 661 – 665. https://doi.org/10.1016/S0969-806X(99)00486-7.

26 Cleland M.R., Parks L.A. Medium and high-energy electron beam radiation processing equipment for commercial applications. *Nuclear Instruments and Methods in Physics Research Section B: Beam Interactions with Materials and Atoms*. 2003, Vol. 208, pp. 74 – 89. https://doi.org/10.1016/S0168-583X(03)00672-4.

27 Mehnert R. Review of industrial applications of electron accelerators. *Nuclear Instruments and Methods in Physics Research Section B: Beam Interactions with Materials and Atoms*. 1996, Vol. 113, pp. 81 – 87. https://doi.org/10.1016/0168-583X(95)01344-X.

28 Martins M.N., Silva T.F. Electron accelerators: History, applications, and perspectives. *Radiation Physics and Chemistry*. 2014, Vol. 95, pp. 78 – 85. https://doi.org/10.1016/j.radphyschem.2012.12.008.

29 Neronov V.A., Voronin A.P., Tatarintseva M.I., et al. Sintering under a high-power electron beam. *Journal of the Less Common Metals*. 1986, Vol. 117, pp. 391 – 394. https://doi.org/10.1016/0022-5088(86)90065-2.

30 Surzhikov A.P., Lysenko E.N., Malyshev A.V., et al. Study of the Radio-Wave Absorbing Properties of a Lithium-Zinc Ferrite Based Composite. *Russian Physics Journal*. 2014, Vol. 57, №. 5, pp. 621 □□626. https://doi.org/10.1007/s11182-014-0284-9.

31 Boldyrev V.V., Voronin A.P., Gribkov O.S., et al. Radiation-thermal synthesis current achievement and outlook. *Solid State Ionics*. 1989, Vol. 36, pp.1 – 6. https://doi.org/10.1016/0167-2738(89)90051-9.

32 Lyakhov N.Z., Boldyrev V.V., Voronin A.P., et al. Electron beam stimulated chemical reaction in solids. *Journal of Thermal Analysis*. 1995. Vol.43, pp.21 – 31. https://doi.org/10.1007/BF02635965.

33 Kostishin V.G., Andreev V.G., Korovushkin V.V., et al. Preparation of 2000NN ferrite ceramics by a complete and a short radiation-enhanced thermal sintering process. *Inorganic Materials*. 2014, Vol.50, pp. 317 – 323. https://doi.org/10.1134/S0020168514110089.

34 Kostishyn V.G., Komlev A.S., Korobeynikov M.V., et al. Effect of a temperature mode of radiation-thermal sintering the structure and magnetic properties of Mn-Zn-ferrites. *Journal of Nano- and Electronic Physics*. 2015, Vol.7, 04044.

35 Lysenko E.N., Surzhikov A.P., Vlasov V.A., et al. Synthesis of substituted lithium ferrites under the pulsed and continuous electron beam heating. *Nuclear Instruments and Methods in Physics Research Section B: Beam Interactions with Materials and Atoms*. 2017, Vol. 392, pp.1 – 7. https://doi.org/10.1016/j.nimb.2016.11.042.

36 Surzhikov A.P., Malyshev A.V., Lysenko E.N., et al. Structural, electromagnetic, and dielectric properties of lithium-zinc ferrite ceramics sintered by pulsed electron beam heating. *Ceramics International*. 2017, Vol. 43, pp. 9778 – 9782. https://doi.org/10.1016/j.ceramint.2017.04.155.

37 Surzhikov A.P., Pritulov A.M., Lysenko E.N., et al. Dependence of lithium–zinc ferrospinel phase composition on the duration of synthesis in an accelerated electron beam. *Journal of Thermal Analysis and Calorimetry*. 2012, Vol. 110, pp. 733 – 738. https://doi.org/10.1007/s10973-011-1947-1.

38 Auslender V.L. ILU-type electron accelerator for industrial technologies. *Nuclear Instruments and Methods in Physical research B*. 1994, Vol. 89, pp. 46 – 48. https://doi.org/10.1016/0168-583X(94)95143-8.

39 Kuczynski G.C. Model experiments and the theory of sintering. *Sintering Key Papers, Elsevier Applied Science*, London and New York. 1990, pp.501 – 502.

40 Johnson D.L. A general model for the intermediate stage of sintering. *Journal of the American Ceramic Society*. 1970, Vol. 53, pp. 574 – 579.https://doi.org/10.1111/j.1151-2916.1970.tb15969.x.

Article accepted for publication 21.10.2020

DOI 10.31489/2020No2/146-152

UDC 530.19

ON THE STRUCTURE OF COHOMOLOGICAL MODELS OF ELECTRODYNAMICS AND GENERAL RELATIVITY

Arkhipov V.V.[1], Aringazin A.K.[2], Kudussov A.S.[3]

[1]Moscow Institute of Physics and Technology, Moscow, 141701, Russia, arkhipov.vv@mipt.ru
[2] L.N. Gumilyov Eurasian National University, Nur-Sultan, Kazakhstan, aringazin@gmail.com
[3] E.A. Buketov Karaganda University, Karaganda, Kazakhstan, akudusov@mail.ru

In the present paper, we take case of a complex scalar field on a Riemannian manifold and study di□erential geometry and cohomological way to construct field theory Lagrangians. The total Lagrangian of the model is proposed as 4-form on Riemannian manifold. To this end, we use inner product of differential (p, q)-forms and Hodge star operators. It is shown that actions, including that for gravity, can be represented in quadratic forms of fields of matter and basic tetrad fields. Our study is limited to the case of the Levi-Civita metric. We stress some features arisen within the approach regarding nil potency property. Within the model, Klein-Gordon, Maxwell and general relativity actions have been reproduced.

Keywords: cohomological theory, exterior calculus, differential forms, field theory, Riemannian manifold.

Introduction

A cohomological approach is used to describe field theory models as a powerful instrument to reveal hidden symmetries and especially topological properties. The use of the theory of differential forms and external calculus is a feature of Einstein-Cartan's theory [1, 2], teleparallel gravity [3] and field theories on symplectic manifolds [4]. We note that the action for gravitational field in general relativity introduced as a 4-volume integral of the scalar curvature of the field, or other scalars are built from metrics and connections (see, for example a review work [5]). The reason for such choice is to keep invariance and follow minimal model set up. Similar approach is used in the gauge theory of gravity, where the covariant derivative is introduced by analogy with the theories of physical fields, but the action of the field itself is postulated in the standard form used in general relativity; see, for example, one of the first work [6].

In our approach, we build the action based on the well-known inner product of differential forms,

$$(\xi,\varphi) = \int \xi \wedge *\varphi, \tag{1}$$

where $*$ is the Hodge star operator. The concept of external differential forms is generalized to the objects defined simultaneously on the tangent and cotangent bundle and written in the antisymmetric basis,

$$\omega = \frac{1}{p!}\frac{1}{q!}\omega_{\alpha_1\cdots\ \alpha_q}^{\beta_1\cdots\ \beta_q} \mathrm{d}x^{\alpha_1} \wedge \ldots \wedge \mathrm{d}x^{\alpha_p} \wedge \partial_{\beta_1} \wedge \ldots \wedge \partial_{\beta_q}.$$

The objects are well-known and called (p, q)-forms. We introducing these and use in such a way that the action can be constructed in a cohomological approach.

We use the following concepts and notations. Let x^μ be coordinates in a certain area of the Riemannian manifold $R^{1,3}$. We naturally assume that a small neighborhood of each point $R^{1,3}$ is isomorphic to Minkowski space. That is, at each point $R^{1,3}$ a local coordinate system x^a (a = 0,1,2,3) can be chosen, in which the metric takes the simple form $\eta_{ab} = diag(1,-1,-1,-1)$.

Here below, we use Latin letter indices for local coordinate system and x^a Greek letter indices for the global system x^μ on $R^{1,3}$.Thus at each point on $R^{1,3}$ the following elements are defined: the elementary interval $ds = \sqrt{\eta_{ab} dx^a dx^b}$, the elementary oriented area $dx^a \wedge dx^b$, volume $dx^a \wedge dx^b \wedge dx^c$, and

4-volume form $\Omega = \frac{1}{4!}\epsilon_{abcd} dx^a \wedge dx^b \wedge dx^c \wedge dx^d$, where ϵ_{abcd} is totally antisymmetric tensor; $\epsilon_{0123} = 1$.

The relation of the differentials of the local coordinate system dx^a with the differentials dx^μ at a given point is determined by the coefficients h^a_μ and h^μ_a ($h^a_\mu h^\mu_b = \delta^a_b$, $h^a_\mu h^\nu_a = \delta^\nu_\mu$):

$$dx^a = h^a_\mu dx^\mu, \qquad dx^\mu = h^\mu_a dx^a.$$

If we define a basis dx^a independently at each point of the space $R^{1,3}$ then the coefficients h^a_μ and h^μ_a turn into functions of the system $h^a_\mu(x^\mu)$, $h^\mu_a(x^\mu)$. Since dx^a is independent at different points in space, they can be considered as a tetrad of basis fields $h^a(x^\mu)$. These are not necessarily holonomic ones [3].

The space-time metric on $R^{1,3}$ in the holonomic basis dx^μ is definedin the standard way: $g_{\mu\nu} = \eta_{ab} h^a_\mu h^b_\nu$.

In the following, along with the notation dx^μ and dx^a for the anti-symmetric basis with multiplication denoted by ∧, we will use notation c^μ and c^a, assuming the antisymmetric property $c^\mu c^\nu = -c^\nu c^\mu$.

On $TR^{1,3}$, an antisymmetric basis dual to c^μ can be introduced, which we denote as $\bar{c}_\mu$. In this basis, contravariant antisymmetric tensors called here as *q*-forms, dual to the usual antisymmetric differential *p*-forms, can be expanded. In particular, vector space can beun derstood due to isomorphism as the space of contravariant 1-forms $\xi = \xi^\mu \bar{c}_\mu$. Generally, $c^a(x^\mu)$ can be treated not only as the differentials of dx^a. For example, one could assign it Fadeev-Popov's ghost fields meaning; see [7] for details. In this set up, the fields c^μ and $\bar{c}_\mu$ acquireghost numbers

$$ghost\#(c^\mu) = 1,\ ghost\#(\bar{c}_\mu) = -1$$

and the total ghost number should be conserved.

The basis for contravariant vectors is usually denoted as $\partial/\partial x^\mu$, as a dual to the differentials of dx^μ. The choice of such a notation is determined by the corresponding law of the gradient transformationof the function $\partial_\mu f(x^a)$. Geometrically, the main this is their transformation rules. Taking into account the possibility of a scalar product between basic elements on $TR^{1,3}$ and $T^*R^{1,3}$, it is more convenient to associate with $\bar{c}_\mu$ the operator $\partial/\partial c^\mu$ rather than ∂_μ. In the conjugate representation, c^μ can be associated with $\partial/\partial \bar{c}_\mu$. We stress that the c^a introduced above are the same as h^a but antisymmetric multiplication through the wedge ∧ should be used.

1. External Calculus on Riemannian Manifold

Let *p*-forms be ordinary differential antisymmetric forms defined on the cotangent bundle $T^*R^{1,3}$. They can be written in a form

$$\omega = \frac{1}{p!}\omega_{\mu_1 \cdots \mu_p} \mathrm{dx}^{\mu_1} \wedge \ldots \wedge \mathrm{dx}^{\mu_p} \qquad \text{or} \qquad \omega = \frac{1}{p!}\omega_{\mu_1 \cdots \mu_p} \mathrm{c}^{\mu_1} \ldots \mathrm{dc}^{\mu_p}$$

Let *q*-forms be contravariant antisymmetric tensors of rank *q* defined on a tangent bundle $TR^{1,3}$. They have a form

$$\chi = \frac{1}{q!}\chi^{\mu_1 \cdots \mu_q} \partial_{\mu 1} \wedge \ldots \wedge \partial_{\mu q} \qquad \text{or} \qquad \chi = \frac{1}{q!}\chi^{\mu_1 \cdots \mu_q} \bar{c}_{\mu 1} \ldots \bar{c}_{\mu q}$$

Let (*p*, *q*)-forms be antisymmetric tensors with *q* contravariant and *p* covariant indices. The tensors are antisymmetric with respect to the both sets of contravariant and covariant indices. Therefore, the (*p*, *q*)-forms defined simultaneously on the tangent $TR^{1,3}$ and on the cotangent $T^*R^{1,3}$ bundles and can be written as

.

$$\eta = \frac{1}{p!}\frac{1}{q!}\eta^{\mu_1 \cdots \mu_q}_{\nu_1 \cdots \nu_p} c^{\nu_1} \ldots c^{\nu_p} \bar{c}_{\mu 1} \ldots \bar{c}_{\mu q}.$$

There is an isomorphism between the tangent and cotangent bundles realized by metric operators

$$\hat{g} = g_{\mu\nu} c^{\mu} \frac{\partial}{\partial \bar{c}_{\nu}}, \; \hat{g}^{-1} = g^{\mu\nu} \bar{c}_{\mu} \frac{\partial}{\partial c^{\nu}}.$$

Let's define the generalizations of these operators $\hat{G}$, which trans-form (*p*, *q*)-forms into (*q*, *p*)-forms using the metric tensor due to the rule

$$\hat{G}_{\eta} = \frac{1}{p!}\frac{1}{q!}\eta^{\mu_1 \cdots \mu_q}_{\nu_1 \cdots \nu_p} g_{\mu_1 \alpha_1} \cdots g_{\mu_q \alpha_q} g^{\nu_1 \beta_1} \ldots g^{\nu_p \beta_p} c^{\alpha_1} \ldots c^{\alpha_q} \bar{c}_{\beta_1} \ldots \bar{c}_{\beta_p}.$$

A covariant exterior differential *d* that converts (*p*, *q*)-forms to (*p+1*, *q*)-forms can be defined as $d = c^{\alpha} \nabla_{\alpha}$, or

$$d = c^{\alpha} \partial_{\alpha} + c^{\alpha} \Gamma^{\gamma}_{\alpha\beta} \bar{c}_{\gamma} \frac{\partial}{\partial \bar{c}_{\beta}}. \quad (2)$$

In particular, when it is acting on (0,1)-form $\chi = \chi_{\tau} \bar{c}_{\tau}$ we have:

$$d_{\chi} = (c^{\alpha} \partial_{\alpha} + c^{\alpha} \Gamma^{\gamma}_{\alpha\beta} \bar{c}_{\gamma} \frac{\partial}{\partial \bar{c}_{\beta}}) \chi_{\tau} \bar{c}_{\tau} = c^{\alpha} \nabla_{\alpha} \chi^{\beta} \bar{c}_{\beta}.$$

Here and after, by $\Gamma^{\gamma}_{\alpha\beta}$ is meant the Levi-Civita connection, consistent with the metric

$$\Gamma^{\gamma}_{\alpha\beta} = \frac{1}{2} g^{\alpha\lambda} (\partial_{\alpha} g_{\lambda\beta} + \partial_{\beta} g_{\lambda\alpha} - \partial_{\lambda} g_{\alpha\beta}).$$

Note that the nil potency property of the exterior differential $d^2 = 0$ is preserved on the space of (*p,0*)-forms. However, on the space of (*0, q*)-forms this property is violated. In particular, for $\chi = \chi_{\tau} \bar{c}_{\tau}$ we have

$$d^2 \chi = \frac{1}{2} c^{\alpha} c^{\mu} \bar{c}_{\alpha} R^{\alpha}_{\nu\alpha\mu} \chi^{\nu}$$

where $R^{\alpha}_{\nu\alpha\mu}$ is the Riemannian curvature tensor.

It can be shown that the dual to *d* operator $\bar{d} = \bar{G} d \bar{G}$ that converts (*p*, *q*)-forms to (*p, q+ 1*)-forms can be represented as $\bar{d} = \bar{c}_{\alpha} g^{\alpha\beta} \nabla_{\beta}$, or

$$\bar{d} = \bar{c}_{\alpha} g^{\alpha\beta} (\partial_{\beta} + \Gamma^{\gamma}_{\lambda\beta} \bar{c}_{\gamma} \frac{\partial}{\partial \bar{c}_{\lambda}} - \Gamma^{\gamma}_{\lambda\beta} c^{\lambda} \frac{\partial}{\partial c^{\gamma}}).$$

Using the 4-form of volume $\Omega = \frac{1}{4!} \sqrt{-g} \epsilon_{\mu_1 \mu_2 \mu_3 \mu_4} c^{\mu_1} c^{\mu_2} c^{\mu_3} c^{\mu_4}$ and its dual, fully antisymmetric contravariant tensor $\bar{\Omega} = \frac{1}{4!} \frac{1}{\sqrt{-g}} \epsilon^{\mu_1 \mu_2 \mu_3 \mu_4} \bar{c}_{\mu_1} \bar{c}_{\mu_2} \bar{c}_{\mu_3} \bar{c}_{\mu_4}$, we can define two types of the Hodge star operators: the operator $*$ which is transforming (*p, q*)-forms into (*4−p, q*)-forms in a standard way and the conjugate operator $\star$ converting (*p, q*)-forms into (*p,4−q*)-forms.

The Hodge star operators $*$ and $\star$ allow us to construct the divergence operator $\hat{\delta} = * d *$, lowering the *p*-rank of the form by one ((*p, q*)→(p−1, q)), and its dual operator $\hat{\bar{\delta}} = \star \bar{d} \star$ acting like (*p, q*)→(*p, q*−1). It can be shown that

$$\hat{\bar{\delta}} = \partial_\mu \frac{\partial}{\partial \bar{c}_\mu} + \frac{\partial}{\partial \bar{c}_\alpha} c^\nu \Gamma^\alpha_{\nu\mu} \frac{\partial}{\partial \bar{c}_\mu}. \quad (3)$$

Note that the operator can be derived from (2) by formal replacing $c^\alpha \to \partial/\partial \bar{c}_\alpha$.

It is easy to check that commutators $[d, \hat{\delta}]$ and $[\bar{d}, \hat{\bar{\delta}}]$ give the same Laplace operator (up to the isomorphism $\hat{G}$). We use the term 'commutator' both to commutators and anti-commutators assuming that the latter applies only for odd (p+q) rank. We now see that methods of cohomology theory (see for example [8]) can be applied here to a full extent. However, it is easy to verify that the commutator of conjugate operators (2) and (3) gives the Ricci tensor when acts at the (0,1)-form:

$$\left(d\hat{\bar{\delta}} + \hat{\bar{\delta}} d\right)\xi = -c^\alpha R_{\alpha\tau}\xi^\tau. \quad (4)$$

The inner product (1) allows to build entities like usual scalar product but it has a wider scope. In this paper, we are using the following formulas. For usual functions (0-forms) $f(x^\mu)$ and $f(g^\mu)$ we have

$$(f,g) = \frac{1}{4!}\int fg\epsilon_{\lambda\alpha\beta\gamma}\sqrt{-g}dx^\lambda \wedge dx^\alpha \wedge dx^\beta \wedge dx^\gamma = \int fg\sqrt{-g}d\Omega, \quad (5)$$

where $d\Omega = dx^0 dx^1 dx^2 dx^3$ is an elementary 4-volume.

For 1-forms $\phi_1 = \phi_\mu c^\mu$ and $\varphi_1 = \varphi_\mu c^\mu$ we have

$$(\phi_1, \varphi_1) = \int \phi_\mu \varphi_\nu \, g^{\mu\nu}\sqrt{-g}d\Omega. \quad (6)$$

For 2-forms $\omega_2 = (1/2)\omega_{\mu\nu}c^\mu c^\nu$ and $\sigma_2 = (1/2)\sigma_{\mu\nu}c^\mu c^\nu$ it follows

$$(\omega_2, \sigma_2) = 2\int \omega_{\mu\nu}\,\sigma_{\alpha\beta}\, g^{\alpha\lambda} g^{\beta\rho}\sqrt{-g}d\Omega. \quad (7)$$

2. Scalar Field

The complex scalar field $\phi(x^\mu)$ can be considered as taking values in 'inner' spaces attached to the points of $R^{1,3}$, with a complex structure C^1 so that $\phi = \phi^1 + i\phi^2$, or Euclidean one R^2 with metrics $\tilde{\eta}_{AB} = diag(1,1)$. In the last case,

$$\phi = \phi^A = (\phi^1, \phi^2).$$

The inner product of two complex scalar fields ϕ and φ gives the invariant with respect to the action of transformation group U(1),

$$(\varphi^\dagger, \phi) = \int \varphi^\dagger \wedge * \phi,$$

where the Hermitian conjugation † is acting only on the internal space. In particular, in the complex representation † is reduced simply to the complex conjugation and in the matrix representation to transpose.
As it follows from (5) and (6) the inner square of the complex scalar field $\phi = \phi(x^\mu)$ and its first differential are

$$(\phi^*, \phi) = \int |\phi|^2\sqrt{|g|}d\Omega,$$

and

$$(d\phi^*, d\phi) = \int g^{\mu\nu}\,\partial_\mu\phi^*\partial_\nu\phi\sqrt{|g|}d\Omega.$$

.

This allows us to represent the action of a complex scalar field,

$$S_\phi = \frac{1}{2}\int (g^{\mu\nu}\,\partial_\mu\phi^*\partial_\nu\phi \;-\; m^2\phi^*\phi)\,\sqrt{|g|}d\Omega,$$

in the following form:

$$S_\phi = \frac{1}{2}(d\phi^*, d\phi) - \frac{m^2}{2}(\phi^*, \phi). \tag{8}$$

This action can be varied directly using properties of the inner product (see [9]) and one can get usual Klein-Gordon equation in the form $(\partial^\mu\partial_\mu - m^2)\phi = 0$. To turn on an interaction with external electromagnetic field let's consider a basis on an 'inner' space e_A (A = 1, 2). Let's define an internal connection in standard way as

$$\delta e_A = e_\beta \tilde{\Gamma}^\beta_{A\mu}\delta x^\mu, \tag{9}$$

with imposed local U(1) symmetry we get

$$\tilde{\Gamma}^\beta_{A\mu} = S^\beta_A A_\mu(x^\mu),$$

where $S^\beta_A = \begin{pmatrix} 0 & 1 \\ -1 & 0 \end{pmatrix}$ is a generator of u(1) algebra.

Thus, the covariant derivative D_μ, which is a variant of the Fock-Ivanenko derivative [3], acts as follows:

$$\mathrm{D}_\mu\phi_A = \partial_\mu\phi_A - S^\beta_A A_\mu(x^\mu)\phi_\beta.$$

In the complex representation $\phi = \phi_0(x^\mu)e^{i\varphi(x^\mu)}$, the covariant derivative takes the form

$$\mathrm{D}_\mu\phi = \partial_\mu\phi + iA_\mu\phi.$$

In field theory, the covariant derivative usually includes the charge *e* as a characteristic of the interaction with the field, $\mathrm{D}_\mu\phi = \partial_\mu\phi + ieA_\mu\phi$. Here we put *e*= 1 for simplicity.

Generalization of external calculus to complex-valued forms implies the replacement $\partial_\mu \to \mathrm{D}_\mu$. The consequence of this is the loss of the nilpotency property of the external differential, as occurred above for the covariant differential on Riemannian manifold. Namely, on Minkowski space we have (see [9] for details)

$$d^2\phi = c^\nu D_\nu\left(c^\mu D_\mu\phi\right) = \frac{i}{2}F_{\mu\nu}\phi c^\mu c^\nu,$$

where $F_{\mu\nu} = \partial_\mu A_\nu - \partial_\nu A_\mu$.

Explicitly, taking into account the rule $\partial_\mu \to \mathrm{D}_\mu$, the action of the scalar field (8) takes the usual form for complex scalar field interacting with exterior vector field A^μ:

$$S_\phi = \left(\partial_\mu\phi^* - iA_\mu\phi^*\right)(\partial^\mu\phi + iA^\mu\phi) - m^2\phi^*\phi.$$

3. The Actions of Electromagnetic and Gravitation Fields

The expression (9) allows us to define the differential of the basis vector in the form

$$de_A = e_B S_A^\beta A_\mu(x^\mu)c^\mu. \tag{10}$$

For double differential we have

$$d^2e_A = e_B S_A^\beta A_\mu(x^\mu)c^\mu + e_B S_A^\beta \partial_\nu A_\mu(x^\mu)c^\nu c^\mu = e_C S_\beta^C A_\nu S_A^\beta A_\mu(x^\mu)c^\nu c^\mu + e_B S_A^\beta \partial_\nu A_\mu(x^\mu)c^\nu c^\mu$$

Obviously, the first term is identically equals to zero. So, we get

$$d^2e_A = \frac{1}{2} e_B S_A^\beta F_{\mu\nu} dx^\mu \wedge \mathrm{d}x^\nu.$$

Taking into account the relation $S_\beta^{A\dagger} = -S_\beta^A$ and (7) we have

$$(d^2e^A, d^2e_A) = -\frac{1}{2}\int e^c S_C^A F_{\mu\nu} g^{\mu\alpha} g^{\nu\beta} e_D S_A^D F_{\alpha\beta}\sqrt{-g}d\Omega = \frac{1}{2}\int e^A F_{\mu\nu} g^{\mu\alpha} g^{\nu\beta} e_A F_{\alpha\beta}\sqrt{-g}d\Omega$$
$$= \int F_{\mu\nu} F^{\mu\nu}\sqrt{-g}d\Omega.$$

Finally, the action of the electromagnetic field $S_{EM} = -\frac{1}{16\pi}\int F_{\mu\nu} F^{\mu\nu}\sqrt{-g}d\Omega$ can be rewritten in the terms of structure elements of tangent bundle space,

$$S_{EM} = -\frac{1}{16\pi}(d^2e^A, d^2e_A).$$

Note that the inner square of the first differentials of the basis vectors (de^A, de_A), by virtue of (10) is proportional to $A_\mu A^\mu$. Such term is not included in the action of charged particles and the electromagnetic field due to the zero-mass assumption for photons. The action for general relativity case can be constructed almost in the same way, with the basis have to be taken due to (4). For basis fields $c^\alpha = h_\mu^\alpha c^\mu$ and $c_\alpha = h_\alpha^\nu \bar{c}_\nu$.we have

$$\left(c^\alpha, \left(d\hat{\bar{\delta}} + \hat{\bar{\delta}}d\right)c_\alpha\right) = -\int h_\alpha^\alpha R_{\nu\chi} h_\alpha^\nu g^{\alpha\chi}\sqrt{-g}d\Omega = -\int R\sqrt{-g}d\Omega,$$

where $R = R_{\alpha\beta} g^{\alpha\beta}$ is the scalar curvature.

Thus, the Einstein-Hilbert action [5] for the gravitational field canbe written as

$$S_{EH} = -\frac{1}{16\pi G}\left(c^\alpha, \left(d\hat{\bar{\delta}} + \hat{\bar{\delta}}d\right)c_\alpha\right).$$

Conclusion

In the present work, we demonstrated that the action for scalar, electromagnetic, and gravitation fields can be represented as the sum of the internal squares of the scalar field, the basis fields and their differentials,

$$S = \frac{1}{2}(d\phi^\dagger, d\phi) - \frac{m^2}{2}(\phi^\dagger, \phi) - \frac{1}{16\pi}(d^2e^A, d^2e_A) - \frac{1}{16\pi G}\left(c^\alpha, \left(d\hat{\bar{\delta}} + \hat{\bar{\delta}}d\right)c_\alpha\right).$$

As a final remark we note that construction of a Lagrangian as 4-form on Riemannian space imposes some restrictions on the acceptable forms of action of field theoretical models.

.

REFERENCES

1 Hehl F.W. and Obukhov Y.N. E´lie Cartan's torsion in geometry and in field theory, an essay. arXiv:0711.1535v1 [gr-qc] 9 Nov2007.

2 Trautman A. Einstein–Cartan Theory. arXiv:gr-qc/0606062v1 14 Jun 2006

3 Aldrovandi R. and Pereira J.G. *Teleparallel Gravity: An Introduction*. New York, London: Springer Dordrecht Heidelberg, 2013, 202p.

4 Eliashberg Y., Givental A. and Hofer H. *Introduction to Symplectic Field Theory*. Basel: Birkhauser Verlag, 2000, 102p.

5 Clifton T., Ferreira P.G., Padilla A. and Skordis C. Modified Gravity and Cosmology. *Physics Reports*, 2012, No 513, pp.1-189.

6 Utiyama R. Invariant theoretical interpretation of interaction. *Phys. Rev*., 1956, Vol. 101, No 5, pp.1597-1608.

7 Aringazin A.K., Arkhipov V.V. and Kudusov A.S. BRST Approach to Hamiltonian systems // arXiv:hep-th/9811026

8 Atiah M.F. and Singer I.M. The index of elliptic operators I. *Uspekhi Mat. Nauk*, 1968, Vol. 23, No 5(143), pp.99–142.

9 Arkhipov V.V. Minimal Cohomological Model of a Scalar Field on a Riemannian Manifold. *Russ. Phys.* J., 2018., Vol. 60, No 12, pp.2051-2063.

Article accepted for publication 03.12.2020

SUMMARIES	ТҮСІНІКТЕМЕЛЕР	АННОТАЦИИ

Stary O., Малышев А.В., Лысенко Е.Н., Петрова А.

Радиациялық-термиялық күйдіру кезіндегі ферриттердің магниттік қасиеттерін қалыптастыру.

Жұмыста жылулық және радиациялы-жылулық режимдерінде күйген феррит гистерезисі циклінің параметрлерін қалыптастыру заңдылықтарын салыстырмалы талдау нәтижелері келтірілген. Радиациялық әсердің өңдеу ұзақтығы мен температурасына байланысты микроқұрылым ақауларының өзара түрленуіне және олардың ферриттердегі құрамына әсері анықталды. Сондай-ақ, сәулелену жағдайындағы қайта кристалдану дәнінің өсуі термиялық қыздыру кезіндегі дәннің өсуінен асып түсетіні көрсетілген. Байқалған радиациялық әсерлер радиацияның микроқұрылымға әсерімен байланысты болды. Магниттік параметрлердің мәндері үлгінің тығыздалуымен бір мәнді анықталады.

Stary O., Малышев А.В., Лысенко Е.Н., Петрова А.

Формирование магнитных свойств ферритов во время радиационно-термического спекания.

В работе представлены результаты сравнительного анализа закономерностей формирования параметров петли гистерезиса феррита, спеченного в тепловом и радиационно-термическом режимах. Установлено влияние радиационного воздействия на взаимопревращение дефектов микроструктуры и их содержание в ферритах в зависимости от продолжительности и температуры обработки. Также было показано, что рост зерна рекристаллизации в условиях облучения опережает рост зерна при термическом нагреве. Наблюдаемые радиационные эффекты были связаны с воздействием излучения на микроструктуру. Значения магнитных параметров однозначно определяются уплотнением образца.

Halamani Koushallya M., Mathad Shalini K., Kulkarni Akshay B., Mathad Shridhar N., Jeergal Pundalik. R., Hiremath Chidanandayya.S., Pujar Appanna S., Pujar Rangappa B.

Алюминиймен қоспаланған никель-кадмий ферриттерінің құрылымдық қасиеттерінің күйдіру кезіндегі өзгерістер.

Берілген жұмыстың мақсаты алюминиймен керамикалық әдіспен қоспаланған Ni-Cd ферриттерінің құрылымдық қасиеттерін синтездеу және зерттеу болып табылады. Үлгілерді күйдіру температурасы 1100 ° С, күйдіру уақыты t = 9, 11, 13, 15 сағат. Үлгілердің сипаттамалары рентгендік дифракция, сканерлеуші электрондық микроскоп, энергиялы-дисперсиялық рентгендік талдау және Фурье түрлендіруімен инфрақызыл сәулелену талдауы арқылы зерттелген. Шпинельдің бір фазалы қарапайым кубтық құрылымы дифрактограммалармен расталды. Тордың параметрі 8.478–8.481 Å аралығында жатыр. Растрлық электронды микроскоптың көмегімен алынған микрофотографияларда өлшемдердің біркелкі таралуы байқалды. Элементтік талдау феррит формуласындағы бүкіл металл иондарының болуын растайтын энергиялы-дисперсиялық рентгендік талдау арқылы жүргізілген. Фурье түрлендіруімен инфрақызыл спектрлер сәйкесінше тетраэдрлік және октаэдрлік позицияларда металдың оттегі байланысының тербелістеріне үлестерін беретін υ_1 *(581-582 см$^{-1}$)* және υ_2 (400 см$^{-1}$-ден аз) екі жолағын көрсетті.

Halamani Koushallya M., Mathad Shalini K., Kulkarni Akshay B., Mathad Shridhar N., Jeergal Pundalik. R., Hiremath Chidanandayya.S., Pujar Appanna S., Pujar Rangappa B.

Изменение структурных свойств никель-кадмиевых ферритов, легированных алюминием, при спекании.

Целью данной работы является синтез и исследование структурных свойств ферритов Ni-Cd, легированных алюминием, керамическим методом. Образцы спекали при температуре 1100 ° С, время спекания t = 9, 11, 13, 15 часов. Характеристики образцов исследовались с помощью рентгеновской дифракции, сканирующего электронного микроскопа, энерго-дисперсионного рентгеновского анализа и инфракрасного излучения с преобразованием Фурье. Однофазная простая кубическая структура шпинели подтверждается дифрактограммами. Параметр решетки находится в диапазоне 8.478–8.481 Å. Равномерное распределение по размерам наблюдалось на микрофотографиях, сделанных с помощью растрового электронного микроскопа. Элементный анализ выполнялся с помощью энергодисперсионного рентгеновского анализа, подтверждающего присутствие всех ионов металлов, присутствующих в формуле феррита. Инфракрасные спектры с преобразованием Фурье показали две полосы υ_1 *(581-582 см$^{-1}$)* и υ_2 *(менее чем 400 см$^{-1}$)* , которые дают вклад колебаниям кислородной связи металла в тетраэдрических и октаэдрических позициях соответственно.

Кадыржанов К.К., Шлимас Д.И., Канюков Е.Ю., Калиекперов М.Е.

Cu-Bi жабындарының фазалық құрамының иондаушы сәулеленуден экрандау тиімділігіне әсерін анықтау.

Жұмыс Cu-Bi жабындарының фазалық құрамына байланысты ауыр иондардың радиациялық әсеріне экрандау тиімділігін зерттеуге арналған. Қорғаныс жабындарын алу әдісі ретінде электрохимиялық тұндыру әдісі қолданылды. Фазалық құрам тұндыру кезінде қолданылатын потенциалдар айырмасын түрлендіру арқылы

өзгертілген. Зерттеу барысында фазалық құрамның өзгеруі, $CuBi_2O_4$ фазасының үстемдігі және құрылымдық реттілік дәрежесінің жоғарылауы нәтижесінде жабындардың тығыздығының артуына әкелетіні анықталды. Экрандау тиімділігін анықтауға бағытталған сынақтар барысында кристалдық деңгейінің ең үлкен төмендеуі мыс жабындары үшін байқалатындығы анықталды, олар үшін максималды сәулелену флюенсі кезінде құрылымның аморфизациясы 12 %-дан жоғары болды, ал $CuBi_2O_4$ негізіндегі жабындарда аморфизация мәні бастапқы мәннен 1,2 %-дан аспайды. Жоғары сәулелену дозалары кезінде дәндердің ұсақталуы мен аморфизациясы экрандау тиімділігінің төмендеуіне, сонымен қатар ΔU ауытқу мәнінің артуына әкеледі.

Кадыржанов К.К., Шлимас Д.И., Канюков Е.Ю., Калиекперов М.Е.

Определение влияния фазового состава Cu-Bi покрытий на эффективность экранирования от ионизирующего излучения.

Работа посвящена изучению эффективности экранирования радиационного воздействия тяжелых ионов в зависимости от фазового состава Cu-Bi покрытий. В качестве метода получения защитных покрытий был применен метод электрохимического осаждения. Изменение фазового состава проводилось путем варьирования разности прикладываемых потенциалов при осаждении. В ходе исследования установлено, что изменение фазового состава приводит к увеличению плотности покрытий, в результате доминирования фазы $CuBi_2O_4$ и увеличению степени структурных упорядочений. В ходе испытаний направленных на определение эффективности экранирования установлено, что наибольшее снижение степени кристалличности наблюдается для медных покрытий, для которых аморфизация структуры при максимальном флюенсе облучения составила более 12 %, в то время как для покрытий на основе $CuBi_2O_4$ величина аморфизации составила не более 1.2 % от начального значения. Аморфизация и дробление зерен при больших дозах облучения приводит к снижению эффективности экранирования, а также увеличению величины отклонения ΔU.

Юров В.М., Гученко С.А., Салькеева А.К., Кусенова А.С.

Гидроцилиндрлер штоктарын азоттау.

Жұмыста гидроцилиндрлердің жылтыратылған штоктарын ионды-плазмалық азоттау әдісі қарастырылған. Иондық азоттау кезінде бөлшектердің беттік беріктенуі айқын көрінеді. Бұл бөлшектің бетттік қабатының 20 нм-ден аспайтындығымен байланысты, яғни ол наноқұрылым болып табылады. Бұл наноқұрылымда азоттың диффузия процестері көлемдік процестерден айтарлықтай ерекшеленеді. Наноқұрылымдағы өлшемдік әсерлер қабатта Фиктің «классикалық» теңдеулерінің жұмыс істемейтіндігіне және бұл қабаттағы азоттың диффузиясы болаттың қасиеттеріне байланысты логарифмді тәуелділігіне әкеледі. Нанопласттағы диффузия массивті үлгінің $Д_0$ диффузия коэффициенті арқылы пластинаның материалына да, өлшемдік факторға да байланысты екендігі теориялық тұрғыдан алынған. Классикалық жағдайда мұндай тәуелділік жоқ.

Юров В.М., Гученко С.А., Салькеева А.К., Кусенова А.С.

Азотирование штоков гидроцилиндров.

В работе рассмотрен метод ионно-плазменного азотирования полированных штоков гидроцилиндров. При ионном азотировании наиболее ярко проявляется поверхностное упрочнение деталей. Это связано с тем, что поверхностный слой детали не превышает 20 нм, то есть представляет собой наноструктуру. В этой наноструктуре процессы диффузии азота существенны отличны от объемных. Размерные эффекты в наноструктуре приводят к тому, что в слое не работают «классические» уравнения Фика и диффузия азота в этом слое зависит логарифмически от свойств стали. Теоретически получено, что диффузия в нанопластине зависит как от материала пластины через коэффициент диффузии массивного образца $Д_0$, так и от размерного фактора α. В классическом случае такой зависимости нет.

Суржиков А. П., Чичерина Н.В., Рогачев, А.В. , Ярмоленко М.А. , Руденков А.С., Рогачев А. А., Wang Jicheng

Электрондармен инициирленген эндотермиялық процестердің ағымында тұндырылған металл оксидтері және ПТФЭ негізіндегі композициялық жабындардың құрамы мен құрылымы.

Металл нитраттары, металдар негіздегі нысан құраушылары арасындағы физика-химиялық процестердің электрондардың төмен энергиялы ағынмен инициирленген ағынның ерекшеліктері анықталған, олардың ұшпа өнімдердің пайда болу кинетикасына әсері, тұндырылған жабындардың химиялық құрамы мен құрылымына әсері анықталды. Электрондар алюминий нитраты мен дисперсті алюминий қоспасына әсер ету кезінде құрамында мырыш наноөзекшелері бар мырыш оксиді жабындарының түзілуі анықталды. Темір нитраты ұнтақтары мен дисперсті алюминий ұнтақтарының механикалық қоспасына электрондар ағынының әсері нысананың жарылғышты булануымен қатар жүреді және металл оксидтері мен нанобөлшектеріне ие жабын бетіндегі нысананың беткі қабаттарында экзотермиялық реакциялар ағымының соңғы сатысында тұндырылатын көптеген микротамшылы түзілімдер тіркелген. ПТФЭ, алюминий және темір нитратының механикалық қоспасының электронды-сәулелік диспергирленуінің ұшпа өнімдерінен тұндырылған жабындардың құрылымының, химиялық құрамының ерекшеліктері анықталды. Мұндай газ фазасының генерациясы жағдайларында полимерлі матрицадан тұратын және құрамында оксид, бос металл және белгілі

бір мөлшерде бастапқы ыдырамайтын тұздарға ие жабындар пайда болатындығы көрсетілген. Тигельдегі экзотермиялық реакциялардың салдары ішінара дефторлану және фторопласт матрицасының молекулалық құрылымындағы жоғары ақаулығы болып табылады.

Суржиков А. П., Чичерина Н.В., Рогачев, А.В. , Ярмоленко М.А. , Руденков А.С., Рогачев А. А., Wang Jicheng

Состав и структура композиционных покрытий на основе оксидов металла, ПТФЭ, осажденных в условиях протекания инициируемых электронами эндотермических процессов.

Установлены особенности инициируемых низкоэнергетичным потоком электронов физико-химических процессов между компонентами мишени на основе нитратов металлов, металлов, их влияние на кинетику образования летучих продуктов, химический состав и структуру осаждающихся покрытий. При воздействии электронов на смесь нитрата алюминия и дисперсного алюминия установлено формирование покрытий оксида цинка, содержащих наностержни цинка. Воздействие потока электронов на механическую смесь порошков нитрата железа и дисперсного алюминия сопровождается взрывным испарением мишени и на поверхности покрытия, содержащего оксиды и наночастицы металла, фиксируются большое количество микрокапельных образований, осаждаемых на заключительном этапе протекания экзотермических реакций в поверхностных слоях мишени. Определены особенности структуры, химического состава покрытий, осажденных из летучих продуктов электроннолучевого диспергирования механической смеси ПТФЭ, алюминия и нитрата железа. Показано, что при таких условиях генерации газовой фазы формируются покрытия, состоящие из полимерной матрицы и содержащие частицы оксида, свободного металла и некоторое количество исходной неразложившейся соли. Следствием протекания в тигле экзотермических реакций является частичная дефторированность и повышенная дефектность молекулярной структуры фторопластовой матрицы.

Жанабаев З.Ж., Икрамова С.Б., Тілеу А.О., Тұрлықожаева Д.А.

Нанокеуекті шалаөткізгіш қабықшалардың энергетикалық тыйым салу зонасының ені.

Жұмыстың мақсаты шалаөткізгіш нанокеуекті құрылым жадтары мен ток мәндерінің секірістерінің пайда болу себептерін тәжірибеде анықтау болып табылады. Кеуекті наноқұрылымдар электрохимиялық жеміру арқылы алынды. Үлгілердің вольт-амперлік сипаттамасы кеуекті кремний және жұқа қабықшалы халькогенді шынытәріздес шалаөткізгіш үшін өлшенген. Лазер сәулесін түсірген кезде кеуекті кремний наноқабықшаларында токтың гистерезисі мен секірмелі ажыратылып-қосылуы болатыны тәжірибеде көрсетілген. Ажыратылып-қосылу кернеуі мәнінің тыйым салу зонасы енінің наноқабықша кеуектілігінен тәуелділігі бойынша байланысы анықталды. Бұл нәтижелер екінші ретті фазалық ауысу теориясының ережелеріне сүйене отырып токтың ажыратылып-қосылу және оның гистерезис теориясын құруға мүмкіндік береді.

Жанабаев З.Ж., Икрамова С.Б., Тілеу А.О., Тұрлықожаева Д.А.

Ширина энергетически запрещенной зоны нанопористых полупроводниковых пленок.

Целью настоящей работы является экспериментальное выяснение причин возникновения скачков величины тока и памяти полупроводниковых нанопористых структур. Пористые наноструктуры были получены методом электрохимического травления. Вольт-амперные характеристики образцов измерялись для пористого кремния и на тонких пленках халькогенидного стеклообразного полупроводника. Экспериментально показано существование скачкообразного переключения и гистерезиса тока в нанопленках пористого кремния при лазерном освещении. Обнаружена связь значений напряжения переключения с зависимостью ширины запрещенной зоны от пористости нанопленок. Эти результаты позволяют построить теорию переключения тока и его гистерезиса по положениям теории фазовых переходов второго рода.

Есжанов А.Б., Досмагамбетова С.С.

Мембраналықсүзу арқылы сұйық радиоактивті қалдықтарды тазалау үшін тректі мембраналарды гидрфобизациялау.

Берілген мақалада полиэтилентерефталаттан жасалған гидрофобты тректік мембраналарды қолдана отырып, тікелей контактілі мембраналық сүзу әдісімен сұйық төмен деңгейлі радиоактивті қалдықтарды тазарту нәтижелері келтірілген. Тректік мембраналарды гидрофобизациялау ультрафиолет сәулелену әсерінен триэтоксивинилсиландыстиролмен егу полимерлеу және фторы бар силандармен арқылы жүзеге асырылды. Гидрофобты мембраналар сканерлеуші электронды микроскоп, Фурье түрленуімен инфрақызыл спектроскопиясы, жанасу бұрышын өлшеу және сұйықтықтың серпіндік қысымын талдау арқылы зерттелген. Алынған мембраналар сұйық төменгі деңгейлі радиоактивті қалдықтарды мембрана сүзу арқылы тазартуда сыналды. Кеуектер мөлшерінің өнімділікке және тұздардан тазару дәрежесіне әсері зерттелген. Тазарту дәрежесі кондуктометриялық және атомдық эмиссия әдістерімен бағаланды. Гамма-спектроскопия көмегімен ^{60}Co, ^{137}Cs және ^{241} Am үшін есептелген дезактивтендіру коэффициенттері – полистирол және триэтоксивинилсилан модификацияланған мембраналар үшін 85,4, 1900 және 5,4 (кеуекдиаметрлері 142 нм), 85,0, 1462 және 4 перфтородецилтрихлорсиланмен модификацияланған мембраналар 150 нм кеуек диаметрі мен

үшін сәйкесінше құрайды.

Ержанов А.Б., Досмагамбетова С.С.

Гидрофобизация полиэтилентерефталатовых трековых мембран для очистки от жидких радиоактивных отходов мембранной дисцилляцией.

В данной статье представлены результаты очистки жидких низкоактивных радиоактивных отходов методом прямой контактной мембранной дистилляции с использованием гидрофобных трековых мембран из полиэтилентерефталата. Гидрофобизация трековых мембран была проведена путем прививочной полимеризации триэтоксивинилсилана со стиролом под действием УФ-излучения и покрытия фторсодержащимисиланами. Гидрофобные мембраны исследовали с помощью сканирующего электронного микроскопа, инфракрасной спектроскопии с преобразованием Фурье, измерения краевого угла и анализа давления проскока жидкости. Полученные мембраны были протестированы в очистке жидких низкоактивных радиоактивных отходов методом мембранной дистилляции. Изучено влияние размеров пор на производительность и степень очистки от солей. Степень очистки оценивали кондуктометрическим и атомно-эмиссионным методами. Коэффициенты дезактивации, оцененные с помощью гамма-спектроскопии для ^{60}Co, ^{137}Cs и ^{241}Am, составляют 85,4, 1900 и 5,4 для мембран, модифицированных полистиролом и триэтоксивинилсиланом с диаметром пор 142 нм и 85.0, 1462 и 4 для мембран, модифицированных перфтордецилтрихлорсиланом, с диаметром пор 150 нм соответственно.

Аймұханов А.К., Зейниденов А. К., Омарбекова Г. И., Плотникова И. В.

NIO/PEDOT:PSS композиттік қабықшаларының оптикалық және электрофизикалық сипаттамаларын зерттеу.

Жұмыста Nickel Oxide/poly(3,4-ethylenedioxythiophene) polystyrene sulfonate (NIO/PEDOT:PSS) композиттік қабықшаларының морфологиялық, оптикалық және электрофизикалық параметрлерін зерттеу нәтижелері көрсетілген. Төсеменің айналу жылдамдығының артуы NiO қабықшалар бетінің кедір-бұдырлығын азайтуға әкелетіні көрсетілген. Никель оксиді бетінің кедір - бұдырлығы төмендеген кезде PEDOT:PSS қабыршағының кедір-бұдырлығы да төмендейді. Төсеменің айналу жылдамдығының жоғарылауы NiO қабыршақтарының, сондай-ақ NIO/PEDOT:PSS композиттік қабыршақтарының жұтылу спектрлерінің оптикалық тығыздығының төмендеуіне алып келеді. NIO/PEDOT:PSS композиттік қабыршақтарының морфологиясының өзгеруі инжекциялық кемтіктердің сыртқы электродқа жылдам тасымалдануына және кері рекомбинация ықтималдығын азайтуға ықпал ететіндігі анықталды.

Аймуханов А.К., Зейниденов А.К., Омарбекова Г.И., Плотникова И. В.

Исследование оптических и электрофизических характеристик композитных пленок NIO/PEDOT:PSS.

В работе представлены результаты исследования морфологических, оптических и электрофизических параметров композитных пленок Nickel Oxide/poly(3,4-ethylenedioxythiophene) polystyrene sulfonate (NiO/PEDOT:PSS.) Показано что увеличение скорости вращения подложки приводит к уменьшению шероховатости поверхности пленок NiO. При уменьшении шероховатости поверхности оксида никеля шероховатость пленки PEDOT:PSS также уменьшается. Увеличение скорости вращения подложки приводит к уменьшению оптической плотности спектров поглощения пленок NiO, а также композитных пленок NiO/PEDOT:PSS. Установлено, что изменение морфологии композитных пленок NiO/PEDOT:PSS способствуют быстрому транспорту инжектированных дырок к внешнему электроду и уменьшению вероятности обратной рекомбинации.

Тұрмұхамбетов А.Ж., Айтманова К.А., Өтегенова С.Б.

Турбуленттік ортадағы конвективтік жылуалмасуды фракталды – құрылымдық тұрғыдан талдау.

Турбулентті ортадағы денелердің конвективті жылу алмасуының ерекшеліктері қарастырған. Тәжірибелік зерттеулер нәтижелері талқыланған. Тәжірибелік зерттеулер жылуалмасу қарқындылығына табиғи конвекция, ортаның жылуфизикалық қасиеттері, ағынның қысаңшылық дәрежесі сияқты көп факторлар әсер ететіндігін көрстекен. Сондықтан конвективті жылуалмасу процесін сипаттайтын белгілі математикалық өрнектер құрамында тура физикалық мағынасы жоқ көп тұрақтыларға ие және күрделі, сондықтан олар практикалық қолданыстар үшін қолайсыз. Жұмыста конвективтік жылуалмасуды тәжірибелік зерттеулер нәтижелері фракталдар теориясы көмегімен сарапталып, жылуды турбуленттік тасымалдау қарқындылығын өзіндік қауымдасу дәрежесі критерийлерімен байланыстыратын сандық қатыстар алынған.

Турмухамбетов А.Ж., Айтманова К.А., Отегенова С.Б.

Фрактально- структурный анализ конвективного теплообмена в турбулентной среде.

Рассматриваются особенности конвективного теплообмена тел в турбулентной среде. Обсуждаются результаты экспериментальных исследований. Данные экспериментов показывают, что на теплоотдачу сферического тела

влияют естественная конвекция, теплофизические свойства среды, стесненность потока, турбулентный режим течения и т.д. В силу указанных факторов формула для расчета конвективного теплообмена, включает множество экспериментальных постоянных, становится громоздкой и неудобной для практического применения. В работе приведены результаты применения методов фрактально-структурного анализа для описания экспериментальных данных конвективного теплообмена плохообтекаемых (цилиндра и сферы) тел в канале. Получены количественные соотношения, связывающие интенсивность турбулентного переноса тепла с критериями степени самоорганизации.

Каян В.П., Лебедь А.Г.

Басқарылатын қалақшарға ие Дарье типті жел турбинасы.

Жел энергиясын пайдалану тиімділігін арттыру және тік қалақшаларға ие Дарье типті жел турбинасының динамикалық сипаттамаларын жақсарту мүмкіндігін зерттеу нәтижелері ұсынылған. Турбина білігіндегі айналу моментінің шамалары турбина қалақшаларының ағынға қатысты орнын басқару арқылы қалай оңтайландыруға болатындығы көрсетілген. Қалақшаларды басқару желідегі арнайы пішінді цилиндрлік жолмен қамтамасыз етіледі. Желідегі жолдың пішіні қалақшаның дөңгелектік жолының әрбір бөлігінде оңтайлы шабуыл бұрышын қамтамасыз етуге мүмкіндік берді. Бұл Ср энергиясын пайдалану коэффициентін 1,5 есе арттыруға және жел турбинасының өздік старт алу болатын жел жылдамдығының мәнін төмендетуге мүмкіндік берді.

Каян В.П., Лебедь А.Г.

Ветротурбина типа Дарье с управляемыми лопастями.

Представлены результаты исследования возможности увеличения эффективности использования энергии ветра и улучшения динамических характеристик ветротурбины типа Дарье с прямыми лопастями. Показано как могут быть оптимизированы величины крутящего момента на валу турбины путем управления положением лопастей турбины относительно набегающего потока. Управление лопастями обеспечивалось цилиндрической дорожкой специальной формы в плане. Форма дорожки в плане позволяла обеспечить на каждом участке круговой траектории лопасти оптимальный угол атаки. Это позволило увеличить коэффициент использования энергии Ср в 1.5 раза и уменьшить значение скорости ветра при которой происходит самостарт ветротурбины.

Ершина А.К., Сақыпова С.Е.

Жел турбинаның тиімділігін арттыру әдісі.

Мақалада жел турбиналарының энергетикалық тұрғыдан тиімділігін арттыру мүмкіндіктері қарастырылған. Баламалы энергетиканың, атап айтқанда Қазақстандағы жел энергетикасының қазіргі даму жағдайына қысқаша талдау берілген. Есептік зерттеулер көрсеткендей, Бидарье-2 қос роторлы жел электр қондырғысының қуатын арттыруға жұмысшы қалақшалары көтеру күшінің айналу моментін білікке жіберетін серперлерінің өзіндік оригинальді конструкциясын қолдану арқылы қол жеткізіледі. Жел ағынынан алынатын қуатты едәуір арттыра алатын Бидарье-2 жел турбинасы конструкциясының қысқаша сипаттамасы келтірілген. Концентраторды қолдана отырып, Бидарье-2 жел турбинасының тиімділігін, ПӘК одан әрі арттыру мүмкіндігі талқыланды. Жел турбинасының сапаттамаларын желдің жоғары жылдамдығында жақсарту үшін бағыттаушы концентратордың жылжымалы қақпақтарын қолданып, жел ағынының жылдамдығын реттеудің ерекше әдісі ұсынылған.

Ершина А.К., Сакипова С.Е.

Способ повышения эффективности ветротурбины.

В статье рассматриваются возможности повышения энергоэффективности ветротурбин. Дан краткий анализ текущего состояния развития альтернативной энергетики, в частности ветроэнергетики в Казахстане. Расчетным исследованием показано, что увеличение мощности двухроторной ветроэнергетической установки Бидарье-2 достигается за счет использования оригинальной конструкции размахов, передающих валу вращательный момент подъемной силы рабочих лопастей. Дано краткое описание конструкции ветроустановки Бидарье-2, которая позволяет значительно увеличить мощность, отбираемую от ветрового потока. Обсуждается возможность дальнейшего повышения КПД ВЭУ Бидарье-2 с помощью концентратора. Предложен уникальный метод регулирования скорости ветрового потока с помощью скользящих заслонок направляющего концентратора с целью улучшения характеристик ветротурбины при высокой скорости ветра.

Безродный М.К., Мисюра Т.О.

Артық ылғал бөлуімен өндірістік бөлмені желдету мен кондиционерлеудің жылу сорғыш жүйесі.

Мақалада жылдың жылы мезгілінде артық ішкі ылғалға ие өндіріс аймағы ішіндегі қолайлы жағдайларды сақтау үшін жылу сорғысы бар желдету және ауаны баптау жүйесінің пайдалану мүмкіндіктері мен энергия тиімділігі зерттелген. Осыған байланысты пайдаланылған ауаның ішінара қайта айналымы және таза сыртқы ауаның ауыспалы үлесімен жылу сорғыш жүйесіне термодинамикалық талдау жүргізілген. Кейін температура мен салыстырмалы ылғалдылықтың өзгеруінің және желдету, сонымен бірге кондиционерлеу объектісінің сипаттамаларының жүйесінің параметрлеріне әсерін бағалау үшін сандық талдау жүргізілген. Бұл берілген

жүйенің өндірістік аймақтағы қолайлы жағдайларды сақтау үшін потенциалды мүмкіндіктерін анықтауға мүмкіндік берді. Сондай-ақ, ауаны кондиционерлеу қажеттіліктері үшін бөлменің кіреберісіндегі ауаны қосымша салқындатуды қарапайым коэффициенттің көмегімен анықтауға болатындығы көрсетілді және мақалада оны есептеу әдісі келтірілген. Температура мен ылғалдылықты сақтаудың жылу сорғыш жүйесі қоршаған ортаның салыстырмалы төмен температуралы аймақтарда ең жоғары энергия тиімділігіне ие және көбінесе сыртқы ауаның салыстырмалы ылғалдылығынан тәуелді. Бұл зерттелген жүйе қоңыржай континенталдік климаты бар елдерде қолдануға жарамды дегенді білдіреді.

Безродный М.К., Мисюра Т.О.

Теплонасосная система вентиляции и кондиционирования производственного помещения с избыточным влаговыделением.

В статье исследуются возможности применения и энергоэффективность системы вентиляции и кондиционирования с тепловым насосом для поддержания комфортных условий внутри производственной зоны с избыточным внутренним влагообразованием в тёплое время года. В связи с этим был проведён термодинамический анализ теплонасосной системы с частичной рециркуляцией отработанного воздуха и переменной долей свежего наружного воздуха. Затем был проведён численный анализ для оценки влияния изменений температуры и относительной влажности окружающей среды и характеристик объекта вентиляции и кондиционирования на параметры системы. Это позволило определить потенциальные возможности данной системы поддерживать комфортные условия в производственной зоне. Также было показано, что необходимое дополнительное охлаждение приточного воздуха на входе в помещение для нужд кондиционирования воздуха можно определить с помощью простого коэффициента, и в статье приведена методика его расчета. Теплонасосная система поддержания температуры и влажности имеет наибольшую энергоэффективность в зоне относительно низких температур окружающей среды и во многом зависит от относительной влажности наружного воздуха. Это говорит о том, что исследуемая система подходит для применения в странах с умеренно-континентальным климатом.

Витюк В.А., Витюк Г.А., Скаков М.К., Жагипарова Л.К.

Импульстік графит реакторында сынақ объектілеріндегі берілген энергия шығарылуын іске асырудың есептік негіздемесі.

Мақалада модельдік твэлдерде және жылу шығарғыш жиынтықтарда энергия шығарылуын берілген аксиалдық және радиалдық таратуын қамтамасыз ету үшін импульстік графит реакторында сынақтарды дайындау тәжірибесінде қолданылатын техникалық шешімдері және тәсілдері ұсынылған. Бөлінетін заттарды жаңғырту үшін пайдаланылатын кемітілген ураны бар отынның қабатымен байытылған отынды екі аймаққа биіктіктік бөліну принципі қолданылған, гетерогендік жылу бөлетін құрастырма мысалында сынақ объектісінде берілген энергия шығарылуын көлемдік таралуын қамтамасыз ететін шешімдердің есептік негіздемесінің тәртібі қарастырылды. Белгіленген тәртіпті іске асыруы және сәйкес техникалық шешімдерді қабылдауы сәулелендіру құрылғысын жобалау сатысында модельдік жылу бөлетін құрастырма энергия шығарылуын аксиалды және радиалды таралуын берілген профильде қамтамасыз етуге мүмкіндік берді. Зерттеу нәтижелері бойынша 90,6 Вт/г (UO_2) және 74 Вт/г (UO_2) сәйкес деңгейде алынуы мүмкін эксперименттік жылу бөлетін құрастырманың үстіңгі және астыңғы бөлу аймақтарда біркелкі радиалды шығару мен белгіленген орта энергия шығаруды қамтамасыз етуге мүмкіндік берген шаралар кешені көрсетілді. Бұл шаралар жылу бөлетін құрастырма қатарлары бойынша отынды таблеткаларды байытуды қалпына келтіруді, аймақтардың шет жақтарында жұтқышы бар отындарды пайдалануды және реактор биіктігінде сәулелендіретін құрылғыны белгілі тұрғыландыруды енгізеді.

Витюк В.А., Витюк Г.А., Скаков М.К., Жагипарова Л.К.

Расчетное обоснование реализации заданного энерговыделения в объектах испытаний на импульсном графитовом реакторе.

В статье представлены подходы и технические решения, применяемые в практике подготовки испытаний в импульсном графитовом реакторе, для обеспечения заданного аксиального и радиального распределения энерговыделения в модельных твэлах и тепловыделяющих сборках. Рассмотрена процедура расчетного обоснования решений, обеспечивающих заданное объемное распределение энерговыделения в объекте испытаний на примере гетерогенной тепловыделяющей сборки, в которой применен принцип высотного разделения обогащенного топлива на две зоны слоем топлива с обедненным ураном, используемым для воспроизводства делящихся веществ. Реализация указанной процедуры и принятие соответствующих технических решений позволили обеспечить заданный профиль аксиального и радиального распределения энерговыделения в модельной тепловыделяющей сборке на стадии проектирования облучательного устройства. По результатам исследования продемонстрирован комплекс мер, позволивший обеспечить равномерное радиальное энерговыделение и заданное среднее энерговыделение в верхней и нижней зонах деления экспериментальной тепловыделяющей сборки может быть получено на уровне 90,6 Вт/г (UO_2) и 74 Вт/г (UO_2)

соответственно. Данные меры включают профилирование обогащения топливных таблеток по рядам тепловыделяющей сборки, использование на торцах зон таблеток с поглотителем и определенное позиционирование облучательного устройства по высоте реактора.

Хасенов А.К., Нусупбеков У.Б., Карабекова Д.Ж., Стоев М., Болатбекова М.М.

Сулы көмір отынына қажетті ұсақ дисперсиялы өнімді алудың электроимпульсті әдісі.

Өзекті мәселелердің бірі - қабатты немесе шаңды жағумен салыстырғанда бірқатар артықшылықтарға ие көмірді су көмірлі отын түрінде жағуды тиімді пайдалану. Көмір отыны бірқатар экономикалық, пайдалану және экологиялық артықшылықтарға ие. Мақалада электр импульсі әдісі көмір отынының ұсақ дисперсті өнімін алу көзі ретінде қарастырылған. Көмірді ұнтақтаудың ұсынылған әдісі сұйықтықтағы ұшқын электр разряды нәтижесінде пайда болатын импульстік соққы толқынының энергиясын пайдалануға негізделген. Көмір отыны құраушыларының қажетті гранулометриялық құрамын алу үшін электримпульсті разряд параметрлері орнатылған.

Хасенов А.К., Нусупбеков У.Б., Карабекова Д.Ж., Стоев М., Болатбекова М.М.

Электроимпульсный метод получения мелкодисперсионного продукта водоугольного топлива.

Одним из актуальных вопросов становится эффективное использования сжигания угля в виде водоугольного топлива, которая имеет ряд преимуществ по сравнению слоевым или пылевидным сжиганием. Водоугольное топливо имеет ряд экономических, эксплуатационных и экологических преимуществ. В статье рассматривается электроимпульсный метод как источник получения мелкодисперсионного продукта водоугольного топлива. Предлагаемый способ измельчения угля основан на использовании энергии импульсной ударной волны, возникающей в результате искрового электрического разряда в жидкости. Установлены параметры электроимпульсного разряда для получения требуемого гранулометрического состава компонентов водоугольного топлива.

Нижегородов А.И., Гаврилин А.Н., Мойзес Б. Б., Кувшинов К.А.

Ковдор кен орнының ірі өлшемді вермикулит слюдаларын қайта өңдеуге арналған технология және құрал-жабдық.

Ковдор кен орнының тау-кен қалдықтарынан алынған ірі көлемді вермикулит слюдаларын қайта өңдеуге арналған технологиялар мен құрал-жабдықтарды әзірлеу - өңдеу өнеркәсібіне ірі көлемді вермикулитті қайтаруға мүмкіндік береді. Берілген мақалада 20 мм және одан да көп өлшемдерге ие ірі көлемді слюданы қайта өңдеу технологиясын дамыту аспектілері қарастырылған. Зерттеудің мақсаты – габаритті бөлшектерді ұнтақтау арқылы ірі өлшемді вермикулит шикізатын ұнтақтау технологиясын зерттеу, технологиялық құрал-жабдықты әзірлеу және оны пайдалану процестерін зерттеу болып табылады. Зерттеу нысаны – ірі өлшемді вермикулит шикізатын ұсақтауға арналған кесу қондырғысының жұмыс процесі және оның конструкциясы. Зерттеу әдістері кесілген ірі өлшемді бөлшектердің қозғалысын аналитикалық модельдеуге және осы негізде кесу қондырғысының жұмыс процесінің негізгі сипаттамаларын анықтауға негізделген. Кесу қондырғыларында ірі бөлшектерді майдаламай күйдіруі - электр пештерінің өнімділігін төмендетуге әкелетін күйдіру уақытын едәуір арттыруын қажет ететіні анықталған Кесу агрегатының қабылдау барабандарының тіліктеріне бөлшектердің түсу уақыты анықталды, соның негізінде қабылдау барабандарының айналу жылдамдығы мен оның пайдалану өнімділігі есептелген.

Нижегородов А.И., Гаврилин А.Н., Мойзес Б.Б., Кувшинов К.А.

Технология и оборудование для переработки крупноразмерных вермикулитовых слюд ковдорского месторождения.

Разработка технологии и оборудования для переработки крупноразмерных вермикулитовых слюд, полученных из отходов горных работ Ковдорского месторождения, позволяет возвращать крупноразмерный вермикулит в перерабатывающую промышленность. В данной статье рассматриваются аспекты разработки технологии переработки крупногабаритной слюды с размерами 20 мм и более. Целью исследования является изучение технологии измельчения крупноразмерного вермикулитового сырья путем измельчения габаритных частиц, разработка технологического оборудования и изучение процессов его эксплуатации. Объектом исследования является рабочий процесс рубительного агрегата для измельчения крупноразмерного вермикулитового сырья и его конструкция. Методы исследования базируются на аналитическом моделировании движения разрубаемых крупноразмерных частиц и определении на этой основе основных характеристик рабочего процесса рубительного агрегата. Установлено, что обжиг крупных частиц без измельчения в рубительных агрегатах требует существенного увеличения времени обжига, что снижает производительность электропечей. Определено время попадания частиц в прорези приемных барабанов рубительного агрегата, исходя из которого рассчитана скорость вращения приемных барабанов и его эксплуатационная производительность.

Хайралиев С.И., Кайшубаева Н., Спитас К., Джундибаев В.Е.

Қалыпты күштің әсерінен тегіс емес беттердің статикалық өзара әрекеті.

Машина жасаудың қазіргі заманғы конструкциялары (және басқалары) үйкеліс бар түйіндердің математикалық модельдерін жасауға көбірек талап қояды. Фрикциялық байланыстың қасиеттерін зерттеуді едәуір қиындататын шарт оның екі байланысатын дененің әр түрлі геометриялық параметрлерімен дискреттілігі болып табылады, соның нәтижесінде түйісу тек үйкелетін денелердің (негізі және сырғануы) бір бөлігінің арасында ғана пайда болады. Жанасатын беттердің геометриясы кездейсоқ функциялармен анағұрлым дәл сипатталады, алайда кездейсоқ функциялар негізінде үйкеліс түйіндерін есептеу әдістері өте күрделі. Бұл жұмыс тегіс емес параметрлері бар кедір-бұдырлы дененің түйіспелі өзара әрекеттесу моделін құрудың бастапқы кезеңі болып табылады, бірақ әр дене үшін тұрақты. Бұдан басқа, байланыс жазықтығында сыртқы көлденең күш болмаған жағдайда байланысатын денелерді қысатын айнымалы күшпен байланыс моделі қарастырылады және бұл жұмыс осы беттердің өзара әрекетінің салыстырмалы қарапайым сұлбасымен үйкеліс беттерінің өзара әрекеттесу моделінің құрылу дәлдігін тексеруге мүмкіндік береді.

Хайралиев С.И., Кайшубаева Н., Спитас К., Джундибаев В.Е.

Статическое взаимодействие шероховатых поверхностей при действии нормальной силы.

Современные конструкции машиностроения (и некоторые другие) предъявляют все больше и больше требований к разработке математических моделей узлов, в которых присутствует трение. Условием, существенно усложняющим исследование свойств фрикционного контакта, является его дискретность с разными геометрическими параметрами двух контактирующих тел, в результате чего контакт образуется только между частью шероховатости трущихся тел (основание и скольжение). Геометрия контактирующих поверхностей наиболее точно описывается случайными функциями, однако методы расчета узлов трения на основе случайных функций очень сложны. Данная работа является начальным этапом построения модели контактного взаимодействия двух шероховатых тел с параметрами шероховатости, которые различны для двух тел, но постоянны для каждого отдельного тела. Кроме того, рассматривается модель контактного взаимодействия с переменной силой, сжимающей контактирующие тела, при отсутствии внешней поперечной силы в плоскости контакта, и данная работа позволяет проверить точность построения модели взаимодействия поверхностей трения с относительно простой схемой взаимодействия этих поверхностей.

Рахадилов Б.К., Скаков М.К., Миниязов А.Ж., Журерова Л.Г., Нугуманова А.Б., Хасенов А.К., Карабекова Д.Ж.

Жоғары температуралы плазмалық сәулелендіру кезінде вольфрам үлгілерінде дейтерийді қармап алуы.

Бұл жұмыс дейтерийдің жинақталып шоғырлануын, сондай-ақ плазмалық шоғырмен сәулелендіру кезінде вольфрам үлгілерінде дейтерийді қармап алу үдерісін зерттеуге арналған. Сәулелендіргеннен соң үлгінің бетіндегі өзгерістер, бірқалыпсыз бедерлеу үдерісінің нәтижесінде пайда болған беткі бедерлер түрінде бақыланды. Сәулелендірілетін үлгілердің беткі қабатының құрылымы мен бедерінің өзгеру дәрежесі сәулелендіру температурасына тәуелді. Плазмамен сәулелендірген кезде вольфрамда дейтерийдің жинақталып шоғырлануы эмиссиялық және термодесорбциялық спектрометрия әдістерімен зерттелінген. Алынған нәтижелерге сәйкес қармап алынған дейтерийдің көп мөлшері 7 мкм тереңдікте жинақталып шоғырланатындығы анықталды.

Рахадилов Б.К., Скаков М.К., Миниязов А.Ж., Журерова Л.Г., Нугуманова А.Б., Хасенов А.К., Карабекова Д.Ж.

Захват дейтерия в образцах вольфрама при высоко-температурном плазменном облучении.

Работа посвящена изучению накопления дейтерия, а также исследованию процесса захвата дейтерия в образцах вольфрама при облучении плазменным пучком. Показано, что после облучения на поверхности наблюдается изменение поверхности как развитии рельефа в результате неоднородного травления поверхности. При этом степень изменения рельефа и структуры поверхностного слоя облученных образцов зависит от температуры облучения. Были изучены накопление дейтерия вольфраме при облучении дейтериевой плазмой. Проведенный термодесорбционный анализ образцов вольфрама, облученных дейтериевой плазмой, показал что, поверхность вольфрама насыщается дейтерием. Данные полученные, методом эмиссинной спектрометрии и термодесорбционной спектрометрии показал, что основная доля захваченного дейтерия аккумулируется на глубине до 7 мкм.

Матвеев И. Г., Карпов К. А., Юрченко А. В., Сименс Э.

Геометриялық белгілерге негізделген анықтау әдісін қолдануымен көше ортасындағы нысандарды бақылау алгоритмі.

Мақалада геометриялық белгілерге негізделген анықтау алгоритмін қолдануымен көше ортасындағы нысандарды бақылау әдісі ұсынылған. Нысандарды бақылауға арналған функционалдылықтан басқа, ұсынылған алгоритм геометриялық белгілерге негізделген анықтау алгоритмінің дәлдігін арттырады. Объектілерді қадағалау үшін ұсынылған тәсіл ұялы топология желісі болып табылатын бірнеше бейнебақылау камераларынан алынған анықтау ақпаратын пайдаланады. Нақты жағдайларда жүргізілген эксперименттер 10-

40% жоғары анықтау дәлдігін көрсетті, бұл ұсынылған тұжырымдаманы растады. Бақылау алгоритмі кішігірім есептеу ресурстарын қажет етеді, бұл оны әсіресе интернет-заттардың өнімділігі төмен инфрақұрылымына қолдануға мүмкіндік береді.

Матвеев И. Г., Карпов К. А., Юрченко А. В., Сименс Э.

Алгоритм отслеживания объектов в уличной среде с применением метода обнаружения на основе геометрических признаков.

В статье предложен подход для отслеживания объектов в уличной среде с использованием алгоритма обнаружения на основе геометрических признаков. Кроме функциональности для отслеживания объектов, предложенный алгоритм повышает точность обнаружения алгоритма обнаружения на основе геометрических признаков. Предложенный подход для отслеживания объектов использует информацию обнаружения полученную с нескольких камер видеонаблюдения, представляющих собой сеть ячеистой топологии. Проведенные эксперименты, проведенные в реальных условиях, показали на 10-40 % более высокую точность обнаружения, что подтвердило предложенную концепцию. Алгоритм отслеживания требует незначительных вычислительных ресурсов, что делает его особенно применимым для низкопроизводительной инфраструктуры Интернета вещей.

Бақтыбеков К. С., Курманбай А., Саханов К., Сыздыков А., Мухамедиев А.

Жеке жылжытылған бөлшектермен және ішінара көлеңкелеу жағдайында максималды қуатпен сенімді бақылау нүктесімен бөлшектердің үйіндісін оңтайландыру.

Қуатты басқарудың тиімді әдістері фотоэлектрлік жүйелерді жобалаудың ажырамас бөлігі болып табылады. Қуаттылықты басқару құралдарының бірі - тұрақты ток түрлендіргішінің жұмыс циклін тұрақты токқа әр түрлі алгоритмдерді қолдана отырып, тек қуат максималды болатын нүктелерде жұмыс істеу. Қуат шығынын азайту үшін, әсіресе динамикалық өзгеретін жарықпен, іздеу мүмкіндігінше тез жүргізілуі керек. Есептің күрделілігі ішінара көлеңкелеу жағдайында фотоэлектрлік жүйенің сызықтық емес тәртіпте тұрады. Фотоэлектрлік панельдердің мөлшері мен құрылымына байланысты бөлшектердің үйіндісі әдісі көптеген жергілікті максимумдары бар P-V қисықтарының үлкен санын жасайды, бұл оңтайлы жұмыс нүктесін анықтайтын ақылды алгоритмді қажет етеді. Бірнеше шыңдарды өңдей алмайтын қолданыстағы ең жоғары қуат нүктесін бақылау алгоритмдері және осы мақалада біз белгілі бір тапсырма үшін бөлшектердің үйіндісін оңтайландыруға бейімделуді ұсынамыз.

Бактыбеков К. С., Курманбай А., Саханов К., Сыздыков А., Мухамедиев А.

Оптимизация роя частиц с помощью индивидуально смещенных частиц и надежного отслеживания точки с максимальной мощностью в условиях частичного затенения.

Эффективные методы управления мощностью являются неотъемлемой частью проектирования фотоэлектрических систем. Одним из средств управления подачей мощности является регулирование рабочего цикла преобразователя постоянного тока в постоянный с помощью различных алгоритмов для работы только в точках, где мощность является максимальной. Поиск должен выполняться как можно быстрее, чтобы минимизировать потери мощности, особенно при динамически изменяющей освещенности. Сложность поставленной задачи заключается в нелинейном поведении фотоэлектрической системы в условиях частичного затенения. В зависимости от размера и структуры фотоэлектрических панелей метод роя частиц создает огромное количество возможных кривых P-V с многочисленными локальными максимумами, что требует интеллектуального алгоритма определения оптимальной рабочей точки. Существующие эталонные алгоритмы отслеживания максимальной точки мощности, которые не могут обрабатывать несколько пиков, и в этой статье мы предлагаем адаптацию оптимизации роя частиц для конкретной задачи.

Суржиков А.П., Лысенко Е. Н., Малышев А. В., Қасымов С. С.

Радиациялық және радиациялы-термиялық жағдайларда күйдіру кезінде ферриттердің магниттік қасиеттері мен микроқұрылымдарының өзарабайланысы.

Зерттеулер литий алмастырылған феррит үлгілерінде жүргізілген. Радиациялы-термиялық күйдіру дайындамаларды (1.5-2.0) МэВ энергиялы электрондардың импульсті шоғымен, (0.5-0.9) А импульстегі шоғыр тогы, сәулелену импульсінің ұзақтығы – 500 мкс, импульстердің жүру жиілігі – (5-50) Гц, дайындамаларды қыздыру жылдамдығы – 1000 °С/мин сәулелендіру арқылы жүзеге асырылды. Термопештерде қақтау (Т-қақтау) алдын ала қыздырылған камералық электр пешінде жүргізілді. Жұмыста магниттік индукцияның феррит дәнінен тәуелсіздігі көрсетілген. Бұл жағдайда коэрцитивті күш дән мөлшеріне кері пропорционал және феррит үлгілерінің ішкі кеуектілігінен тәуелді. Термиялық қақтаумен салыстырғанда радиациялы-термиялық қақтау өсіп келе жатқан дәндермен дәндер арасындағы қуыстардың қармауына әкелмейді және дән ішілік кеуектердің коагуляциялауға ықпал етеді.

Суржиков А.П., Лысенко Е. Н., Малышев А. В., Касымов С. С.

Взаимосвязь магнитных свойств и микроструктуры ферритов при спекании в радиационных и радиационно-термических условиях.

Исследования проводились на образцах литий замещенного феррита. Радиационно-термическое спекание осуществлялось облучением заготовок импульсным пучком электронов с энергией (1.5-2.0) МэВ, токе пучка в импульсе (0.5-0.9) А, длительности импульса облучения – 500 мкс, частоте следования импульсов – (5-50) Гц, скорости разогрева заготовок – 1000 °С/мин. Спекание в термопечах (Т-спекание) производилось в предварительно разогретой камерной электрической печи. В работе показана независимость магнитной индукции от зернистости феррита. При этом коэрцитивная сила обратно пропорциональна размеру зерна и зависит от внутризеренной пористости ферритовых образцов. Радиационно-термическое спекание, в отличие от термического спекания, не приводит к захвату межзеренных пустот растущими зернами и способствует коагуляции внутризеренных пор.

Архипов В.В., Арынгазин А.К., Кудусов А.С.

Электродинамиканың және салыстырмалылықтың жалпы теориясының когомологиялық модельдерінің құрылымы туралы.

Ұсынылған жұмыста Риман алуан түрлілігіндегі күрделі скаляр өріс қарастырылып, өріс теориясының лагранжиандарын құрудың когомологиялық әдісі және дифференциалды геометрияның сәйкесті аспектілері зерттелген. Толық лагранжиан моделі Риман алуан түрлілігінде 4-форма түрінде ұсынылады. Әдіс-тәсілді жүзеге асыру үшін дифференциалдық (p, q)-формалар мен Ходждың жұлдызды операторларының ішкі скалярлы көбейтіндісі қолданылған. Модель әрекетінің құраушылары, оның ішінде гравитациялық құраушысы, материя өрістерінің квадраттық формалары және негізгі тетрадты өрістері ретінде ұсынылуы мүмкіндігі көрсетілген. Зерттеу Леви-Чивита метрика жағдайымен шектелді. Модельдің ерекшелігі жалпыланған сыртқы дифференциалдың нильпотенттілік қасиетінің жоғалуымен байланысты. Модель аясында Клейн-Гордон, Максвелл және жалпы салыстырмалылық әрекеттері жаңғыртылған.

Архипов В.В., Арынгазин А.К., Кудусов А.С.

О структуре когомологических моделей электродинамики и общей теории относительности.

В представленной работе рассматривается комплексное скалярное поле на римановом многообразии, изучается когомологический способ построения лагранжианов теории поля и соответствующие аспекты дифференциальной геометрии. Полный лагранжиан модели предлагается в виде 4-формы на римановом многообразии. Для реализации подхода используется внутреннее скалярное произведение дифференциальных (p, q)-форм и звездных операторов Ходжа. Показано, что составляющие действия модели, в том числе гравитационная, могут быть представлены как квадратичные формы полей материи и основных тетрадных полей. Исследование ограничивается случаем метрики Леви-Чивиты. Особенность модели связана с исчезновением свойства нильпотентности обобщенного внешнего дифференциала. В рамках модели воспроизведены действия Клейна-Гордона, Максвелла и общей теории относительности.

INFORMATION ABOUT AUTHORS | **АВТОРЛАР ТУРАЛЫ МӘЛІМЕТТЕР** | **СВЕДЕНИЯ ОБ АВТОРАХ**

Aimukhanov, A.K. – PhD, Professor, Physical-Technical Faculty, E.A. Buketov Karaganda University, Karaganda, Kazakhstan

Aitmanova, K.A. — Postgraduate student, al-Farabi Kazakh National University, Almaty, Kazakhstan

Aringazin, A.K. - Doctor of phys.-math.sciences, Professor, L.N. Gumilyov Eurasian National University, Nur-Sultan, Kazakhstan, aringazin@gmail.com

Arkhipov, V.V. - Candidate of phys.-math.sciences, Associate Professor, Moscow Institute of Physics and Technology, Moscow, Russia, arkhipov.vv@mipt.ru

Baktybekov, K.S. - Doctor of phys.-math. sciences, Professor, JSC National Company «Kazakhstan Gharysh Sapary», Nur-Sultan, Kazakhstan, professor MEPHI, Moscow, Russia

Bezrodny, M.K. - Doctor of tech. sciences, Professor, Heat-and-Power Engineering Faculty, National Technical University of Ukraine "Igor Sikorsky Kyiv Polytechnic Institute", Kyiv, Ukraine

Bolatbekova, M.M. - master student, Physical-Technical Faculty, E.A. Buketov Karaganda University, Karaganda, Kazakhstan

Chicherina, N.V., PhD., Professor Assistant, National Research Tomsk Polytechnic University, School of Non-Destructive Testing, Tomsk, Russia, chicherina@tpu.ru

Dosmagambetova, S.S. - Doctor of chem. science, Chemistry department, L.N. Gumilyov Eurasian National University, Nur-Sultan, Kazakhstan

Dzhundibayev, V.E. - Doctor of techn.sciences, Professor, L.N. Gumilyov Eurasian National University, Nur-Sultan, Kazakhstan

Gavrilin, A.N. - Candidate of techn.sciences, Associate Professor, National Research Tomsk Polytechnic University, Tomsk, Russia

Guchenko, S.A. - PhD student, Researcher, E.A. Buketov Karaganda University, Karaganda, Kazakhstan

Halamani, Koushallya M. - M.Sc (Physics), Department of Physics, P.C. Jabin Science College, Karnataka, India

Hiremath, Chidanandayya S. - PhD, Professor and Head, Department of Physics, Shri Kadasiddheshwar Arts College & H.S.Kotambri Science Institute, Vidyanagar, Hubballi, India

Ikramova, S.B. – PhD student, Senior Lecturer, al-Farabi Kazakh National University, Almaty, Kazakhstan

Jeergal, Pundalik. R, - PhD, Professor, Head, Department of Physics, P.C. Jabin Science College, Karnataka, India

Kadyrzhanov, K.K. – Doctor of phys.-math.sciences, Professor, L.N. Gumilyov Eurasian National University, Nur-Sultan, Kazakhstan

Kaishubayeva, N. - Master, Engineer, First Wind Power Station, Nur-Sultan, Kazakhstan

Kaliyekperov, M.E. – PhD student, L.N. Gumilyov Eurasian National University, Nur-Sultan, Kazakhstan

Kaniukov, E.Yu. – PhD, Scientific-Practical Materials Research Centre of National Academy of Sciences of Belarus, Minsk, Belarus

Karabekova, D.Zh. - PhD, Associate Professor, Physical-Technical Faculty, E.A. Buketov Karaganda University, Karaganda, Kazakhstan

Karpov, K. A. – M.Sc (Eng.), Research Engineer, Anhalt University of Applied Sciences, Koethen, Germany

Kassymov, S.S. - Candidate of phys.-math.sciences, Associate Professor, Head of Innovation techniques center, E.A.Buketov Karaganda State University, Karaganda, Kazakhstan

Kayan, V.P. – Candidate of tech. sciences, Senior Researcher, Institute of Telecommunications and Global Information Space, National Academy of Sciences of Ukraine, Kyiv, Ukraine

Khairaliyev, S.I. - Candidate of techn.sciences, Technical director, INTEKKO Ltd., Nur-Sultan, Kazakhstan

Khassenov, A. – PhD, Associate Professor, Physical-Technical Faculty, E.A. Buketov Karaganda University, Karaganda, Kazakhstan

Kudussov, A.S. - Candidate of phys.-math.sciences, Associate Professor, E.A. Buketov Karaganda University, Karaganda, Kazakhstan, akudusov@mail.ru

Kulkarni, Akshay B. - PhD, Assistant Professor, Department of Physics, South Konkan Education Society's(SKES's) Govindram Seksaria Science College, Belagavi, India

Kurmanbay, A. – Engineer, JSC National Company «Kazakhstan Gharysh Sapary», Nur-Sultan, Kazakhstan, a.kurmanbay.sh@gmail.com

Kusenova, A.S. - Candidate of chem.sciences, Senior Lecturer, Department of Physics, Karaganda Technical University, Karaganda, Kazakhstan

Kuvshinov, K.A. – Master of engineering and technology**,** Senior Lecturer, National Research Tomsk Polytechnic University, Tomsk, Russia

Lebid, O.G. - Candidate of tech. sciences, Senior Researcher, Deputy Director, Institute of Telecommunications and Global Information Space of the National Academy of Sciences of Ukraine, Kyiv, Ukraine

Lysenko, E.N. - Doctor of techn.sciences, Head of the Research Laboratory for Electronics, Dielectrics and Semiconductors, National Research Tomsk Polytechnic University, Tomsk, Russia

Malyshev, A.V. – Candidate of phys.-math.sciences**,** Senior Researcher, National Research Tomsk Polytechnic University, Tomsk, Russia

Mathad, Shalini K. - M.Sc (Physics), Department of Physics, South Konkan Education Society's(SKES's) Govindram Seksaria Science College, Belagavi, India

Mathad, Shridhar.N. - PhD, Assistant Professor, Department of Engineering Physics, Karnataka Lingayat Education (K.L.E) Institute of Technology, Gokul, Hubballi, Karnataka, India

Matveev, I. G. – M.Sc (Eng.), Research Engineer, Anhalt University of Applied Sciences, Koethen, Germany

Miniazov, A.Zh. - Head of the Laboratory for Testing Materials under Conditions of a Fusion Reactor, National Nuclear Center of the Republic of Kazakhstan, Kurchatov, Kazakhstan.

Misiura, T.O. - Master, National Technical University of Ukraine "Igor Sikorsky Kyiv Polytechnic Institute", Kyiv, Ukraine

Moyzes, B.B. - Candidate of techn.sciences, Associate Professor, National Research Tomsk Polytechnic University, Tomsk, Russia, mbb@tpu.ru

Mukhamediyev, A. - Engineer, JSC National Company «Kazakhstan Gharysh Sapary», Nur-Sultan, Kazakhstan, a.mukhamediyev@gharysh.kz

Nizhegorodov, A.I. – Doctor of techn.sciences, Professor, Irkutsk National Research Technical University, Irkutsk, Russia, nastromo_irkutsk@mail.ru

Nugumanova, A.B. - PhD (Inf.Syst.), Head of the Laboratory of Digital Technologies and Modeling, S.Amanzholov East Kazakhstan State University, Ust-Kamenogorsk, Kazakhstan

Nussupbekov, U.B. - PhD student, Physical-Technical Faculty, E.A. Buketov Karaganda University, Karaganda, Kazakhstan

Omarbekova, G.I. - PhD student, Physical-Technical Faculty, E.A. Buketov Karaganda University, Karaganda, Kazakhstan

Otegenova, S.B. - Postgraduate student, al-Farabi Kazakh National University, Almaty, Kazakhstan

Petrova, A. – Master, Junior Researcher, National Research Tomsk Polytechnic University, Tomsk, Russia.

Plotnikova, I.V. - Candidate of techn.sciences, Associate Professor, School of Non-Destructive Testing, National Research Tomsk Polytechnic University, Tomsk, Russia

Pujar, Appanna S. - M.Sc (Physics), Associate Professor, Department of Physics, Raja Lakhamagouda Science Institute, Belgavi, India

Pujar, Rangappa B. - PhD, Professor, Department of Physics, P.C. Jabin Science College, Karnataka, India

Rakhadilov, B.K. - PhD (Techn.phys.), Head of the National scientific laboratory, S. Amanzholov East Kazakhstan State University, National Nuclear Center of the Republic of Kazakhstan, Ust-Kamenogorsk, Kazakhstan

Rogachev, A.A. - Doctor of tech. sciences, Professor, Director Institute of Chemistry of New Materials of the National Academy of Sciences of Belarus, rogachev78@mail.ru

Rogachev, A.V., Doctor of chem.sciences, Professor, Corresponding Member of the National Academy of Sciences of Belarus, Head of International Chinese-Belarusian scientific Laboratory on Vacuum-Plasma Technology, FranciskSkorina Gomel State University, Gomel, Belarus, rogachevav@mail.ru

Rudenkov, A.S., PhD (Eng.), Associate Professor, Francisk Skorina Gomel State University, Gomel, Belarus, arudenkov05@gmail.com

Sakhanov, K. - Candidate of tech. sciences, JSC National Company «Kazakhstan Gharysh Sapary», Nur-Sultan, Kazakhstan, k.sakhanov@gharysh.kz

Sakipova, S.E. – Candidate of phys.-math.sciences, Professor, E.A. Buketov Karaganda University, Karaganda, Kazakhstan

Salkeeva, A.K. - Candidate of phys.-math.sciences, Associate Professor, Department of Physics, Karaganda Technical University, Karaganda, Kazakhstan

Shlimas, D.I. – PhD, Researcher, L.N. Gumilyov Eurasian National University, Nur-Sultan, Kazakhstan

Siemens, E. – Doctor of Engineering, Professor, Anhalt University of Applied Sciences, Koethen, Germany

Skakov, M.K. - Doctor of phys.-math. sciences, Professor, Chief Researcher, National Nuclear Center of the Republic of Kazakhstan, Kurchatov, Kazakhstan

Spitas, Ch. - PhD, Associate Professor, School of Engineering, Nazarbayev University, Nur-Sultan, Kazakhstan

Starý, O. - PhD, Associate Professor, Vice rector, Czech Technical University in Prague, Prague, Czech Republic

Stoev, M. - Doctor of tech. sciences, Professor, South-West University «NeofitRilski», Blagoevgrad, Bulgaria

Surzhikov, A.P. - Doctor of phys.-math.sciences, Professor, Head of Control and Diagnostics Department, National Research Tomsk Polytechnic University, Tomsk, Russia, surzhikov@tpu.ru

Syzdykov, A. - Engineer, JSC National Company «Kazakhstan Gharysh Sapary», Nur-Sultan, Kazakhstan, a.syzdykov@gharysh.kz

Tileu, A.O. – M.Sc (Eng.), Assistant Professor, al-Farabi Kazakh National University, Almaty, Kazakhstan

Turlykozhayeva, D.A. – PhD student, Lecturer, al-Farabi Kazakh National University, Almaty, Kazakhstan

Turmukhambetov, A. Zh. - Doctor of phys.-math. sciences, Professor, al-Farabi Kazakh National University, Almaty, Kazakhstan

Vityuk, G.A. - PhD student, D. Serikbayev East Kazakhstan technical university; Head of the group laboratory, National Nuclear Center of the Republic of Kazakhstan, Kurchatov, Kazakhstan

Vityuk, V.A. - Candidate of phys.-math. sciences, Deputy Director General for Science, National Nuclear Center of the Republic of Kazakhstan, Kurchatov, Kazakhstan

Wang Jicheng, PhD, Professor, Jiangnan University, Wuxi, China, jiangxh24@mail.njust.edu.cn

Yarmolenko, M.A., Doctor of tech. sciences, Professor, Francisk Skorina Gomel State University, Gomel, Belarus, simmak79@mail.ru

Yershina A.K. - Doctor of phys.-math. sciences, Professor, Kazakh National Women's Teacher Training University, Almaty, Kazakhstan

Yeszhanov, A.B. - PhD student, L.N. Gumilyov Eurasian National University; Scientist, Technological laboratory of track-etched membranes, Astana branch of Institute of Nuclear Physics, Nur-Sultan, Kazakhstan

Yurchenko, A.V. – Doctor of techn. sciences, Professor, National Research Tomsk Polytechnic University, Tomsk, Russia

Yurov, V.M. - Candidate of phys.-math.sciences, Professor, Director of the Scientific Research Center, E.A. Buketov Karaganda University, Karaganda, Kazakhstan

Zeinidenov, A.K. – PhD, Associate Professor, Dean of the Physical-Technical Faculty, E.A. Buketov Karaganda University, Karaganda, Kazakhstan

Zhagiparova, L.K. - Engineer of the 1st category, Laboratory for testing reactor fuel, National Nuclear Center of the Republic of Kazakhstan, Kurchatov, Kazakhstan

Zhanabaev, Z.Zh. – Doctor of phys.-math. sciences, Professor, Chief Researcher, al-Farabi Kazakh National University, Almaty, Kazakhstan

Zhurerova, L.G. – PhD (Techn.phys.), Senior Researcher, National scientific laboratory, S.Amanzholov East Kazakhstan State University, Ust-Kamenogorsk, Kazakhstan

About «Eurasian Physical Technical Journal»

ISSN 1811-1165 Key title: Eurasian physical technical journal (Print)
Abbreviated key title: Eurasian phys. tech. j.

ISSN 2413-2179 Key title: Eurasian physical technical journal (Online)
Abbreviated key title: Eurasian phys. tech. j.

Eurasian Physical Technical Journal (Eurasian phys. tech. j.) is a peer-reviewed open access international scientific journal publishing original research results on actual problems of Technical Physics and other related fields.

Since 2004 «Eurasian phys. tech. j.» is published in English. E.A. Buketov Karaganda University is the main organizer and financial sponsor of Eurasian phys. tech. j. The international editorial board consists of leading physicists from 8 countries.

Since 2008 «Eurasian phys. tech.j.» is included in the list of publications recommended by the Ministry of Science Education and Science of the Republic of Kazakhstan for publication of the master's and PhD doctoral dissertations main results on Physical and Mathematical sciences.

Since May 2019 «Eurasian phys. tech.j.» has been indexed in the Scopus database on four scientific areas: Energy, Engineering, Materials Science, Physics and Astronomy. As of December 7, 2020 (data is updated monthly) Journal's CiteScoreTracker is 0.4 with a maximum percentile of 16% in Energy, https://www2.scopus.com/sourceid /21100920795#tabs=0

Re-registration Certificate No.KZ50VPY00027647 of the «Eurasian phys. tech. j.» issued October 6, 2020 by Information Committee of the Ministry of Information and Public Development of the Republic of Kazakhstan.According this since 2021 Eurasian phys. tech. j. will be published quarterly.

Publication Ethics and Malpractice Statement

Submission of an article to the Eurasian phys. tech. j. implies that the paper described has not been published previously, that it is not under consideration for publication elsewhere, that its publication is approved by all authors and tacitly or explicitly by the responsible authorities where the paper was carried out, and that, if accepted, it will not be published elsewhere in the same form, in English or in any other language, including electronically without the written consent of the copyright holder. In particular, translations into English of papers already published in another language are not accepted.

For information on Ethics in publishing and Ethical guidelines for journal publication see http://www.elsevier.com/publishingethics and http://www.elsevier.com/journal-authors/ethics.

The Eurasian phys. tech. j. follows the Code of Conduct of the Committee on Publication Ethics (COPE), and follows the COPE Flowcharts for Resolving Cases of Suspected Misconduct (http://publicationethics.org/files/u2/New_Code.pdf).

To verify originality, your article may be checked by the originality detection service Cross Check http://www.elsevier.com/editors/plagdetect.

Authors are responsible for the content of their publications. No other forms of scientific misconduct are allowed, such as plagiarism, falsification, fraudu-lent data, incorrect interpretation of other works, incorrect citations, etc. Authors are obliged to participate in peer review process and be ready to provide corrections, clarifications, retractions and apologies when needed. All authors of a paper should have significantly contributed to the research.

Reviewers should provide objective judgments and should point out relevant published works which are not yet cited. Reviewed articles should be treated confidentially. The reviewers will be chosen in such a way that there is no conflict of interests with respect to the research, the authors and/or the research funders.

Editors have complete responsibility and authority to reject or accept a paper, and they will only accept a paper when reasonably certain. They will preserve anonymity of reviewers and promote publication of corrections, clarifications, retractions and apologies when needed.

The acceptance of a paper automatically implies the copyright transfer to the Eurasian phys. tech. j.

All submitted papers will the sent for reviewing to leading experts in the given area.

The Editorial Board of the Eurasian phys. tech. j. will monitor and safeguard publishing ethics. The editors reserve the right to accept or reject manuscripts.

GUIDELINES FOR AUTHORS

Research articles, survey papers and short notes are accepted for exclusive publication in the **Eurasian phys. tech. j.** in English. The manuscripts and short notes must contain original results of investigation in the following scientific areas of Physics:

ENERGY.

ENGINEERING.

MATERIALS SCIENCE.

PHYSICS AND ASTRONOMY

All publishing manuscripts and short notes must have been recommended by a member of the editor board or by the organization (University), where the work was performed. The author who submitted an article for publication will be considered as a corresponding author.

The paper, short note or review paper shall include an abstract of the contents, not exceeding 200 words and keywords (no more than 10). The abstract must not coincide with the introduction or conclusive part of the work and must not contain references, abbreviations and other unknown words.

All articles should have list of keywords or terms (3 to 10) for indexing purposes.

The text of a paper must not exceed 6-10 pages including tables, figures (no more than 6) and references (no more than 30). A short note must not exceed 4-5 pages including no more than 2 figures. A review paper must not be more than 15-20 pages (including no more than 10 figures).

The text should be divided on structural parts: **Introduction, Theoretical part, Experimental technique, Results and Discussion, Conclusion,** etc.

Printed copies shall be on good quality paper of International size A4. All texts must be printed in Microsoft Word. It is preferable to use the Times fonts. The text must be printed in 11 point letters, with 1 interval. There shall be a margin of 30 mm at the left-hand edge, of 15 mm at the fore edge, of 30 mm at the head of the page and of 30 mm at the tail.

Acknowledgments may be shown at the end of the article text, before **REFERENCES**.

All references must be numbered in the text (for example, [1], [2-4]) and listed in numerical order.

Equations in your paper have to be written using the **Microsoft Equation Editor or the MathType** (http://www.mathtype.com) for (Insert | Object | Create New | Microsoft Equation or MathType Equation).

Tables must be inserted into the text.

Figures should be prepared in a digital form suitable for direct reproduction. Figures shall be submitted on the separate sheets and not included into the text.

The following files must be submitted via e-mail:

- Article text (*.doc);
- Figures (fig1.jpg, fig2.pcx);
- Figure captions (*.txt, *.doc).

The text file containing all Authors' names, organizations, postal code, postal address, telephone, fax, E-mail, scientific topic of the paper.

It is possible to use **rar** or **zip** compressors and to transmit the files as an attachment.

Title page (specimen)

UDC

TITLE

Smith J.H., Cooper H.J.

E.A. Buketov Karaganda State University, Karaganda, Kazakhstan, email@for_correspondence.kz

Abstract: 5-6 sentences

Keywords: no less 3, but no more 10 words

Introduction

Article text. Article text. Article text. Article text. Article text. Article text. Article text. Article text. Article text. Article text Article text. Article text. Article text. Article text. Article text Article text. Article text. Article text. Article text Article text. Article text. Article text. Article text. Article text Article text. Article text. Article text. Article text. Article text…

References Format (specimen)

1 Nahar J., Wahedra M. Elastic scattering of positrons and electrons by argon. *Physical Rewiew A,* 2016, Vol. 35, No. 5, pp. 2051 – 2064.

2 Rivoalen H. Electrotubular heat exchanger in chemical industry. *Proceeding of the 12th Intern. Congress on Electricity Applications*. Birmingham, 2017, pp. 29 – 39.

3 Conrad H., Muhlbauer A., Thomas R. *Elektrothermische Verfahrenstechnik*. Vulkan-Verlag, Essen Publ.House, 2008, 240 p.

The authors should represent References according to the requirements of international journals on physics, but should to consult preliminarily for standard abbrevi-ations of journal's names.

For more information on references guidelines for journal publication you see Harvard reference system: http://www.emeraldgrouppublishing.com/authors/guides/write/harvard.htm?part=2